Diss. ETH No. 13107

Brownian Dynamics Simulation of Stable and of Coagulating Colloids in Aqueous Suspension

A dissertation submitted to the
SWISS FEDERAL INSTITUTE OF TECHNOLOGY
ZURICH

for the degree of
Doctor of Natural Sciences

presented by
Markus Hütter
Dipl. Phys. ETH
born on April 10, 1969
citizen of Schönenbuch, BL, Switzerland
and of Basel, BS, Switzerland

accepted on the recommendation of
Prof. Dr. H. C. Öttinger, examiner
Prof. Dr. L. J. Gauckler, co-examiner

Zürich, 1999

Acknowledgments

I would like to thank my advisor Prof. Dr. Hans Christian Öttinger for teaching me how to, and sometimes how not to, do research. His confidence in my work was very supporting and encouraged me a lot. I always had the freedom to follow my own ideas which I am very grateful for.

I would like to thank my co-advisor Prof. Dr. L. J. Gauckler, who initiated this project. The fact that I could spend my whole Ph.D. time at his institute gave me the opportunity to learn not only about colloid chemistry but also about other aspects of ceramics and materials science in general.

The quality of this manuscript has improved substantially through the help of Prof. G. Bayer and my friends Anja Bieberle, Jens Helbig, and Urs Schönholzer. I really admire their patience and staying power to carefully read the whole manuscript and would like to thank them for their helpful advice.

The members of the colloid group never ceased from getting me involved in experimental aspects, although my own work was mainly concerned with theoretical aspects of colloid science as well as with computer programming. I would like to thank them for doing so. In particular, I enjoyed the numerous thought provoking and fruitful discussions with Jens Helbig, Urs Schönholzer, and Hans Wyss. They often helped me to step back and to get a different perspective on the problems.

I would like to thank all my colleagues at the Polymer Physics Group and at the Institute of Nonmetallic Inorganic Materials for the good times we shared, not only in the office but also in our free time. I will always recall the ski trips to the Swiss mountains as well as our common journeys to foreign countries.

I would like to thank my parents for always believing in me. I am grateful for their constant support and encouragement during all these years.

The financial support from the Swiss National Science Foundation is gratefully acknowledged.

Table of Contents

Synopsis/ Zusammenfassung 1

Chapter 1 General Introduction

1.1 Background 6

1.2 Approach 11

1.3 Outline of the Thesis 13

1.4 References 15

Chapter 2 Stable Suspensions

2.1 Introduction 20

2.1.1 Electrostatic and Steric Stabilization 20

2.1.2 Suspensions in Equilibrium 23

2.1.3 Suspensions in Shear Flow 24

2.2 Simulation Method:
Nonequilibrium Brownian Dynamics Technique 27

2.2.1 Equations of Motion 27

2.2.2 Periodic Boundary Conditions 31

2.2.3 Linked-Cell List Method 33

2.2.4 Integration of the Equations 35

2.3 Equilibrium Properties 37

2.3.1 Simulation Input 37

2.3.2 Self Diffusion 41

2.3.3 Linear Viscoelastic Properties 48

2.3.4 Probing a Frequency Dependent Stokes-Einstein Relation 56

2.3.5 Summary and Conclusions 63

2.4 Simple Shear Flow 65

2.4.1 Simulation Input, Method 65

2.4.2 Shear Stress 67

2.4.3 Normal Stress Differences 73

2.4.4 Ordering at High Shear Rates 81

2.4.5 Long-Time Diffusion under Shear 88
2.4.6 Summary and Conclusions 90
2.5 Hydrodynamic Interaction 91
2.5.1 Many-Body Hydrodynamic Interactions 91
2.5.2 Implementation of Lubrication Forces 95
2.6 Efficient Simulation of Hydrodynamic Lubrication 108
2.6.1 Introduction 108
2.6.2 Multi-dimensional Definition of the "Kinetic Stochastic Integral" 110
2.6.3 Construction of a Numerical Integration Scheme .. 111
2.6.4 Conclusions 114
2.7 Simple Shear Flow Revisited 115
2.7.1 Simulation Input 115
2.7.2 Shear Stress 119
2.7.3 Normal Stresses 121
2.7.4 Performance 124
2.7.5 Summary and Conclusions 128
2.8 Summary and Conclusions 129
2.9 References 132

Chapter 3 Coagulation

3.1 Introduction 140
3.1.1 Colloidal Stability 140
3.1.2 Coagulation Kinetics 144
3.1.3 Structure of the Particle Network 146
3.2 Simulation Details 148
3.2.1 Rigid versus Stiff Bonds 148
3.2.2 Neglecting Hydrodynamic Interaction 151
3.2.3 Liquid-Solid Transition at Constant Volume 152
3.2.4 Simulation Input 153
3.2.5 Performance of the Stiff-Bond Algorithm 157
3.3 Reaction Rates 160
3.3.1 Monitoring the Coagulation 160
3.3.2 Characteristic Time Scales 167
3.3.3 Summary and Conclusions 180

3.4 Structural Development 182
3.4.1 Nucleation 182
3.4.2 Cross-Linking 188
3.4.3 Network Structure 196
3.4.4 Summary and Conclusions 210
3.5 Summary and Conclusions 212
3.6 References 215

Chapter 4 Outlook

4.1 Stable Suspension 220
4.1.1 General 220
4.1.2 Hydrodynamic Interaction 221
4.2 Coagulation and Particle Gel 223
4.2.1 Way of Destabilization 223
4.2.2 Bonds and Their Effects 224
4.3 References 226

Appendix: Calculation of the Resistance Tensors 229

Curriculum Vitae 233

List of Symbols 235

Synopsis

Colloidal suspensions exhibit complex material properties such as the non-Newtonian flow behavior in the stable state and the nonlinear viscoelasticity of the coagulated wet bodies. These properties are governed by the microstructure which, in turn, originates from the particle dynamics and the interaction forces. Although much is known about the particle interactions themselves, only little is known about their effect on the microstructure of the whole system.

Two main goals are pursued in this thesis. On the one hand, the equilibrium properties and the effect of simple shear on the microstructure and the rheological behavior of monodisperse colloidal suspensions are studied. For this purpose, we have developed a nonequilibrium Brownian dynamics algorithm which is then extended to account for many-body hydrodynamic lubrication forces in an efficient manner. On the other hand, the destabilization of electrostatically stabilized suspensions is examined with emphasis on the coagulation rates and on the development of the particle network. For this purpose, a Brownian dynamics algorithm has been developed which is capable of efficiently handling the increasing number of bonds, i.e. constraints, during the coagulation process.

In the first part (Chapter 2), stable suspensions are studied under equilibrium conditions for various solid contents, neglecting many-body hydrodynamic interactions. In particular, we examine the stress autocorrelation function and the self diffusion of the particles. Both quantities indicate that the suspension attains solid-like properties as the solid content is raised. We test the validity of an extended Stokes-Einstein relation between the stress relaxation modulus and the mean square displacement of the particles.

Furthermore, the influence of shear flow on the shear stress as well as on the normal stress differences is studied. The suspensions show pronounced shear thinning, which is enhanced by increasing the solid content. This shear thinning is accompanied by a disorder-order transition, where the particles arrange in a hexagonally ordered array of strings. We find that the elements of the anisotropic self-diffusion tensor are a more sensitive measure for the onset of shear ordering than the viscosity. The analysis of the self-diffusion tensor is also used to reconstruct the hopping mechanism of strings which slide over each other due to their relative velocity. No shear thickening is observed if many-body hydrodynamic forces are neglected.

In order to produce shear thickening at high shear rates, many-body hydrodynamic interaction needs to be included. This study is restricted to the short range hydrodynamic lubrication; long-range interactions are neglected. However, even in this approximation the handling of large particle numbers is prohibitive for standard numerical techniques, in particular, due to the implication of the stochastic Brownian forces. In order to allow large scale simulations, we have devel-

oped an efficient simulation scheme which is based on a thorough analysis of stochastic calculus and the stochastic integral definitions.

In the second part (Chapter 3), the destabilization of colloidal suspensions due to reduction of the double layer repulsion is studied. Various time scales are identified and their dependence on the solid content and the interaction potential is measured. The lowering of the coagulation times due to raising solid content and/or due to more attraction between the particles is quantified. The comparison of the different time scales allows to draw conclusions on the mechanism of bond formation between clusters in the intermediate stages of coagulation.

The structural changes in the coagulating suspensions are monitored by the increasing degree of cross-linking as well as by the pair correlation function and by the bond angle distribution function. In the absence of an energy barrier in the interaction potential, the coagulated structures increasingly show quenching for higher solid contents. By the introduction of a shallow secondary energy minimum the quenching effect can be reduced significantly and the degree of cross-linking is increased. It is therefore suggested that slow coagulation is preferable if the main interest is in a low degree of quenching, in a high degree of cross-linking and in good mechanical properties of the final particle network.

Zusammenfassung

Kolloidale Suspensionen zeigen komplexe Materialeigenschaften, wie zum Beispiel das nicht-Newtonsche Fließverhalten im stabilen Zustand oder die nichtlineare Viskoelastizität des koagulierten nassen Körpers. Diese Eigenschaften sind durch die Mikrostruktur bestimmt, welche ihrerseits auf die Dynamik der Partikel und auf die Wechselwirkungskräfte zurückgeht. Obwohl viel über die Partikelwechselwirkungen bekannt ist, weiß man nur wenig über ihre Auswirkungen auf die Mikrostruktur des Gesamtsystems.

In dieser Doktorarbeit werden zwei Hauptziele verfolgt. Auf der einen Seite werden die Gleichgewichtseigenschaften sowie der Einfluß von Scherströmung auf die Mikrostruktur und auf die rheologischen Eigenschaften von monodispersen kolloidalen Suspensionen untersucht. Zu diesem Zweck haben wir einen Algorithmus für Brownsche Nichtgleichgewichts-Dynamik entwickelt. Dieser wurde dann erweitert um die hydrodynamischen Vielteilchenwechselwirkungen in effizienter Weise zu behandeln. Auf der anderen Seite wird die Destabilisierung von elektrostatisch stabilisierten Suspensionen besonders hinsichtlich der Koagulationsraten und der Entwicklung des Partikelnetzwerkes untersucht. Um dies zu erreichen, wurde ein Algorithmus für Brownsche Dynamik entwikkelt, der es erlaubt, die während der Koagulation stetig zunehmende Anzahl von Bindungen effizient einzubeziehen.

Im ersten Teil (Kapitel 2) werden stabile Suspensionen unter Gleichgewichtsbedingungen für verschiedene Feststoffgehalte unter Vernachlässigung der hydrodynamischen Vielteilchenwechselwirkung untersucht. Hierbei wird sowohl auf die Spannungskorrelationsfunktion als auch auf die Selbstdiffusion der Partikel Wert gelegt. Beide Größen deuten darauf hin, daß sich die Suspension bei Erhöhung des Feststoffgehaltes in zunehmendem Masse wie ein Festkörper verhält. Danach wird die Gültigkeit einer erweiterten Stokes-Einstein Beziehung zwischen dem Spannungsrelaxationsmodul und dem mittleren Verschiebungsquadrat der Partikel überprüft.

Im weiteren wird der Einfluß von Scherströmung auf die Scherspannung sowie auf die Normalspannungsdifferenzen untersucht. Die Suspensionen zeigen eine deutliche Scherverflüssigung, welche durch Erhöhung des Feststoffgehaltes verstärkt wird. Diese Scherverflüssigung geht mit einer Strukturierung der vorgangs ungeordneten Partikel-konfiguration einher, wobei sich die Partikel zu Ketten gruppieren, welche hexagonal angeordnet sind. Wir zeigen, daß die Komponenten des Selbstdiffusionstensors ein empfindlicheres Maß für das Einsetzen der Scherordnung sind als die Viskosität. Aus der Kenntnis über die Selbstdiffusion läßt sich auch der Hüpfmechanismus rekonstruieren, durch den sich Partikelketten aneinander vorbeigewegen. Solange die hydrodynamischen Vielteilchenwechselwirkungen vernachlässigt werden, kann an der Suspension keine Scherverfestigung beobachtet werden.

Damit die simulierte Suspension bei hohen Scherraten Scherverfestigung zeigt, ist es notwendig, hydrodynamische Vielteilchenwechselwirkungen zu betrachten. In dieser Arbeit werden lediglich kurzreichweitige Wechselwirkungen betrachtet, langreichweitige hydrodynamische Effekte werden vernachlässigt. Trotz dieser Näherung ist die Behandlung von Systemen mit vielen Partikeln mittels numerischer Standardmethoden immer noch nicht durchführbar, vor allem wegen der stochastischen Brownschen Kräfte. Um Simulationen von Systemen mit vielen Partikeln zu ermöglichen, haben wir eine effiziente Simulationsmethode entwickelt, welcher ein detailliertes Studium des stochastischen Kalküls und der Definitionen von stochastischen Integralen zugrunde liegt.

Im zweiten Teil (Kapitel 3) wird die Destabilisierung von kolloidalen Suspensionen untersucht, welche durch eine Verminderung der Doppelschichtabstossung hervorgerufen wird. Verschiedene Zeitskalen werden identifiziert und ihre Abhängigkeit vom Feststoffgehalt und vom Oberflächenpotential gemessen. Die Erniedrigung der Koagulationszeiten aufgrund höheren Feststoffgehaltes oder aufgrund stärkerer Anziehung zwischen den Partikeln wird quantifiziert. Ein Vergleich der verschiedenen Zeitskalen erlaubt uns, Schlußfolgerungen über den Bindungsmechanismus zwischen Aggregaten in Zwischenstadien der Koagulation zu ziehen.

Die strukturellen Änderungen in der koagulierenden Suspension werden sowohl anhand des zunehmenden Vernetzungsgrades als auch anhand der Paarkorrelationsfunktion und der Bindungswinkelverteilung verfolgt. Unter Abwesenheit einer Energiebarriere im Wechselwirkungspotential sieht die Struktur des Partikelnetzwerkes bei Erhöhung des Feststoffgehaltes in zunehmendem Masse der einer abgeschreckten, eingefrorenen Flüssigkeit ähnlich. Der Grad an Abschreckung kann durch die Einführung eines schwachen sekundären Minimums im Wechselwirkungspotential wesentlich reduziert werden, was mit einer Erhöhung des Vernetzungsgrades einhergeht. Es wird deshalb vorgeschlagen, eine Suspension über ein schwaches sekundäres Minimum zu destabilisieren sofern das Hauptinteresse einem niederen Grad an Abschreckung, d.h. einem hohen Vernetzungsgrad und guten mechanischen Eigenschaften des Partikelnetzwerkes gilt.

Chapter 1

General Introduction

Abstract

An overview over some experimental aspects of colloidal suspensions is given in section 1.1. In particular, the behavior under shear flow and the gelation of dense systems are highlighted as they are of major interest for the simulations in this study. Section 1.2 describes various simulation techniques that have been used to model colloidal suspensions and gives reasons for why this study employed the nonequilibrium Brownian dynamics technique. Section 1.3 concludes the chapter with an outline of the thesis.

1.1 Background

Stabilized colloidal suspensions and their transition to destabilized suspensions are involved in many different production processes in industry. Processing of food, paint, pharmaceuticals, cosmetics, lubricants, drug delivery systems and increasingly also the manufacturing of high quality ceramic parts are examples for the broad range of applications of these complex fluids.

The interest in gaining a better understanding of stable as well as of destabilized colloidal suspensions, however, results not only from the large scale industrial use. There are many fundamental aspects which make them an interesting topic to study on its own. The following three points will be considered in detail below: the use of colloids as model for atomic systems, the complex flow behavior, and the process of coagulation. With regard to the further chapters of this study, a view-point that emphasizes a particle interpretation is adopted whenever possible.

a) Colloids: a model for atomic systems

The main difference between complex fluids (e.g. polymeric solutions and colloidal suspensions) and simple atomic fluids (e.g. water) is the combination of very different components: the suspending medium and the relatively large particles. Thus, for a thorough understanding of colloidal systems one should be aware of the manifold length and time scales involved. The length scales range from the size of the molecules of the suspending medium, over the submicron sized colloidal particles, up to the size of the particle flocs and aggregates in the visible regime. The time scales cover an equally impressive range, which extends from the femtosecond motions of the suspension atoms up to the seconds of a structural relaxation or up to hours in a coagulation process of the colloidal particle system. Having these characteristics in mind, one can understand that separating the relevant from the irrelevant features is a rather challenging task. This may be among the reasons why the understanding of simple atomic fluids has progressed much more in the last decades than it has for complex fluids.

Due to the slow time scales with respect to the femtosecond motions in atomic systems, one can see the colloidal particles under certain conditions as large and

slow atoms. In this way relaxation related phenomena in atomic systems are moved to experimentally accessible time scales.

b) Complex flow behavior

The flow behavior of colloidal suspensions, which are a typical example for complex fluids, is an interesting topic of its own. In the past decades, enormous effort has been spent on getting a better understanding of flowing suspensions by means of rheological as well as structural investigations.

In particular, the shear rate dependent viscosity and the first and second normal stress differences are in the focus of numerous studies. When increasing the shear rate in a colloidal suspension, the viscosity of the system first undergoes a shear thinning transition [85Kru, 89Wer] (region ① in Fig. 1.1).

Further increase of the shear rate, however, results in shear thickening [89Bar, 90Boe] (region ② in Fig. 1.1). Throughout these shear rate regimes, the suspension may also have viscoelastic properties [92Boe, 94Shi].

The shear thinning transition, which can easily be observed in experiments on colloidal suspensions, should in principle also occur in atomic fluids. However, the very fast time scales in atomic fluids shifts this transition to very high shear rates, which hardly can be realized under laboratory conditions. This emphasizes again the fundamental need for studying colloidal suspensions.

Both the shear thinning and the shear thickening transitions have been suggested to be accompanied by structural transitions in the particle arrangements. Small angle neutron scattering (SANS) and light scattering experiments are

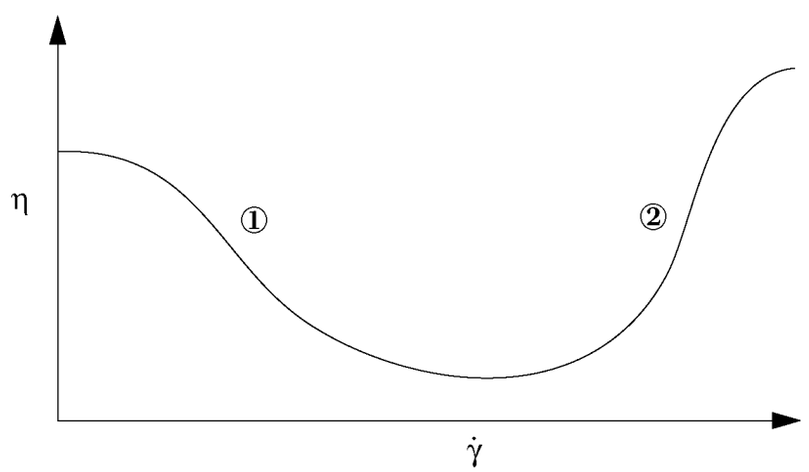

Fig. 1.1: Typical shear rate-viscosity dependence of a colloidal suspension: ① shear thinning and ② shear thickening transition.

among the techniques most often used to study the particle configuration. Several scattering experiments have shown that the shear thinning transition may go along with an ordering of the particles [95Cho, 97Dux, 98Dux]. Concerning the onset of shear thickening transition, two reasons are under debate. Some authors claim, that the thickening is mainly associated with an order-disorder transition [92Hae, 98Hof], whereas others attribute the origin of the thickening to the formation of so-called nonpermanent hydrodynamic clusters [95Ben, 96Ben].

In computer simulations, shear thickening has also been observed [89Bos, 96Phu], as well as the existence of the proposed hydrodynamic clusters. It is not clear if these clusters are a necessary condition for the onset of shear thickening and if the shear thickening is always accompanied by an order-disorder transition.

The experimental results presented above cover both macroscopic and microscopic properties of colloidal suspensions. In some cases a relation between the two could be established, in others this still needs to be done.

c) Coagulation and gelation

Apart from the interesting rheological behavior of electrostatically stabilized colloidal suspensions, their solidification is an other main point of interest. The possibility of directly altering the interaction between the particles is in contrast to atomic fluids. Inducing the transition from liquid to solid in colloidal suspensions does not need a change in pressure or temperature, but can rather be achieved by raising the ionic strength I or changing the pH in the suspending liquid (Fig. 1.2).

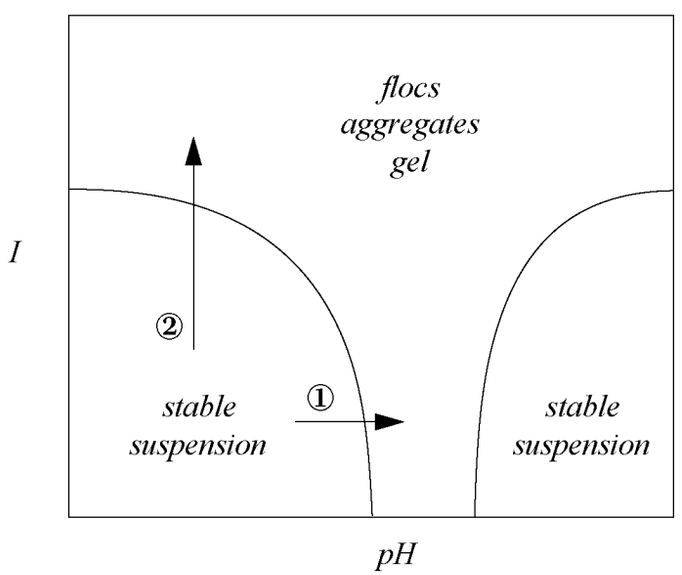

Fig. 1.2: The two regions of stability for a colloidal suspension depending on the pH and the ionic strength I. Possible pathways to destabilization: ① pH-change, ② ionic strength-change.

Knowing the dependence of the interaction potential on the ionic strength and on the pH offers a method to induce the flocculation and gelation, respectively. This method is nowadays used, for example in colloidal processing, where an enzyme reaction shifts the pH from the repulsive to the attractive regime, leading to a network of particles of high spatial homogeneity [94Gra].

There are two main areas of interest when studying the destabilization of colloidal suspensions, the coagulation kinetics and the resulting structure. Apart from any other parameter under consideration, the density of the suspension determines the particle configuration of the destabilized suspension in a fundamental manner. If the solid content of particles is lower than a certain percolation threshold, the destabilization leads to loose flocs and aggregates of fractal nature [84Wei, 86Wei, 87Mar, 97Bur]. On-lattice computer simulations, have not only confirmed the fractal nature of the flocs and aggregates in a qualitative manner, but also lead to the same fractal dimensions as those determined from experiments [88Mea1, 88Mea2]. In contrast, a solid content above the percolation threshold leads to a gel-like network. For concentrated suspensions, less experimental data are available on the structure due to the high degree of multiple scattering. In contrast to the influence of the solid content, the effect of the interparticle potential on the structure is more subtle and will be discussed later in detail.

Besides the particle arrangement, also the coagulation kinetics have been studied using optical techniques. They are not limited to measure only one characteristic time scale of the coagulation process [87Cam, 96Bar, 96Hol]. Recently, it has even been possible to monitor the time dependent populations of particle singlets, doublets and triplets, allowing for a much more refined comparison with theoretical model predictions [97Hol].

A number of experiments have revealed the destabilization kinetics and the microstructure of coagulating suspensions. Now, the relation of these results to parameters such as interparticle potential and solid content is of primary interest.

All three fields in colloid research which have been specified above suggest that a link between the microscopic world of the particles and our macroscopic world is desirable. But, a satisfactory interpretation of the flow behavior and of the coagulation process, respectively, can not directly be given in terms of first principles. Although colloid physics and chemistry offer much of qualitative guidance to understand certain features of the system, the interplay of various effects in this many-particle system is prohibitive for making quantitative predictions from basic principles. For example, the critical shear rates for both the shear thinning as well as the shear thickening transition can be estimated as functions of particle size and solid content in the form of scaling laws [77Cha, 96Ben, 97Oga, 98Hof]. However, the corresponding particle configuration is still unknown. Considering the coagulation process, the well known DLVO-theory by

Derjaguin, Landau, Vervey and Overbeek [89Rus, 91Isr] allows for a rather accurate prediction of the rate of coagulation [91Wan, 98Beh]. But, as for flowing suspensions, the structure is far from being determined.

In order to close the gap between first principles, which govern the particle dynamics, and the macroscopic behavior of colloidal suspensions, one needs to design model systems. The most common simplification when going from the real system in the experimental setup to the model system is the approximation of the particle shape and size distribution by a monomodal, or sometimes bimodal, distribution of spheres. Further approximations include the reduction of the many-particle interactions to only pair-interactions, as described by the DLVO-theory. It captures the main features of particle interaction in a colloidal suspension in a two-body interaction, van der Waals attraction and electric double layer repulsion, and is often used when formulating stability criteria or when estimating the strength of a network.

The derivation of the macroscopically observed material properties from the underlying dynamics of the spheres can then either be achieved by theoretical or computational techniques. The advantage of theoretical over computational techniques is the capability to capture the result in a analytical from. The main disadvantage of the purely theoretical approach is that further simplifications, often the reduction of the many-body to a two-body problem, are needed so that the problem can be handled. In contrast, the simulations allow one to treat large systems of pairwise interacting particles, but they do not lead to any analytical link between the input and output of the simulations. A series of simulations with variable input parameters has therefore to be done in order to understand the dependencies of the material properties on the conditions given.

1.2 Approach

The main interest of this work is to establish a direct connection between the first principles governing the particle dynamics and the macroscopically observed material properties in colloidal suspensions. Computer simulations are the method chosen in this study to achieve this goal. The results obtained can then be compared with the real experiment in the laboratory as well as with the theoretical model predictions. On one hand, this can help to judge whether the model studied in the computer simulation was too crude for describing the real system. On the other hand, one can test whether the theoretical predictions are detailed enough to grasp the essential features of the multi-particle system. Computer simulations shall therefore be viewed as an intermediate level between the real world and the analytically accessible, very simplified models.

The simulation techniques used for studying the behavior of colloidal suspensions cover, as the real world system itself, a large range of spatial resolutions. Molecular dynamics simulations are used to study the atomic details of the double layer interaction and have even been used to model the flow behavior of the much larger colloidal particles themselves [90Hes, 95Hey]. The latter use of molecular dynamics does, however, not include the Brownian motion which is ubiquitous in colloidal suspensions due to the random kicks of the solvent molecules.

Thus, rather than using the time-reversible molecular simulation technique, one is led to use so-called mesoscopic simulation techniques for the particle dynamics. The most commonly used are the Brownian dynamics [90Bha, 93Hey, 94Hey, 96But, 96Ras] and the Stokesian dynamics technique [84Bos, 88Bra, 93Bra, 96Phu]. Both include dissipative friction forces and random forces due to the noise of the solvent molecules. Brownian dynamics further assumes relaxed, i.e. equilibrated, particle momenta. In contrary, Stokesian dynamics in the original sense uses unrelaxed momenta and, much more important, includes the many-particle hydrodynamic interactions. They are supposed to be responsible for shear thickening at high shear rates. In recent years, the differences between the two techniques have been diminished as Stokesian dynamics sometimes uses relaxed momenta and Brownian dynamics includes hydrodynamic interaction. The Brownian dynamics technique has also been used to study both the coagulation kinetics in dense suspensions [85Ans, 87Ans] as well as the structure [96Bos] and mechanical properties [98Whi] of the resulting gel.

The most coarse grained level of modeling a colloidal suspension is the continuum description, which can be used to model the flow behavior of the suspension in a complex geometry or the plastic deformation of the coagulated body. The corresponding equations are solved by finite element methods. In this case, already a lot of information about the material characteristics has to be built into the model by means of constitutive equations, such as the stress-strain relationship. Thus, this technique is not suitable for establishing the link between first principles and material properties.

Apart from all these dynamic simulation techniques mentioned above, static on-lattice Monte-Carlo techniques are used especially when studying the fractal nature of flocs and aggregates in dilute suspensions [88Mea1, 88Mea2, 95Mea, 96Shi]. They allow to study large samples, which is necessary when characterizing fractal properties and their scaling laws. The two main drawbacks of these on-lattice simulations are the undefined link to the real dynamic process of coagulation and the lack of any spatial detail as far as bond angles and local structure are concerned.

The simulation technique, which is best suited for establishing the link between the basic principles of particle dynamics and macroscopically observable material properties, is most probably the Brownian dynamics simulation. It is applied in this work for both studying the flow behavior of the stable suspension as well as for monitoring the process of destabilization.

The software used for all simulations reported in this study have been developed by the author himself in order to have the possibility of optimizing the code and of facilitating any further extensions. The latter include the implementation of many-body hydrodynamic interaction and the touching particles during gelation. The programming language used was standard `Fortran77`.

1.3 Outline of the Thesis

The main objectives of this thesis are: to develop a tool for studying the particle dynamics, the structure and material properties of dense colloidal suspensions in equilibrium as well as under simple shear conditions; to include efficiently the hydrodynamic interactions, which are necessary for understanding the shear thickening behavior; and to study both the coagulation kinetics and the resulting particle structure when destabilizing the suspension. The thesis is divided into two main parts. The first one (Chapter 2) deals with stable suspensions, whereas the second part (Chapter 3) is concerned with the destabilization process and the resulting structure.

The first of the two main parts begins with a survey over experimental techniques and their results on both equilibrium as well as flow properties of stable colloidal suspensions (section 2.1). The basics of the Brownian dynamics simulation method are then presented in section 2.2 without including the hydrodynamic interactions, which are considered later in sections 2.5 -2.7. This method is shown to be an obvious implementation of the relevant underlying physics and some details concerning the algorithm are presented, such as the periodic boundary conditions and the efficiency of the algorithm.

In section 2.3, several properties of the particle system under equilibrium conditions are examined, including their dependence on the solid content of the suspension. The mean square displacements of the particles are measured, as well as the stress-autocorrelation function. The latter is then used to determine the zero-shear rate viscosity by means of the Green-Kubo relation [91Kub]. The validity of a generalized, frequency-dependent Stokes-Einstein relationship, which relates the relaxation modulus of the suspension to the mean square displacements of the particles, is tested. The behavior under simple shear is the focus of section 2.4, where the viscosity, the first and second normal stress differences as well as the shear rate dependent diffusion coefficients are examined in detail.

In order to be able to study the phenomenon of shear thickening, the theoretical basis for an efficient implementation of the hydrodynamic interactions is given in sections 2.5 and 2.6. It is shown how all complications associated with the inclusion of this hydrodynamic interaction can be solved in such a way that also large systems can be handled. This is one of the major achievements of this study and can generally be considered to be a corner-stone for the simulation of many-particle hydrodynamic interaction in systems with a large number of particles. As a result of implementing the hydrodynamic interaction, the suspension is shown to exhibit shear thickening (section 2.7), which has not been observed when neglecting hydrodynamic interaction.

The second part, which is concerned with the destabilization process, begins with an overview of experiments in section 3.1, including certain relations to theoretical models that help to predict or interpret experimental findings. In

section 3.2, the changes introduced to the simulation tool, which are necessary in order to treat the touching particles, are discussed. The efficiency of this modified algorithm with increasing coordination, i.e. coagulation, is studied. In the following chapters, computer simulations of the destabilization process are performed for various interaction potentials and solid contents.

Section 3.3 is concerned with the coagulation kinetics, especially with the scaling of the characteristic coagulation times in potential parameters and solid content. Furthermore, parameters describing the degree of coordination in the structure are monitored as the coagulation proceeds. These functions are then used to give a criterion on the completeness of the coagulation process. Information on the development of the network structure is then given in section 3.4. The long range properties of the structure are studied using the pair-correlation function. The study of the short range structure by means of the distribution of bond angles concludes the second part of the thesis. It will be discussed in as far these structural informations can be used for characterizing the final gel structure which is not accessible with this type of simulation.

In Chapter 4, an outlook and recommendations for possible future work conclude this study.

1.4 References

[77Cha] C. E. Chaffey, "Mechanisms and equations for shear thinning and thickening in dispersions", *Coll. & Polym. Sci.*, *255*, 691–698 (1977).

[84Bos] G. Bossis and J. F. Brady, "Dynamic simulation of sheared suspensions. I. General method", *J. Chem. Phys.*, *80*(10), 5141–5154 (1984).

[84Wei] D. A. Weitz and M. Oliveria, "Fractal structures formed by kinetic aggregation of aqueous gold colloids", *Phys. Rev. Lett.*, *52*(16), 1433–1436 (1984).

[85Ans] G. C. Ansell and E. Dickinson, "Aggregate structure and coagulation kinetics in a concentrated dispersion of interacting colloidal particles", *Chem. Phys. Lett.*, *122*(6), 594–598 (1985).

[85Kru] C. G. de Kruif, E. M. F. van Iersel, A. Vrij, and W. B. Russel, "Hard-sphere colloidal dispersions: viscosity as a function of shear-rate and volume fraction", *J. Chem. Phys.*, *83*(9), 4717–4725 (1985).

[86Wei] D. A. Weitz and Y. Lin, "Dynamic scaling of cluster-mass distributions in kinetic colloid aggregation", *Phys. Rev. Lett.*, *57*(16), 2037–2040 (1986).

[87Ans] G. C. Ansell and E. Dickinson, "Brownian dynamics simulation of the formation of colloidal aggregate and sediment structure", *Farad. Disc. Chem. Soc.*, *83*, 167–177 (1987).

[87Cam] C. Cametti, P. Codastefano, and P. Tartaglia, "Light-scattering measurements of slow coagulation in colloids: Deviations from assymptotic time scaling", *Phys. Rev. A*, *36*(10), 4916–4921 (1987).

[87Mar] J. E. Martin, "Slow aggregation of colloidal silica", *Phys. Rev. A*, *36*(7), 3415–3426 (1987).

[88Bra] J. F. Brady and G. Bossis, "Stokesian dynamics", *Ann. Rev. Fluid Mech.*, *20*, 111–157 (1988).

[88Mea1] P. Meakin, "Fractal aggregates", *Adv. Coll. Interf. Sci.*, *28*, 249–331 (1988).

[88Mea2] P. Meakin, "Models for colloidal aggregation", *Ann. Rev. Phys. Chem.*, *39*, 237–267 (1988).

[89Bar] H. A. Barnes, "Shear-thickening (dilatancy) in suspensions of nonaggregating solid particles dispersed in Newtonian liquids", *J. Rheol.*, *33*(2), 329–366 (1989).

[89Bos] G. Bossis and J. F. Brady, "The rheology of Brownian suspensions", *J. Chem. Phys.*, *91*(3), 1866–1874 (1989).

[89Rus] W. B. Russel, D. A. Saville, and W. R. Schowalter, ***Colloidal dispersions***, Cambridge Univ. Press (1989).

[89Wer] J. C. V. der Werff and C. G. de Kruif, "Hard-sphere colloidal dispersions: the scaling of rheological properties with particle size, volume fraction, and shear rate", *J. Rheol.*, *33*(3), 421–454 (1989).

[90Bha] D. Bhattacharia and E. Clementi, "Brownian dynamic simulations of a complex fluid system", MOTECC (1990).

[90Boe] W. H. Boersma, J. Laven, and H. N. Stein, "Shear thickening (dilatancy) in concentrated dispersions", *AIChE J.*, *36*(3), 321–332 (1990).

[90Hes] S. Hess and W. Loose, "Flow properties and shear-induced structural changes in fluids: a case study on the interplay between theory, simulation, experiment and application", *Ber. Bunsenges. Phys. Chem.*, *94*, 216–222 (1990).

[91Isr] J. Israelachvili, ***Intermolecular and surface forces***, Academic Press, London, 2nd ed. (1991).

[91Kub] R. Kubo, M. Toda, and N. Hashitsume, ***Statistical physics II: nonequilibrium mechanics***, No. 31 in Solid-State Sciences, Springer, 2 ed. (1991).

[91Wan] Q. Wang, "On colloidal suspension Brownian stability ratios: theoretical approaches", *J. Coll. Interf. Sci.*, *145*(1), 99–107 (1991).

[92Boe] W. H. Boersma, J. Laven, and H. N. Stein, "Viscoelastic properties of concentrated shear thickening dispersions", *J. Coll. Interf. Sci.*, *149*, 10–22 (1992).

[92Hae] P. D'Haene, G. G. Fuller, and J. Mewis, ***Theoretical and Applied Rheology***, Elsevier, Amsterdam, Netherlands, chapter Shear thickening effect in concentrated dispersions, pp. 595–597 (1992).

[93Bra] J. F. Brady, "The rheological behaviour of concentrated colloidal dispersions", *J. Chem. Phys.*, *99*(1), 567–581 (1993).

[93Hey] D. M. Heyes and J. R. Melrose, "Brownian dynamics simulations of model hard-sphere suspensions", *J. Non-Newt. Fluid Flow*, *46*, 1–28 (1993).

[94Gra] T. J. Graule, F. H. Baader, and L. J. Gauckler, "Enzyme catalysis of ceramic forming", *J. Mat. Edu.*, *16*, 243–267 (1994).

[94Hey] M. D. Heyes and P. J. Mitchell, "Self-diffusion and viscoelasticity of dense hard-sphere colloids", *J. Chem. Soc. Farad. Trans.*, *90*(13), 1931–1940 (1994).

[94Shi] T. Shikata, "Viscoelastic behaviour of concentrated spherical suspensions", *J. Rheol.*, *38*(3), 601–616 (1994).

[95Ben] J. W. Bender and N. J. Wagner, "Optical measurement of the contributions of colloidal forces to the rheology of concentrated suspensions", *J. Coll. Interf. Sci.*, *172*(1), 171–184 (1995).

[95Cho] M. K. Chow and C. F. Zukoski, "Nonequilibrium behaviour of dense suspensions of uniform particles: volume fraction and size dependence of rheology and microstructure", *J. Rheol.*, *39*(1), 33–60 (1995).

[95Hey] D. M. Heyes and P. J. Mitchell, "Nonequilibrium molecular and Brownian dynamics simulations of shear thinning of inverse power fluids", *J. Mol. Phys.*, *84*(2), 261–280 (1995).

[95Mea] P. Meakin, "Progress in DLA research", *Physica D*, *86*, 104–112 (1995).

[96Bar] S. Barany, M. A. C. Stuart, and G. J. Fleer, "Coagulation rate of silica dispersions investigated by single-particle optical sizing", *Coll. Surf. A*, *106*(2-3), 213–221 (1996).

[96Ben] J. W. Bender and N. J. Wagner, "Reversible shear thickening in monodisperse and bidisperse colloidal dispersions", *J. Rheol.*, *40*(5), 899–916 (1996).

[96Bos] M. T. A. Bos and J. H. J. van Opheusden, "Brownian dynamics simulation of gelation and aging in interacting colloidal systems", *Phys. Rev. E*, *53*(5), 5044–5050 (1996).

[96But] S. Butler and P. Harrowell, "Shear induced ordering in simulations of colloidal suspensions: oscillatory shear and computational artefacts", *J. Chem. Phys.*, *105*(2), 605–613 (1996).

[96Hol] H. Holthoff, S. U. Egelhaaf, M. Borkovec, P. Schurtenberger, and H. Sticher, "Coagulation rate measurements of colloidal particles by simultaneous static and dynamic light scattering", *Langmuir*, *12*(23), 5541–5549 (1996).

[96Phu] T. N. Phung, J. F. Brady, and G. Bossis, "Stokesian Dynamics simulation of Brownian suspensions", *J. Fluid Mech.*, *313*, 181–207 (1996).

[96Ras] S. R. Rastogi, N. J. Wagner, and S. R. Lustig, "Rheology, self-diffusion and microstructure of chraged colloids under simple shear by massively-parallel nonequilibrium Brownian dynamics", *J. Chem. Phys.*, *104*(22), 9234–9248 (1996).

[96Shi] W. Y. Shih, W.-H. Shih, and I. A. Aksay, "Heteroflocculation in binary colloidal suspensions: Monte Carlo simulations", *J. Am. Ceram. Soc.*, *79*(10), 2587–2591 (1996).

[97Bur] J. L. Burns, Y. Yan, G. J. Jameson, and S. Biggs, "A light scattering study of the fractal aggregation behaviour of a model colloidal system", *Langmuir*, *13*(24), 6413–6420 (1997).

[97Dux] C. Dux and H. Versmold, "Light diffraction from shear-ordered colloidal dispersions", *Phys. Rev. Lett.*, *78*(9), 1811–1814 (1997).

[97Hol] H. Holthoff, A. Schmitt, A. Fernández-Barbero, M. Borkovec, M. A. Cabrerízo-Vílchez, P. Schurtenberger, and R. Higalgo-Álvarez, "Measurement of absolute coagulation rate constants for colloidal particles: comparison of single and multiparticle light scattering techniques", *J. Coll. Interf. Sci.*, *192*, 463–470 (1997).

[97Oga] A. Ogawa, H. Yamada, S. Matsuda, and K. Okajima, "Viscosity equation for concentrated suspensions of charged colloidal particles", *J. Rheol.*, *41*(3), 769–785 (1997).

[98Beh] S. H. Behrens, M. Borkovec, and P. Schurtenberger, "Aggregation in charge-stabilized colloidal suspensions revisited", *Langmuir*, *14*, 1951–1954 (1998).

[98Dux] C. Dux, S. Musa, V. Reus, H. Versmold, D. Schwahn, and P. Lindner, "Small angle neutron scattering experiments from colloidal dispersions at rest and under shear conditions", *J. Chem. Phys.*, *109*(6), 2556–2561 (1998).

[98Hof] R. L. Hoffman, "Explanations for the cause of shear thickening in concentrated colloidal suspensions", *J. Rheol.*, *42*(1), 111–123 (1998).

[98Whi] M. Whittle and E. Dickinson, "Large deformation rheological behaviour of a model particle gel", *J. Chem. Soc. Farad. Trans.*, *94*(16), 2453–2462 (1998).

Chapter 2

Stable Suspensions

Abstract

Chapter 2 is concerned with the properties of stable colloidal suspensions. After a brief introduction (section 2.1), the Brownian dynamics simulation method is presented (section 2.2). Subsequently, the simulation results for the suspension at equilibrium (section 2.3) and in shear flow (section 2.4) are discussed. This is followed by a detailed analysis of the influence of many-body hydrodynamic interaction on the high shear rate rheology and a corresponding efficient simulation scheme is presented (section 2.5 and 2.6). The chapter is concluded by simulation results from a shear thickening suspension at high shear rates (section 2.7).

2.1 Introduction

An overview of the stabilization of colloidal suspensions is given in subsection 2.1.1. The following two subsections highlight the fundamental aspects of suspensions at equilibrium and in shear flow. There, the focus is not only on the suspension properties and behavior, but also on the experimental techniques that have been used. Attention is paid to experiments that illuminate the relation between the microscopic particle level and the macroscopic material characteristics.

For a general introduction to the field of stable colloidal systems, the reader is referred to the book entitled "Colloidal Dispersions" by Russel, Saville and Schowalter [89Rus].

2.1.1 Electrostatic and Steric Stabilization

The tendency of colloidal particles to form aggregates has already been observed in the nineteenth century by microscopic observations. The reason for this particle attraction was explained in the 1920s by the van der Waals forces between molecules [89Rus, 91Isr]. More detailed studies on the dispersion forces followed [36Boe, 37Ham]. Hence, the stabilization of colloidal suspensions has become a central topic in colloid science [48Ver, 89Hun]. There are basically two ways to compensate the van der Waals attraction, namely by electrostatic and/or by steric stabilization [89Rus, 91Isr], which will be discussed briefly in the following.

a) Electrostatic Stabilization

In an aqueous suspension of oxide particles, hydroxyl groups are produced on the particle surface (*M-OH*). These groups then induce a charge on the particle surface by reacting with the H^+- and OH^--ions of the suspending medium:

$$\begin{array}{ccccc} low\ pH & & M\text{-}OH & & high\ pH \\ M\text{-}OH_2^+ & \leftrightarrows & & \leftrightarrows & M\text{-}(OH)_2^- \end{array} \qquad (2.1)$$

The sign of the surface charge therefore depends on the pH of the suspension. In order to maintain charge neutrality, the surface charge is compensated by counter-ions in the solvent. These ions arrange in a diffuse double layer around the colloidal particle because their distribution is not only controlled by electrostatics but also by thermodynamics: thermal equilibrium requires that the concentration of counter-ions follows the Boltzmann distribution, leading to the Poisson-Boltzmann equation for the potential of the ion concentration.

The thickness of the diffuse double layer, which is also called Debye screening length, is inversely proportional to the square root of the ionic strength in the solution. The overlap of the double layers of two approaching particles leads to an increased osmotic pressure between the particles. This pressure is equivalent to a repulsive force which is exponentially decaying with distance in first approximation. The resulting total interaction, the sum of the van der Waals attraction V^{vdW} and the double layer repulsion V^{el}, is denoted by

$$V^{DLVO} = V^{vdW} + V^{el} \qquad (2.2)$$

This potential, which originates from the Derjaguin-Landau-Vervey-Overbeek-(DLVO) theory, leads to stable suspensions for sufficiently high surface charges and not too high ionic strengths (see Fig. 2.1(a)).

Under stable conditions, the particles are often considered as soft unities with an effective volume increased by the electric double layer. Recent experiments have confirmed that the difference between the effective hydrodynamic and the real radius of a particle is an accurate measure for the double layer thickness in dilute suspensions [98Xu].

b) Steric Stabilization

The adsorption of molecules onto the surface of colloidal particles is an alternative method to stabilize colloidal suspensions and has already been used by the ancient Egyptians to stabilize inks [83Nap]. The main purpose of the molecules attached to the surface is to hinder the particles to get into the regime of van der Waals attraction, i.e. to shield the attraction through steric repulsion. If the size of the surfactant molecule is small with respect to the particle diameter, sterically stabilized particles (in contrast to double layer stabilized) are rather hard particles without long range repulsion but with strong short range repulsion. Thus, they are often used to test theoretical predictions for hard sphere model suspensions. The effect of steric repulsion is then either expressed as an ex-

cluded volume effect or as a very steep repulsion in the total interaction potential (see Fig 2.1(b)). If the surfactant molecules are of the same size as the colloidal particles, the steric repulsion has a more long-range and softer interaction potential than for small surfactant molecules.

The above subsection has shown the methods by which colloidal suspensions are stabilized. We may now proceed to an overview over the equilibrium and shear flow properties of stable suspensions.

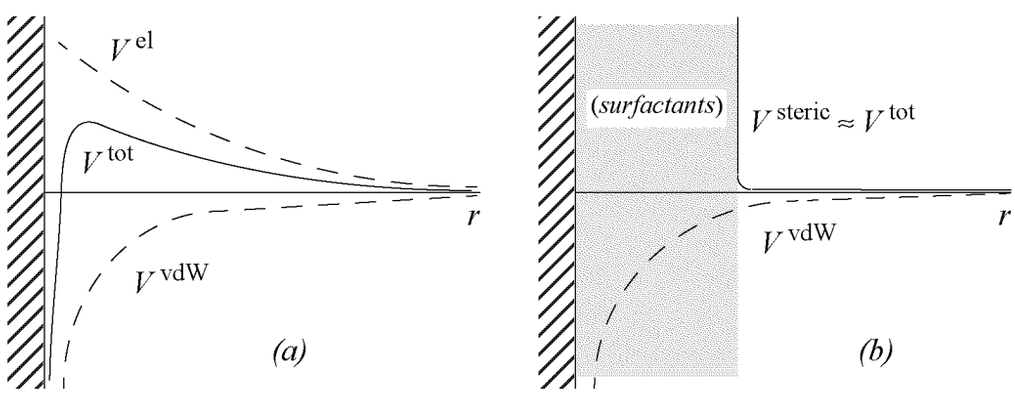

Fig. 2.1: Interaction potentials (a) for double layer and (b) for steric repulsion with short surfactant molecules.

2.1.2 Suspensions in Equilibrium

Most of the systematic studies on colloidal suspensions in equilibrium have been done on nearly ideal systems such as monodisperse spherical particles. They show different structures at equilibrium depending on their shape and on the way of stabilization. It has been found that long range repulsion tends to order the system. Short range repulsive forces, whether caused by steric or by electrostatic stabilization, lead to a fluid-like structure. An overview over the equilibrium phase behavior of colloidal suspensions can be found in Chapter 10 of "Colloidal Dispersions" [89Rus].

Some insight into the dynamics of the colloidal particles can be gained by measuring the mean square displacements or the self-diffusion coefficients. Dynamic light scattering [85Pus] and diffusing-wave spectroscopy [93Wei] are useful tools for studying the diffusive properties in dilute and in dense suspensions respectively. (The terms 'dilute' and 'dense' in this context refer to the behavior in scattering experiments: dense suspensions show significant multiple scattering, whereas dilute systems do not.)

In colloidal suspensions of interacting particles, the diffusion of the particles can basically be subdivided into three regimes. At very short times, the particles diffuse freely as long as they do not interact with their nearest neighbors. In the intermediate regime, the diffusion is lowered by the repulsion of the neighboring particles, before leveling off to a low value for long-time diffusion. In systems with long range repulsion, the particles can even have decreased diffusion on all time scales because they are always interacting with the other particles.

The diffusion of the colloidal particles can be observed experimentally. Long time self-diffusion coefficients have been determined by fluorescence techniques [92Bla], fiber optical quasi elastic light scattering [98Wil] and dark-field light microscopy [98Kas]. Diffusing wave spectroscopy experiments [93Wei] is even able to cover the whole range from short- to long-time diffusion. The experimental results correspond to the characteristics of the particle diffusion described above. Furthermore, they offer a possibility to compare the particle dynamics gained by Brownian dynamics simulations directly to the real suspension in the experiment.

2.1.3 Suspensions in Shear Flow

A Newtonian incompressible liquid is characterized by a linear relationship between the stress tensor σ and the rate of strain tensor $(\nabla \boldsymbol{v} + [\nabla \boldsymbol{v}]^T)$ of the velocity field $\boldsymbol{v}$, the proportionality constant being the viscosity η

$$\sigma = -\eta \, (\nabla \boldsymbol{v} + [\nabla \boldsymbol{v}]^T) \tag{2.3}$$

However, many liquids such as polymer solutions, polymer melts, and colloidal suspensions exhibit non-Newtonian behavior due to their complex microstructure. In colloidal suspensions, the interrelation between rheology and microstructure of the particle system is of major importance [91Wag, 92Lau], because the systems responds to applied strain by structural transitions and relaxations. This connection then is also the basis for the so-called rheo-optics, or optical rheometry, allowing for optical rather than mechanical measurement of the rheological properties [98Wag].

An overview of the interesting rheology of colloidal suspensions can be found in the review articles by Goodwin [75Goo] and Kamal and Mutel [85Kam]. The most characteristic parameters studied are the viscosity and the first and second normal stress differences. With regard to Brownian dynamics simulation, the following overview emphasizes the relation between particle structure and the flow properties of the suspension. A schematic representation of the shear rate dependent viscosity (Fig. 2.2) will be used to discuss the characteristics of the flow-curve.

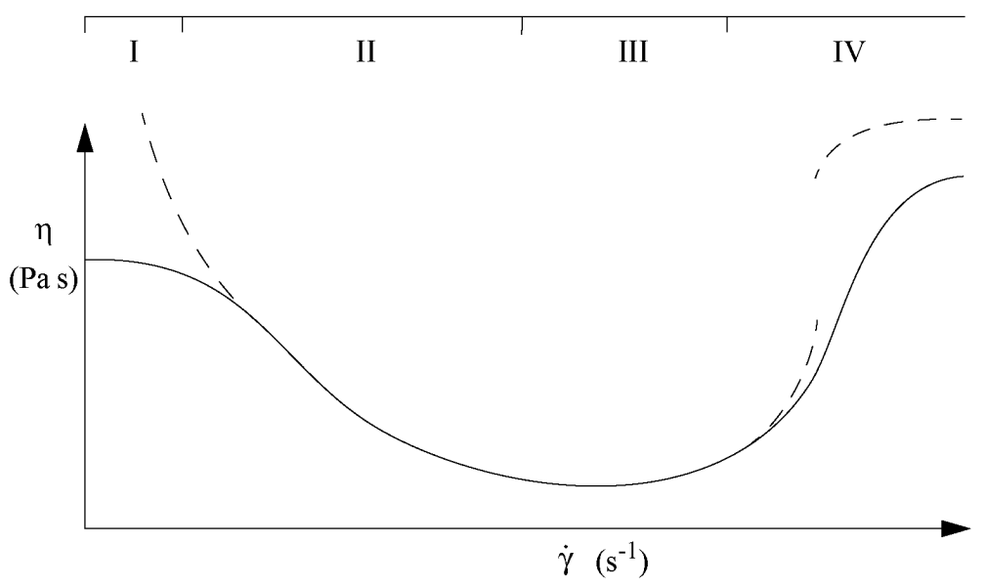

Fig. 2.2: Schematic viscosity-shear rate relation for a typical colloidal suspension.

At low shear rates, a colloidal suspensions can exhibit yielding behavior (region I, dashed line) [92Ngu] prior to flowing or be viscoelastic (region I, solid line) [92Boe], depending on the particle shape, size, and interaction potential. For viscoelastic suspensions, this region is called the first Newtonian plateau: the viscosity is only weakly dependent of the shear rate.

The linear viscoelastic properties of the suspension can be measured either by mechanical techniques or by the so-called microrheology. The latter is of special interest for this study because it allows to interpret the linear viscoelastic properties directly in terms of the motion of the colloidal particles. The method can be summarized as follows. A generalized Stokes-Einstein relationship between the mean square displacement of the particles at equilibrium and the shear relaxation modulus [89Bar1] of the suspension is employed: it is based on the idea that each colloidal particle diffuses in an effective viscoelastic continuum, given by the ensemble of the other particles. Various optical techniques have been applied to determine the mean square displacement of the particles, including dynamic light scattering [95Mas], diffusing wave spectroscopy [88Pin, 97Mas1], particle tracking [97Mas2] and interferometric microscopy [97Git]. The resulting shear relaxation moduli have been found to compare reasonably well to the mechanical rheometer measurements.

Fig. 2.2 shows that increasing the shear rate typically drives the system through a shear thinning transition (region II) into the so-called second Newtonian plateau (region III), where the viscosity shows again only little dependence on the shear rate.

This shear thinning transition is often accompanied by drastic changes in the particle configuration. Small angle neutron scattering [95Cho, 98Dux] and light scattering [97Dux] experiments have revealed the ordered structure of soft sphere systems in the shear thinned regime. The particles have been found to order into layers, which slide in the direction of the velocity field. This ordering is attributed to the long-range repulsion between the electrostatically stabilized particles. It is believed that at these shear rates sliding layers are more stable than a random configuration of particles due to the larger separation between the layers than the average separation between particles within the same layer.

In contrast, sterically stabilized hard sphere systems do not necessarily exhibit such a pronounced change in microstructure. Some experiments have found the coexistence of ordered and disordered sliding layers [96Cla], whereas others report no substantial ordering in the shear thinning transition [98Wat].

A further increase in shear rate leads to a significant shear thickening (Fig. 2.2, region IV) [89Bar2], which can even be discontinuous under certain conditions [72Hof] (region IV, dashed line).

The microstructural origin of the shear thickening is still under debate. Two major reasons for the transition are usually considered, an order-disorder transition and the existence of nonpermanent hydrodynamic clusters. For systems,

which order into layers in the shear thinned regime, a flow-instability and the breakup of ordered structures, similar to an acoustic resonance [98Kal], is seen as the main reason for thickening [72Hof, 92DHa, 98Hof]. However, also hard sphere suspensions, that do not order while undergoing the shear thinning transition, show shear thickening. Therefore, an order-disorder transition can not be the only reason for thickening.

An other reason for the onset of shear thickening might be the following. Apart from potential interactions between the particles, there is also hydrodynamic interaction which is conveyed through the suspending medium from one particle to the other. Many-body hydrodynamic interactions have been demonstrated to be important for understanding the suspension rheology [90Wag]. It was possible to show by computer simulation that they lead to the formation of so-called nonpermanent hydrodynamic clusters [85Bra, 88Bra]. Contrary to the order-disorder argument, these clusters are thought to be one of the major reasons for thickening both for ordered as well as for disordered colloidal suspensions [95Ben, 96Ben, 97Rag]. This view is also supported by scattering experiments [90Wer, 96Ben].

The contribution of the hydrodynamic interactions to the shear stress could be derived from dichroism measurements [88Wag, 95Ben, 96Ben] and from stress-jump measurements [95Mac, 97Wat]. Both illustrate the dominance of the hydrodynamic over all other stress contributions when going to high shear rates. One can conclude that hydrodynamic interactions are essential for understanding the shear thickening transition, independent on the particle structure built up.

2.2 SimulationMethod:NonequilibriumBrownianDynamicsTechnique

This section describes the basic principles of the simulation tool called non-equilibrium Brownian dynamics (NEBD) simulation. The source code used in this study has been written and implemented by the author himself in order to facilitate further modifications, extensions, and optimization.

The fundamental equations of motion for the particles are derived in a straightforward manner before going into details of the algorithm itself. The illustration of the periodic boundary conditions is followed by the discussion about the linked-cell list method which allows to treat also large systems. A description of the second-order integration scheme concludes the section. The many-body hydrodynamic interaction is given later in sections 2.5 and 2.6, and the proper treatment of touching particles is postponed to chapter 3, which deals with the coagulation process generally.

2.2.1 Equations of Motion

On the femtosecond time scale, the motion of the colloidal particles and of the solvent molecules can be described by Newton's equation of motion. However, the vast amount of information obtained by following the exact motion of all the solvent molecules is not needed to understand the main characteristics of the colloidal particle system. This can be justified by considering the difference in time scales of the solvent molecules and of the colloidal particles. The disparity in characteristic time scales suggests that structural relaxations of the solvent molecules do not need to be taken into account when studying the rheological behavior or the coagulation of colloidal suspensions. A 'coarse graining' of the time scale, as well as of the length scale, is therefore appropriate. On such a coarse grained level, the solvent molecules influence the colloidal particles in only two ways, by hindering the particle motion relative to the solvent and by the random forces acting on the particles. Due to their common origin, both effects are intimately related which is expressed in the so-called fluctuation-dissipation theorem [91Kub].

The equation of motion for the colloidal particles can either be derived from the Newton's equation of motion including the solvent molecules and then doing the coarse graining in a mathematically rigorous, but rather tedious, manner. This procedure would explicitly derive the expressions for the friction and random forces on the colloidal particles. An alternative method to establish the equations of motion for the colloidal particles only is to use a modified type of Newton's equation which includes both friction and random forces in an ***ad hoc*** manner.

The forces acting on the particles result from potential interactions between the particles and from friction as well as from thermal noise due to the suspending liquid. All three contributions are briefly discussed in the following.

a) Potential Force

For the potential forces, the pairwise additivity of two-body interactions is supposed to be a good approximation since the interaction potentials considered are short ranged. In the present study it was assumed that the particles are stabilized by electrostatic double layer repulsion only and not by steric repulsion. The interaction potential between two colloidal particles is then the sum given by eqn. (2.2) of the van der Waals attraction V^{vdW} and the electrostatic double layer repulsion V^{el} according to the DLVO-theory [89Rus] with

$$V^{\mathrm{vdW}}(r) = \frac{-A_{\mathrm{H}}}{12}\left[\frac{d^2}{r^2-d^2}+\frac{d^2}{r^2}+2\ln\left(\frac{r^2-d^2}{d^2}\right)\right] \tag{2.4}$$

$$V^{\mathrm{el}}(r) = \pi\varepsilon_{\mathrm{r}}\varepsilon_0\left(\left[\frac{4k_{\mathrm{B}}T}{ze}\tanh\left(\frac{ze\psi_0}{4k_{\mathrm{B}}T}\right)\right]^2 d\,\exp(-\kappa\{r-d\})\right) \tag{2.5}$$

Although the DLVO-potential is valid only in dilute suspensions, it is here used also for higher solid contents since only main characteristics such as interaction range and energy barrier are relevant in the present study. All parameters and constants are specified in Table 2.1 and Table 2.2, respectively.

Parameter	Symbol	Units (SI)
Hamaker constant	A_{H}	J
Particle diameter	d	m
Particle separation (center-to-center)	r	m
Relative dielectric constant of solvent	ε_{r}	-
Absolute temperature	T	K
Valency of ions	z	-
Surface potential	ψ_0	V
Inverse Debye screening length	κ	m

Table 2.1: Parameters for the DLVO-interaction potential.

Constant	Symbol	Value	Units (SI)
Dielectric constant	ε_0	$8.854 \cdot 10^{-12}$	C/(V m)
Boltzmann constant	k_B	$1.381 \cdot 10^{-23}$	J/K
Elementary charge	e	$1.602 \cdot 10^{-19}$	C

Table 2.2: Constants used in the DLVO-interaction potential.

The force between two particles due to the potential interactions is then given by

$$\boldsymbol{F}^{\mathrm{pot}}(r) = -\frac{d}{d\boldsymbol{r}} V^{\mathrm{DLVO}}(r). \tag{2.6}$$

The stabilization of the colloidal suspension can be achieved through the pH-dependent surface potential, $\psi_0 = \psi_0(\mathrm{pH})$, or the screening length which varies with the ionic strength I of the suspension as $\kappa^{-1} \sim I^{-1/2}$.

b) Friction Force

In contrast to these energy conserving potential forces between the particles described above, the friction force and random force exerted by the solvent on the particles are dissipative in origin. The loss of information implied by the coarse graining, which was needed to obtain these forces, is the origin of the irreversible nature introduced to the equations of motion. Neglecting many-body hydrodynamic interaction between the particles, the sole friction force on the particles is the well known Stokes' drag

$$\boldsymbol{F}^{\mathrm{Stokes}} = -\zeta(\boldsymbol{v} - \boldsymbol{v}^{\infty}) \tag{2.7}$$

In eqn. (2.7), ζ (kg/s) stands for the friction coefficient of the particle, $\boldsymbol{v}$ for the particle velocity, and $\boldsymbol{v}^{\infty}$ for the imposed flow field for infinite dilution evaluated at the particle's position. It should be noted that only the particle velocity relative to the background flow leads to the friction force.

c) Random Force

The random Brownian force $\boldsymbol{F}^{\mathrm{B}}$ on the particles due to the kicks of the solvent molecules must meet certain requirements. Apart from having a mean value of zero and being uncorrelated in time, the strength of the force is linked to the friction force by the fluctuation-dissipation theorem. With T denoting the absolute

temperature and t and t' two times, one writes (see e.g. [96Dho, 96Ött]):

$$\langle \boldsymbol{F}^{\mathrm{B}}(t) \rangle = \mathbf{0} \tag{2.8}$$

$$\langle \boldsymbol{F}^{\mathrm{B}}(t) \boldsymbol{F}^{\mathrm{B}}(t')^{T} \rangle = 2k_{\mathrm{B}}T\zeta\, \delta(t-t')\, \mathbf{1} \tag{2.9}$$

Here $\delta(t)$ denotes the Dirac delta function. As implied in eq. (2.9), the amplitude of the fluctuations is coupled to the dissipative friction coefficient through $\sqrt{2k_BT\zeta}$. Apart from a probably temperature dependent friction coefficient, the temperature of the suspending solvent is transferred to the particles through the $\sqrt{T}$-dependence of the Brownian forces. A rigorous treatment of the random forces can be given with the stochastic calculus of Wiener processes $\boldsymbol{W}(t)$ [92Klo, 96Ött], which have the properties $\langle \boldsymbol{W}(t) \rangle = \mathbf{0}$ and $\langle \boldsymbol{W}(t) \boldsymbol{W}(t')^{T} \rangle = \min(t, t')\, \mathbf{1}$. The Brownian forces are then related to the Wiener processes through $\boldsymbol{F}^{\mathrm{B}}(t)dt = \sqrt{2k_{\mathrm{B}}T\zeta}\, d\boldsymbol{W}(t)$ with $\langle d\boldsymbol{W}(t) \rangle = \mathbf{0}$ and $\langle d\boldsymbol{W}(t) d\boldsymbol{W}(t)^{T} \rangle = dt\, \mathbf{1}$.

A preliminary version of the equation of motion of particle i, with i=1...N, is given by setting up a modified Newton's equation including all three force contributions:

$$m\frac{d\boldsymbol{v}_i}{dt} = \boldsymbol{F}_i^{\mathrm{Stokes}} + \boldsymbol{F}_i^{\mathrm{pot}} + \boldsymbol{F}_i^{\mathrm{B}} . \tag{2.10}$$

The mass of the colloidal particle is denoted by m. On time scales much larger than the relaxation time for the particle velocity $\tau_p = m/\zeta$, one can set the left-hand side of (2.10) to zero. For the displacements $d\boldsymbol{r}_i = \boldsymbol{v}_i dt$, this leads to the fundamental equation for the Brownian dynamics simulation (see e.g. [96Dho, 96Ött])

$$\boxed{d\boldsymbol{r}_i = \left(\boldsymbol{v}_i^{\infty} + \frac{1}{\zeta} \boldsymbol{F}_i^{\mathrm{pot}} \right) dt + \sqrt{2k_{\mathrm{B}}T/\zeta}\, d\boldsymbol{W}_i} \quad (i=1,\ldots,N) \tag{2.11}$$

This equation is the basis for the simulations performed in sections 2.3 and 2.4, where many-body hydrodynamic interactions are not included. It relates the particle displacement to the momentary coordinates of all particles. On this time scale, momenta always relax to thermal equilibrium and are therefore not included in the equations.

2.2.2 *Periodic Boundary Conditions*

The number of particles involved in an experiment usually is much larger than what can be dealt with on a computer. To take care of this discrepancy, one studies only a small part of the system but replicates it in all three coordinate directions by using periodic boundary conditions. This is equivalent to paving the whole space with replicas of the primary box [87All]. The system is then described by storing the coordinates of the particles in the primary box and setting up rules for the interaction between particles and for where to place a particle when it attempts to leave the box. In Fig. 2.3, the periodic boundary conditions are illustrated on a square primary box in two dimensions in the case of simple shear flow. The primary box, outlined by continuous boundaries, is shown with all neighboring replicas.

The flow field within this box is given by a linear flow profile according to $v_x = \dot{\gamma} y$. On a scale larger than the box size, the flow field enters through the periodic boundary conditions. The boundary conditions have an influence both on the calculation of the interaction forces and on the move steps of the particles due to these forces. At shear rate zero, the primary box and its replicas are arranged in a fixed primitive cubic lattice. Under simple shear conditions, however, planes of the replicas are moving with respect to the plane which contains the primary box as indicated in Fig. 2.3. This illustrates that the primary box is just a small part of a bigger flow event.

As illustrated in Fig. 2.3(a), one always has to use an image of the closest pair of the particles when calculating distances between particles, even if they are not both in the primary box. A shell around a particle P, as well as around two of its images P' and P'', is drawn. It shows that this shell, shaded grey in the figure, is split up into separate regions if viewed in the primary box only. Although the second particle Q in the primary box is not within the interaction range of P, the replica Q' does interact with P. This means that the physically nearest neighbors of a given particle do not need to be nearest neighbors in the primary box: although particles P and Q are widely separated in the primary box, they still interact because of the periodic boundary conditions.

In Fig 2.3(b), a particle is shown which leaves the box at the upper side. The particle is then reintroduced at the bottom side of the box with the x-coordinate being shifted due to the strain between the sliding planes. This procedure is summarized in the so-called Lees-Edwards sliding boundary conditions [72Lee].

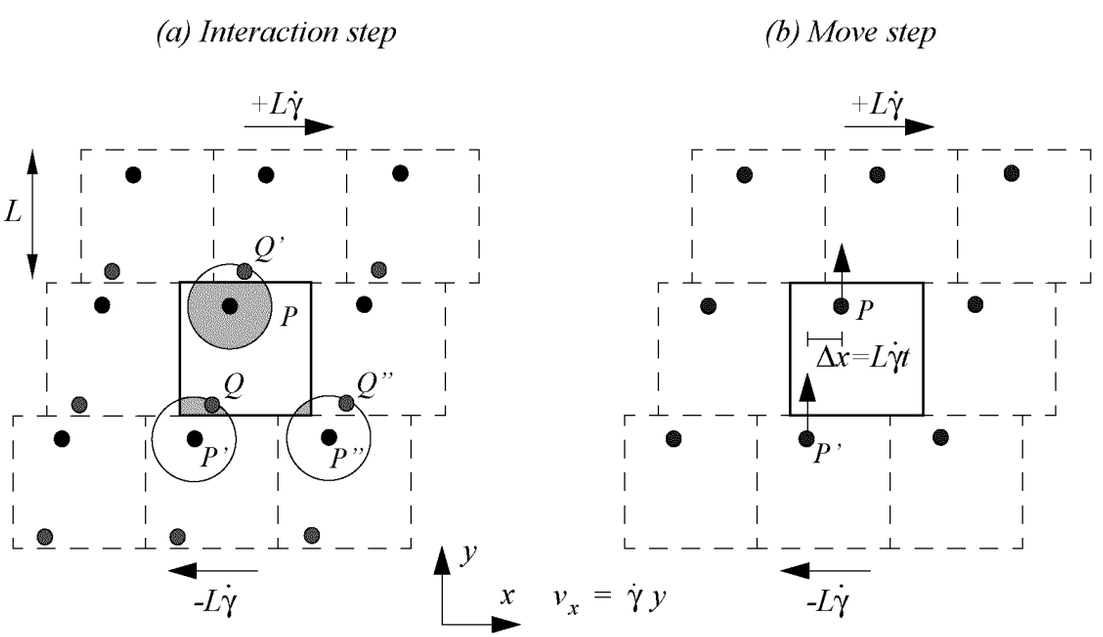

Fig. 2.3: Illustration of the periodic boundary conditions under simple shear flow in two dimensions: (a) calculation of interactions, (b) integration step; boxes have height L, $\dot{\gamma}$ denotes the shear rate of the imposed flow field in x-direction.

2.2.3 *Linked-Cell List Method*

The computation of the interaction potentials or forces is usually the most time consuming step in systems where the number of particles N is large. In principle, every particle interacts with all other N-1 particles which leads to a computational effort of the order $O(N^2)$. For short range interaction forces, such as DLVO-forces under moderate conditions, a cut-off in the interaction range can be introduced.

One method among others to exploit the short cut-off in the interaction in the computations is the linked-cell list method [87All]. The basic idea is to subdivide the primary simulation box into small cells with dimensions at least as large as the range of the interaction. This implies that only particles within the same cell or particles of neighboring cells have to be considered for the calculation of the interaction. An illustration for two dimensions is given in Fig. 2.4, where a particle located in cell number 3 and the range of the interaction potential is shown. Because the interaction range is shorter than the length of the cell, the particle can interact only with particles within the cells shaded grey. Apart from the sliding neighboring cells in plane 5, the neighbors to cell 3 are always the same.

The efficiency of the linked-cell method for large numbers of particles can thus be explained as follows. The number of cells grows linearly with the number of particles if the number of particles per cell is kept constant. The loop for the calculation of all interaction terms then goes rather over the cell indices than over

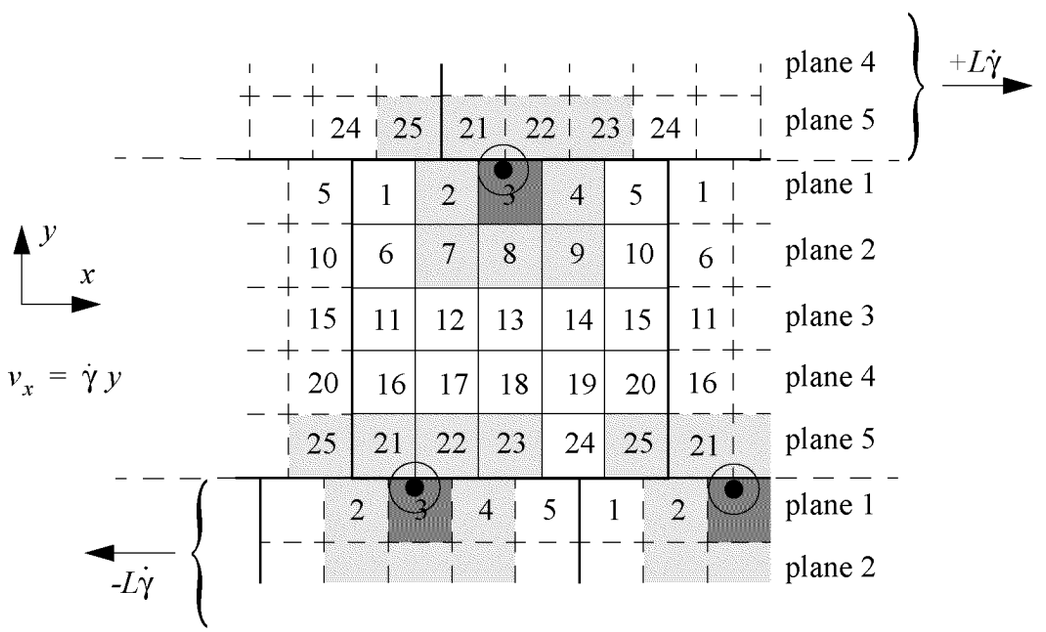

Fig. 2.4: Illustration of the linked-cell list method in two dimensions.

the particle indices. For each cell, all interactions with particles within the cell as well as with particles in any of the neighboring cells are computed. This is only an $O(1)$ problem because both the number of particles per cell as well as the number of neighboring cells do not depend on the overall system size N. Since the number of cells grows linearly with the particle number, the total computational effort is $O(N)$. The linked-cell list methods allows to study large systems containing several thousand particles on a workstation if many-body hydrodynamic interactions are not included.

2.2.4 *Integration of the Equations*

The inclusion of the random forces by means of Wiener processes into the equations of motion leads to stochastic differential equations. For this type of equations, one of the criteria for testing the quality of an integration scheme is the so-called weak convergence. Rather than looking at the trajectories for different realizations of noise themselves, it gives a measure for the accuracy of averages and higher moments built on the trajectories. The numerical integration of differential equations over a finite time interval is done by propagating the system by small, but finite, time steps. After the integration over the whole time interval, the difference in the sense of weak convergence between the numerical and the analytical solution depends on the time step Δt to an exponent w, which is called the order of weak convergence. Thus, reducing the integration errors can be achieved through a reduction of the time step Δt or through an increase in the order w. The former leads, however, to longer computation times if a fixed physical time interval needs to be covered by the simulation. The augmentation of the order of convergence w is therefore often considered to be a valuable alternative which motivates the need for higher order integration schemes [92Klo, 96Ött].

Before illustrating the integration scheme used throughout sections 2.3 and 2.4, it is sensible to simplify the notation used in the equations of motion (2.11). We introduce vectors of length $3N$, which accommodate the 3-component vectors of all particles, e.g. $\boldsymbol{r}_t = (\boldsymbol{r}_1, \boldsymbol{r}_2 \ldots \boldsymbol{r}_N)$ for the coordinates at time t. In the $3N$-vector notation the equation of motion then reads

$$d\boldsymbol{r}_t = \left[\boldsymbol{v}^{\infty}(\boldsymbol{r}_t) + \frac{1}{\zeta}\boldsymbol{F}^{\mathrm{pot}}(\boldsymbol{r}_t)\right]dt + \sqrt{2k_{\mathrm{B}}T/\zeta}\, d\boldsymbol{W}_t \qquad (2.12)$$

The integration technique used in sections 2.3 and 2.4 is a two-step scheme composed of a predictor and of a corrector step, respectively. The first step is a common Euler integration step leading to the predicted positions (2.13) $\boldsymbol{r}^{\mathrm{p}}_{t+\Delta t} = \boldsymbol{r}_t + \Delta\boldsymbol{r}^{\mathrm{p}}_t$, which are then used in the corrector step (2.14). In detail, the integration scheme looks as follows:

$$\Delta\boldsymbol{r}^{\mathrm{p}}_t = \left[\boldsymbol{v}^{\infty}(\boldsymbol{r}_t) + \frac{1}{\zeta}\boldsymbol{F}^{\mathrm{pot}}(\boldsymbol{r}_t)\right]\Delta t + \sqrt{2k_{\mathrm{B}}T/\zeta}\,\Delta\boldsymbol{W}_t \qquad (2.13)$$

$$\Delta\boldsymbol{r}^{\mathrm{c}}_t = \frac{1}{2}[\boldsymbol{v}^{\infty}(\boldsymbol{r}_t) + \boldsymbol{v}^{\infty}(\boldsymbol{r}^{\mathrm{p}}_{t+\Delta t})]\Delta t + \frac{1}{2\zeta}[\boldsymbol{F}^{\mathrm{pot}}(\boldsymbol{r}_t) + \boldsymbol{F}^{\mathrm{pot}}(\boldsymbol{r}^{\mathrm{p}}_{t+\Delta t})]\Delta t + \sqrt{2k_{\mathrm{B}}T/\zeta}\,\Delta\boldsymbol{W}_t \quad . \qquad (2.14)$$

The Wiener increments $\Delta\boldsymbol{W}_t$ are determined from a sequence of uncorrelated Gaussian distributed random numbers with $\langle\Delta\boldsymbol{W}_t\rangle = \boldsymbol{0}$ and

$\langle \Delta \boldsymbol{W}_t \, \Delta \boldsymbol{W}_t^T \rangle = \Delta t \, \mathbf{1}$, leading to a $\sqrt{\Delta t}$-dependence of the noise amplitude. Equations (2.13-2.14) seem to suggest that the noise term dominates the deterministic Δt-contributions when going to small time steps. However, the increasing strength of the force is compensated by the increase in irregularity in the noise since more random numbers are needed for spanning a fixed time interval.

The simplest integration scheme that is commonly used is the Euler step given by eqn. (2.13) which leads to an order of weak convergence w equal to 1. Doubling the computational effort by determining a corrected value through eqn. (2.14) leads to an increase in the order of convergence to w equal to 2 [92Klo, 96Ött]. The additional effort of the second integration step in usually accepted if the accuracy gained is more than a factor of two for the typical time steps used in the simulations.

The lower limit on the time step Δt is set by the number of iterations used to cover a given physical time interval. The upper limit is set by the three different displacement contributions in eqns. (2.13-2.14), which shall all be very small with respect to the particle diameter d. The time it takes a particle to travel its own diameter by random motion is given by the diffusive time scale $\tau_{\mathrm{Br}} = d^2/6D_0$, where D_0 denotes the diffusion coefficient

$$D_0 = k_{\mathrm{B}} T / \zeta \tag{2.15}$$

of a single particle. Since the random contributions are usually the largest for small time steps, the upper limit on the step size is given by the random term.

2.3 Equilibrium Properties

This section presents the results obtained by Brownian dynamics computer simulation of a colloidal suspension at equilibrium. No external influences such as gravitational force and imposed flow field are considered.

Because the sample volume V, the particle number N and the temperature T are kept constant in the simulation, the appropriate thermodynamic description of the system on a macroscopic level is given by the Helmholtz free energy $F = F(T, V, N)$. The simulations performed are to be seen as microscopic samples of the thermodynamic ensemble. Although equilibrium thermodynamics has proved useful in numerous situations, it does not provide us with any microscopic detail. Therefore, it is not the goal of this section to deduce the thermodynamic properties of the material from the particle description level, but rather to extract some interesting information about dynamic properties of the many-particle system. In particular, the self diffusion of particles and the viscoelastic memory function are studied.

2.3.1 Simulation Input

The input parameters in the simulation can be divided into physical parameters and those that originate from tackling the problem numerically on a computer. The physical parameters describe the particles, the interaction between them and the suspending solvent. The numerical input deals with the integration steps, the linked-cell list algorithm and the starting configuration.

a) Interaction Potential

The parameters for the interaction potential given by eqn. (2.4-5) are listed in Table 2.3. The resulting potential is shown in Fig. 2.5. The center-to-center separation r between two particles, where the interaction energy equals the thermal energy $k_B T$, is at $r = 1.514\,d$. The attractive range at small separations, which is due to the van der Waals forces, is never reached in the simulation because the energy maximum of more than $70\,k_B T$ is practically insurmountable at room temperature.

The short interaction range of both the van der Waals attraction and the electric double layer repulsion allows us to introduce a cut-off in the potential (and in the force) at $r_{cutoff} = 1.8\,d$. For larger separation, DLVO-interaction is absent, which is equivalent to neglecting interaction energies that are smaller than five percent of the thermal energy (see Fig 2.5).

The interaction potential and force was not calculated again and again for each pair of interacting particles, but values for a finite set of separations between $r = d$ and $r = r_{cutoff}$ were stored in a list. The number of equally spaced separations, for which the potential and force were stored in the list, was `Nbin` = 10'000.

Parameter	Symbol	Value	Units (SI)
Hamaker Constant of Al_2O_3 in Water	A_H	$4.76 \cdot 10^{-20}$	J
Particle Diameter	d	$5 \cdot 10^{-7}$	m
Relative Dielectric Constant of Water	ε_r	81	-
Absolute Temperature	T	293	K
Valency of Ions	z	1	-
Surface Potential	ψ_0	0.02	V
Inverse Debye Screening Length	κ	$1.8 \cdot 10^{7}$	m^{-1}

Table 2.3: Potential parameters for the stable suspension.

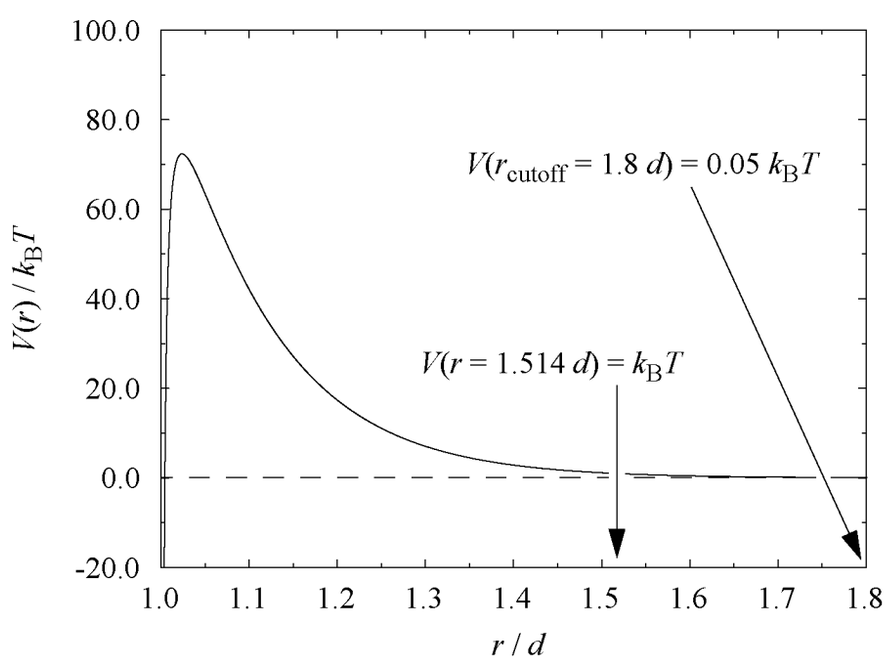

Fig. 2.5: DLVO-interaction potential for the stabilized suspension.

b) Solvent

Apart from the temperature T of the whole colloidal suspension, the friction coefficient ζ is the only parameter which represents the solvent in the equations of motion for the colloidal particles. Due to the spherical shape of the particles, the friction coefficient can be related to the solvent viscosity η_s through Stokes' law

$$\zeta = 3\pi d\eta_s \tag{2.16}$$

The viscosity value used in all simulations is $\eta_s = 10^{-3}$ Pa s , which corresponds to the viscosity of water at room temperature.
The imposed flow field, which has to be accounted for in the calculation of the Stokes' drag force, is equal to zero in all equilibrium runs: $\boldsymbol{v}^{\infty} \equiv 0$.

c) System Size and Linked-Cell List Algorithm

All simulations in this section were performed with N = 1'000 particles. The cubic simulation box was subdivided into cubic cells for the linked-cell list algorithm (see subsection 2.2.3). The number of cells in each of the x-, y- and z-direction was chosen `Ncell` = 6. In total, the simulation box consisted of `Ncell`^{3} = 216 small cells, leading to 4.63 particles per cell on average.

For a fixed number of particles N with diameter d, the solid content ϕ of the suspension is tuned by varying the size of the cubic simulation box, `Lbox`. ϕ and `Lbox` are related by equating the given solid content to the ratio between particle volume and suspension volume

$$\phi = \frac{Nd^3\pi/6}{\texttt{Lbox}^3} \tag{2.17}$$

For all solid contents considered in the simulations of stable suspensions $(0.1 \le \phi \le 0.3)$, the length `Lcell` of the linked-cells

$$\texttt{Lcell} = \frac{\texttt{Lbox}}{\texttt{Ncell}} \tag{2.18}$$

was smaller than the interaction range r_{cutoff} of the potential, which is a necessary condition as mentioned in subsection 2.2.3.

From the simulation results presented in sections 2.3 and 2.4 it will become clear why the range of solid content $0.1 \le \phi \le 0.3$ is particularly interesting, both at equilibrium as well as under shear flow conditions.

d) Integration Steps

The integration of the particle equations of motion requires an appropriate choice of the finite time step Δt used in eqns. (2.13-14). Both the size of one time step and the number of steps depend on characteristic time scales in the real system as follows. The real time span covered with the simulation has to be long enough to allow structural rearrangements in the system and to allow the particles to travel large distances with respect to their own diameter. This is a necessary requirement if the time averages calculated in one simulation shall be a good approximation to the ensemble averages over a large set of statistically independent systems. Here, we studied only one system but over a very long time with respect to the characteristic time scale τ of the system, rather than simulating a large set of independent systems. The typical time scale τ is given by the time a particle needs to travel its own diameter d due to Brownian motion. In three dimensions one finds:

$$\tau_{\mathrm{Br}} = \frac{d^2}{6D_0} \tag{2.19}$$

where D_0 denotes the scalar diffusion coefficient given in eqn. (2.15). Using the parameters defined above, the diffusion coefficient is $D_0 = 8.58 \cdot 10^{-13}\ \mathrm{m}^2/\mathrm{s}$, which results in a characteristic time scale $\tau_{\mathrm{Br}} = 4.84 \cdot 10^{-2}$ s. The time step used for all equilibrium runs was

$$\Delta t = 3.5 \cdot 10^{-6}\ \mathrm{s} \approx 7 \cdot 10^{-5}\ \tau_{\mathrm{Br}} \tag{2.20}$$

Assuming that structural transitions and relaxation phenomena at equilibrium are mainly occurring on the Brownian time scale, the real time span covered by the simulation needs to be large enough to lead to time averages close to the ensemble averages. With a number $N^{\mathrm{step}} = 2 \cdot 10^6$ of time steps chosen in this study, the simulations covered a real time span of

$$\tau_{\mathrm{span}} = 7\ \mathrm{s} \approx 144\ \tau_{\mathrm{Br}} \tag{2.21}$$

e) Starting Configurations

The starting configurations for the equilibrium runs were structures obtained by arranging the particles in a simple cubic lattice and by propagating the particle positions according to the equations of motion (2.13-14). The criteria for accepting the structures were steady values over time for the total potential energy and for all components of the stress tensor. These criteria were usually met after a few Brownian relaxation times τ_{Br}.

2.3.2 Self Diffusion

a) General Procedure

If a single submicron-sized particle is put in a solvent, its motion is purely diffusive due to the Brownian forces of the solvent. The average mean square displacement $\langle \Delta \boldsymbol{r}(t)^2 \rangle \equiv \langle [\boldsymbol{r}(t) - \boldsymbol{r}(t_0)]^2 \rangle$ is then a linear function of time. The slope of the mean square displacement is twice the diffusion coefficient D_0 of a single particle. Adding more particles to the system changes the behavior drastically to a nonlinear $\langle \Delta \boldsymbol{r}^2 \rangle \leftrightarrow t$-relation for longer times. The motion of each of the particles is now hindered by the presence of the other particles, whether only due to the occupied volume or also due to the potential interaction. Therefore, the mean square displacement for the many-particle system is an interesting indicator for the interaction effects in the many-particle system.

The average denoted by $\langle \ldots \rangle$ is an average over all particles and over different samples. They are all from the same simulation but have starting values t_0 that differ by $10\ \tau_{Br}$ (see Fig. 2.6). This ensures that the samples are statistically independent and cover a time window long enough to observe the long-time diffusion of the particles.

With respect to anisotropic diffusion in shear flow which will be discussed later in subsection 2.4.4, the tensorial rather than the scalar mean square displacement is used already in this section. If the indices i and k denote the Cartesian components (x, y, z), the mean square displacement is given by

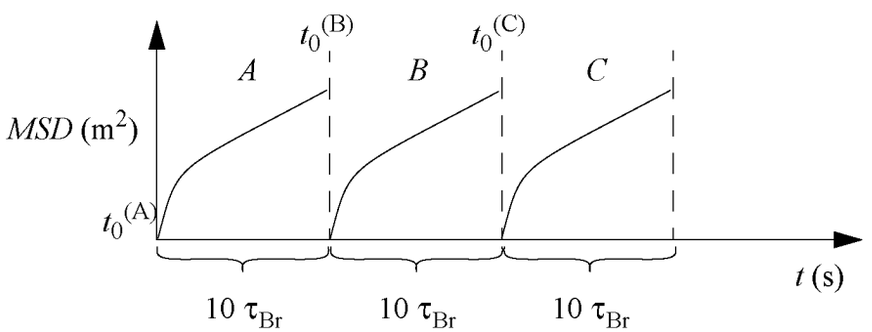

Fig. 2.6: Illustration of the averaging procedure used for the calculation of the mean square displacements (MSD). The average is determined from the samples A, B, C,... in the same simulation run.

$$\langle \Delta \boldsymbol{r}_i(t) \Delta \boldsymbol{r}_k(t) \rangle \equiv \langle [\boldsymbol{r}_i(t) - \boldsymbol{r}_i(t_0)][\boldsymbol{r}_k(t) - \boldsymbol{r}_k(t_0)] \rangle = 2D_{ik}t \quad (i,k=x,y,z) \qquad (2.22)$$

where D_{ik} denote the components of the diffusion tensor. At equilibrium, the system is isotropic which leads to $D_{xx} = D_{yy} = D_{zz}$. Because the components of the Brownian forces are uncorrelated, $D_{ik} = 0$ for all $i \neq k$. For only one single particle, the diagonal components of the diffusion tensor are given by the Stokes-Einstein relation $D_{ii} = D_0 = k_B T/\zeta$ for $i=x, y, z$.

In principle, the curve of the mean square displacement vs. time can be divided into three regimes [96Dho] (see Fig. 2.7). At very short time scales (I), the particles diffuse freely with a diffusion coefficient equal to the single particle diffusion coefficient D_0. On the long time scale (III), the particle diffusion is decreased due to the interaction with the other particles. The intermediate range (II) is the crossover regime interpolating between short- and long-time diffusion.The division into these three regimes has also been observed in diffusing-wave spectroscopy experiments (for an overview see [93Wei]).

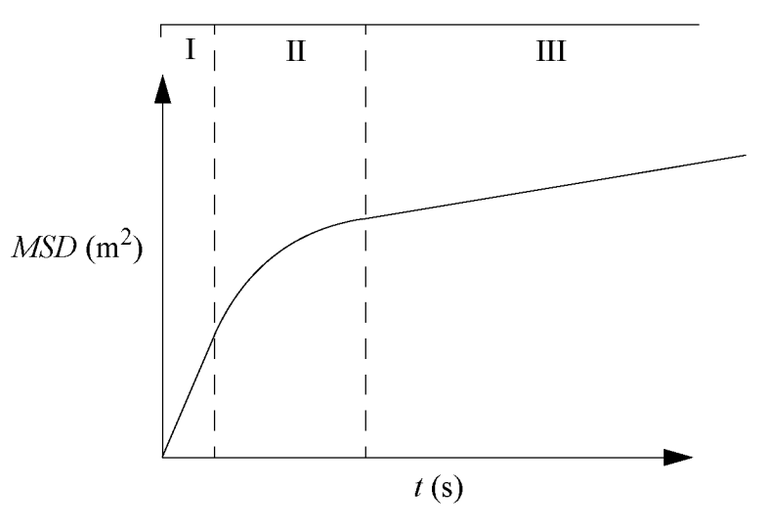

Fig. 2.7: Schematic representation of the mean square displacement (MSD).

b) Results

The simulations were performed at five different solid contents: ϕ = 0.10, 0.15, 0.20, 0.25 and 0.30. Fig. 2.8 shows the mean square displacement measured at a solid content of ϕ = 0.2. The inset is a logarithmic plot to show the nonlinear behavior even for short times. The error bars are never larger than two percent of the mean square displacement value at all times shown in Fig. 2.8. This upper limit on the error bars is also valid for all other solid contents under consideration.

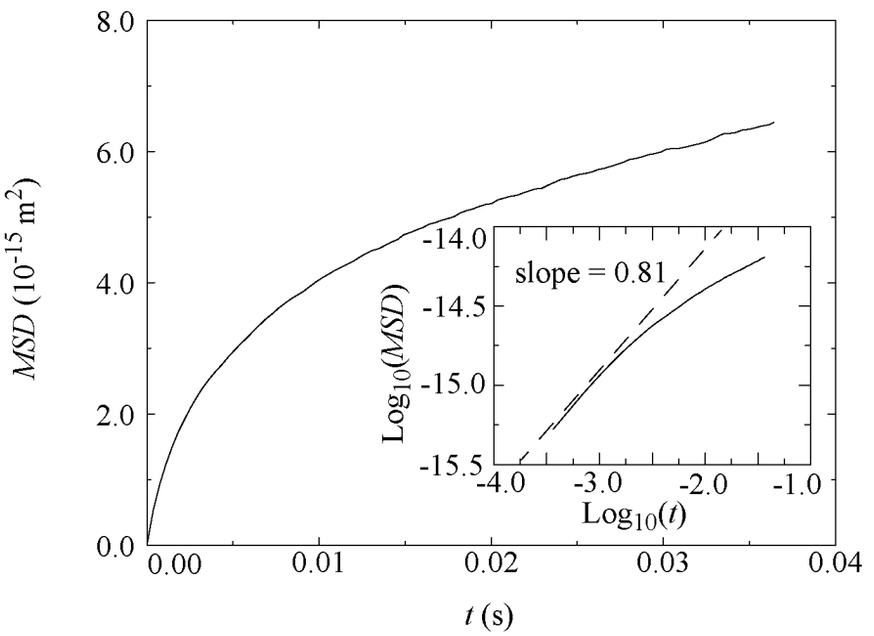

Fig. 2.8: Simulated mean square displacement (MSD) for a stable suspension for a solid content ϕ = 0.2. Error bars are smaller than 2 % of the MSD. The inset is a double logarithmic plot of the same data.

The resolution τ_{res} of the mean square displacement at short times is $\tau_{res} = 3.5 \cdot 10^{-4}$ s $\approx 7 \cdot 10^{-3}\ \tau_{Br}$, which corresponds to 100 integration steps. Beyond this time scale, the short-time linear region (see region I in Fig. 2.7) could not be observed for any of the solid contents studied. Table 2.4 lists the diffusion coefficients as determined from the initial slope in the data by

$$D^S = \frac{1}{6}\frac{d}{dt}\langle \Delta \boldsymbol{r}(t)^2 \rangle \Big|_{t = t_0} \qquad (2.23)$$

Solid content ϕ	D^S / D_0
0.10	0.97 ± 0.02
0.15	0.92 ± 0.02
0.20	0.84 ± 0.02
0.25	0.71 ± 0.02
0.30	0.55 ± 0.02

Table 2.4: Short time diffusion coefficients D^S, as determined from the initial slope in the non-linear regime, in units of the single particle diffusion coefficient D_0.

It should be noted that the data in Table 2.4 are pseudo short time diffusion coefficients in the sense that no finite linear regime could be detected for short times. A possible solution would be to monitor the mean square displacement on scales corresponding to less than 100 integration steps.

A quantitative comparison of the transition region and the long time diffusion behavior (Fig. 2.7, regions II and III) for different solid contents is done by comparing the parameters of a suitable fit-function. We propose to fit the mean square displacement data with a stretched exponential function for the transition region according to

$$\frac{1}{3}\langle \Delta \boldsymbol{r}(t)^2 \rangle = \alpha_1 \left(1 - \exp\left[-\left(\frac{t}{\tau_d} \right)^{\alpha_2} \right] \right) + \alpha_3 \, t \qquad (2.24)$$

with the fit-parameters α_1, α_2, α_3 and τ_d. This fit-function ranked substantially better than a normal exponential ($\alpha_2 = 1$) in fitting the intermediate transition region. The limitation of eq. (2.24) is the diverging slope at short times which leads to an infinitely large short-time diffusion coefficient. Note that the long-time diffusion coefficient is given by

$$D^L = \frac{1}{6} \frac{d}{dt} \langle \Delta \boldsymbol{r}(t)^2 \rangle \Big|_{t=\infty} = \frac{1}{2} \alpha_3 \qquad (2.25)$$

The quality of the fit-function on the simulation data was tested by calculating the error integral for both the transition region only as well as for the whole time span. The resulting error was smaller than 5 % for both criteria and for all solid contents listed in Table 2.5.

The error bars on the fit-parameters were calculated in the following way. From the simulation data and the corresponding error bars, a set of one thousand independent samples was reconstructed with the appropriate mean value and standard deviation. For each sample in this set, the fitting procedure was executed which leads to a set of one thousand values for each of the fitting parameters, from which mean values and standard deviations were determined.

Solid C. ϕ	α_1 (10^{-15} m^2)	τ_d (10^{-3} s)	α_2 (1)	α_3 (10^{-14} m^2/s)	D^L/D_0 (10^{-2})
0.10	11.8 ± 0.1	16.0 ± 2.5	0.93 ± 0.05	65.7 ± 0.9	38.3 ± 0.5
0.15	9.05 ± 0.44	12.8 ± 1.5	0.79 ± 0.04	27.8 ± 0.4	16.2 ± 0.2
0.20	6.75 ± 0.11	12.5 ± 0.8	0.62 ± 0.02	1.92 ± 0.06	1.12 ± 0.04
0.25	2.74 ± 0.04	6.21 ± 0.50	0.55 ± 0.02	0.27 ± 0.02	0.16 ± 0.01
0.30	1.45 ± 0.02	4.46 ± 0.35	0.47 ± 0.01	0.18 ± 0.01	0.10 ± 0.01

Table 2.5: Fit-parameters for the stretched exponential function (eqn. (2.24)) versus solid content.

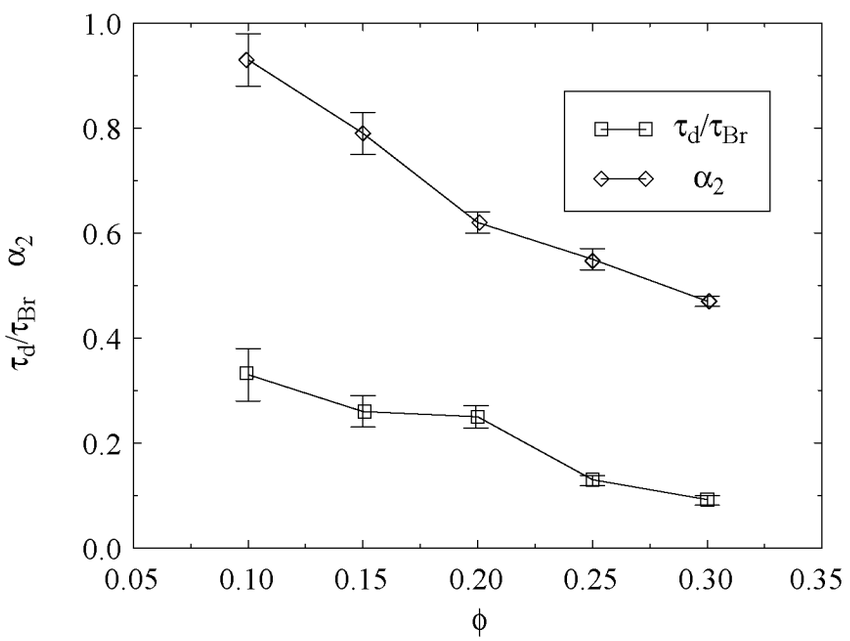

Fig. 2.9: Characteristics of the fit-function for the transition from short- to long-time diffusion: transition time τ_d and exponent α_2. Data are from Table 2.5. The lines are only drawn as visual guide.

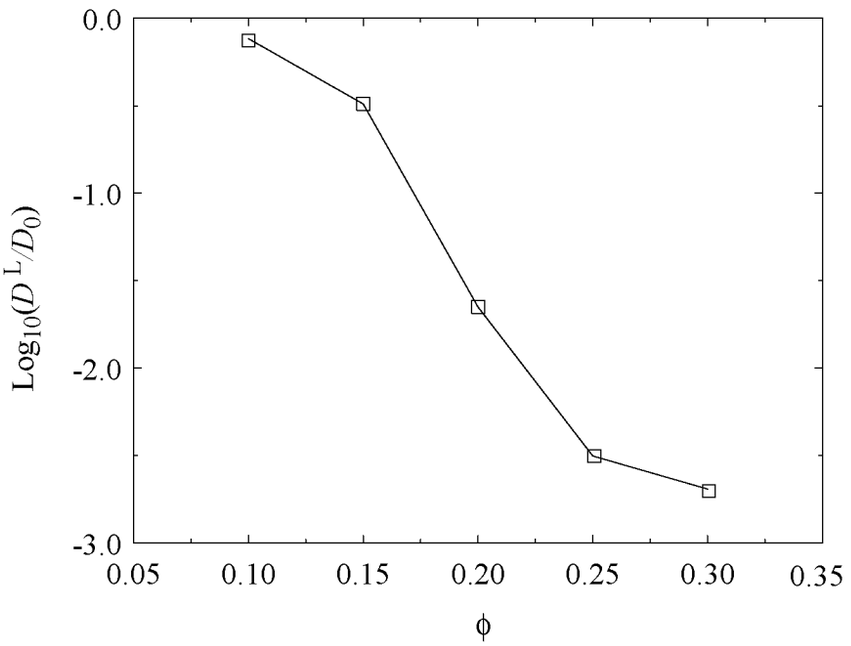

Fig. 2.10: Logarithmic plot of the long time diffusion coefficient D^L as obtained from the fit-function by eqn. (2.25). Error bars are smaller than the symbol size. Data are from Table 2.5. The line is only drawn as visual guide.

The data for the transition time τ_d and the exponent α_2 plotted in Fig. 2.9 illustrate that the transition to the long time diffusion is steeper and occurs in a shorter time interval for increasing solid content. The physical origin of this behavior is the following: the higher the solid content in the system, the less far a particle has to travel in order to get into the interaction range of a neighboring particle.

The fact that smaller traveling distances also mean shorter time scales has implications on the short time diffusion coefficient of the particles. Although the short time diffusion coefficient could not be determined from the simulation as described above, one still can draw the following conclusion: the short time diffusion coefficient does not decrease as much as the square of nearest neighbor separation for increasing solid content, thus leading to a decreasing transition time.

Fig. 2.10 shows the drastic change in the long time diffusion coefficient for increasing solid content. The ability of the particles to travel long distances is decreased by two and a half orders of magnitude. It will be shown in the next subsection that this is due to a transition from a viscoelastic liquid at $\phi = 0.1$ to a viscoelastic solid at $\phi = 0.3$ for the potential given in Fig. 2.5.

Summary

The above discussion has shown that no finite regime at short times could be detected in our simulation results which has a constant diffusion coefficient. Nevertheless, the initial slope in the mean square displacement data indicate that the self diffusion at short times of the particles is considerably reduced when increasing the solid content. The transition to long time diffusion has been characterized by a stretched exponential function. The corresponding fitted parameters quantify the decrease in the transition time and the reduction in the long time diffusion coefficient (more than two orders of magnitude) as the solid content is raised.

2.3.3 Linear Viscoelastic Properties

a) Background and General Procedure

In linear viscoelasticity, one studies the response of a material subjected to small applied deformations. The following notation is usually employed for relating the system response, the shear stress σ_{xy}, to the applied perturbation, the shear rate $\dot{\gamma}$ [89Bar1]:

$$\sigma_{xy}(t) = -\int_{-\infty}^{t} \Phi(t-t')\dot{\gamma}(t')dt' \tag{2.26}$$

The integral over the parameter t' is summing over the whole history of the shear rate applied to the system. The weight function, or relaxation function, $\Phi(t-t')$ expresses how much the shear rate at a given moment in the past still influences the current stress. For a liquid, the system can recover to any applied shear rate after a long enough time, i.e. the relaxation function decays to zero for the far past,

$$\lim_{t' \to -\infty} \Phi(t-t') = 0 \tag{2.27}$$

A viscoelastic solid, on the other hand, has a non-vanishing relaxation function at long times

$$\lim_{t' \to -\infty} \Phi(t-t') \neq 0 \tag{2.28}$$

This means that a viscoelastic solid always remembers deformations that have been applied to it in the past.

There is an alternative method to measure the linear viscoelastic behavior of a colloidal suspension than by its response to small deformations. In theory and in computer simulations, the linear viscoelastic behavior can be studied by measuring the autocorrelation function $C_s(t)$ of the off-diagonal stress-component σ_{xy} in the colloidal suspension ***at equilibrium***,

$$C_s(t) = \langle \sigma_{xy}(t)\sigma_{xy}(0) \rangle_{eq} \tag{2.29}$$

In simulations, the off-diagonal components of the stress tensor σ_{ik} are directly related to the interparticle forces $\boldsymbol{F}$. For a system with pairwise additive interaction, the interparticle contribution of N particles in a volume V to the stress is given by

$$\sigma_{ik} = -\frac{1}{2V}\sum_{m\neq n}^{N}\sum_{n=1}^{N}(\boldsymbol{r}_{mn})_i(\boldsymbol{F}_{mn})_k \quad (i,k=x,y,z) \tag{2.30}$$

Exploiting the isotropy in the system at equilibrium, the average over all three off-diagonal elements σ_{xy}, σ_{xz} and σ_{yz} leads to better statistics:

$$C_s(t) = \frac{1}{3}\langle\sigma_{xy}(t)\sigma_{xy}(0)+\sigma_{xz}(t)\sigma_{xz}(0)+\sigma_{yz}(t)\sigma_{yz}(0)\rangle_{eq} \tag{2.31}$$

Equation (2.31) will be employed when evaluating the simulation data. For explaining the meaning of the correlation the mathematically identical expression from eqn. (2.29) will be used.

The physical meaning of the stress autocorrelation function can be elucidated by its link to the viscoelastic behavior of the suspension. It is one of the main results of 'linear response theory' [91Kub] that near equilibrium material properties can be expressed in terms of equilibrium correlation functions. Applied to our system, it relates the particle contribution to the viscosity of the suspension η^{part} at vanishingly small shear rates to the correlation function $C_s(t)$ by the so-called Green-Kubo relation [91Kub]

$$\eta^{part}_{GK}(\dot{\gamma}\to 0) = \frac{V}{k_B T}\int_0^\infty C_s(t)dt = \frac{V}{k_B T}\int_0^\infty \langle\sigma_{xy}(t)\sigma_{xy}(0)\rangle_{eq}dt \tag{2.32}$$

Although the stress autocorrelation function is mostly used as in eqn. (2.32), it contains in principle the full description of the linear viscoelastic behavior of the colloidal suspension [91Kub]. This implies in our system the following relation between the relaxation function and the stress autocorrelation function:

$$\Phi(t) = \frac{V}{k_B T}C_s(t) \tag{2.33}$$

Equation (2.33) allows us to determine the full viscoelastic behavior contained in the relaxation function $\Phi(t)$ by measuring the stress autocorrelation function $C_s(t)$. This leads to a different interpretation of the relaxation phenomena. In the following, we concentrate on discussing the stress autocorrelation function, while always keeping in mind its relation to the viscoelastic properties of the system.

Before proceeding to the presentation of the simulation results, there is one conclusion to be drawn from eqn. (2.33). It has been stated that the difference between a viscoelastic solid and a viscoelastic liquid is a finite value in the relaxation function even for the longest times. This can now be translated into a criterion for the stress autocorrelation function. By separating the average value from the off-diagonal stress component $\sigma_{xy}(t) = \langle\sigma_{xy}\rangle_{eq} + \Delta\sigma_{xy}(t)$ one finds

$$C_s(t) = \langle \sigma_{xy} \rangle_{eq}^2 + \langle \Delta\sigma_{xy}(t)\, \Delta\sigma_{xy}(0) \rangle_{eq} \qquad (2.34)$$

There are hence two reasons for a finite stress autocorrelation for long times: (i) a non-zero equilibrium average of the off-diagonal stress component and (ii) long-time correlated fluctuations around the average value. Since both characteristics are absent in a quiescent liquid, they can be used to quantify the solid-like properties of the system. A non-zero value in eqn. (2.34) indicates that the systems is caged in a quasi-stable configuration in the simulation box.

The average $\langle ... \rangle$ implied in the correlation function (2.31) is calculated from the time series of the off-diagonal stress components σ_{xy}, σ_{xz} and σ_{yz}. The average for fixed t is given by the average over all stress-component pairs which were measured at times that differ by t. For illustration, the evaluation of the σ_{xy}-component is shown in Fig. 2.11 according to the method described in the book of Allen and Tildesley [87All]. For a time span of fixed length, the average for a small t is based on more pairs than that for a time in the range of the time series length.

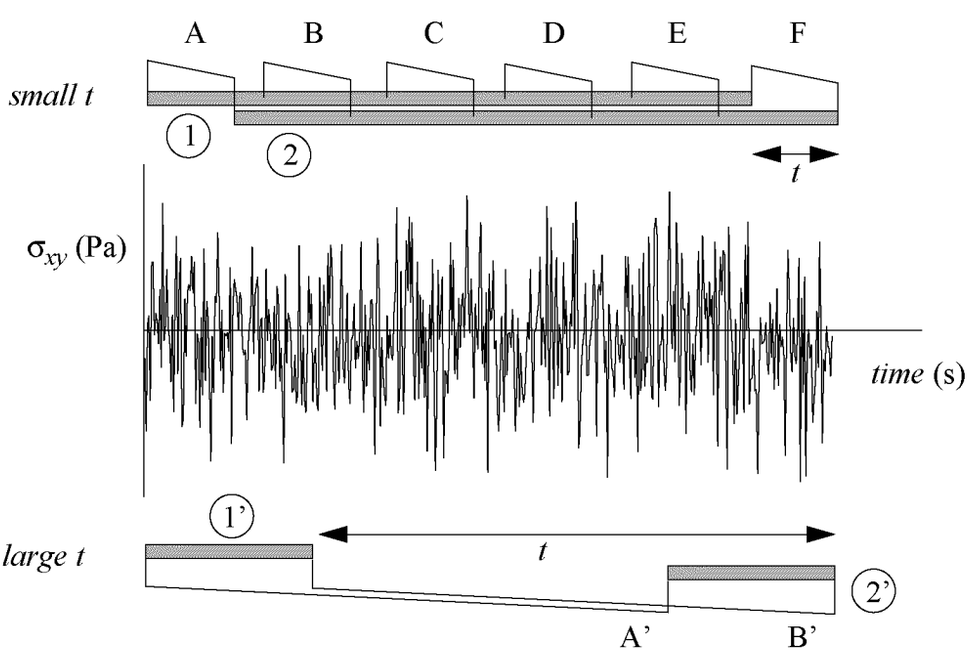

Fig. 2.11: Illustration of averaging procedure used in the stress autocorrelation function $C_s(t)$. The grey bars indicate the set of values available for building pairs (denoted by bridges) that differ by t. For a given time series (middle part), there are more pairs to be built that differ by a small t (upper part) than such that differ by a large t (lower part).

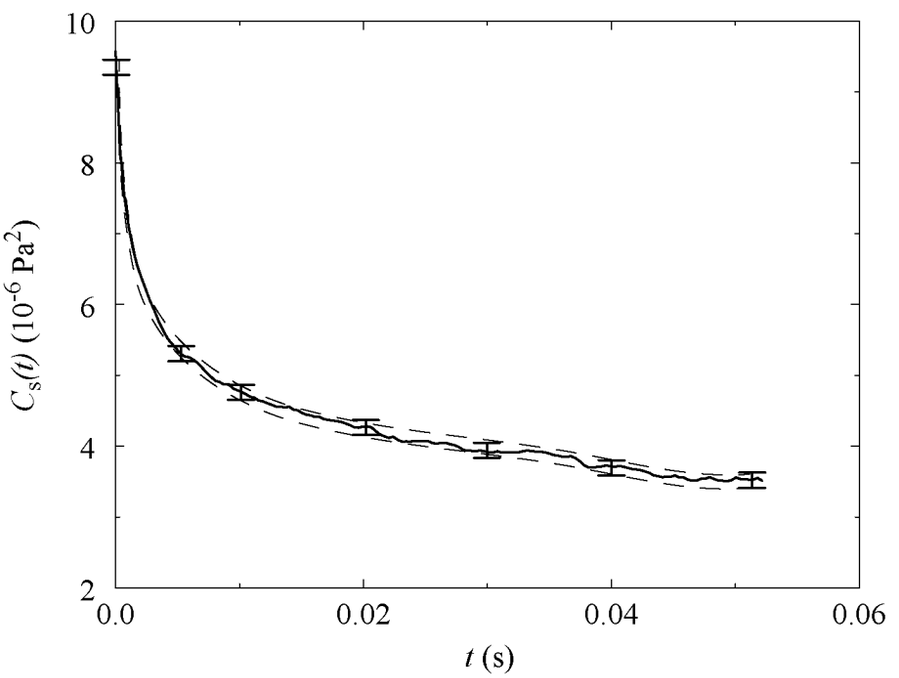

Fig. 2.12: Simulated stress autocorrelation function for a stable suspension at $\phi = 0.2$. For clarity, the error bars are given only for a few data points. The region between the two dashed lines is the envelope of a smoothed correlation function with the same error bars as in the raw data.

b) Results

As in the case of the mean square displacements, simulations were performed at five different solid contents: $\phi = 0.10$, 0.15, 0.20, 0.25 and 0.30. The stress autocorrelation functions for the different solid contents under consideration were compared using the fit-functions of the corresponding data. Three fit-functions have been used to sample the correlation function: power law decay, simple exponential decay and stretched exponential decay. Using the error integral as the criterion for the quality of the fit-function, the stretched exponential fit-function [94Hey1, 94Hey2, 95Hey]

$$C_s(t) = C_s(0)\left((1-\beta_1)\exp\left[-\left(\frac{t}{\tau_s}\right)^{\beta_2}\right]+\beta_1\right) \tag{2.35}$$

gave the best results. A simple exponential decay ($\beta_2 = 1$) has shown to drop too fast. The parameters τ_s and β_2 in eqn. (2.35) denote the time scale on which the correlation fades and at what rate. The parameter β_1 measures the offset at infinity because

$$\lim_{t\to\infty} C_s(t) = C_s(0)\,\beta_1 \tag{2.36}$$

The values for the fitted parameters are listed in Table 2.6. The error bars of the parameters are calculated as described in subsection 2.3.2.

Let us first consider the values of the off-set parameter β_1. Only at a solid content of $\phi = 0.1$ the stress autocorrelation function decays to zero at infinity. For all higher solid contents, the stress components are correlated even over the longest times, which means that the system behaves rather as viscoelastic solid (maximum: $\beta_1 = 1$) than as a viscoelastic liquid (ideally: $\beta_1 = 0$).

It has been shown in eqn. (2.34) that a non-zero off-set in the stress autocorrelation function is due to a non-zero average and/or due to the long-time correlation of the fluctuations. The contribution of the non-zero average to the total off-set (given by eqn. 2.36)) is quantified by $\langle\sigma_{xy}\rangle_{eq}^2 / C_s(0)\beta_1$. The corresponding values in Table 2.6 indicate that for low solid contents ($\phi = 0.10$ and 0.15) the non-zero average does not give a significant contribution. For the higher solid contents however, it gives raise to approximately half of the total off-set value.

The exponent β_2 does not show a dramatic change at the liquid-solid transition between $\phi = 0.1$ and $\phi = 0.15$. In contrast, the stress relaxation time τ_s makes a large jump at this transition, followed by an almost linear decrease beyond the solid content $\phi = 0.15$.

A possibility to compare the stress autocorrelation $C_s(t)$ function with experiments would be by means of the relation (2.33) to the relaxation function $\Phi(t)$. The

latter can be measured through step-strain experiments or its Fourier transform through oscillation measurements. For a quantitative comparison, experimental data are needed on exactly the same system as the one used in our simulations. Such data could not be found in the literature and either the simulation or the experiments would have to be redone in order to have a good comparison.

ϕ	β_1 (1)	$C_s(0)$ (Pa^2)	$\langle\sigma_{xy}\rangle_{eq}^2 / C_s(0)\beta_1$	τ_s (10^{-3} s)	β_2 (1)
0.10	-0.031 ± 0.050	$3.83 \cdot 10^{-7}$	0.001 ± 0.001	5.3 ± 0.2	0.51 ± 0.02
0.15	0.016 ± 0.010	$2.30 \cdot 10^{-6}$	0.04 ± 0.03	6.7 ± 0.4	0.45 ± 0.02
0.20	0.346 ± 0.008	$8.63 \cdot 10^{-6}$	0.59 ± 0.04	4.9 ± 0.2	0.42 ± 0.02
0.25	0.573 ± 0.008	$1.79 \cdot 10^{-5}$	0.54 ± 0.03	2.7 ± 0.2	0.41 ± 0.02
0.30	0.709 ± 0.004	$5.91 \cdot 10^{-5}$	0.56 ± 0.03	1.4 ± 0.1	0.41 ± 0.01

Table 2.6: Parameters for the stretched exponential fit of the stress autocorrelation function: offset β_1, variance $C_s(0) = \langle\sigma_{xy}^2\rangle_{eq}$, stress relaxation time τ_s and exponent β_2.

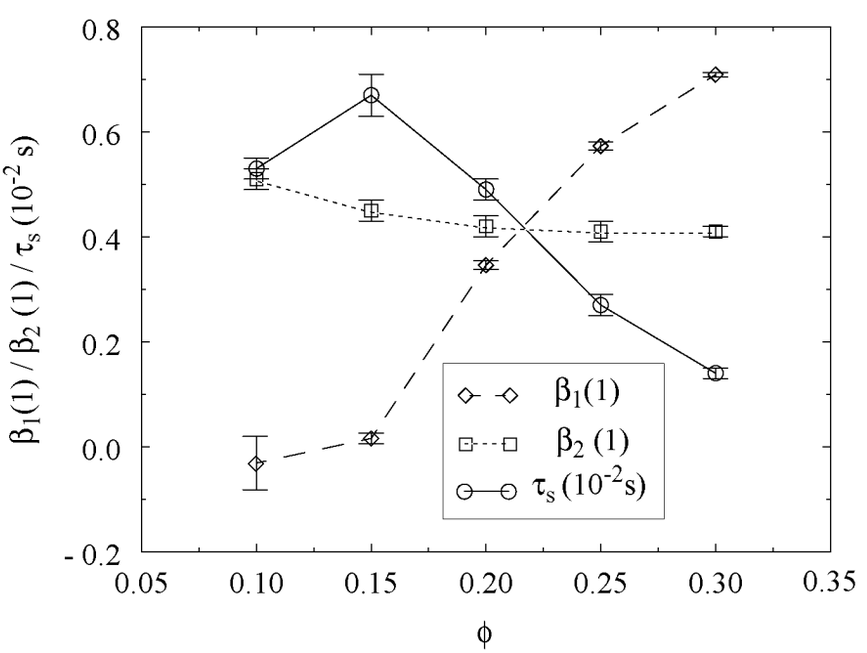

Fig. 2.13: Parameters for the stretched exponential fit as listed in Table 2.6: off-set β_1, stress relaxation time τ_s and exponent β_2. The lines are only drawn as visual guide.

After discussing the results for the stress autocorrelation function and relaxation function, respectively, one can employ the fit-parameters to determine the particle contribution to the zero-shear rate viscosity by means of the Green-Kubo relation (2.32). The non-zero offset β_1 in the correlation function leads to a infinite value for the zero-shear rate viscosity. This means that all systems with $\phi > 0.10$ exhibit yielding behavior, i.e. a finite stress has to be applied before the onset of flow. Only at the solid content $\phi = 0.1$, the suspension has a finite zero-shear rate viscosity, i.e. $\beta_1 = 0$ within error bars. The value determined by using the fit-function (2.35) with the parameters from Table 2.6 and with forcing $\beta_1 = 0$ within error bars is

$$\eta_{GK}^{part}(\dot{\gamma} \to 0)\Big|_{\phi = 0.1} = (6.50 \pm 0.34) \cdot 10^{-4} \text{ Pa s} \qquad (2.37)$$

It may be surprising that suspensions at solid contents as low as 15 vol % have an infinite zero-shear rate viscosity and show yielding behavior. If one considers however the interaction potential between the particles shown in Fig. 2.5, the following idea could help as an explanation. The interaction potential at $r = 1.2\,d$ is already in the order of $20\,k_B T$. Because there are no external driving forces on the particles, one can assume that any two particles never approach closer than this separation. This increases the effective radius of the particle and leads to an increase of the effective solid content by a factor of $(1.2)^3 \approx 1.73$. The range of effective solid content covered in our simulations is therefore $0.173 \le \phi_{eff} \le 0.519$. In addition, these new pseudo-particles have a rather strong interaction in the region above $r = 1.2\,d$ as shown by the potential curve in Fig. 2.5. In this respect, the infinite zero-shear rate viscosity and the yielding behavior are plausible.

The zero-shear rate viscosity in eqn. (2.37) depends on the solid content of the suspension and, in particular, vanishes for infinite dilution. Einstein has studied the influence of low solid contents on the viscosity which is summarized for spherical particles in the famous equation $\eta^{part}/\eta_s = 2.5\,\phi$ [06Ein, 11Ein]. With the value in eqn. (2.37) we find in our system $\eta^{part}/\eta_s = (6.50 \pm 0.34)\,\phi$ for $\phi = 0.10$. Even when reformulating the repulsive DLVO-potential in terms of an increased effective solid content as described above, i.e. $\phi = 0.10 \rightarrow \phi_{eff} = 0.173$, the simulation result still overestimates the Einstein prediction: $\eta^{part}/\eta_s = (3.75 \pm 0.20)\,\phi_{eff}$. Therefore, the discrepancy to the theoretical model has the following reason. The suspension for $\phi = 0.10$ (or $\phi_{eff} = 0.173$) is not dilute in the sense of ***non***-interacting particles which is a necessary condition for the applicability of the Einstein equation.

Summary

The viscoelastic properties of the suspension have been studied by means of the stress autocorrelation function, which could be well described by a stretched exponential decay and an offset at long times. First, the above results reveal a decrease in the characteristic decay time when raising the solid content. This is in agreement with the findings on the scaling of the transition time from short to long time diffusion (subsection 2.3.2). Second, the system has been found to change from a viscoelastic liquid to a viscoelastic solid for increasing solid content, which is represented by a growing value for the offset parameter. And third, the Green-Kubo relation has been used to calculate the zero-shear rate viscosity at the lowest solid content only, since all other samples had a finite offset in the stress autocorrelation function (leading to an infinite viscosity).

2.3.4 *Probing a Frequency Dependent Stokes-Einstein Relation*

a) Background

In a dilute suspension, where the particles do not interact, the diffusion coefficient D_0 of the colloidal particles and the viscosity η_s of the suspending Newtonian liquid are intimately related through eqns. (2.15-16). Recently, an extension of this relation between diffusive and rheological properties to complex fluids has been proposed and successfully applied [95Mas, 97Mas1, 97Mas2]. The goal of this subsection is to verify whether this relation is also valid in the case of the dense colloidal suspensions studied here.

The basic idea behind the generalized Stokes-Einstein relation proposed by Mason, Weitz ***et al.*** [95Mas, 97Mas1, 97Mas2] originates from mean field theory. One particle is singled out from the whole colloidal suspension and denoted as tracer particle. All the other particles are called host particles. In the following mean field procedure, the ensemble of all host particles is then considered as a continuum which is characterized only through its viscoelastic behavior (see Fig. 2.14).

As the tracer particle is moving around in this sea of 'smeared' particles, its diffusive behavior is influenced by the viscoelastic response of the particle suspension. The final result is then the following relation between the Laplace transform of the relaxation function, $\Phi^*(s)$, and the mean square displacement, $\langle \Delta \boldsymbol{r}^2(s) \rangle^*$:

$$\Phi^*(s) = \frac{2k_B T}{\pi d} \frac{1}{s^2 \langle \Delta \boldsymbol{r}^2(s) \rangle^*} \tag{2.38}$$

The variable s denotes the Laplace frequency. This relation holds for a single particle in a Newtonian liquid: with the mean square displacement $\langle \Delta \boldsymbol{r}^2(s) \rangle = 6D/s^2$ and the relations (2.15-16), one finds that $\Phi^*(s)$ equals the viscosity of the suspending liquid η_s. An inverse Laplace transformation results in the relaxation function $\Phi(t) = \eta_s \delta(t)$ ($\delta(t)$ denoting the Dirac delta function) and with help of eqn. (2.26) in the well known linear stress-strain rate relation of a Newtonian liquid, $\sigma_{xy}(t) = -\eta_s \dot{\gamma}(t)$. For all not infinitely diluted suspensions, eqn. (2.38) is only an approximation.

Because the data measured in the simulations include the stress autocorrelation function and not the relaxation function, eqn. (2.38) has to be transformed. Using the Laplace transform of eqn. (2.33), one finds for the stress autocorrelation function expressed in terms of the mean square displacement

$$C_s^*(s) = \frac{2(k_B T)^2}{\pi d} \frac{N}{V} \frac{1}{s^2 \langle \Delta \boldsymbol{r}^2(s) \rangle^*} \tag{2.39}$$

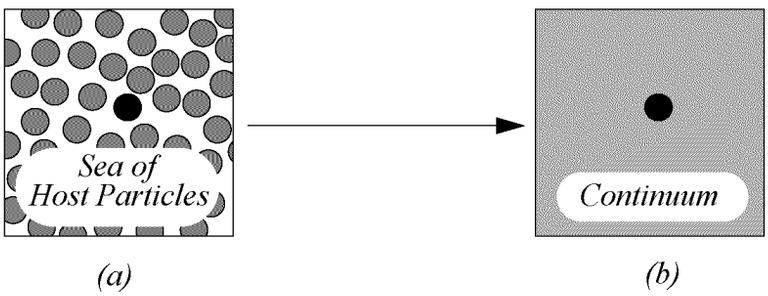

Fig. 2.14: Illustration of the generalized Stokes-Einstein relation. After selecting a tracer particle (black in (a)), the sea of the remaining host particles (grey in (a)) is considered as an effective continuum (grey in (b)) with a viscoelastic behavior identical to the viscoelastic behavior of the whole suspension.

Fig. 2.15 gives an illustration of the relation between the correlation function and the mean square displacement as implied by eqn. (2.39). Usually, the correlation function can not be determined analytically from eqn. (2.39) for any given expression for the mean square displacement. For illustrative reasons, a form that leads to an analytical solution has been chosen in Fig. 2.15. It contains all the characteristic features of self diffusion measured in colloidal systems: distinct short- and long-time diffusion and a smooth transition region.

One can see that the exponential decay in the stress autocorrelation function is only due to the difference in the short- and long-time diffusion coefficients D^S and D^L: the smaller the difference in the diffusion coefficients, the smaller is the amplitude A of the exponential and the closer are the two time scales τ_d and τ_s. On the other hand, the bigger the difference between the diffusion coefficients, the slower is the decay in the stress autocorrelation function.

The limiting case of equal short- and long-time diffusion coefficients should be emphasized. In this case, the stress autocorrelation function consists only of a Dirac delta-function $\delta(t)$ which means that the stresses are completely uncorrelated over any non-zero time interval. This leads to the conclusion that the lack of a transition region in the diffusive behavior of the particles corresponds to the complete lack of any memory in the system. The suspension is then purely viscous and has no elastic behavior.

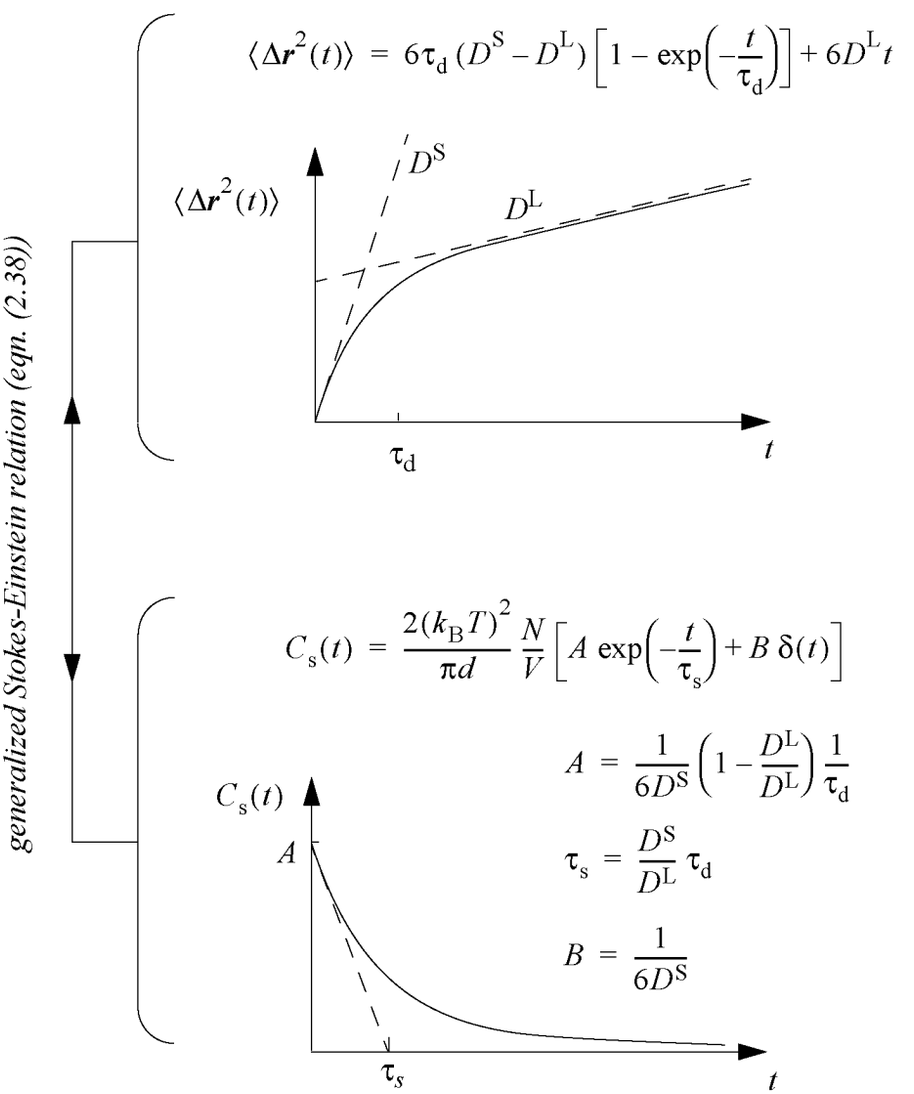

Fig. 2.15: Illustration of the generalized Stokes-Einstein relation given by eqn. (2.39). D^S and D^L denotes the short- and long-time diffusion coefficients, respectively, and τ_d is the cross-over time.

Before proceeding to the interpretation of the simulation data, one should note the following. For any arbitrary form of the mean square displacement, the Dirac delta-function in the correlation function $C_s(t)$ has its origin in the following restriction on the initial condition of the diffusion coefficient

$$0 < \frac{d}{dt}\langle \Delta \boldsymbol{r}^2(t) \rangle \Big|_{t=0} < \infty \qquad (2.40)$$

As mentioned previously, the stretched exponential fit-function used for the mean square displacement leads to an infinitely large short-time diffusion coefficient. The discussion below will show in as far this affects the interpretation of the data.

b) Results

For the stretched exponential functions (2.24) and (2.35), the relation (2.39) can not be verified analytically but only numerically by constructing the functions with the fitted parameters, followed by a numeric Laplace transformation. Fig. 2.16 shows the results for solid contents of $\phi = 0.1, 0.2, 0{,}3$.

The simulation data for the stress autocorrelation function and the mean square displacement are only available in a limited range $[t_{min}, t_{max}]$. For the stress autocorrelation as well as for the mean square displacement, $t_{min} = 0$ s and the time resolution in the data $\tau_{res} = 3.5 \cdot 10^{-4}$ s. The upper limit on the Laplace variable s, beyond which the time discretization becomes noticeable, is given by $1/\tau_{res}$. The lower limit on the s-value was determined as follows. Beyond t_{max}, the function is extrapolated according to the corresponding fit-function. For s-values, where the contribution of this extrapolated part of the function to the Laplace-integral was larger than 1 %, no values for the Laplace-transform are reported. In the case of the stress autocorrelation data, $t_{max,s} = 0.052$ s, whereas for the mean square displacement series $t_{max,d} = 0.364$ s. The symbols in Fig. 2.16 are only to distinguish the different samples. Due to the high density of s-values, the set of $C_s^*(s)$-data is represented in lines rather than as single data points.

The following four points are worthy a note. (i) For all solid contents, the mean square displacement data (filled symbols) level off to a constant value for increasing s. Using the left hand side of eqn. 2.39, this means that $\langle \Delta \boldsymbol{r}^2(s) \rangle^* \sim s^{-2}$ $(s \to s_{max})$, or equivalently $\langle \Delta \boldsymbol{r}^2(t) \rangle \sim t$ $(t \to t_{min} \sim 1/s_{max})$. Since $1/s_{max} = 10^{-4}$ s has the same magnitude as the finite resolution in the mean square displacement data, $\tau_{res} = 3.5 \cdot 10^{-4}$ s from subsection 2.3.2 b), the linearity in $\langle \Delta \boldsymbol{r}^2(t) \rangle$ originates from the linearization between the data points and not from the existence of a short time diffusion coefficient. (ii) The dependency of the left hand side of eqn. (2.39), $s^2 \langle \Delta \boldsymbol{r}^2(s) \rangle^*$, on the variable s is strongest for the higher solid content and lessens as the solid content decreases. Thus, the higher the solid content, the stronger is the non-linearity in the $\langle \Delta \boldsymbol{r}^2(t) \rangle \leftrightarrow t$-relation. (iii) The Laplace transform of the correlation function $C_s^*(s)$ (open symbols) not only underestimates the $s^2 \langle \Delta \boldsymbol{r}^2(s) \rangle^*$-data but also does not have the appropriate functional dependence on s (apart from limited s-range for $\phi = 0.3$). (iv) Only at $\phi = 0.1$, $C_s^*(s) \to \text{const}$ as $s \to s_{min}$. This means that the correlation function decays to zero for large times, i.e. $C_s(t) \to 0$ as $t \to 1/s_{min}$ (or larger) for the lowest of all solid contents, which is in agreement with the values for the offset parameters β_1 in Table 2.6 and Fig. 2.13.

The data in Fig. 2.16 show that the frequency dependent Stokes-Einstein relation is not respected by any of the solid contents, best agreement is found for $\phi = 0.3$ (triangles). This discrepancy is even more pronounced if one considers the logarithmic derivative of the function $C_s^*(s)$ (Fig. 2.17).

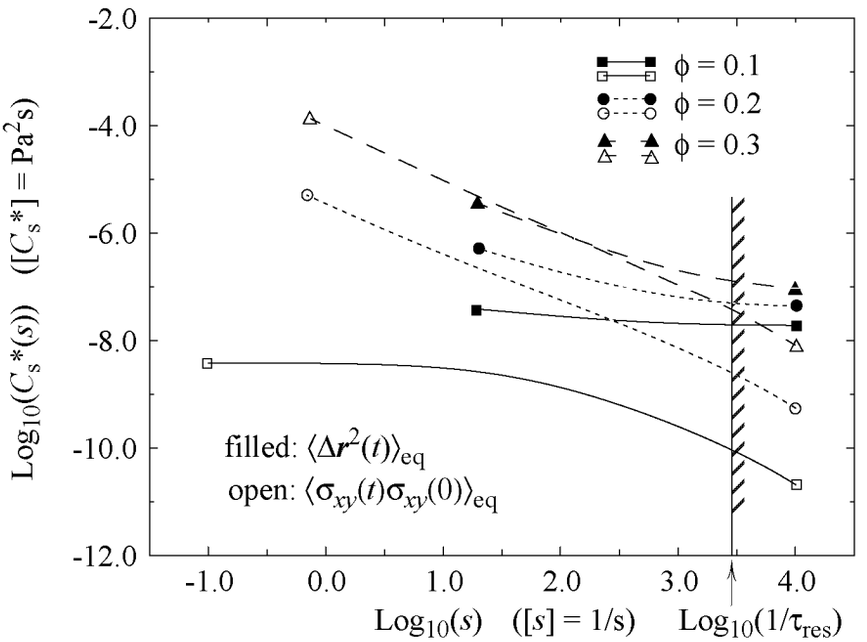

Fig. 2.16: Test of the generalized Stokes-Einstein relation (2.39). Filled symbols represent the function $C_s^*(s)$ as calculated from $\langle \Delta r^2(t) \rangle$ through relation (2.39), open symbols stand for $C_s^*(s)$ as determined directly from $\langle \sigma_{xy}(t)\sigma_{xy}(0) \rangle_{eq}$.

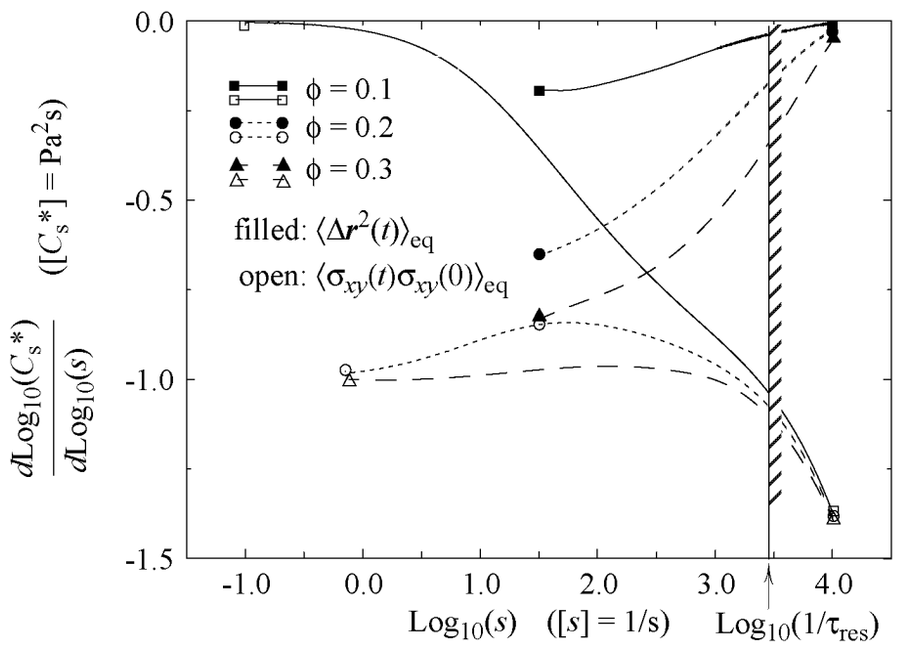

Fig. 2.17: Logarithmic derivative of $C_s^*(s)$ for the data presented in Fig. 2.16.

Apart from the discretization errors for small t-values discussed above, there is a second reason for the large discrepancy in the $C_s^*(s)$-data calculated by the two distinct methods shown in Fig. 2.17. Let us concentrate on the region of large s-values or small t-values, respectively. On one hand, the fit-function for the mean square displacement given in eqn. (2.24) behaves for small t as

$$\langle \Delta \boldsymbol{r}^2(t) \rangle \Big|_{t \to 0} = \alpha_1 \left(\frac{t}{\tau_d} \right)^{\alpha_2} \tag{2.41}$$

For large s, this leads to a $s^{\alpha_2 - 1}$-dependence for the left hand side of eqn. (2.39), resulting in a $t^{-\alpha_2}$-dependence of the short-time behavior of the stress correlation function $C_s(t)$. On the other hand, a Taylor expansion of expression (2.35) for small t leads to

$$C_s(t) = C_s(0) \left[1 - (1 - \beta_1) \left(\frac{t}{\tau_s} \right)^{\beta_2} \right] \qquad (t \ll \tau_s) \tag{2.42}$$

which is finite for vanishing t. We therefore conclude that the fit-functions chosen for the mean square displacement and the stress autocorrelation function are incompatible with respect to the generalized Stokes-Einstein relation, irrespective of the precise values of the fitted parameters.

It is not clear and has not been in the focus of investigations in this study whether there exist other fit-functions for the simulation data that fulfill the following two requirements: (a) that they are equally good or better fit-functions for the simulation data and (b) that they allow to fulfill (at least in principle, irrespective of the fitted parameters) the generalized Stokes-Einstein relation.

Summary

The focus of the above subsection has been to test a frequency-dependent Stokes-Einstein relation between the viscoelastic and the diffusive properties of the suspension. It has been shown that the proposed relation does not hold if both the decay in the stress autocorrelation as well as the transition to long time diffusion are represented by a stretched exponential function. At given solid content, the proposed relation fails most for the shortest time scales. Surprisingly enough, best agreement between the two sides of the generalized Stokes-Einstein relation is found for the highest solid content.

2.3.5 *Summary and Conclusions*

Equilibrium properties of colloidal suspensions have been examined in section 2.3. The stretched exponential function has been found to be a good representation of the stress relaxation and of the transition from short to long time diffusion. It has been shown that the relaxation in the stress autocorrelation function and the transition from short to long time diffusion both occur in shorter time intervals as the solid content is increased. Furthermore, raising the solid content has shown to decrease the long-time diffusion coefficient and to enhance the (viscoelastic) long-time memory of the system.

The reason of all these effects is the stronger interaction between the particles as they are closer together at higher solid content. In dilute systems, particles interact only weakly as the interaction potential for large separations is small and they need to approach each other either by diffusion or by any other process in order to interact more strongly. In denser systems, the coupling between the particles happens directly over the strong interactions between close particles. Any particle motion or perturbation is conveyed faster to the neighboring particles and hence through the whole suspension. Higher solid contents also lead to a reduced long time diffusion since a particle needs more energy to pass by the repulsive interaction range of adjacent particles. The stronger coupling between the particles also serves as an explanation for the increasingly solid-like behavior at higher solid content. It is well known that attractive particles arrange in a structure with lowest total or free energy, respectively. The same is true for repulsive particles in a confined geometry. Since the particles cannot escape from the simulation box (or from a real cavity), the repulsion between the particles forces them to separate as far as possible. If the interaction forces are strong enough, the particles are immobilized in a cage built from the surrounding particles. Therefore, the increase of solid content leads to a transition from liquid-like to solid-like behavior as far as the equilibrium in a confined geometry is concerned.

The stress autocorrelation function has been employed to calculate the zero shear rate viscosity of the suspension by using the Green-Kubo formula. Due to the finite long-time memory at higher solid contents, a finite viscosity value could only be calculated for the solid content $\phi = 0.1$, whereas the suspensions at higher solid contents have an infinite zero shear rate viscosity. This is in agreement with the change towards a solid-like behavior.

An extended, generalized Stokes-Einstein relationship has been discussed in detail. It has been found that the selection of the fit functions for the stress autocorrelation data and for the mean square displacement has a strong influence on the validity of the relation. Although the stretched exponential fit function gives a good representation of the simulation data (stress auto correlation and mean square displacement), they are incompatible with respect to the proposed extended Stokes-Einstein relation.

Apart from the selection of the fit functions, it is not clear whether the proposed relation holds or not. For a definitive answer, the following is recommended. Firstly, much longer simulation runs are needed to get a better description of the long-time tail of the stress autocorrelation function, which would result in better selection criteria for the fit function. Secondly, an appropriate function has to be found for the description of the mean square displacement. It should meet the requirement of a finite short- and long-time diffusion coefficient.

2.4 Simple Shear Flow

Results of Brownian dynamics simulation for a colloidal suspension under shear flow are presented in this section. The shear rate dependent shear stress and normal stress differences are discussed in detail. Measurements of the shear rate dependent particle diffusion and the ordering of the suspension at high shear rate will conclude the section.

2.4.1 Simulation Input, Method

The system under consideration in this section is identical to the system studied at equilibrium except for the non-zero shear rate. The parameters defined in subsection 2.3.1 are therefore also valid for this section.

The flow field imposed on the system enters through the Stokes' drag force (see eqn. (2.7)) into the equations of motion (2.11). Only the particle velocity relative to the imposed flow field leads to a friction force. Therefore each particle is driven to have the same velocity as the background flow field at the particle's actual position. The shear flow field imposed on the colloidal suspension is of the form

$$\begin{pmatrix} v_x(\boldsymbol{r}) \\ v_y(\boldsymbol{r}) \\ v_z(\boldsymbol{r}) \end{pmatrix} = \Gamma \cdot \boldsymbol{r} = \begin{pmatrix} 0 & \dot{\gamma} & 0 \\ 0 & 0 & 0 \\ 0 & 0 & 0 \end{pmatrix} \cdot \begin{pmatrix} x \\ y \\ z \end{pmatrix} = \begin{pmatrix} \dot{\gamma}\, y \\ 0 \\ 0 \end{pmatrix} \tag{2.43}$$

The effect of the flow situation on the periodic boundary conditions has been implemented by the Lees-Edwards method as described in subsection 2.2.2.

Simulations have been performed for different solid contents and shear rates. The mean values and standard deviations of a quantity A reported in this section are all determined by analyzing a time series $A(t)$ $(t_0 \le t \le \tau_{\text{span}})$. The shear rates, for which the rheology of the suspension has been measured, were in the range

$$1\ \text{s}^{-1} \le \dot{\gamma} \le 200\ \text{s}^{-1}$$

The rate of deformation can also be measured with respect to the characteristic relaxation time τ_{Br} (see eqn. (2.19)) of the suspension and is then called Péclet-number [89Rus, 96Dho]: $Pe = \dot{\gamma}\,\tau_{\text{Br}}$. In these nondimensional units, the range of shear rates covered in our simulations becomes

$$0.084 \le Pe \le 9.68$$

The Péclet-number is the ratio between shear forces and thermodynamic forces and can be used as a measure for the shear thinning transition. Experiments have shown that changes in the rheological behavior and in the particle arrangement can best be observed when increasing the Péclet number from $Pe < 1$ to

$Pe > 1$ [89Wer, 90Wag, 90Wer]. For small Péclet numbers, the thermal forces dominate and the system is still close to equilibrium, whereas for large Péclet numbers, the shear forces drive the system far from equilibrium. The shear rates used in our simulations therefore cover the interesting transition range around $Pe \approx 1$.

The components of the stress tensor, which are the responses of the suspension to the applied shear rate, are calculated as described in eqn. (2.30).

2.4.2 Shear Stress

a) Finite Shear Rates

In order to compare the shear stresses measured for the different solid contents, the data were fitted with fit-functions proposed by Eu and Ohr [84Eu]. They predict an asinh-dependence at low shear rates and a power law for high shear rates, respectively. Because the shear rates studied in our simulations are around $Pe \approx 1$, both functions were used to fit the whole range of shear rates.

Both functions lead to zero stress at zero shear rate. Due to the yield stress behavior observed in the equilibrium simulations, we introduce an offset in the stress which allows for a finite stress at zero shear rate. The two functions used to fit the simulation data are

$$-\sigma_{xy} = \alpha_1 \operatorname{asinh}(\dot{\gamma}\tau_{Eu}) + \alpha_2 \qquad \text{(small } \dot{\gamma}\text{)} \qquad (2.44)$$

and

$$-\sigma_{xy} = \beta_1 \dot{\gamma}^{\beta_2} + \beta_3 \qquad \text{(large } \dot{\gamma}\text{)} \qquad (2.45)$$

The function in eqn. (2.45) should actually read $-\sigma_{xy} = \beta_1(\dot{\gamma}/\tau_{Eu}')^{\beta_2} + \beta_3$. However, this expression cannot be used for the fitting procedure because it contains redundant information: multiplying the characteristic time τ_{Eu}' by a given constant can be compensated by rescaling the parameter β_1 appropriately. The resulting fit-parameters would then lack any physical meaning because they depend on the optimization procedure. Therefore, we have used expression (2.45) where the shear rate is measured in units of 1 s^{-1}. It is worthy a note that the parameter β_2 is a useful measure for the shear thinning of the suspension: for $\beta_2 = 1$, the shear stress grows linearly in the shear rate (i.e. the viscosity is constant), whereas a sublinear growth (and thus decreasing viscosity) is obtained for $\beta_2 < 1$.

We notice that both expressions (2.44) and (2.45) do not account for a finite viscosity as $\dot{\gamma} \to \infty$: although the simulations in this study showed a pronounced shear thinning transition, they did not fully reach the second Newtonian plateau. It is therefore not possible to determine (i.e. extrapolate) the viscosity in the shear thinned regime from our data to acceptable accuracy.

The above fit functions were used to fit the measured shear stresses σ_{xy} themselves rather than to fit the viscosity values $\eta = -\sigma_{xy}/\dot{\gamma}$. Fig. 2.18 and 2.19 show the shear stresses measured for a suspension at a solid content of $\phi = 0.2$ and the corresponding fit-function: asinh- and powerlaw-fit, respectively. The corre-

sponding fit-parameters are listed in Tables 2.7 and 2.8. The error bars on the fit-parameters were calculated as described in subsection 2.3.2.

For all three solid contents, both functions (2.44) and (2.45) fitted the shear stress data equally well and none of these two could be singled out in favor of the other.

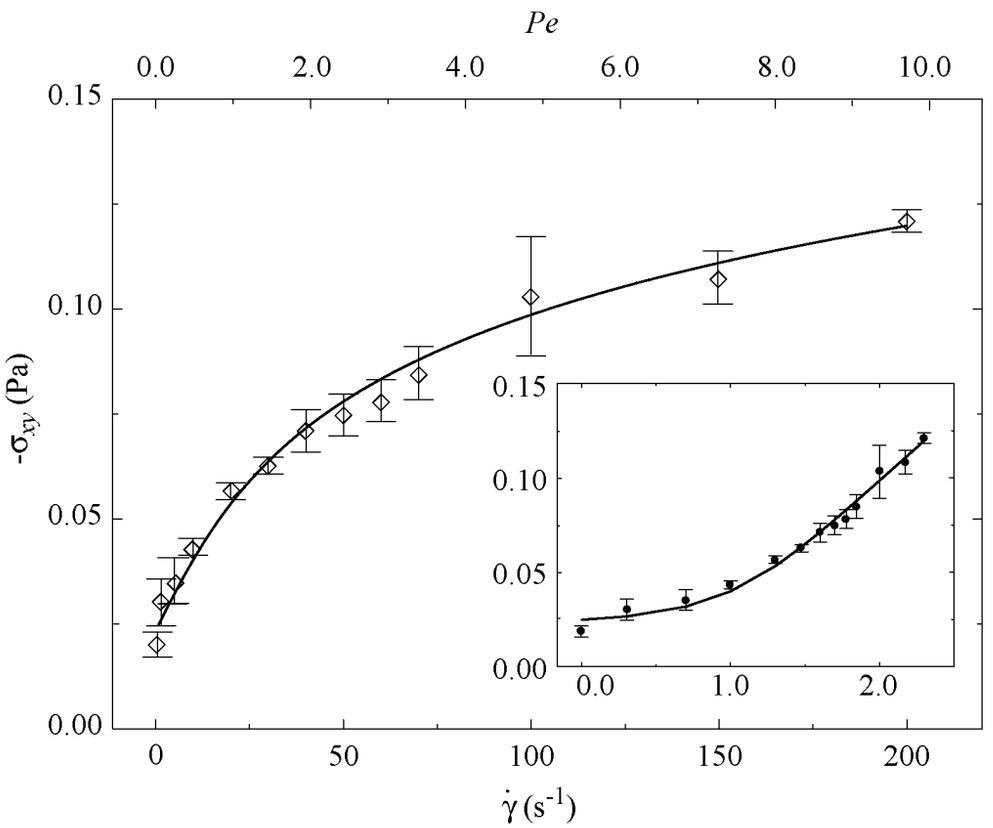

Fig. 2.18: Shear stress σ_{xy} for $\phi = 0.2$. Diamond symbols denote the simulation data, the solid line is the fit with the asinh-function (2.44). The inset is the same plot with logarithmic shear rate values to show the low shear rate behavior.

Solid content ϕ	α_1 (10^{-3} Pa)	τ_{Eu} (10^{-3} s)	α_2 (10^{-3} Pa)
0.10	8.40 ± 0.06	29.1 ± 0.4	0.64 ± 0.01
0.20	30.0 ± 0.4	57.5 ± 1.6	23.1 ± 0.2
0.30	66.9 ± 3.4	270.1 ± 5.7	78.7 ± 4.4

Table 2.7: Shear stress σ_{xy}. Fit-parameters for the fit-function defined in eqn. (2.44).

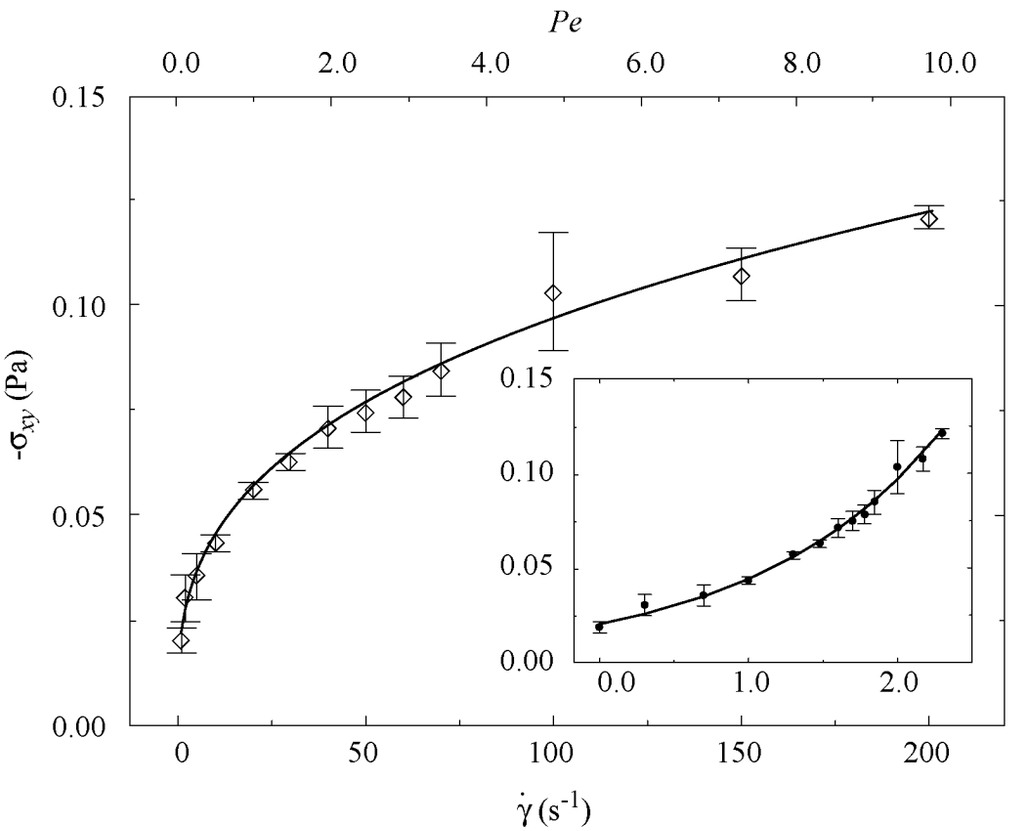

Fig. 2.19: Shear stress σ_{xy} for ϕ = 0.2. Diamond symbols denote the simulation data, the solid line is the fit with the powerlaw-function (2.45). The inset is the same plot with logarithmic shear rate values to show the low shear rate behavior.

Solid content ϕ	β_1 (10^{-3} Pa)	β_2 (1)	β_3 (10^{-3} Pa)
0.10	1.66 ± 0.01	0.499 ± 0.001	-1.44 ± 0.001
0.20	19.7 ± 0.4	0.344 ± 0.003	0.52 ± 0.45
0.30	469 ± 25.5	0.108 ± 0.035	-38 ± 26

Table 2.8: Shear stress σ_{xy}. Fit-parameters for the fit-function defined in eqn. (2.45).

When looking at the fit parameters of the asinh-function in Table 2.7, the characteristic time scale τ_{Eu} can also be considered as the inverse of a characteristic shear rate because it rescales the shear rate in eqn. (2.44) to a dimensionless quantity. The values for τ_{Eu} listed in Table 2.7 show that the characteristic time increases for increasing solid content. This means that the corresponding shear rate decreases with increasing solid content. We conclude that the shear thinning transition (Fig. 2.2) is moved to smaller shear rates as the solid content increases, in accordance with experimental results [89Wer, 90Wer].

The fact that the characteristic time scales τ_{Eu} increase when raising the solid content is in clear contrast to the simulation results about the time scales at equilibrium. However, the following fundamental difference between these situations resolves the problem. At equilibrium, the characteristic time scale refers to the transition to a stationary state. However, this stationary state does not necessarily have to be the same for all solid contents. The particles may diffuse over large distances for low solid content, whereas for higher solid content the particles are merely captured in a cage by the surrounding particles, resulting in a completely different stationary state. The situation changes when considering the flow behavior of the suspension under steady shear. Here, the particles need to roll over each other sooner or later, irrespective of how strong they are repelled. Therefore, the equilibrium considerations illustrated above are invalid in shear flow. The increasing time scales, or equivalently decreasing shear rates, when raising the solid content, are explained by the stronger and more direct interaction between the particles. Since the shear thinning transition is due to the potential interaction between the particles, we conclude that increasing this interaction leads to a more pronounced transition at lower shear rates.

The amplitude α_1 clearly indicates that the shear stress is higher for higher solid contents. This is explained by the fact that at higher solid contents the particles are closer and therefore repel each other more strongly.

The offset parameters of the two fit functions, α_2 and β_3, differ greatly. Whereas α_2 shows a clear increase with increasing solid content, β_3 does not show a clear trend. This might be a criterion to rule out the power law-fit completely, or to consider it only in the high shear rate regime. Considering the offset-parameter α_2, Table 2.7 indicates that although the equilibrium simulations have shown no yielding behavior at $\phi = 0.1$, the offset-parameter α_2 is not equal to zero. This discrepancy might be due to the relatively large error bars in the shear stress data. The increasing offset parameters listed in Table 2.7 indicate the tendency of the suspension to show yielding behavior at the higher solid contents.

Although the power law function is not useful for the characterization of the low shear rate regime, it can be used to capture the main features at high shear rates. Table 2.8 lists the values for the power β_2 in eqn. (2.45). A strong decrease of β_2 with increasing solid content can be observed. For a Newtonian liquid, we would have $\beta_2 = 1$. For $\beta_2 < 1$, the liquid begins to show shear thinning because

the viscosity $\eta = -\sigma_{xy}/\dot{\gamma}$ decreases with increasing shear rate. The shear thinning is the stronger the higher the solid content in the suspension.

The simulation results show a substantial shear thinning, i.e. a decrease of the viscosity $\eta = -\sigma_{xy}/\dot{\gamma}$ with increasing shear rate for all solid contents, as has been observed also in numerous experiments. For an overview the reader is referred to Chapter 14 in [89Rus]. Shear thinning is common for model systems in non-equilibrium Brownian dynamics simulations (see for example [96Ras])

None of the simulations showed any sign of shear thickening, i.e. an increase of viscosity with shear rate. The reason for this is not that measurements at high enough shear rates were not carried out but rather in the incomplete model equations (2.11). A thorough discussion of this phenomenon is presented in sections 2.5 and 2.6.

b) Compatibility with the Green-Kubo relation

In order to test whether the zero-shear rate viscosity, as determined by the Green-Kubo relation at equilibrium (see eqn. (2.37)), corresponds to the nonequilibrium simulation data, the viscosity for $\phi = 0.1$ was plotted as shown in Fig. 2.20.

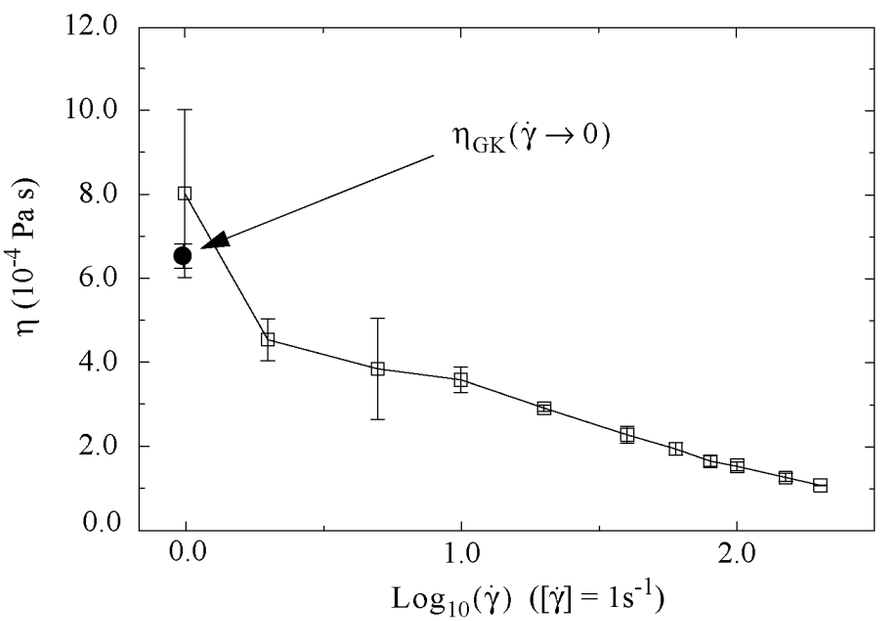

Fig. 2.20: Viscosity-shear rate relation at $\phi = 0.1$. The black dot denotes the zero-shear rate viscosity determined from the Green-Kubo relation (2.32). The line is only drawn as visual guide.

Fig. 2.20 shows that the zero-shear rate viscosity derived from the Green-Kubo relation (2.32) lies in the range of the viscosity found at the lowest shear rate value in the nonequilibrium simulations, $\dot{\gamma} = 1\,\mathrm{s}^{-1}$. The question arises whether the viscosity for smaller shear rates increases further above the Green-Kubo value. On one hand, we concluded from the finite size of the Green-Kubo viscosity that the suspension shows no yielding. On the other hand, the viscosity for smaller shear rates is supposed not to increase further because the lowest shear rate corresponds to a Péclet number much smaller than one. The value for the viscosity at the lowest shear rate is therefore supposed to lie in the first Newtonian plateau. Thus, the Green-Kubo value for the viscosity should not differ more from the limiting value of the flow curve if smaller shear rates would be probed.

The calculation of the zero-shear rate viscosity by means of the Green-Kubo relation is difficult for the following reason. The fluctuations in the stress autocorrelation function are too large for long times in order to give a good estimate of the long-time behavior of the correlation. Therefore, fit-functions need to be employed. However, a good selection of the fit function is arbitrary to some degree due to the large fluctuations in the simulation data. Since the Green-Kubo value for the viscosity is strongly influenced by the extrapolating fit function, the confidence in the resulting zero shear rate viscosity is limited. It has also been noted in other simulations [96Ras], that the Green-Kubo viscosity cannot be used as an accurate value but rather as an estimate.

Summary

The above discussion of the shear stress has shown that increasing the solid content results in higher stresses, in lower characteristic shear rates (for the shear thinning transition), and in higher extrapolated yield stresses at zero shear rate. The latter are in agreement with the infinite value for the zero shear rate viscosities determined by using the Green-Kubo relation in section 2.3. For the lowest solid content, the low-shear rate viscosities compared reasonably well to the value of the Green-Kubo viscosity. Furthermore, the suspensions are increasingly shear thinning as the solid content is raised. No shear thickening has been observed, even at the highest shear rates and at the highest solid content.

2.4.3 *Normal Stress Differences*

Besides the shear viscosity, also the normal stresses $N_1 = \sigma_{xx} - \sigma_{yy}$ and $N_2 = \sigma_{yy} - \sigma_{zz}$ are of interest when studying the flow behavior of colloidal suspensions [89Bar1]. Observable consequences of the normal stresses include the 'rod-climbing' phenomenon (also known as Weissenberg effect) and post-extrusion swelling. In order to compare the normal stresses for the different solid contents, again fit-functions proposed by Eu and Ohr [84Eu] have been applied. The fit-parameters are then compared to study the influence of the solid content.

The predictions of Eu and Ohr have been extended here to allow a finite offset at zero shear rate, in order to account for the anisotropic property of the suspension at the higher solid contents. One can assume that also the diagonal elements of the stress tensor show a certain anisotropy at higher solid contents. The fit-functions for both N_1 and N_2 in this study are:

$$N_{1,2} = \alpha_1 [\operatorname{asinh}(\dot{\gamma}\tau_{Eu})]^2 + \alpha_2 \qquad \text{(small } \dot{\gamma}\text{)} \qquad (2.46)$$

and

$$N_{1,2} = \beta_1 \dot{\gamma}^{\beta_2} + \beta_3 \qquad \text{(large } \dot{\gamma}\text{)} \qquad (2.47)$$

Figures 2.21-2.22 and 2.24-2.25 show the data for the normal stresses obtained at a solid content $\phi = 0.2$. A comparison of Fig. 2.21 and Fig. 2.22 suggests that the expressions (2.46) and (2.47) fit the data of N_1 equally well in the range of shear rates probed in our simulations. The same can also be said for N_2 by comparing Fig. 2.24 and Fig. 2.25. Both fit-functions rank also equally well at $\phi = 0.1$, whereas at $\phi = 0.3$ the first normal stress difference N_1 could neither be described by expression (2.46) nor by (2.47). The main problem with the data for $\phi = 0.3$ was that the curve has a relatively large flat region for small shear rates ($\dot{\gamma} \leq 5\ s^{-1}$) which requires a small τ_{Eu}, followed by a steep slope, before a sharp bending off already above $\dot{\gamma} = 30\ s^{-1}$ (Fig. 2.23) which requires a high τ_{Eu}.

All parameters of the fit-functions for N_1 are listed in Table 2.9 and Table 2.10, respectively. No reasonable fit-parameters for the asinh-function could be found for $\phi = 0.3$, where the fitted function overestimates the data at low shear rates and underestimates them at high shear rates.

From the α_1-values listed in Table 2.9 and the β_1-values listed in Table 2.10, one can see that the normal stress is larger for higher solid contents. This is due to the smaller separation distances between the particles and, thus, stronger interaction.

As already observed in the shear stress, the characteristic time scale τ_{Eu} is larg-

er for the higher solid contents, i.e. the characteristic shear rate decreases when increasing the solid content.

The offset parameters α_2 and β_3, respectively, increase with increasing solid contents. However, if the offset is measured in reduced units with respect to the corresponding amplitudes, α_2/α_1 and β_3/β_1, then the increase is less strong. One may therefore assume that the offset originates from inaccurate data or from choosing an inappropriate fit-function.

The exponent β_2 in the power law (2.47) is decreasing for increasing solid content. It drops by more than a factor of ten when changing the solid content from $\phi = 0.1$ to $\phi = 0.3$. This means that the normal stress difference N_1 levels off rapidly and has only a weak dependence on the shear rate at high solid contents.

Everything that has been stated concerning the data for the first normal stress difference N_1, is also true for the second normal stress difference N_2. For increasing solid contents, the normal stress N_2 becomes larger (see values for α_1 in Table 2.11 and for β_1 in Table 2.12) and also the characteristic time scale τ_{Eu} is increasing (see Table 2.11). At high shear rates, the values for the power β_2 indicate a weak shear rate dependence for high solid contents. The offset parameters (see values for α_2 in Table 2.11 and for β_3 in Table 2.12) increase significantly only in absolute values, but not if they are measured in units of the amplitudes α_1 and β_1. Therefore, as in the case of the first normal stress difference, this offset may therefore only be due to inaccurate data or to selecting the wrong fit-function.

The main differences between the first and second normal stress difference is the following. For the asinh-function, higher values for τ_{Eu} mean a compression of the normal stress curve with respect to the shear rate, i.e. a larger curvature and a steeper slope at small shear rates and in particular a stronger leveling-off beyond. A comparison of the τ_{Eu}-values for N_1 (Table 2.9) and for N_2 (Table 2.11) shows that they have a stronger solid content dependence for N_2 than for N_1. We therefore conclude that the leveling-off at high shear rates increases more with solid content for the second normal stress difference than for the first normal stress difference. The same can be seen from the exponent β_2 in the power law function (2.47), where the values for β_2 show a stronger decrease with increasing solid content for N_2 (Table 2.12) than for N_1 (Table 2.10).

A comparison of the values in Table 2.9 and in Table 2.11 shows that the time scales τ_{Eu} of N_1 and of N_2 for $\phi = 0.2$ differ by a factor of approximately five. We notice by comparing Fig. 2.21 and Fig. 2.24 that the major difference between both fits lies in the fact that the asinh-function underestimates not only the low-shear rate data for N_1 but also the curvature in this range, resulting in a too low value for τ_{Eu}. However, increasing τ_{Eu} would reduce the fit-quality at higher shear rates. The value reported in Table 2.9 is the optimal value for the whole range of shear rates studied here. It is not understood whether all this indicates that the used fit-function is not appropriate or whether the discrepancy in the τ_{Eu}-values of N_1 and N_2 is inherent to the system.

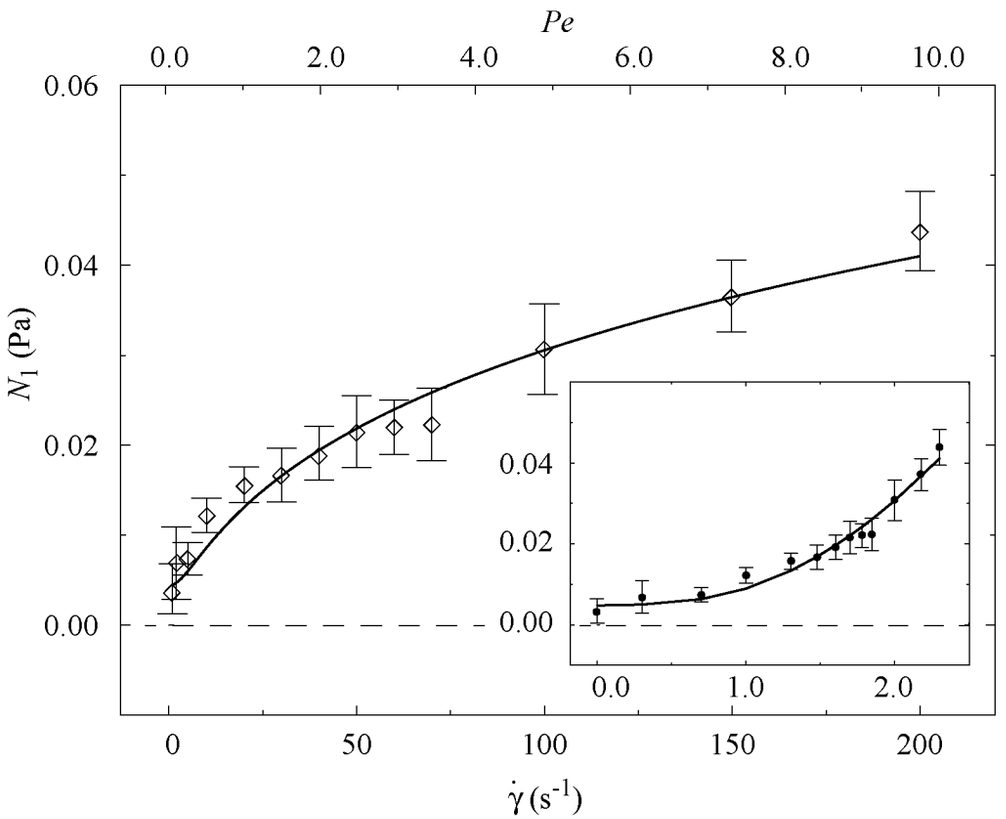

Fig. 2.21: First normal stress difference N_1 for ϕ = 0.2. Diamond symbols denote the simulation data, the solid line is the fit with the asinh-function (2.46). The inset is the same plot with logarithmic shear rate values to show the low shear rate behavior.

Solid content ϕ	α_1 (10^{-3} Pa)	τ_{Eu} (10^{-3} s)	α_2 (10^{-3} Pa)
0.10	0.71 ± 0.01	68.2 ± 0.2	0.182 ± 0.001
0.20	1.82 ± 0.03	220 ± 7	4.67 ± 0.06
0.30	-	-	-

Table 2.9: First normal stress difference N_1. Fit-parameters for the fit-function defined in eqn. (2.46).

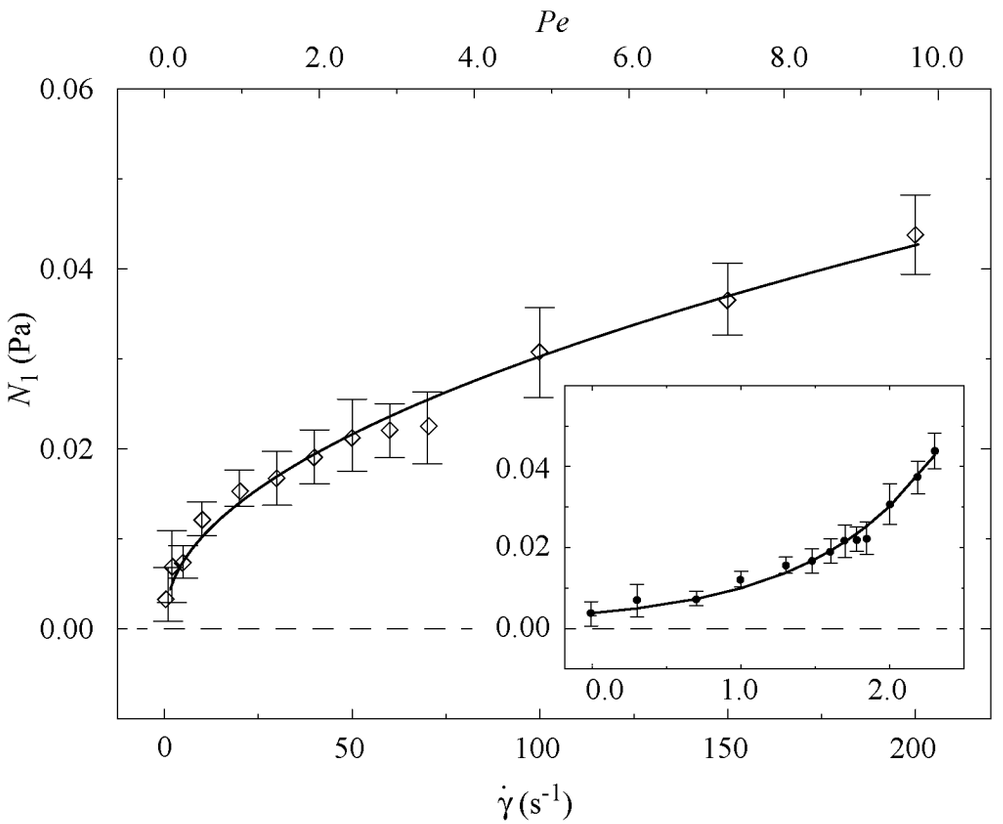

Fig. 2.22: First normal stress difference N_1 for ϕ = 0.2. Diamond symbols denote the simulation data, the solid line is the fit with the powerlaw-function (2.47). The inset is the same plot with logarithmic shear rate values to show the low shear rate behavior.

Solid content ϕ	β_1 (10^{-3} Pa)	β_2 (1)	β_3 (10^{-3} Pa)
0.10	0.166 ± 0.001	0.740 ± 0.001	-0.178 ± 0.001
0.20	2.67 ± 0.08	0.518 ± 0.006	1.2 ± 0.1
0.30	-	-	-

Table 2.10: First normal stress difference N_1. Fit-parameters for the fit-function defined in eqn. (2.47).

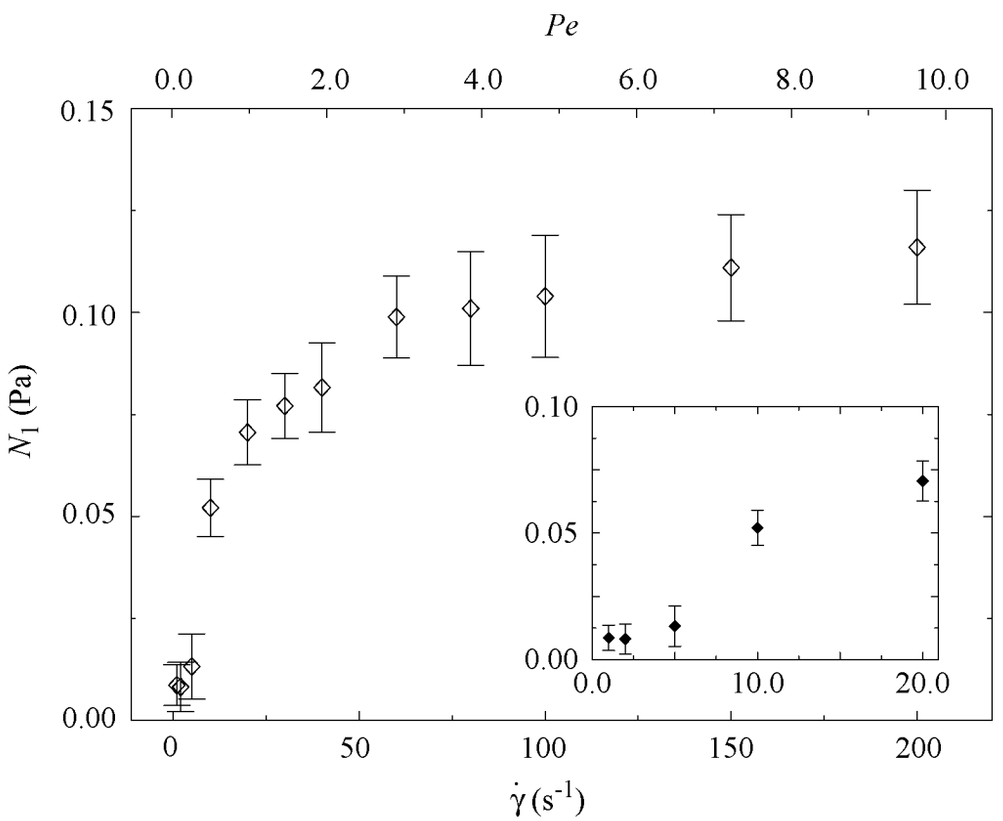

Fig. 2.23: First normal stress difference N_1 for $\phi = 0.3$. The inset is to show the low shear rate behavior.

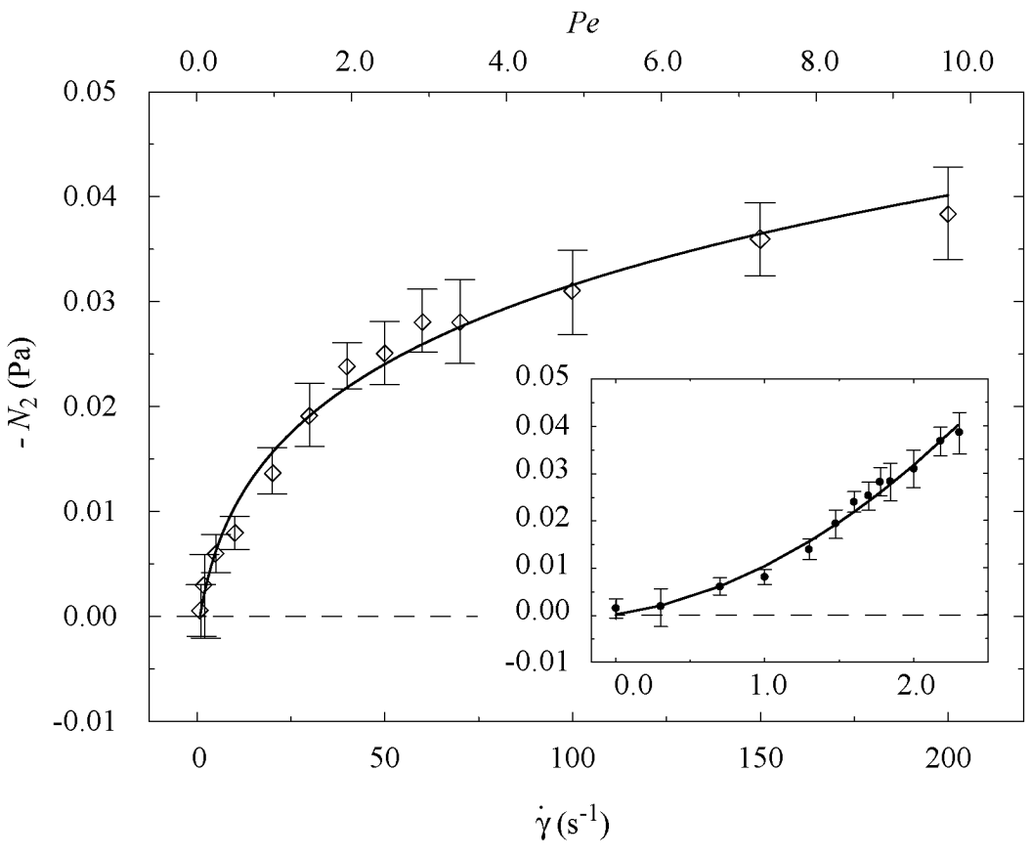

Fig. 2.24: Second normal stress difference N_2 for ϕ = 0.2. Diamond symbols denote the simulation data, the solid line is the fit with the asinh-function (2.46). The inset is the same plot with logarithmic shear rate values to show the behavior at low shear rates.

Solid content ϕ	α_1 (10^{-3} Pa)	τ_{Eu} (10^{-3} s)	α_2 (10^{-3} Pa)
0.10	- 0.831 ± 0.002	74.4 ± 0.2	- 0.020 ± 0.001
0.20	- 1.03 ± 0.02	1440 ± 50	+1.32 ± 0.08
0.30	- 3.53 ± 0.24	1704 ± 101	+ 9.36 ± 1.9

Table 2.11: Second normal stress difference N_2. Fit-parameters for the fit-function defined in eqn. (2.46).

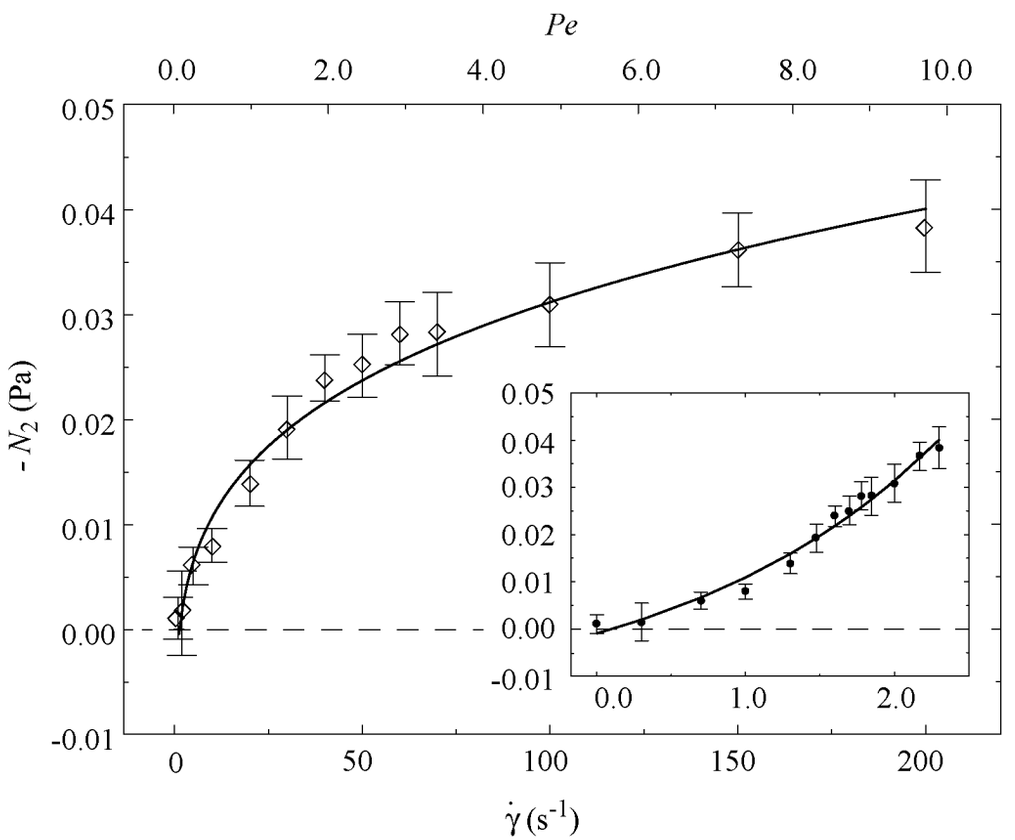

Fig. 2.25: Second normal stress difference N_2 for ϕ = 0.2. Diamond symbols denote the simulation data, the solid line is the fit with the power-law-function (2.47). The inset is the same plot with logarithmic shear rate values to show the behavior at low shear rates.

Solid content ϕ	β_1 (10^{-3} Pa)	β_2 (1)	β_3 (10^{-3} Pa)
0.10	- 0.223 ± 0.001	0.724 ± 0.001	+ 0.435 ± 0.02
0.20	- 14.2 ± 0.4	0.257 ± 0.004	+ 14.9 ± 0.4
0.30	- 61.3 ± 7.5	0.231 ± 0.018	+ 68.2 ± 7.8

Table 2.12: Second normal stress difference N_2. Fit-parameters for the fit-function defined in eqn. (2.47).

Experimental measurements of the first and second normal stress differences are rare and characterize only systems with non-Newtonian solvents. Experiments on concentrated PVC plastosols show a linear increase of the first normal stress difference with shear rate [78Wil], in agreement with experiments on titaniumdioxyde particles in polymer solutions [75Mew]. A square root dependence of the first normal stress difference has been found for carbon black dispersions in mineral oil [78Sch].

The simulation data shown above can be related to the better known polymeric systems as follows. In our simulations, the first normal stress difference has a positive sign whereas the second normal stress difference is negative, as in polymeric systems. We also note that both stress differences are of the same order of magnitude contrary to experimental results on polymeric systems [87Bir]. There, the second normal stress difference is an order of magnitude smaller than the first normal stress difference.

Summary

The first and second normal stress differences have been studied, in particular their dependence on the shear rate and on the solid content. Increasing the solid content leads to higher stresses and to lower characteristic shear rates, which is in agreement with the results from the shear stress studies (subsection 2.4.2). Furthermore, the sublinearity in the shear rate - normal stress relations is enhanced as the solid content is raised. The second normal stress difference has been found to be influenced stronger than the first normal stress difference.

2.4.4 *Ordering at High Shear Rates*

Scattering experiments and computer simulations have shown that the shear thinning of colloidal suspensions may be accompanied by a transition from a random to an ordered particle configuration at high enough solid contents. It has been observed in experiments that suspensions under steady high shear rate order into a layered structure [94Che, 95Cho, 97Dux, 98Dux], where the layers are oriented perpendicular to the velocity gradient axis y (Fig. 2.26(a)). The suspension of particles can then be seen as a set of sheets that slide above each other according to their relative velocity. The particle density within the layers is larger than the overall particle density which leads to relatively large separations between different layers. Thus, the coupling between different layers is reduced resulting in a decrease in the viscosity. In contrast to the layered structure, only scarce experimental evidence exists for the existence of a hexagonally ordered array of particle strings (Fig. 2.26(b)) [88Ack].

The particle arrangement can also be determined from our computer simulations. A typical snapshot of the suspension with a solid content $\phi = 0.3$ at a shear rate of $\dot{\gamma} = 200\ s^{-1}$ is shown for different projections in Fig. 2.27(a-c). The particle size has been reduced for clarity and the particle coordinates are rescaled with respect to the length of the simulation box. The left hand side of Fig. 2.27(a-c) gives a schematic representation of the flow field. The plane of projection, to which the configuration on the right hand side corresponds, is shaded grey.

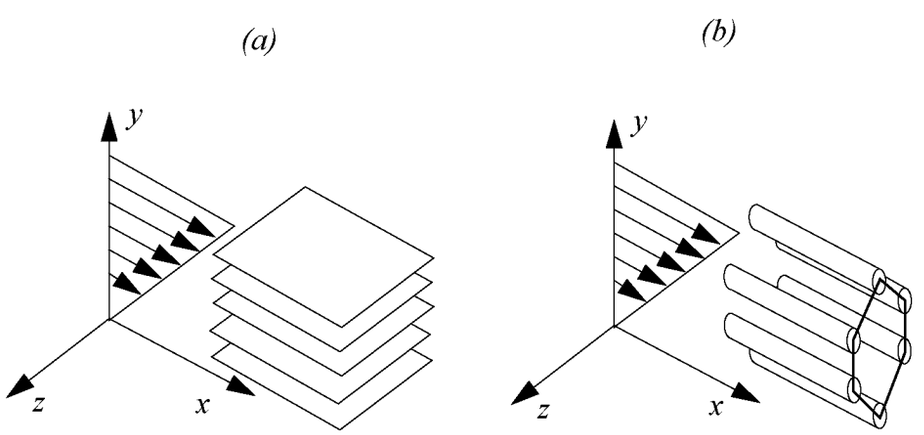

Fig. 2.26: Particle arrangement under steady shear in the shear thinning regime for strongly repulsive interaction: scattering experiments usually detect layers (a); observations of the hexagonal string phase (b) are scarce in experiments but common in computer simulation.

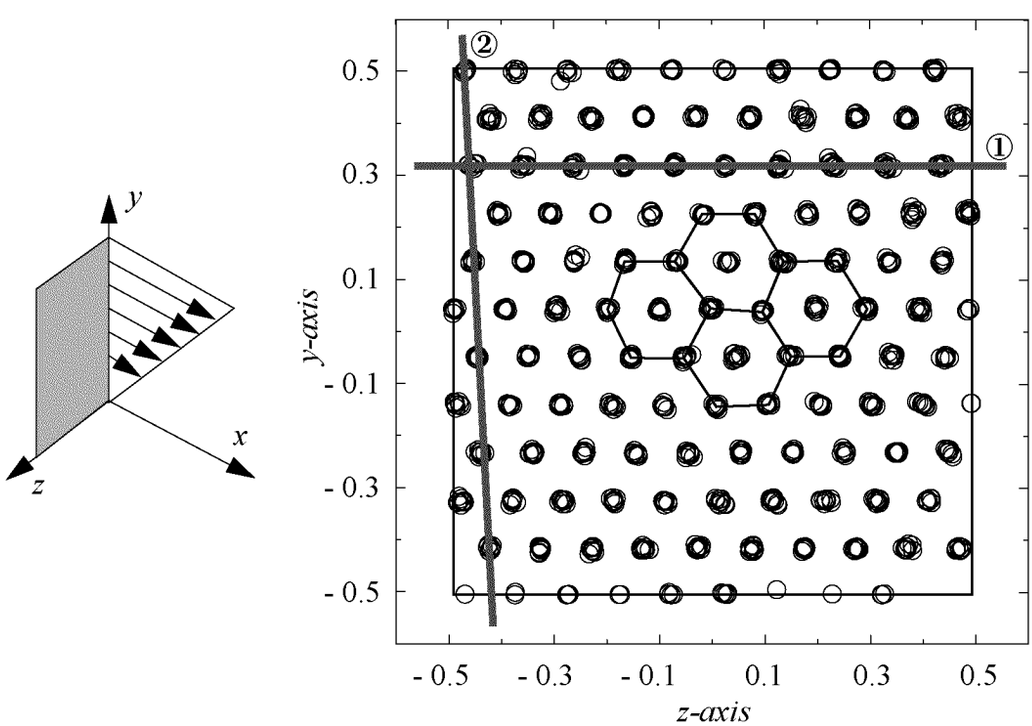

Fig. 2.27(a): yz-projection of particle configuration at $\phi = 0.3$ and $\dot{\gamma} = 200\ s^{-1}$. The bold lines ① and ② refer to features discussed in the text.

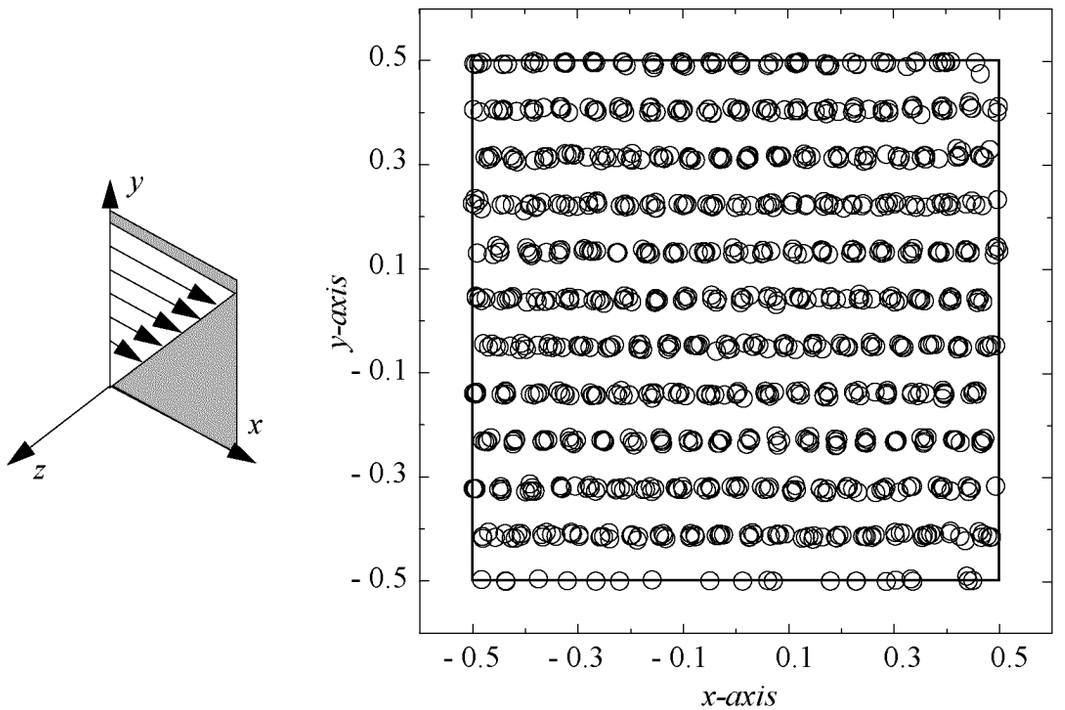

Fig. 2.27(b): xy-projection of particle configuration at $\phi = 0.3$ and $\dot{\gamma} = 200\ s^{-1}$.

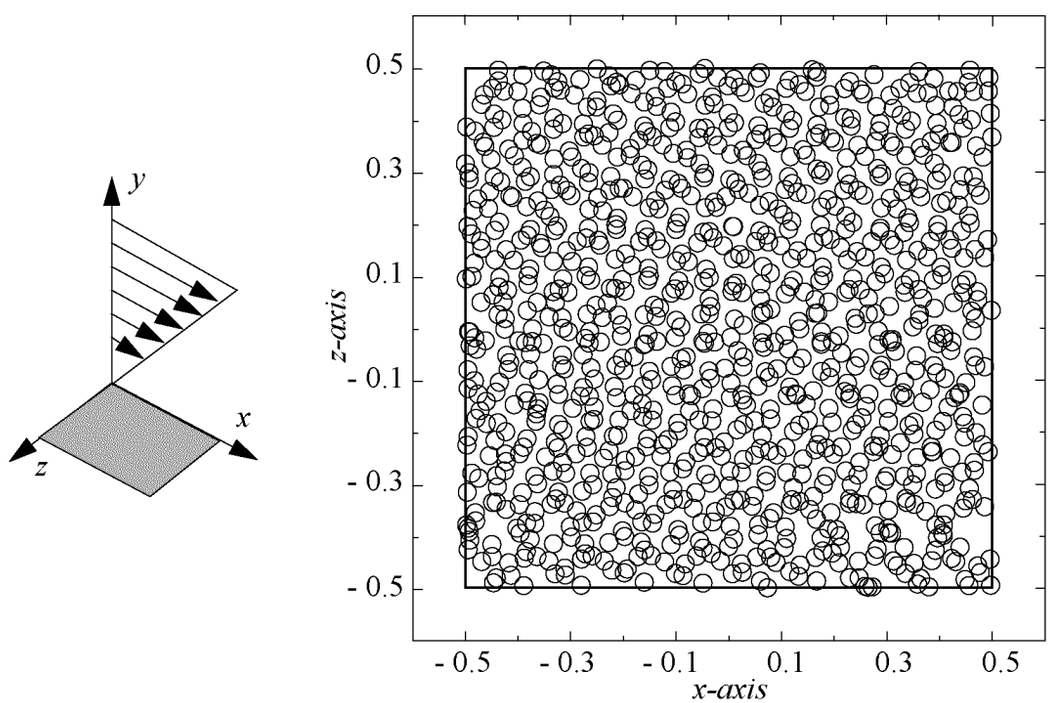

Fig. 2.27(c): xz-projection of particle configuration at $\phi = 0.3$ and $\dot{\gamma} = 200\ s^{-1}$.

Fig. 2.27(a) shows that the particles are arranged in a hexagonally ordered array of strings. The line denoted by ① indicates perfect alignment in the x-direction for constant y. The tilt of line ② away from the y-axis emphasizes that the hexagonal structure is not perfect which can also be observed from the slightly deformed hexagons.

A side-view of the string structure is given in Fig. 2.27(b). Due to the high degree of order with respect to the x-axis (indicated by line ① in Fig. 2.27(a)), one can clearly see the strings from the side.

The view from the top shown in Fig. 2.27(c) is more difficult to interpret. Because the hexagonal structure is slightly tilted away from the y-axis (indicated by line ② in Fig. 2.27(a)), the strings at different y-values are not perfectly aligned. A top-view then does not show a set of strings, as in Fig. 2.27(b), but a seemingly unstructured particle arrangement. This example illustrates that single snapshots of a particle configuration can lead to a misinterpretation and, thus, it is necessary to view the particle structure from different angles.

In contrast to most scattering experiments detecting layers, the simulation shows a hexagonal array of strings as also observed in other simulations [90Bha, 93Hey, 93Mel, 95Hey, 96Ras]. This discrepancy has been explained by the spatial periodicity introduced by the finite size of the simulation box [96But]. Although the rheological behavior determined in our simulation qualitatively corresponds to the experimental results, the structure is to be considered an artifact which may be cured by reducing the boundary effects, i.e. by increasing the system size.

The motion of the particles and of the strings, respectively, can be monitored by measuring the mean square displacement of the particles. In shear flow it is given by $\langle \delta \boldsymbol{r}_k(t) \delta \boldsymbol{r}_l(t) \rangle$ $(k, l = x, y, z)$ where

$$\delta \boldsymbol{r}_k(t) = \sum_{\Delta t} (\Delta \boldsymbol{r}_k - \boldsymbol{v}_k^{\infty} \Delta t) \tag{2.48}$$

is the displacement relative to the motion of the flow field, i.e. convective contributions are excluded. The sum in eqn. (2.48) runs over the relative displacements of all integration steps which have been performed in the time interval $[0, t]$ under consideration. The average denoted by $\langle \ldots \rangle$ is an average over all particles and over different samples as discussed in subsection 2.3.2. The data corresponding to the snapshots in Fig. 2.27(a-c) are given in Fig. 2.28.

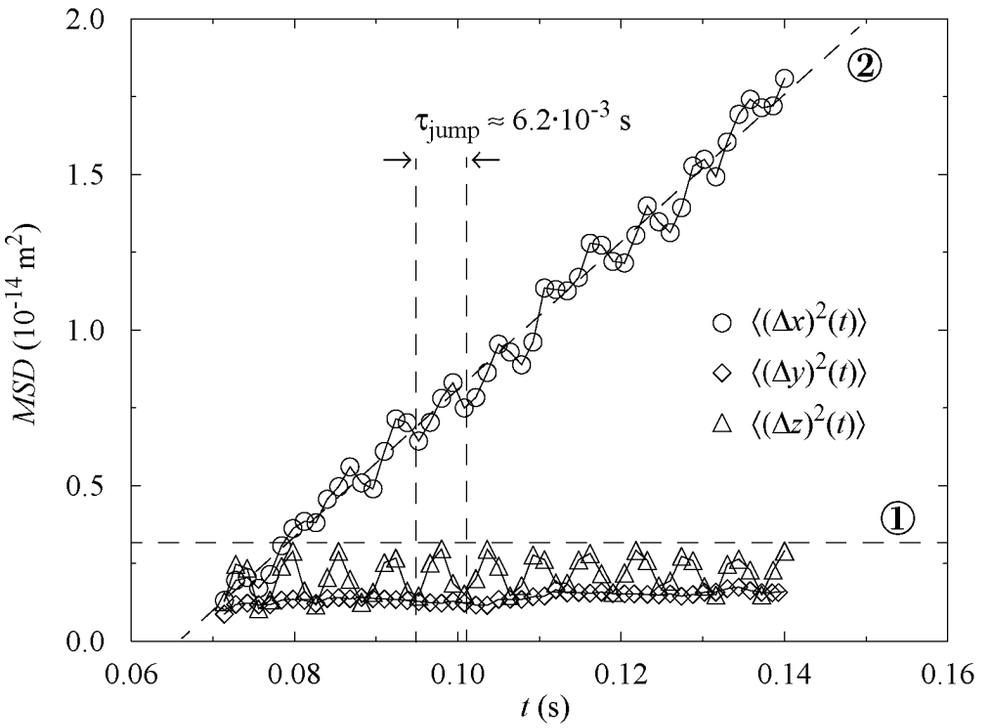

Fig. 2.28: Mean square displacement (MSD) for a suspension at a solid content of $\phi = 0.3$ at a shear rate of $\dot{\gamma} = 200\ s^{-1}$.

There are two important features of the data presented in Fig. 2.28. First, the *yy*- and the *zz*-component of the mean square displacement are constant, i.e. there is no diffusion at all. And second, the *xx*- and *zz*-component show periodically appearing jumps.

The existence of an upper limit on the *yy*- and the *zz*-component (dashed horizontal line ①) indicates that the particles do not show any diffusive behavior but are loosely tied to their initial position. Only small fluctuations are occurring as if the particles were in a narrow potential well. The dashed line ② shows a diffusive behavior for the *xx*-component, at least on average.

The periodically appearing jumps indicate that there are collective rearrangements in the particle configuration. These may be attributed to neighboring strings sliding past each other due to their different position in the flow field, and hence due to their relative velocity. Fig. 2.29 illustrates why sliding strings can lead to the jumps in the mean square displacement.

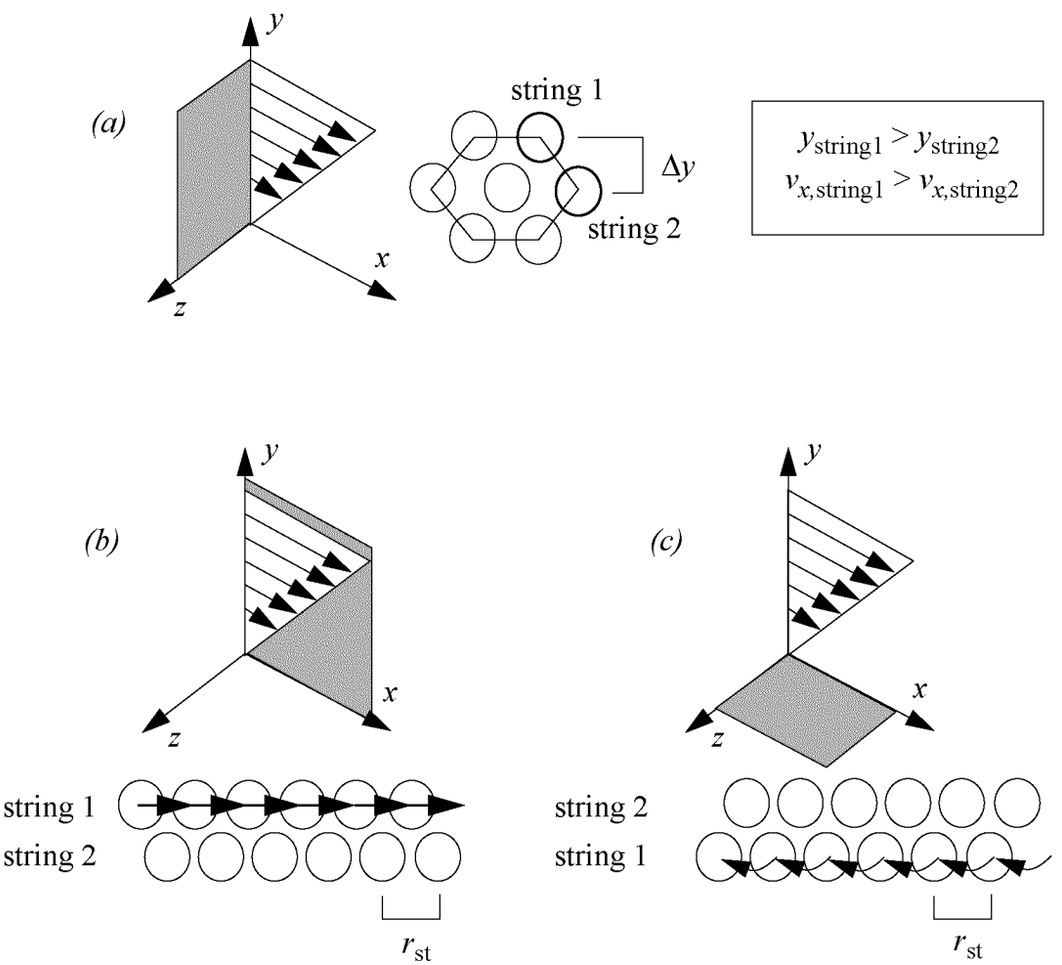

Fig. 2.29: Hexagonal string phase in the shear thinning regime. Sliding strings lead to jumps in the mean square displacement of the particles.

It gives a schematic representation of the collective jump of a string (denoted by 1) with higher velocity relative to a string with a lower velocity (denoted by 2). Before jumping, the particles in string 1 are held back due to the repulsive interaction with the particles in the lower string 2. If the force due to the relative velocities between the strings is large enough, all particles in string 1 make a collective jump over a distance r_{st}, where r_{st} denotes the separation between the particles in one string. However, the jump is not in the y-direction but is restricted to the *xz*-plane, as indicated in Fig. 2.29(b-c). This view is supported by the data in Fig. 2.28: the particles do not perform any collective jumps in the y-direction, but only in the *x*- and *z*-direction. Thus, the order in the *y*-direction is stronger

than in the *xz*-plane, as it has already been observed in the configuration snapshots in Fig. 2.27(a-c).

The jump time τ_{jump} can be related to the particle separation r_{st} in one string and to the relative velocities of the strings $v_{rel} = \Delta y\,\dot{\gamma}$ through

$$\tau_{jump} = \frac{r_{st}}{\Delta y}\frac{1}{\dot{\gamma}} \tag{2.49}$$

Under the given conditions, one finds for the ratio $r_{st}/\Delta y \approx 1.24$. This value can be cross-checked with the particle configurations in Fig. 2.27(a-b). There are eleven 'layers' of strings in the *y*-direction which leads to $\Delta y = 1/11$ in units of the box length, furthermore, the total number of strings is $N_{strings} = 110$. Because the total number of particles in the box is $N = 1000$, each string contains $1000/110$ particles on average. Therefore, the separation between particles in the same string is $r_{st} = 110/1000$ in units of the box length. Using all this information from Fig. 2.27(a-b), the value calculated for the ratio $r_{st}/\Delta y$ is 1.21, which is close to $r_{st}/\Delta y \approx 1.24$ determined from the jump time τ_{jump}. We conclude that the origin of the periodically appearing jumps in the mean square displacement is indeed the collective jumps of the particles when the strings are moving relative to each other.

It may be surprising that the number of particles with $1000/110 \approx 9.1$ is smaller than $\sqrt[3]{1000} = 10$, which means that the density of particles within a string is ***smaller*** than the overall density in the suspension. A possible explanation may be that if the density within the strings were higher, the strong repulsive forces would make the strings instable: from time to time, particles would be expelled from one string which then would disrupt one of the neighboring strings.

Summary

It has been shown that the particles arrange at high shear rates in a hexagonally ordered array of strings, which are alined in the direction of flow. This has been attributed to a minimization of interaction forces. The hexagonal order is not perfect but is slightly distorted in the vorticity direction (*z*-direction in Fig. 2.27(a-c)). The mean square displacement data have shown that the particle diffusion is restricted to the flow direction. Furthermore, it has been found that the particle strings of different velocities move past each other by a hopping mechanism which is restricted to the shear planes (*xz*-plane in Fig. 2.27(a-c)).

2.4.5 Long-Time Diffusion under Shear

The previous subsection has shown that the *xx*-component of the mean square displacement is a useful quantity for studying a suspension in shear flow. In the following, the dependence of the long-time diffusion coefficient for the *x*-direction on the shear rate will be discussed.

The data in Fig. 2.30 show an increase in the diffusion coefficient for increasing shear rates. For those solid contents which show the hexagonal string phase at higher shear rates (ϕ = 0.2 and 0.3), this increase is disrupted by a drop in the diffusion coefficient. The smaller diffusion coefficients in the hexagonal string phase are due to a disorder-order transition which also has been noticed in previous simulations (see for example [90Bha]). The particles are not moving through the

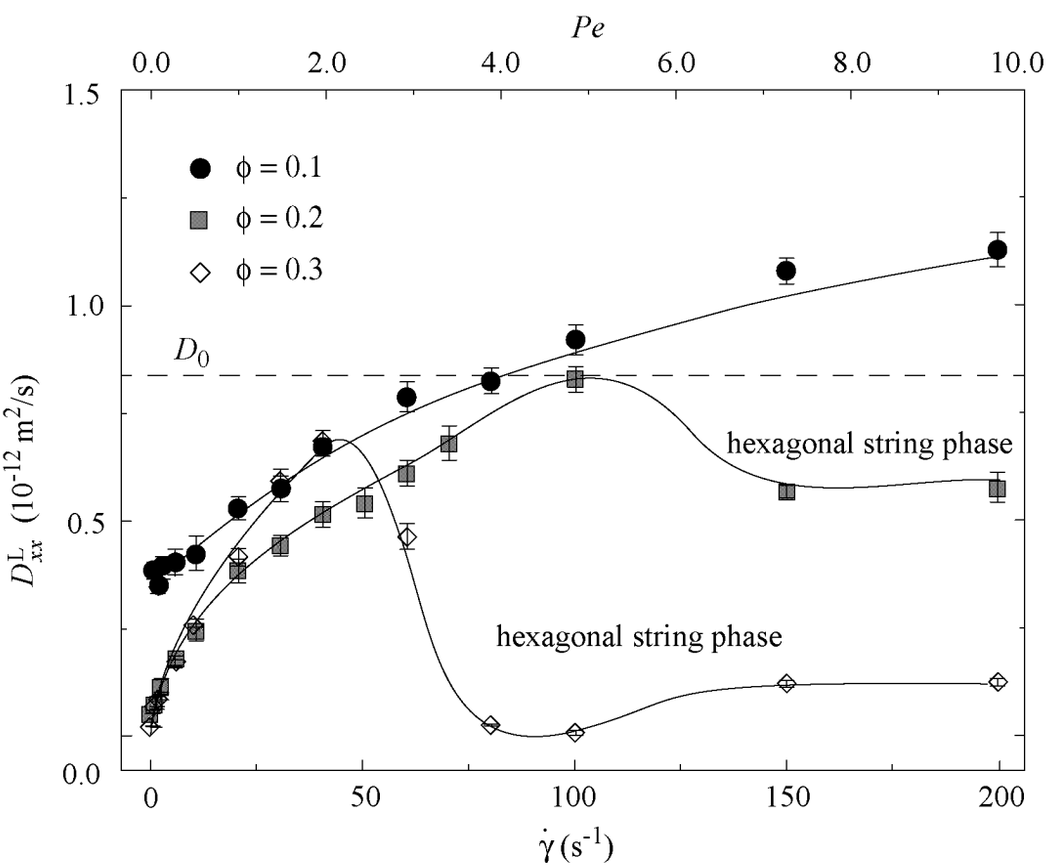

Fig. 2.30: Long-time diffusion coefficient D^L_{xx} in x-direction for different solid contents ϕ at different shear rates $\dot{\gamma}$. D_0 denotes the diffusion coefficient at infinite dilution and zero shear rate. The lines are only drawn as visual guide.

suspension on their own but assemble to bigger units, the strings. The latter can move (more or less) only as a whole which leads to a decrease in the diffusion due to the collective motion of the particles.

The critical shear rates for the disorder-order transition for $\phi = 0.2$ and 0.3 can be determined not only from the arrangement of particles alone. It can also be estimated roughly from the decrease in the diffusion coefficient at high shear rates. From Fig. 2.30 we find a transition shear rate for $\phi = 0.2$ of $\dot{\gamma}_{order} \approx 120\ s^{-1}$, whereas for $\phi = 0.3$ the transition shear rate is $\dot{\gamma}_{order} \approx 60\ s^{-1}$. Within the uncertainty due to the smeared transition region in Fig. 2.30, the same shear rates are determined directly from analyzing the particle configurations themselves.

Summary

The long-time diffusion coefficient in the flow direction exhibits a 'shear thinning' effect for increasing shear rate, similar to the viscosity. After an initial increase in the diffusion coefficient upon raising the shear rate, we have found a pronounced drop in the diffusivity for solid contents for which shear ordering can be observed. The higher the solid content, the stronger is the drop in the diffusion coefficient over the shear rate transition regime. A further increase of the shear rate results again in a slow tendency towards higher diffusion coefficients.

2.4.6 Summary and Conclusions

Section 2.4 was concerned with both the rheology as well as with the shear rate dependent self-diffusion and structure of the particles in the suspension.

It has been found that increasing the solid content results in larger shear stress and normal stress differences and in lower characteristic shear rates. The suspension increasingly shows yield stress behavior as the solid content is raised. This is in agreement with the results from section 2.3 for the infinite zero shear rate viscosity. Furthermore, the sublinear high-shear rate dependence of the shear stress and of the normal stress differences becomes even weaker for the higher solid contents, which means that shear thinning becomes stronger. The second normal stress difference is more influenced than the first normal stress difference by a change in the solid content. Finally, we notice that no shear thickening has been observed even at the highest shear rates.

More information about the suspension under shear has been gained by analyzing the particle structure and the diffusion behavior. It could be shown that, at high shear rates and for high solid content, the particles arrange in a hexagonally ordered array of strings which are directed along the flow field. By measuring the mean square displacement, a hopping mechanism of sliding strings has been proposed. The particles exert only collective motions, and diffusion is mainly restricted to the direction of flow due to caging effects. The long-time diffusion coefficient in this direction can be used to measure the onset of shear ordering in terms of a significant drop of the value. Apart from this transition regime, the long-time diffusion coefficient is a steadily increasing function of shear rate.

The following conclusions can be drawn from the above results. The rheological properties such as shear stress and normal stress differences give only a crude representation of the suspension in shear flow. Shear thinning can be observed, irrespective of whether the particles undergo a disorder-order transition or not. Only the structural analysis of the particle arrangement gives deeper insight into the mechanisms involved. A rather good picture of the particle dynamics can be obtained by the combination of a configuration snapshot with the mean square displacement data. An alternative and more costly method would be to follow the motion of each particle by analyzing a large series of snapshots. We also conclude from the above results that the long-time diffusion coefficient is a more sensitive indicator for shear ordering than the viscosity.

Apart from these comments on the simulation results, we should finally not forget that a typical property of colloidal suspensions could ***not*** be observed in our simulation: shear thickening. We notice that the equations of motion for the particles, upon which the results in section 2.4 are based, need further changes in order to account for this phenomenon.

2.5 Hydrodynamic Interaction

This section deals with the failure of the previously presented Brownian dynamics simulation technique to produce shear thickening at high shear rates. The first subsection gives an overview of the many-body hydrodynamic interaction which has not been included in the previous simulations. Experimental evidence for the connection between these many-body effects and the shear thickening in dense colloidal suspensions is given in the following. The implementation of the hydrodynamic interaction in a numerically efficient manner amounts to a rather challenging task. A summary of the difficulties encountered and their solution concludes the section.

2.5.1 Many-Body Hydrodynamic Interactions

Numerous Brownian dynamics simulations have shown that the equations of motion (2.11) fail to reproduce the effect of shear thickening in colloidal suspensions. Even at high shear rates, i.e. for $Pe \gg 1$, the viscosity is not increasing but levels off at a low, stationary value. It will be demonstrated that the lack of shear thickening can be attributed to hydrodynamic interaction forces which have not been included in the equations of motion (2.11) for the colloidal particles.

The system which is in the focus of this study consists of colloidal particles that are suspended in a liquid. Since we are mainly interested in the motion of the particles, the liquid was only accounted for by forces acting on the single particles: Stokes' drag force and Brownian force. Only these two forces tell us that the colloidal particles are not moving in a vacuum but are surrounded by a viscous liquid. However, there are also other effects of the liquid that have to be included.

It is well known that acoustic waves can not only propagate in air, but also in solids and in liquids. These waves need a material which can convey the mechanical excitation. The following thought experiment illustrates how an acoustic wave propagates in a liquid. Suppose two membranes are placed opposite to each other in water with a finite gap in between. Let the first membrane oscillate. If the viscosity of water were zero, the second membrane would not feel the oscillation because the water in between would compensate the volume fluctuation by flowing sidewards in and out of the gap. But, due to the finite viscosity, the water can not fully compensate the oscillation of the first membrane. Thus, the other membrane can feel the acoustic wave.

Effects similar to the acoustic wave propagation described above also occur in colloidal suspensions. There, each particle which moves through the liquid produces a wave which propagates to the other particles. The result is a complex many-body hydrodynamic interaction which acts in addition to all forces previously discussed (potential interaction, Stokes' drag and Brownian forces).

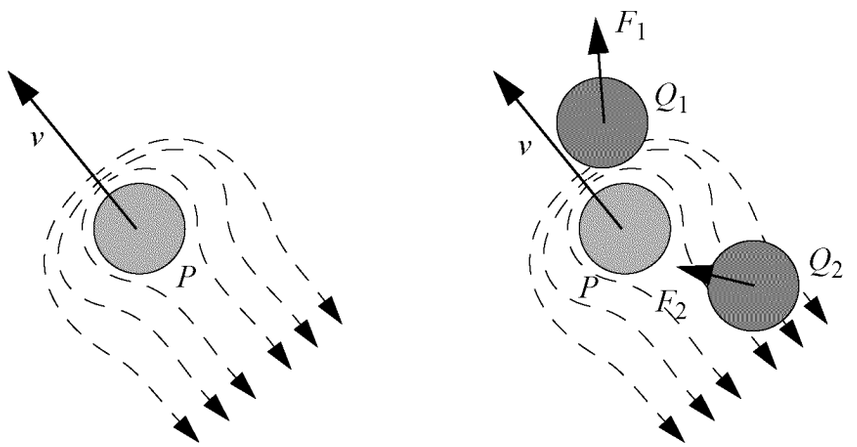

(a) Stokes' drag

(b) Many-body hydrodynamic interaction

Fig. 2.31: Illustration of (a) Stokes' drag and of (b) many-body hydrodynamic interaction. The particle P with velocity v produces a fluid flow field. Other particles, Q_1 and Q_2, that are placed in this flow field, experience a force F_1 and F_2 respectively.

The difference between the single-particle Stokes' drag and the many-body hydrodynamic interactions is depicted in Fig. 2.31. Both effects originate from the finite viscosity of the (nearly) incompressible suspending medium. For a single particle, the friction force is caused by the fluid flow around the moving particle alone. If a second particle is placed in the vicinity of the first, it experiences a force due to the fluid flow of the first particle.

Fig. 2.31 is only a very crude representation of the problem. As a matter of fact, the many-body hydrodynamic interactions are symmetric with respect to the particle labelling. The particles Q_1 and Q_2 not only react to the flow field around particle P, but also influence the motion of particle P. A thorough treatment of the problem would include a full description of the fluid motion around the particles by means of the Navier-Stokes equation of hydrodynamics. However, this is not feasible as soon as the system contains more than two particles, whereas the solution for only two particles can be determined analytically [91Kim]. The many-body system of hydrodynamically interacting particles is then considered as a sum of two-particle subsystems, similar to the pairwise additivity used for the calculation of the potential interactions.

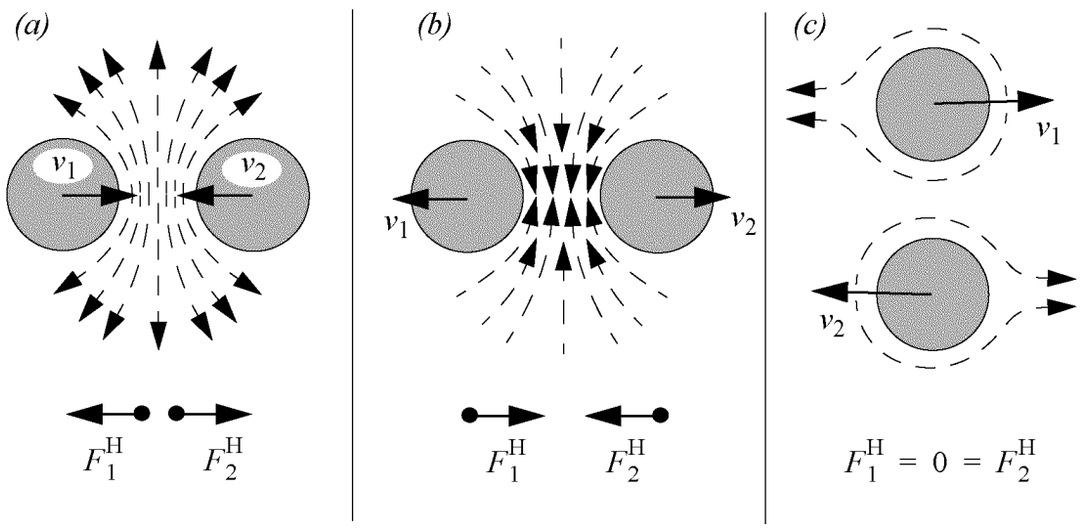

Fig. 2.32: Hydrodynamic lubrication between two particles. Full arrows stand for the particle velocities v and forces F, dashed arrows symbolize the fluid flow. The resulting hydrodynamic forces F^H are given below the graphs. Velocities along the line of centers lead to forces in the opposite direction (a b); passing particles do not interact (in first approximation) (c).

A special case of hydrodynamic interaction is found for particles with their surfaces much closer than the particle diameter. This limit is called hydrodynamic lubrication. The lubricating effect of two close particles is shown in Fig. 2.32. The velocities of the two equal particles are given in the center-of-mass reference frame in order to highlight the symmetry of the interaction.

The limiting case of hydrodynamic lubrication is also called 'squeezing' mode, which becomes clear when looking at graph (a): the fluid has to be squeezed out between two approaching particles leading to a force which retards the approach of the particles. The motion of two separating particles is also damped due to the fluid motion, but this time the fluid has to enter into the gap and fill the void space between the particles (b). In both situations (a) and (b) the resulting force opposes the velocity of each particle what illustrates that the interaction can be interpreted as if there was a glue between the particles.

For the two passing particles in (c), there is no hydrodynamic interaction force in first approximation. In all considerations above as well as in the equation of motions in this study, rotational degrees of freedom are not included. Therefore, the torques that would act on the particles in Fig. 2.32(c) are neglected.

The lubrication approximation of the many-body hydrodynamic interaction is assumed to be a good first estimate of the hydrodynamic effects in dense colloidal systems for the following reason. The lubrication forces described above diverge for touching particles which means that very close particles can hardly be moved along the line of centers. These forces therefore dominate over the far-field hydrodynamic interactions in the suspension of particles [97Bal].

It has been noted in subsection 2.3.1 that the shear thickening transition might go along with the formation of non-permanent hydrodynamic clusters. The above mentioned gluing-effect, which becomes stronger the closer the particles approach, is thought to be the origin of these clusters. This would establish a direct connection between the lubrication forces and the shear thickening at high shear rates which is supported by experimental evidence.

When measuring the viscosity of colloidal suspensions, only the sum over many effects is usually recorded. This is in clear contrast to the model on the microscopic particle level where one intuitively tends to separate the different forces. For a better understanding of lubrication effects in the suspension, a similar partition is therefore desirable for the viscosity, too. The contribution of the many-body hydrodynamic interaction to the viscosity of the particle suspension can be singled out not only in theory and simulation, as will be shown below. It is also accessible through experimental techniques such as optical dichroism measurements [88Wag, 95Ben, 96Ben] and stress jump measurements [95Mac, 97Wat]. Both methods, although very different, have come to the same conclusion: the shear thickening of colloidal suspensions at high shear rates can be attributed to the many-body hydrodynamic interactions between the particles.

Considering these experimental results, we will start with the implementation of hydrodynamic lubrication effects in the following.

2.5.2 *Implementation of Lubrication Forces*

There are different ways to incorporate the effects of hydrodynamic interaction in particulate systems, namely Dissipative Particle Dynamics [93Koe, 97Boe], Stokesian Dynamics [84Bos, 88Bra, 96Phu], and Brownian Dynamics [90Bha, 93Hey, 96Ras].

Dissipative Particle Dynamics considers the suspending liquid as being composed from so-called fluid particles and allows to model the flow around complex shaped bodies. In contrast, the other two methods treat the liquid on a continuum level and are merely applied to spherical particles. Stokesian dynamics has been proposed for modeling and simulating suspensions at non-dilute concentrations including hydrodynamic interactions. In contrast, Brownian dynamics simulations have been widely used in connection with diluted systems and far-field hydrodynamic interaction and the application to dense systems is quite new [95Bal, 96Mel, 97Bal]. Following is an illustration of the technique which has been used in this study.

The scope of the next paragraphs is the mathematical formulation of the hydrodynamic forces in dense colloidal suspensions and of the generation of the equations of motion. A detailed discussion of the many-body hydrodynamic interactions can be found in the book "Microhydrodynamics" by Kim and Karrila [91Kim].

a) Hydrodynamic Forces

Let us first consider the case of two particles only. The lubrication forces of two close particles ($\boldsymbol{F}_1^V$ and $\boldsymbol{F}_2^V$) due to their velocities relative to the background flow field ($\boldsymbol{w}_1$and $\boldsymbol{w}_2$ with $\boldsymbol{w}_i \equiv \boldsymbol{v}_i - \boldsymbol{v}^\infty(\boldsymbol{r}_i)$ with i=1, 2), are given by the following equation [91Kim]:

$$\begin{bmatrix} \boldsymbol{F}_1^V \\ \boldsymbol{F}_2^V \end{bmatrix} = \frac{3}{8}\pi\eta_s \frac{d}{\xi} \begin{bmatrix} \boldsymbol{P}_{12} \cdot (\boldsymbol{w}_2 - \boldsymbol{w}_1) \\ \boldsymbol{P}_{12} \cdot (\boldsymbol{w}_1 - \boldsymbol{w}_2) \end{bmatrix} = -\boldsymbol{R}_{FV} \cdot \begin{bmatrix} \boldsymbol{w}_1 \\ \boldsymbol{w}_2 \end{bmatrix} \qquad (\text{for } \xi \ll 1) \quad (2.50)$$

The parameter ξ denotes the normalized surface-surface separation $\xi = (r-d)/d$ between the particles and the operator $\boldsymbol{P}_{12}$ projects the velocities on the connector vector. The introduction of a resistance matrix $\boldsymbol{R}_{FV}$ on the right hand side allows to simplify the notation for further use.

Eqn. (2.50) is only valid for very small separations, and the ξ^{-1}-dependence does not imply any long-range interaction. Corresponding to the interpretation of lubrication forces, eqn. (2.50) can only be applied for nearest-neighbor hydrodynamic interaction. There are two possibilities to determine the nearest neighbors in the simulation. One can either use the Voronoi construction and the dual Delaunay tetrahedra [97Bal] or one can introduce a cut-off separation for the in-

teraction form given in (2.50). In our study, the latter method has been adopted with a lubrication cut-off $r_{\text{cutoff}}^{\text{lubr}} = \sqrt{2}d$ (i.e. $\xi_{\text{cutoff}}^{\text{lubr}} = \sqrt{2} - 1 \approx 0.41$). This value can be motivated as follows. Imagine four touching (or very close) particles at the corners of a square. Two particles on the diagonal, which are separated by $\sqrt{2}d$, can be thought as an estimate for the limiting case where the term 'nearest neighbor' is appropriate in the hydrodynamic lubrication sense and where the two-particle squeezing mode is adequate. Any particle-pair which is farther separated does not interact through lubrication. This value also relates to the effective cut-off radius introduced by the Delaunay tetrahedra method [97Bal]. The determination of nearest neighbors and the cut-off separation in the hydrodynamic lubrication approximation is probably the weakest point in the whole discussion and should be the topic of further studies.

The following three points of eqn. (2.50) shall be emphasized. First, the lubrication force diverges as particles come closer and closer. Second, only the velocity component in the direction of the connector vector between the particles contributes, in agreement with Fig. 2.32(c). And third, the lubrication forces oppose the relative motion of two close particles as illustrated in Fig. 2.32(a-b).

The above relation (2.50) between the velocities and the forces implies that particles do not interact if they have the same velocity as the background flow field. This corresponds to the idea of how an acoustic wave is produced. However, one might argue that this is not true anymore at concentrations where lubrication becomes relevant. In dense suspensions, e.g. above 50 vol % of monodisperse particles, there is so little liquid between the particles that it is difficult to identify anything that deserves the term 'background' flow field. Then the imposed flow field acts only through the periodic boundary conditions (see Fig. 2.3). In the present study, the flow field is included, because no simulations were done at such high solid contents where no flow field could be identified. However, when going to higher solid contents one should consider the possibility of reformulating the equations.

The forces in eqn. (2.50) are linear in the particle velocities. Using the $3N$-vector notation, the force vector is proportional to the velocity vector, where the proportionality factor is a $3N \times 3N$-resistance matrix. The pairwise additivity of the hydrodynamic forces then results in the pairwise additivity of the two-body resistance matrices. This is illustrated in Fig. 2.33 for a small system of ten particles. The filled squares and circles symbolize the projection operator (the 3×3-matrix $\boldsymbol{P}$ in eqn. (2.50)) for the corresponding pair. The interaction between particles 3 and 6 is denoted by squares, the interaction between particles 3 and 9 by circles.

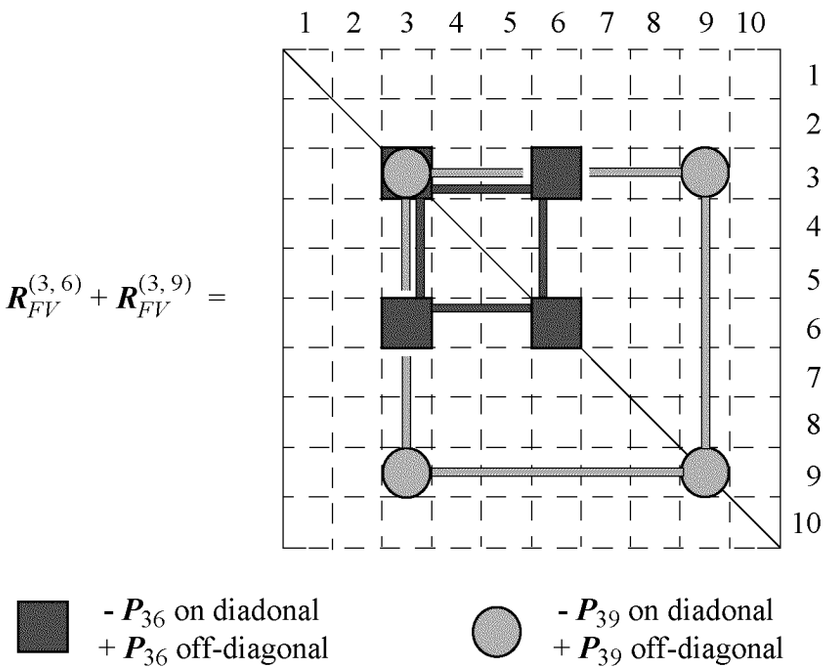

Fig. 2.33: Pairwise additivity in the resistance matrix for a system of ten particles and for two interacting particle pairs (3,6) and (3,9).

From Fig. 2.33 it is clear that each 3×3-matrix on the diagonal of the resistance matrix is a sum over different projection operators, where each projection operator stands for a hydrodynamic interaction neighbor with the corresponding particle. One can also see that the resistance matrix becomes very sparse for systems with a large number N of particles for the following reason. Due to the short interaction range of the lubrication force, each particle can only have $O(1)$ interacting neighbors. This leads in total to $O(N)$ non-zero matrix elements, so the more particles the systems contains the sparser the resistance matrix becomes.

The velocity of the particles does not only lead to many-body interactions but, at least in principle, also to single particle drag. However, the Stokes' drag considered in the previous version of the equations is omitted here: the fluid flow around an isolated particle is an invalid model at solid contents where the hydrodynamic lubrication becomes important.

Particle velocities are not the only source of hydrodynamic forces on the particles, also forces due to the strain rate of the liquid have to be accounted for. If the rate of strain tensor is denoted by $\boldsymbol{E}^{\infty}$, one finds with the third rank tensor $\boldsymbol{R}_{FE}$ [91Kim]

$$\begin{bmatrix} \boldsymbol{F}_1^E \\ \boldsymbol{F}_2^E \end{bmatrix} = \boldsymbol{R}_{FE} : \begin{bmatrix} \boldsymbol{E}^{\infty} \\ -\boldsymbol{E}^{\infty} \end{bmatrix} \tag{2.51}$$

The symbol ':' stands for the summation over two indices. The tensor $\boldsymbol{R}_{FE}$ depends on the relative positions of the particles, as the matrix $\boldsymbol{R}_{FV}$ in eqn. (2.50). The mathematical form of $\boldsymbol{R}_{FE}$ can be found in the Appendix. We only note here that the strain rate forces are short range and diverge for touching particles.

Using the $3N$-component notation from subsection 2.2.4 for all vectors and tensors and assuming pairwise additivity in the forces, we find for the hydrodynamic force $\boldsymbol{F}^{\mathrm{H}}$ due the particle velocities $\boldsymbol{v}$ and the strain rate $\boldsymbol{E}^{\infty}$

$$\boldsymbol{F}^{\mathrm{H}} = \boldsymbol{F}^{V} + \boldsymbol{F}^{E} = -\boldsymbol{R}_{FV} \cdot [\boldsymbol{v} - \boldsymbol{v}^{\infty}(\boldsymbol{r})] + \boldsymbol{R}_{FE} : \boldsymbol{E}^{\infty} \tag{2.52}$$

b) Equations of motion

As in eqn. (2.10), the equation of motion for the colloidal particles can be set up by the force balance between hydrodynamic $\boldsymbol{F}^{\mathrm{H}}$, interparticle $\boldsymbol{F}^{\mathrm{pot}}$, and Brownian forces $\boldsymbol{F}^{\mathrm{B}}$

$$m\frac{d\boldsymbol{v}_t}{dt} = \boldsymbol{F}_t^{\mathrm{H}} + \boldsymbol{F}_t^{\mathrm{pot}} + \boldsymbol{F}_t^{\mathrm{B}} \tag{2.53}$$

which is the basis of the Stokesian dynamics simulation technique.

On the contrary, equilibrated particle momenta are inherent to the Brownian dynamics technique. A thorough analysis of momentum relaxation in eqn. (2.53) leads to the following result for the particle displacements $d\boldsymbol{r}_t = \boldsymbol{v}_t\, dt$ with the at first unexpected divergence term in the second line (see for example [96Phu]):

$$\begin{aligned} d\boldsymbol{r}_t = {} & [\boldsymbol{v}_t^{\infty} + \boldsymbol{R}_{FV,t}^{-1} \cdot (\boldsymbol{F}_t^{\mathrm{pot}} + \boldsymbol{R}_{FE} : \boldsymbol{E}^{\infty})]dt \\ & + k_{\mathrm{B}}T(\nabla \cdot \boldsymbol{R}_{FV,t}^{-1})dt + \boldsymbol{B}_t \cdot d\boldsymbol{W}_t \end{aligned} \tag{2.54}$$

All quantities with the subscript t are functions of the particle positions and hence depend on time. Let us now discuss the different contributions in eqn. (2.54) one after the other.

(1) Imposed Flow Field
The first contribution is the displacement of the particles due to the background flow field $\boldsymbol{v}^{\infty}$.

(2) *Deterministic Forces*
The second term in (2.54), $\boldsymbol{R}_{FV,t}^{-1} \cdot (\boldsymbol{F}_t^{\mathrm{pot}} + \boldsymbol{F}_t^{E})$, originates from the potential interactions (2.6) and the strain forces (2.51).

(3) Divergence Term
The first term on the second line of eqn. (2.54), $k_{\mathrm{B}}T(\nabla \cdot \boldsymbol{R}_{FV,t}^{-1})$, can be derived in two ways. One either makes a limiting procedure for the momentum relaxation [97Bal] or one considers the suspension at equilibrium: it can be shown that if the Boltzmann distribution is to hold for the particle positions at equilibrium, the divergence term is a necessary condition [78Fix, 88Bra, 96Ött].

(4) Brownian Displacements
The Brownian displacements $\boldsymbol{B}_t \cdot d\boldsymbol{W}_t$ are built from Wiener processes, as discussed in 2.2.1, and a matrix $\boldsymbol{B}_t$. The latter is coupled to the mobility matrix $\boldsymbol{R}_{FV}^{-1}$, or the resistance matrix $\boldsymbol{R}_{FV}$ respectively, by the fluctuation-dissipation theorem [66Kub, 88Bra, 96Ött]

$$\boldsymbol{B} \cdot \boldsymbol{B}^{T} = 2k_{\mathrm{B}}T\, \boldsymbol{R}_{FV}^{-1} \tag{2.55}$$

We note that eqn. (2.54) can be reduced to the equation (2.12) without hydrodynamic interaction: with the replacements $\boldsymbol{R}_{FV} = \zeta \mathbf{1}$ and $\boldsymbol{R}_{FE} = \mathbf{0}$, the strain-rate force and the divergence term vanish and we recover the equations with single particle Stokes' drag.

It has been mentioned previously that reduction of the real suspension to the small system in the simulation box with periodic boundary condition is only imposed by the limited performance of the computers. This restricts the size of the simulation box and hence the number of simulated particles.

For a suspension without hydrodynamic interaction, the linked-cell list method has been employed to reduce the computational effort for calculating the interparticle forces. The same method can be applied to the determination of the position dependent tensors $\boldsymbol{R}_{FV}$ and $\boldsymbol{R}_{FE}$ because of the short interaction range of hydrodynamic lubrication. Both tensors can therefore be determined rather efficiently. However, the burden implied by accounting for many-body hydrodynamic interactions is still incomparably larger than for the interparticle forces alone: having in mind that the resistance matrix has $3N \times 3N$ elements, the difficulties in eqn. (2.54) arise from the operations on the resistance matrix as the following synopsis shows.

(I) *Inverse of Resistance Matrix*

The inversion of the resistance matrix is characteristic for Brownian dynamics simulations and does not appear in the Stokesian dynamics technique. It originates from the relaxation of the particle momenta in eqn. (2.53) followed by solving the resulting equation for the particle displacements. Simple numerics would require $O(N^3)$ floating point operations for every matrix inversion, if N is the number of particles. One should note that the inversion has to be done at every time step because the matrix depends on the propagating particle positions. Thus, one might attempt to eliminate this drawback by simply not relaxing the particle momenta. But, because the physical time resolution would then be much shorter, many more time steps would be necessary to cover a fixed time span which increases the computational effort again.

The solution to the problem in this study has been found in the ***Pre-conditioned Conjugate Gradient Method***, which is an iterative technique. For a thorough description of the method, the reader is referred for example to "Numerical Recipes in Fortran: The Art of Scientific Computing" [92Pre].

Several pre-conditioners have been used to increase the efficiency of the simulation. The best choice was found to be a reduction of the resistance matrix where all off-diagonal 3×3-matrices are set to zero (see Fig. 2.33). Generally, the number of iterations also strongly depends on the starting value used in the iteration. In our study, the two-step integration scheme for the equations of motion, which in-

cludes a matrix inversion in both steps, leads to the following result. For the first step no general rule has been found to allow a good guess on the starting value. However, for the second step the solution of the first step has proven to lower the number of iterations by a factor of almost two. A detailed analysis of the efficiency of the method can be found in section 2.7.

(II) *Divergence of Inverse Resistance Matrix*

It has been shown above that already the inverse of the resistance matrix itself causes considerable computational problems. A solution has been found in the conjugate gradient method which does not compute the inverse of the matrix but determines the particle displacements by an iterative technique.

One might wonder how one can determine the derivative of the inverse of a matrix, which has never been calculated. As a matter of fact, for a long time the calculation of this divergence term has been the corner stone when doing simulations of hydrodynamically interacting particles. The usual procedure was to invert the resistance matrix and build differential quotients which is again an $O(N^3)$ solution.

Since the divergence term has its origin in the Brownian forces and hence in the stochastic Wiener processes, a solution can only be found within the framework of stochastic calculus. The idea is to construct the divergence-term with a two-step scheme (similar to the first-order term in a Taylor expansion) rather than to calculate it explicitly. Recently, two ways have been proposed to achieve this goal. On one hand, one tried to give new definitions and rules for stochastic integrals. Among these, the formal definitions have not shown to be useful in numerical applications [90Kli, 92Kli, 92Sch], and others have failed for multidimensional stochastic processes [97Tse]. On the other hand, a powerful numerical scheme has been presented without formulating it generally in terms of a stochastic integral definition [96Phu, 97Bal].

Subsection 2.6 entitled 'Efficient Simulation of Hydrodynamic Lubrication' shows how to merge both the stochastic integral definition and a useful numerical integration scheme for stochastic differential equations as (2.54). This is to be considered as one of the key results of this study for two reasons. First, it leads the way to an efficient solution to the divergence-problem in our simulations and also offers a powerful simulation tool for a much wider class of stochastic differential equations. And second, the method is not defined by its numerical application through an operational definition, rather a definition in terms of a new type of stochastic integral is presented. We realize that this new definition needs further mathematical testing. So, the achievement is not in having given a complete answer for a long standing problem. We have much more tried to establish a link between mathematics and simulation and have finally succeeded in proposing a, probably definitive, answer.

The solution presented in section 2.6 replaces the calculation of the divergence in eqn. (2.54) by a two-step integration scheme which does not imply this complicated term.

(III) *Choleski-Decomposition of Resistance Matrix*

The Choleski-decomposition (2.55) for an arbitrary $3N\times3N$-resistance matrix usually requires $O(N^3)$ floating point operations which is prohibitive for studying large particle numbers N. In the following, we present a solution which is not generally applicable but which substantially reduces the computational needs in our simulations.

It is usually assumed that the 'square root' $\boldsymbol{B}$ is also a $3N\times3N$-matrix. In principle however, eqn. (2.55) also allows solutions with non-square $3N\times M$-matrices $\boldsymbol{B}$ where $M > 3N$. This might not lessen the problem in general if no natural choice for M is given. Under special circumstances, as in our system, a good choice for M is suggested by the physical system. The physics behind going from $M = 3N$ to $M > 3N$ lies in the interpretation of the Brownian forces. The inclusion of the Brownian forces into the equation of motion for the particles has been motivated by the random kicks of the solvent particles on each colloidal particle. This is a rather single-particle interpretation and suggests to apply the noise to each particle separately. It has been shown in eqn. (2.9) via the fluctuation-dissipation theorem that this interpretation goes along with the single particle Stokes' drag.

The situation changes drastically with the inclusion of many-body hydrodynamic interaction. These forces explicitly couple the dissipative motions of the particles in a nontrivial manner. According to the fluctuation-dissipation theorem (2.55), also the Brownian forces on the particles are intimately related.

There are now two alternative ways to implement the Brownian forces. One can either have noise on the particles themselves (Fig. 2.34(a)), which leads to an ordinary $3N\times3N$-solution for $\boldsymbol{B}$. Or one can put noise on the connector vectors between hydrodynamically interacting particles emphasizing the term 'interaction' (Fig. 2.34(b)). This latter solution is inspired by Dissipative Particle Dynamics [93Koe, 97Boe]. Their use for our Brownian dynamic simulation shall now briefly be discussed.

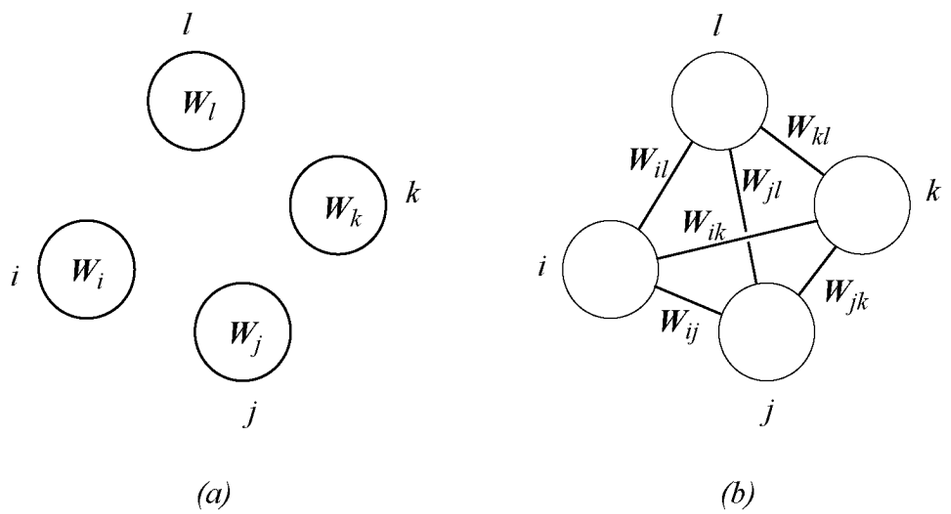

Fig. 2.34: Wiener processes and Brownian forces: Wiener processes W (a) on particle positions (common Brownian dynamics method) and (b) on connector vectors of interacting pairs (Dissipative Particle Dynamics method).

We first note that the Brownian increments can be rewritten in the form

$$\boldsymbol{B}_t \cdot d\boldsymbol{W}_t = \boldsymbol{R}_{FV,t}^{-1} \cdot \tilde{\boldsymbol{B}}_t \cdot d\boldsymbol{W}_t \qquad (2.56)$$

where the condition (2.55) for the matrix $\boldsymbol{B}$ is consecutively recast into the equivalent condition for $\tilde{\boldsymbol{B}}$ [88Bra]

$$\tilde{\boldsymbol{B}} \cdot \tilde{\boldsymbol{B}}^T = 2k_{\mathrm{B}}T\,\boldsymbol{R}_{FV} \qquad (2.57)$$

The inversion of the resistance matrix is needed anyway in eqn. (2.54) and can be dealt with by the conjugate gradient method as described above. We may therefore concentrate on the decomposition of the resistance matrix (2.57) rather than of its inverse. The Dissipative Particle Dynamics technique shows how to find a decomposition for matrices similar to the resistance matrix of hydrodynamic lubrication. Basically, the Choleski-decomposition of the whole resistance matrix is reduced to the decomposition of the pairwise resistance matrices. If the hydrodynamic interaction of particle *i* with particles *j* is given by

$$\boldsymbol{F}_i^{\mathrm{H}} dt = -\sum_{j \neq i} \omega(r_{ij}) \boldsymbol{P}_{ij} \cdot (\boldsymbol{v}_i - \boldsymbol{v}_j) \tag{2.58}$$

the corresponding Brownian force on the particle is [93Koe, 97Boe]

$$\boldsymbol{F}_i^{\mathrm{B}} dt = \sqrt{2k_{\mathrm{B}}T} \sum_{j \neq i} \sqrt{\omega(r_{ij})} \boldsymbol{P}_{ij} \cdot d\boldsymbol{W}_{ij} \tag{2.59}$$

The function $\omega(r)$ is the radial dependence of the interaction, in our case the prefactor in eqn. (2.50), and $\boldsymbol{W}_{ij}$ denotes the Wiener process on the particle pair (i, j). In this manner, the pairwise additivity from the hydrodynamic forces is transferred to the Brownian forces.

We furthermore conclude from (2.59) that the reduction of computational effort due to short range hydrodynamic lubrication is also directly carried over to the Brownian forces. This is essential for our simulations. The calculation of the Brownian forces needs to account only for $O(1)$ interacting neighbors for each particle which leads to an $O(N)$ overall computational effort in each integration step. The calculation of the Brownian increments in eqn. (2.54) is then only limited by the matrix inversion implied in eqn. (2.56).

The following restriction to this solution should be noted. It is a necessary requirement for the above procedure that no hydrodynamic force acts on the particles if all velocities are the same. This is respected in the lubrication approximation (2.50). If Stokes' drag were included one would have to combine Wiener processes on the pairs with Wiener processes on the single particles.

Summary of the Main Computational Difficulties

Table 2.13 gives a summary of the main computational difficulties implied by including lubrication hydrodynamics. For each of the three problems discussed above, the computational efficiency of the algorithm used in this study is compared with simple numerics. The efficiency of the divergence-term calculation in our simulations is not listed because it was replaced by a two-step integration scheme.

In the simulation one could get rid of all the above three problems (I, II, and III) if the resistance matrix was not dependent on the particle positions. This could be achieved by replacing the configuration dependent matrix by a pre-averaged matrix, i.e. the average resistance matrix at equilibrium. Then, the matrix inversion and the Choleski-decomposition would have to be done only once and the divergence term would vanish. It has been shown that this pre-averaging approximation is reasonable in the low-shear rate regime [97Ras]. However, it fails to reproduce the high-shear rate characteristics such as shear thickening. Therefore, we did not consider this method in our study.

Task	Simple Numerics	This Study	Method
Inversion of $\boldsymbol{R}_{FV}$	$O(N^3)$	$O(N^x)$, $x \leq 1.5$	Pre-conditioned Conjugate Gradient Technique
Divergence of $\boldsymbol{R}_{FV}^{-1}$	$O(N^3)$	-	(Replaced by Two-Step Integration Scheme)
Choleski-Decomp. of $\boldsymbol{R}_{FV}^{-1}$	$O(N^3)$	$O(N^1)$	Analytical Decomposition using Dissipative Particle Dynamics

Table 2.13: Computational efficiency when accounting for hydrodynamic lubrication. The two middle rows indicate the number of floating point operations of the corresponding implementation.

Final Version of the Integration Scheme

The integration scheme for the equations of motion eqn. (2.54), which results from implementing the three methods discussed above, is given in the following. If the particle displacement relative to the background flow is denoted by $\Delta \boldsymbol{x}_t = \Delta \boldsymbol{r}_t - \boldsymbol{v}_t^{\infty} \Delta t$ and if further the sum of the potential force and of the strain force is $\boldsymbol{F}_t \equiv \boldsymbol{F}_t^{\mathrm{pot}} + \boldsymbol{R}_{FE,t} : \boldsymbol{E}^{\infty}$, the two-step scheme, which is of order of weak convergence $w = 1$, reads

$$\boldsymbol{R}_{FV,t}^{(0)} \cdot \Delta \boldsymbol{x}_t^{\mathrm{p}} = \boldsymbol{F}_t^{(0)} \Delta t + \tilde{\boldsymbol{B}}_t^{(0)} \cdot \Delta \boldsymbol{W}_t \tag{2.60}$$

$$\boldsymbol{R}_{FV,t}^{(\mathrm{p})} \cdot \Delta \boldsymbol{x}_t^{\mathrm{c}} = \frac{1}{2} \boldsymbol{R}_{FV,t}^{(\mathrm{p})} \cdot \Delta \boldsymbol{x}_t^{\mathrm{p}} + \frac{1}{2} \boldsymbol{F}_t^{(\mathrm{p})} \Delta t + \frac{1}{2} \tilde{\boldsymbol{B}}_t^{(0)} \cdot \Delta \boldsymbol{W}_t \tag{2.61}$$

Here, the superscript (0) indicates that the corresponding quantity is to be evaluated at the particle configuration given by $\boldsymbol{r}_t$, whereas the superscript (p) denotes evaluation at the predicted configuration $\boldsymbol{r}_t + \Delta \boldsymbol{r}_t^{\mathrm{p}}$.

We briefly recapitulate the three key points of the scheme (2.60-61).

(I) The calculation of the inverse of the resistance matrix is replaced by using the iterative preconditioned conjugate gradient technique which finds an approximate solution for the particle displacement. The iteration has to be performed twice in each time step, once to find the predicted displacement $\Delta \boldsymbol{x}_t^{\mathrm{p}}$ (eqn. (2.60)) and once to determine the corrected value $\Delta \boldsymbol{x}_t^{\mathrm{c}}$ (via iteration for $\Delta \boldsymbol{x}_t^{\mathrm{c}} - \Delta \boldsymbol{x}_t^{\mathrm{p}}/2$ in eqn. (2.61)).

(II) The divergence of the inverse which is implied in eqn. (2.54) is completely absent and is replaced by a less time-consuming two-step procedure. For this, it is crucial that the configuration dependent quantities ($\boldsymbol{R}_{FV}$, $\boldsymbol{F}$, and $\tilde{\boldsymbol{B}}$) are evaluated for the different configurations as indicated by the superscripts (0) and (p). Furthermore, the Wiener increments $\Delta \boldsymbol{W}$ need to be the same for the predictor and for the corrector step in order to build up the divergence term correctly.

(III) The Brownian displacements $\boldsymbol{B} \cdot \Delta \boldsymbol{W}$ are reinterpreted in terms of Brownian forces $\tilde{\boldsymbol{B}} \cdot \Delta \boldsymbol{W}$ via the relation $\boldsymbol{B} = \boldsymbol{R}_{FV}^{-1} \cdot \tilde{\boldsymbol{B}}$. These Brownian forces can be determined efficiently for the limiting case of short range hydrodynamic lubrication.

c) Hydrodynamic Stress Tensor Contributions

In the following, a brief summary of all stress tensor contributions in a suspension of hydrodynamically interacting particles is given. For further details, the reader is referred to the book "Microhydrodynamics" [91Kim] or to the original publications [84Jef, 92Jef].

The total stress σ^{total} in the suspension consists of five contributions, where the last three are due to the various interactions between the colloidal particles [96Phu]:

$$\sigma^{\text{total}} = IT + 2\eta_s \boldsymbol{E}^{\infty} + \{\sigma^{\text{H}} + \sigma^{\text{P}} + \sigma^{\text{B}}\} \tag{2.62}$$

Here IT stands for an isotropic pressure term which is of no further interest in shear flow situations. The second term is the stress of the Newtonian liquid between the particles. The remaining terms are hydrodynamic σ^{H}, potential interaction σ^{P}, and Brownian force contributions σ^{B}. Using the $3N$-component notation, they are given by

$$\sigma^{\text{H}} = -\frac{1}{V}\langle \boldsymbol{R}_{SV} \cdot \boldsymbol{R}_{FV}^{-1} \cdot \boldsymbol{R}_{FE} - \boldsymbol{R}_{SE} \rangle : \boldsymbol{E}^{\infty} \tag{2.63}$$

$$\sigma^{\text{P}} = -\frac{1}{V}\langle (\boldsymbol{R}_{SV} \cdot \boldsymbol{R}_{FV}^{-1} + \boldsymbol{r}\mathbf{1}) \cdot \boldsymbol{F}^{\text{pot}} \rangle \tag{2.64}$$

$$\sigma^{\text{B}} = -\frac{k_{\text{B}}T}{V}\langle \nabla \cdot (\boldsymbol{R}_{SV} \cdot \boldsymbol{R}_{FV}^{-1}) \rangle \tag{2.65}$$

$\boldsymbol{R}_{SV}$ and $\boldsymbol{R}_{SE}$ are third- and fourth-rank tensors respectively. The explicit form of the tensors can be found in the Appendix.

The divergence term in the Brownian stress tensor does not have to be calculated explicitly. A two-step method can be used which is similar to the integration scheme for the equations of motion [97Bal]. One finds for the particle contribution to the stress

$$\begin{aligned} \sigma^{\text{part}} = \sigma^{\text{H}} + \sigma^{\text{P}} + \sigma^{\text{B}} = &-\frac{1}{2V\Delta t}\langle (\boldsymbol{R}_{SV}^{(\text{c})} + \boldsymbol{R}_{SV}^{(0)}) \cdot \Delta \boldsymbol{x}_t^{\text{c}} \rangle \\ &- \frac{1}{V}\langle \boldsymbol{r}\mathbf{1} \cdot \boldsymbol{F}^{\text{pot}(0)} \rangle + \frac{1}{V}\langle \boldsymbol{R}_{SE}^{(0)} \rangle : \langle \boldsymbol{E}^{\infty} \rangle \end{aligned} \tag{2.66}$$

where $\Delta \boldsymbol{x}_t^{\text{c}}$ denotes the corrected particle displacement relative to the background flow according to eqn. (2.61). The superscripts (0) and (c) indicate the evaluation of the corresponding quantity for the configuration $\boldsymbol{r}_t$ and $\boldsymbol{r}_t + \Delta \boldsymbol{r}_t^{\text{c}}$, respectively.

2.6 Efficient Simulation of Hydrodynamic Lubrication

Published in J. Chem. Soc., Faraday Trans., 94(10), 1403-1405 (1998)

Fluctuation-dissipation theorem, kinetic stochastic integral and efficient simulations

Markus Hütter, Hans Christian Öttinger

Institute of Polymers

ETH-Zentrum

CH-8092 Zürich, Switzerland

Abstract

Diffusive systems respecting the fluctuation-dissipation theorem with multiplicative noise are studied on the level of stochastic differential equations. We propose an efficient simulation scheme motivated by the direct definition of the 'Kinetic stochastic integral', which differs from the better known Itô and the Stratonovich integrals. This simulation scheme is based on introducing the identity matrix, expressed in terms of the diffusion tensor and its inverse, in front of the noise term, and evaluating these factors at different times.

2.6.1 Introduction

Diffusion equations are studied whenever fluctuations or irreversible behaviour in general are involved; examples being particle diffusion, heat conduction, viscous flow and the description of complex fluids. For a d-dimensional variable $\boldsymbol{x}$, these equations can be written in the form

$$\frac{\partial}{\partial t}p(\boldsymbol{x},t) = -\frac{\partial}{\partial \boldsymbol{x}}\cdot[\boldsymbol{A}(\boldsymbol{x},t)p(\boldsymbol{x},t)] + \frac{1}{2}\frac{\partial}{\partial \boldsymbol{x}}\cdot\left[\boldsymbol{D}(\boldsymbol{x},t)\cdot\frac{\partial}{\partial \boldsymbol{x}}p(\boldsymbol{x},t)\right] \qquad (2.67)$$

where the term containing the d-dimensional vector $\boldsymbol{A}$ is called drift, and the other containing the positive semi-definite $d\otimes d$-matrix $\boldsymbol{D}$ is called the diffusion term. For the following, it is essential to notice that the diffusion tensor $\boldsymbol{D}$ is placed ***between*** the two partial derivatives. In systems where the drift originates from a gradient of a potential that is mediated through the diffusion or mobility tensor, i.e. $\boldsymbol{A}$ is of the form

$$\boldsymbol{A}(\boldsymbol{x}, t) = -\frac{1}{2}\boldsymbol{D}(\boldsymbol{x}, t) \cdot \left[\frac{\partial}{\partial \boldsymbol{x}}\phi(\boldsymbol{x}, t)\right] \tag{2.68}$$

one then finds that the 'Boltzmann distribution' $p(\boldsymbol{x}, t) \sim \exp[-\phi(\boldsymbol{x}, t)]$ is a stationary solution of the above diffusion equation (2.67).

A solution of the diffusion equation can often not be found in closed form if the diffusion tensor depends on the state of the system, i.e. for multiplicative noise, and one is lead to solve the diffusion equation numerically with finite element methods. However, for many complex systems, such as polymer solutions or colloidal suspensions, the large number of degrees of freedom is prohibitive for a numerical solution of the diffusion equation. Rather than studying the system by means of the distribution function $p(\boldsymbol{x},t)$ for the variable $\boldsymbol{x}$, one thus looks for a set of trajectories $\boldsymbol{x}$ which have the distribution $p(\boldsymbol{x},t)$, meaning that one tries to solve stochastic differential equations [92Klo, 96Ött]. A trajectory, which is a sample for the diffusion equation (2.67), is given by the following stochastic differential equation [85Gar, 92Klo, 96Ött] (Itô version, denoted by the symbol "•"):

$$d\boldsymbol{x} = \left[\boldsymbol{A}(\boldsymbol{x}, t) + \frac{1}{2}\left(\frac{\partial}{\partial \boldsymbol{x}} \cdot \boldsymbol{D}(\boldsymbol{x}, t)\right)\right]dt + \boldsymbol{B}(\boldsymbol{x}, t) \bullet d\boldsymbol{W}, \tag{2.69}$$

where the random increments are composed of d'-dimensional Wiener increments $d\boldsymbol{W}$ and a $d\otimes d'$-matrix $\boldsymbol{B}$, the latter being related to the diffusion tensor by

$$\boldsymbol{B}(\boldsymbol{x}, t) \cdot \boldsymbol{B}(\boldsymbol{x}, t)^T = \boldsymbol{D}(\boldsymbol{x}, t). \tag{2.70}$$

Equation (2.70) relating random forces and diffusive/dissipative dynamics is the well known fluctuation-dissipation theorem of the second kind [66Kub, 96Ött], which is a key result of statistical mechanics. Choosing the Itô version of the stochastic differential equation (2.69) means that the random increments $\boldsymbol{B}(\boldsymbol{x}, t) \bullet d\boldsymbol{W}$ have mean value zero. Notice the divergence term in eqn. (2.69): putting the diffusion tensor in eqn. (2.67) ***between*** the two derivatives is the reason for the divergence term in eqn. (2.69). In other words, for systems given by eqn. (2.67) with a drift term given by eqn. (2.68), the fluctuation-dissipation theorem and the Boltzmann stationary solution lead to an Itô-stochastic differential equa-

tion with this additional contribution to the drift term. We here propose a numerical integration scheme for stochastic differential equations given by eqn. (2.69), that circumvents the calculation of the divergence term completely, but rather constructs it by using a two-step scheme with the main goal of substantially reducing the computational needs in simulations. In order to motivate this integration scheme, we first define a new stochastic integral, from which we then heuristically show how the divergence term is constructed.

One should mention that a stochastic integral definition, which naturally respects the fluctuation-dissipation theorem, has been given already for the one-dimensional case by Tsekov [97Tse], but we give here a non-trivial generalization to arbitrary dimensions. The latter stochastic integral shall be called 'kinetic', as proposed by Klimontovich [90Kli, 92Kli].

2.6.2 Multi-dimensional Definition of the "Kinetic Stochastic Integral"

There are currently three different definitions for stochastic integrals, the most famous of which are the Itô and Stratonovich versions[85Gar, 92Klo] respectively. While the transformations among different types of integrals are straightforward in principle, certain integrals may be much more convenient for developing efficient simulation algorithms. They differ by the time point at which the integrand is evaluated, when writing the integral as a sum over finite time intervals: Itô evaluates the integrand at the starting point of the time interval, whereas Stratonovich uses the midpoint values. A third stochastic integral definition has recently been given by Tsekov [97Tse], using the endpoint values of the integrand. He proved this integral to respect the fluctuation-dissipation theorem naturally in the one-dimensional case. However, it does not possess this desirable property in the multi-dimensional case. We give here a definition for the kinetic stochastic integral with the main property of naturally respecting the fluctuation-dissipation theorem, i.e. of incorporating the divergence term in eqn. (2.69), also for an arbitrary multidimensional case. A definition of this new integral, which shall be denoted by the symbol ◊, in terms of the Itô integral by

$$\int \boldsymbol{B}(\boldsymbol{x}) \lozenge d\boldsymbol{W} := \int \boldsymbol{B}(\boldsymbol{x}) \bullet d\boldsymbol{W} + \frac{1}{2}\int \left[\frac{\partial}{\partial \boldsymbol{x}} \cdot \boldsymbol{D}(\boldsymbol{x})\right] dt$$

does not provide us with any more insight for the construction of the desired integration scheme. Much more useful is the key result of this paper, which is the definition of this integral in terms of the mean-square limit of a time-discretized sum,

$$\int \boldsymbol{B}(\boldsymbol{x}) \lozenge d\boldsymbol{W} := \underset{M \to \infty}{\text{ms–lim}} \sum_{i=1}^{M} \frac{1}{2}[\boldsymbol{D}(\boldsymbol{x}_{t_{i+1}}) \cdot \boldsymbol{D}_{\text{inv}}(\boldsymbol{x}_{t_i}) + \mathbf{1}] \cdot \boldsymbol{B}(\boldsymbol{x}_{t_i}) \cdot [\boldsymbol{W}_{t_{i+1}} - \boldsymbol{W}_{t_i}] \quad (2.71)$$

with $\boldsymbol{D} := \boldsymbol{B} \cdot \boldsymbol{B}^T$ and the Wiener increments $\Delta \boldsymbol{W}_{t_i} := \boldsymbol{W}_{t_{i+1}} - \boldsymbol{W}_{t_i}$ having mean value $\langle \Delta \boldsymbol{W}_{t_i} \rangle = \boldsymbol{0}$ and variance $\langle \Delta \boldsymbol{W}_{t_i} \Delta \boldsymbol{W}_{t_k} \rangle = \delta_{ik} \Delta t \mathbf{1}$. The definition of the inverse $\boldsymbol{D}_{\text{inv}}$ has to account for the fact that the null-space of $\boldsymbol{D}$ might be non-trivial, i.e. that some linear combinations of the variables $\boldsymbol{x}$ are not affected by the random and diffusive motion. We therefore define the matrix $\boldsymbol{D}_{\text{inv}}$ to be the null-matrix on the null-space of $\boldsymbol{D}$ and the inverse of $\boldsymbol{D}$ on the remaining subspace, i.e. the inverse of the diagonalized matrix $\boldsymbol{D}$ is defined by taking the inverse of the eigenvalues with the definition $\frac{1}{0} := 0$. (As a consequence, the null-spaces of $\boldsymbol{D}$ and $\boldsymbol{D}_{\text{inv}}$ are identical at a given time t_i). It is essential that $\boldsymbol{D}_{\text{inv}}$ is evaluated at the same time as $\boldsymbol{B}$ for the image of $\boldsymbol{B}$ and the image of $\boldsymbol{D}$ to be the same subspace. Furthermore, this makes clear that the definition $\frac{1}{0} := 0$ on the null-space does not lead to any complications and is not related to any physical singularities, but only stands for excluding the non-diffusive subspace from the definition of the stochastic integral. For a strictly positive-definite diffusion tensor, $\boldsymbol{D}_{\text{inv}}$ is simply the inverse of $\boldsymbol{D}$.

One can show heuristically that the above definition (2.71) for the kinetic stochastic integral is indeed the sum of the Itô integral and the desired divergence term by making a Taylor expansion of the first diffusion tensor in eqn. (2.71) and expressing the endpoint value $\boldsymbol{x}_{t_{i+1}}$ in terms of the startpoint value $\boldsymbol{x}_{t_i}$ through the stochastic integral equation (2.69) to first order in $\Delta \boldsymbol{W}_{t_i}$. One finds in the mean-square sense

$$\int \boldsymbol{B}(\boldsymbol{x}) \lozenge d\boldsymbol{W} = \int \boldsymbol{B}(\boldsymbol{x}) \bullet d\boldsymbol{W} + \frac{1}{2} \int \left[\frac{\partial}{\partial \boldsymbol{x}} \cdot \boldsymbol{D}(\boldsymbol{x}) \right] dt , \tag{2.72}$$

illustrating the existence of the non-random contribution in the kinetic integral, as the expectation value $\langle \boldsymbol{B}(\boldsymbol{x}) \lozenge d\boldsymbol{W} \rangle = \langle (\partial / \partial \boldsymbol{x}) \cdot \boldsymbol{D}(\boldsymbol{x}) \rangle dt$ is non-vanishing in general. We point out that the factorization in the integrand and the evaluation of the integrand factors at different times are essential for producing the divergence term. The occurrence of the divergence term when going to non-vanishing time steps, i.e. finite time resolution, was used by Fixman [78Fix] when constructing Langevin equations and the numerical integration scheme for the simulation of polymer dynamics, but it was not formulated in terms of stochastic integration.

2.6.3 Construction of a Numerical Integration Scheme

It has been shown in the previous section that the differences between the Itô and the kinetic versions of the stochastic integral is the inclusion of the extra divergence term in the kinetic integral, ***formally*** changing the equations for $d\boldsymbol{x}$ but leaving the solution $\boldsymbol{x}$ unchanged, since

$$\left\{ \boldsymbol{A}(\boldsymbol{x}) + \frac{1}{2} \left[\frac{\partial}{\partial \boldsymbol{x}} \cdot \boldsymbol{D}(\boldsymbol{x}) \right] \right\} dt + \boldsymbol{B}(\boldsymbol{x}) \cdot d\boldsymbol{W} = \boldsymbol{A}(\boldsymbol{x}) dt + \boldsymbol{B}(\boldsymbol{x}) \lozenge d\boldsymbol{W}$$

The main advantage of this kinetic integral definition lies, however, in the possibility of constructing efficient numerical integration schemes for stochastic processes as in eqn. (2.69), ***without*** ever calculating the divergence of the diffusion tensor. Such integration schemes have already been used in Brownian dynamics simulations of dense colloidal suspensions [97Bal], being of first order in the time step Δt. However, to the best of our knowledge, no direct mathematical definition of a kinetic stochastic integral for arbitrary dimensions has ever been given. We think that a definition by means of stochastic integrals, such as eqn. (2.71), is necessary to derive more efficient numerical integration schemes, especially to develop higher order integration schemes.

In the following, we heuristically derive a weak [92Klo] first order numerical integration scheme from our kinetic integral definition. Writing down the kinetic version of the stochastic differential equation,

$$\begin{aligned} d\boldsymbol{x}_t &= \boldsymbol{A}(\boldsymbol{x}_t)dt + \boldsymbol{B}(\boldsymbol{x}_t) \lozenge d\boldsymbol{W}_t \\ &= \boldsymbol{A}(\boldsymbol{x}_t)dt + \frac{1}{2}[\boldsymbol{D}(\boldsymbol{x}_t + d\boldsymbol{x}_t) \cdot \boldsymbol{D}_{\mathrm{inv}}(\boldsymbol{x}_t) + \mathbf{1}] \cdot \boldsymbol{B}(\boldsymbol{x}_t) \cdot d\boldsymbol{W}_t \end{aligned} \tag{2.73}$$

suggests the following two-step scheme for the numerical integration. The predictor step is given by

$$\Delta \boldsymbol{x}_{t_i}^{\mathrm{p}} = \boldsymbol{A}(\boldsymbol{x}_{t_i})\Delta t + \boldsymbol{B}(\boldsymbol{x}_{t_i}) \cdot \Delta \boldsymbol{W}_{t_i}, \tag{2.74}$$

where $\Delta \boldsymbol{W}_{t_i} = \boldsymbol{W}_{t_{i+1}} - \boldsymbol{W}_{t_i}$ are the Wiener increments with mean value $\langle \Delta \boldsymbol{W}_{t_i} \rangle = \mathbf{0}$ and variance $\langle \Delta \boldsymbol{W}_{t_i} \Delta \boldsymbol{W}_{t_k} \rangle = \delta_{ik} \Delta t \mathbf{1}$. This predictor value is now used in the first diffusion tensor term on the second line of eqn. (2.73) for the corrector step:

$$\begin{aligned} \Delta \boldsymbol{x}_{t_i}^{\mathrm{c}} &= \frac{1}{2}[\boldsymbol{A}(\boldsymbol{x}_{t_i} + \Delta \boldsymbol{x}_{t_i}^{\mathrm{p}}) + \boldsymbol{A}(\boldsymbol{x}_{t_i})]\Delta t \\ &\quad + \frac{1}{2}[\boldsymbol{D}(\boldsymbol{x}_{t_i} + \Delta \boldsymbol{x}_{t_i}^{\mathrm{p}}) \cdot \boldsymbol{D}_{\mathrm{inv}}(\boldsymbol{x}_{t_i}) + \mathbf{1}] \cdot \boldsymbol{B}(\boldsymbol{x}_{t_i}) \cdot \Delta \boldsymbol{W}_{t_i} \end{aligned} \tag{2.75}$$

It can be shown that the above two-step integration scheme is weakly convergent to first order in the time step Δt by expanding $\boldsymbol{D}(\boldsymbol{x}_{t_i} + \Delta \boldsymbol{x}_{t_i}^{\mathrm{p}})$ up to first order in $\Delta \boldsymbol{W}_{t_i}$. For a constant diffusion tensor, the above scheme is even weakly convergent to second order. The term involving $\boldsymbol{D}(\boldsymbol{x}_{t_i} + \Delta \boldsymbol{x}_{t_i}^{\mathrm{p}})$ replaces the calculation of the divergence of the diffusion tensor in the Itô stochastic differential equation (2.69). Thus, the kinetic version is to be favoured to the Itô version, except in cases where a closed expression for $(\partial / \partial \boldsymbol{x}) \cdot \boldsymbol{D}(\boldsymbol{x})$ can be given.

For cases where only $\boldsymbol{D}_{\text{inv}}$ but not $\boldsymbol{D}$ itself is explicitly known (the connection between $\boldsymbol{D}_{\text{inv}}$ and $\boldsymbol{D}$ being as described in subsection 2.6.2), the determination of $\boldsymbol{B}$ and especially of $(\partial/\partial\boldsymbol{x})\cdot\boldsymbol{D}(\boldsymbol{x})$ is computationally very time consuming. However, the definition of the kinetic stochastic integral can be reformulated in a way to circumvent this problem: using $\boldsymbol{D}\cdot\boldsymbol{D}_{\text{inv}}\cdot\boldsymbol{B}=\boldsymbol{B}$, we find with $\boldsymbol{B}_{\text{inv}}:=\boldsymbol{D}_{\text{inv}}\cdot\boldsymbol{B}$ from the definition of the kinetic stochastic integral

$$\int \boldsymbol{B}(\boldsymbol{x})\lozenge d\boldsymbol{W} = \underset{M\to\infty}{\text{ms–lim}} \sum_{i=1}^{M} \frac{1}{2}[\boldsymbol{D}(\boldsymbol{x}_{t_{i+1}})+\boldsymbol{D}(\boldsymbol{x}_{t_i})]\cdot\boldsymbol{B}_{\text{inv}}(\boldsymbol{x}_{t_i})\cdot[\boldsymbol{W}_{t_{i+1}}-\boldsymbol{W}_{t_i}] \quad , \quad (2.76)$$

with $\boldsymbol{B}_{\text{inv}}\cdot\boldsymbol{B}_{\text{inv}}^{T}=\boldsymbol{D}_{\text{inv}}\cdot\boldsymbol{B}\cdot\boldsymbol{B}^{T}\cdot\boldsymbol{D}_{\text{inv}}^{T}=\boldsymbol{D}_{\text{inv}}\cdot\boldsymbol{D}\cdot\boldsymbol{D}_{\text{inv}}^{T}=\boldsymbol{D}_{\text{inv}}^{T}=\boldsymbol{D}_{\text{inv}}$. For such systems, the predictor step is then put into the form

$$\Delta\boldsymbol{x}_{t_i}^{\text{p}} = \boldsymbol{A}(\boldsymbol{x}_{t_i})\Delta t + \boldsymbol{D}(\boldsymbol{x}_{t_i})\cdot\boldsymbol{B}_{\text{inv}}(\boldsymbol{x}_{t_i})\cdot\Delta\boldsymbol{W}_{t_i} \quad (2.77)$$

and the corrector step is given by

$$\begin{aligned}\Delta\boldsymbol{x}_{t_i}^{\text{c}} = {} & \frac{1}{2}[\boldsymbol{A}(\boldsymbol{x}_{t_i}+\Delta\boldsymbol{x}_{t_i}^{\text{p}})+\boldsymbol{A}(\boldsymbol{x}_{t_i})]\Delta t \\ & + \frac{1}{2}[\boldsymbol{D}(\boldsymbol{x}_{t_i}+\Delta\boldsymbol{x}_{t_i}^{\text{p}})+\boldsymbol{D}(\boldsymbol{x}_{t_i})]\cdot\boldsymbol{B}_{\text{inv}}(\boldsymbol{x}_{t_i})\cdot\Delta\boldsymbol{W}_{t_i}\end{aligned} \quad (2.78)$$

The contributions to $\Delta\boldsymbol{x}_{t_i}^{\text{p}}$ and $\Delta\boldsymbol{x}_{t_i}^{\text{c}}$ in eqns. (2.77) and (2.78), respectively, which involve the diffusion tensor $\boldsymbol{D}$, can then be solved for by using the tensor $\boldsymbol{D}_{\text{inv}}$ and a conjugate gradient method. In this sense, it is crucial to note that the integral in eqn. (2.76) is only well defined if the null-space of $\boldsymbol{D}_{\text{inv}}$ at t_{i+1} is equal to, or a subset of, the null-space at t_i; this was not a restriction to eqn. (2.71). Again, the term involving $\boldsymbol{D}(\boldsymbol{x}_{t_i}+\Delta\boldsymbol{x}_{t_i}^{\text{p}})$ replaces the calculation of the divergence of the diffusion tensor. This latter integration scheme has been used by Ball and Melrose in Brownian dynamics simulations of dense colloidal suspensions [97Bal], where the time invariance of the nullspace of $\boldsymbol{D}_{\text{inv}}$ is motivated by the Galilean invariance of the equations of motions (i.e. total particle momentum lies in the nullspace of $\boldsymbol{D}_{\text{inv}}$ for all times).

It should be recalled that the integration scheme proposed in eqns. (2.74-75) applies to a larger class of problems than that in eqns. (2.77-78), as the former requires no restrictions on the nullspace of $\boldsymbol{D}_{\text{inv}}$ or $\boldsymbol{D}$. The definition of the kinetic integral in eqn. (2.71) (and not eqn. (2.76)) is thus to be considered as the starting point when developing numerical integration schemes.

2.6.4 Conclusions

A definition for a stochastic integral was given that naturally respects the fluctuation dissipation theorem by including the divergence of the diffusion tensor in the arbitrarily multidimensional case. It has been shown that this integral definition can be used to construct numerical integration schemes for stochastic differential equations without ever calculating the divergence of the diffusion tensor and thereby substantially reducing the computational needs.

This work was supported by grant no. 2100-046728.96/1 from the Swiss National Science Foundation.

2.7 Simple Shear Flow Revisited

Using the simulation method discussed in sections 2.5 and 2.6, the effect of hydrodynamic lubrication interaction on the high shear rate rheology of colloidal suspensions is studied. The performance of the numerical scheme is discussed, in particular its dependence on the system size and on the shear rate. It is shown that the previously discussed and developed (sections 2.5 and 2.6) algorithm allows to study the thickening at high shear rates. It is hence not the intention of this subsection to give a complete description of hydrodynamically interacting particle suspensions at high shear rates.

2.7.1 Simulation Input

a) Potential and Lubrication Interaction

Since the main interest in this chapter is on the effect of the short-range hydrodynamic lubrication, it is desirable to have a very short range potential interaction in order to allow for close approach of particles. If such a short interaction range is to be formulated in terms of the DLVO-potential used in previous sections, a secondary energy minimum occurs and the suspension is not sufficiently stable against coagulation. Therefore, we use the Yukawa potential here

$$V(r) = V_0 \frac{d}{r-d} \exp\left(\frac{\kappa_0}{d}[r-d]\right) \qquad (2.79)$$

The strength of the interaction is denoted by V_0. κ_0 is the inverse screening length relative to the particle diameter d. The values for the parameters are listed in Table 2.14. As shown in Fig. 2.35, the interaction potential is strongly repulsive at short particle separations and decays fast at larger separations.

Due to the short range of the Yukawa interaction, a cut-off in the potential at $r_{\text{cutoff}} = 1.5\,d$ is large enough. The interaction potential for larger separation is set to zero, which is equivalent to neglecting interaction energies that are smaller than 10^{-20} of the thermal energy. As far as the hydrodynamic lubrication is concerned, we use the corresponding expressions presented in subsection 2.5.2 and in the Appendix with the cut-off $r_{\text{cutoff}}^{\text{lubr}} = \sqrt{2}\,d$.

Parameter	Symbol	Value	Units (SI)
Potential Strength	V_0	$8.78 \cdot 10^{-22}$	J
Screening Length	κ_0	90	-
Particle Diameter	d	$5 \cdot 10^{-7}$	m

Table 2.14: Potential parameters for the stable suspension.

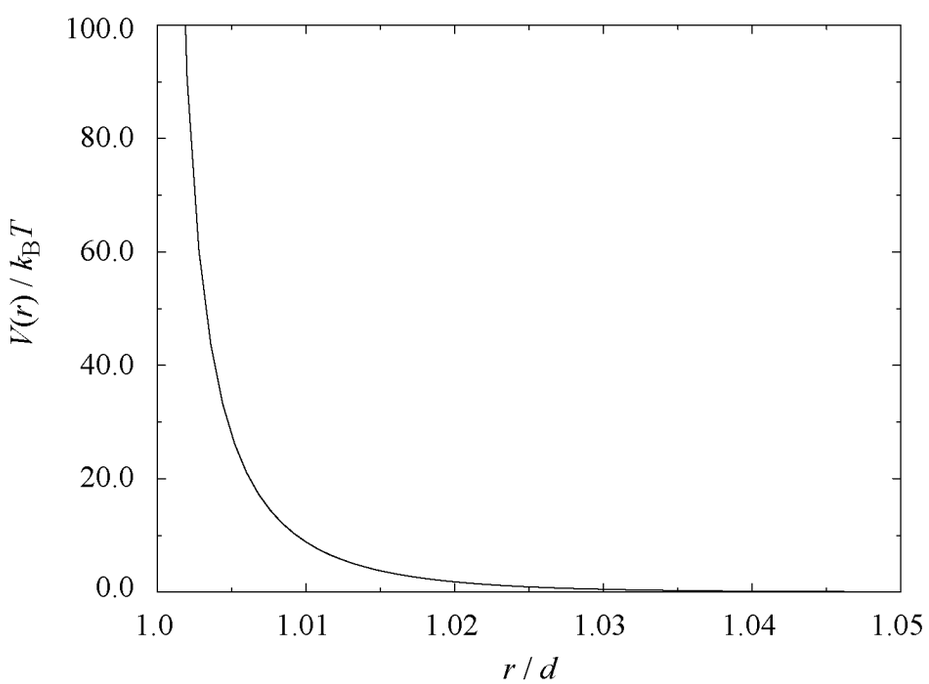

Fig. 2.35: Yukawa interaction potential for the stable suspension.

b) Solvent

In the previous sections 2.3 and 2.4, the influence of the solvent entered only through the temperature T of the whole colloidal suspension and the friction coefficient $\zeta = 3\pi d\eta_s$. In this chapter, the single particle friction is replaced by the many-body hydrodynamic lubrication. However, T and η_s are still the only parameters characterizing the solvent. The values used are $T = 293$ K and $\eta_s = 10^{-3}$ Pa s for water.

c) System Size and Linked-Cell List Algorithm

All simulations in this section were performed with $N = 125$ particles for a solid content of $\phi = 0.4$. The cubic simulation box was subdivided into cubic cells for the linked-cell list algorithm (see subsection 2.2.3). The number of cells in each of the x-, y- and z-direction was chosen as `Ncell = 3`. In total, the simulation box thus consisted of $\texttt{Ncell}^3 = 27$ small cells, leading to 4.63 particles per cell on average. Although the linked-cell list method is only favorable over the rudimentary technique of calculating interacting neighbors if $N > 100$, it is still employed here since we also will discuss the possibility of up-scaling the system to larger particle numbers.

d) Integration Steps

The integration of the equations of motion for the particles requires an appropriate choice of the finite time step Δt used in eqns. (2.60-61). Due to the short range Yukawa repulsion, particles can approach closely. Therefore, one has to take care that the finite integration step does not lead to an overlap between any close particles. In the simulations presented in this chapter, the following value has been found to be a reasonable choice:

$$\Delta t = 10^{-8}\ \mathrm{s} \tag{2.80}$$

We emphasize that this integration step is 350 times smaller than the one used in section 2.4 where many-body hydrodynamic interaction has not been considered.

e) Starting Configurations

The starting configurations for the shear runs were generated by equilibrating a simple cubic array of particles which interact through the Yukawa potential. Since the hydrodynamic lubrication is believed to primarily affect the high shear rate behavior of the suspension, it has been excluded in the equilibration procedure. We expect that this approximation has only a negligible effect on the measured high shear rate behavior because the particle structure is altered by applying the shear flow.

f) Tolerance in the Conjugate Gradient Routine

It has been shown in section 2.5 that the integration scheme includes the use of the pre-conditioned conjugate gradient technique in order to solve linear equations of the type $\boldsymbol{b} = \boldsymbol{A} \cdot \boldsymbol{x}$ for the vector $\boldsymbol{x}$ (here $\boldsymbol{b}$ denotes a given vector and $\boldsymbol{A}$

is a given square matrix). The value of the iterated solutions $\boldsymbol{x}_{\mathrm{it}}$ is rated by their relative error from the correct solution in terms of

$$\varepsilon_{\mathrm{it}} = \frac{\left|\boldsymbol{A} \cdot \boldsymbol{x}_{\mathrm{it}} - \boldsymbol{b}\right|}{|\boldsymbol{b}|} \tag{2.81}$$

We notice that this is a measure for the approximation of the vector $\boldsymbol{b}_{\mathrm{it}} \equiv \boldsymbol{A} \cdot \boldsymbol{x}_{\mathrm{it}}$ to $\boldsymbol{b}$, rather than for the approximation $\boldsymbol{x}_{\mathrm{it}}$ to $\boldsymbol{x} = \boldsymbol{A}^{-1} \cdot \boldsymbol{b}$. The criterion for finishing the iterative procedure is fulfilled if $\varepsilon_{\mathrm{it}} \leq \varepsilon_{\mathrm{it,max}} = 10^{-6}$.

2.7.2 *Shear Stress*

The particle contribution σ^{part} to the stress in the suspension (eqn. 2.62) is subdivided into a purely hydrodynamic σ^{H}, a potential interaction σ^{P}, and a Brownian term σ^{B}. In the following, we summarize the latter two in the 'thermodynamic stress' σ^{T}, i.e. $\sigma^{T} = \sigma^{P} + \sigma^{B}$. The particle stress then consists of two contributions, namely

$$\sigma^{part} = \sigma^{H} + \sigma^{T} \tag{2.82}$$

The results for the viscosities, which correspond to the stresses listed in eqn. (2.82), are shown in Fig. 2.36. As in section 2.4, *Pe* denotes the reduced shear rate, i.e. the Péclet-number $Pe = \dot{\gamma}\,\tau_{Br}$. One can see that the ***thermodynamic*** viscosity η^{T} exhibits a pronounced shear thinning and does not increase again, even at the highest shear rates. This tendency is in agreement with the simulations in section 2.4 which did not account for the many-body hydrodynamic interactions. The occurrence of shear thinning and a second Newtonian plateau seems therefore to exist generally in colloidal suspensions as long as only the thermodynamic stress is considered, irrespective of whether only single- or also multi-particle hydrodynamic interactions are included.

In contrast, Fig. 2.36 shows that the ***hydrodynamic*** viscosity η^{H} increases steadily as the shear rate is raised. Conclusively, the reason for shear thickening in the colloidal suspension is the stress contribution due to hydrodynamic lubrication. Furthermore, the total viscosity η^{part} is dominated by the hydrodynamic contribution over the whole range of shear rates in our simulation. However, we mention that this is not necessarily true for lower shear rates as shown in other simulations [96Phu, 97Bal]. The resulting curve for the total particle stress indicates that the colloidal suspension is indeed shear thickening, although only to a small extent.

The viscosity values from our simulations agree qualitatively with simulation results by others [96Phu, 97Bal]. There, it is also concluded that the shear thickening at high shear rates is due to the hydrodynamic interactions. The slightly higher values from our simulations can be attributed to the following point. Since we have extended the expression for the first order lubrication approximation up to $r_{cutoff}^{lubr} = \sqrt{2}\,d$, particle separations just below this cut-off overestimate the strength of hydrodynamic interaction. This finally results in overestimating the values for the rheological properties of the suspension which depend on the forces between the particles.

Our simulation results are also in agreement with experimental results. The dichroism experiments by Bender and Wagner [95Ben, 96Ben] as well as the stress jump measurements by Mackay and Kaffashi [95Mac] and Watanabe ***et al.*** [97Wat] have shown that the hydrodynamic stress dominates over the thermodynamic stress at high shear rates.

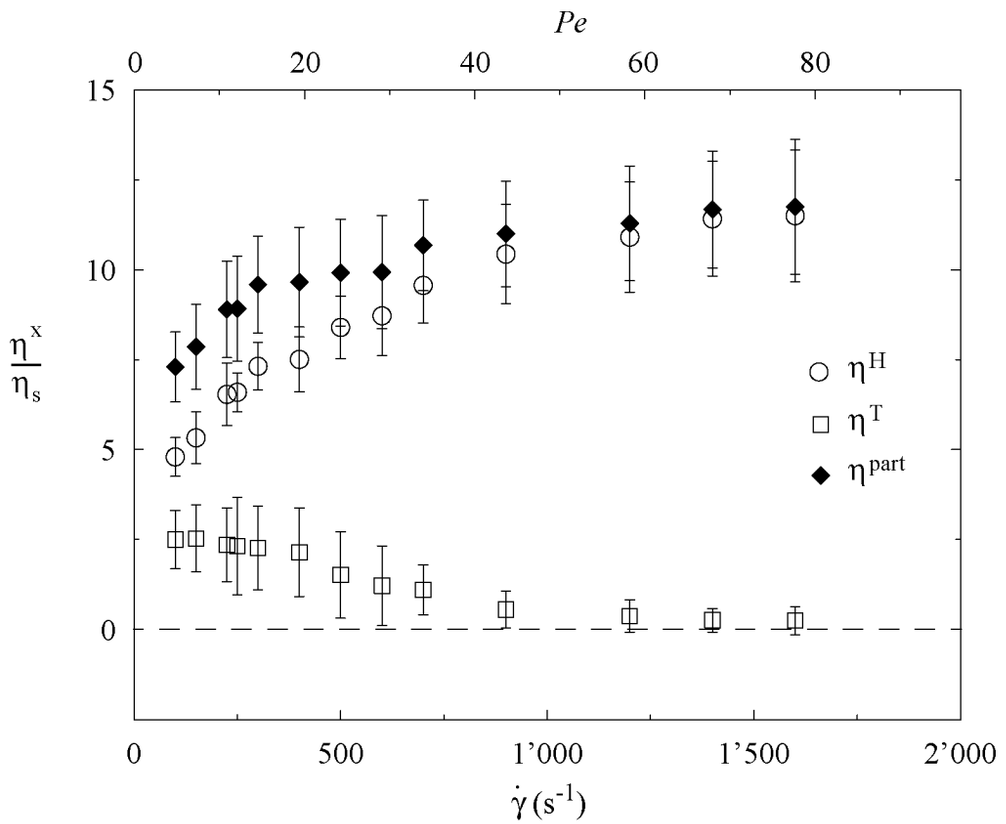

Fig. 2.36: Hydrodynamic η^H, thermodynamic η^T, and total particle viscosity η^{part} for a shear thickening suspension for $\phi = 0.4$.

Summary

The above results show that the short range hydrodynamic lubrication interaction overcompensates the shear thinning of the thermodynamic viscosity contribution at high shear rates. The shear thickening in colloidal suspensions can thus be attributed to hydrodynamic stresses.

2.7.3 *Normal Stresses*

According to the splitting of the total particle contribution to the stress tensor given in eqn. (2.82), there is a purely hydrodynamic N^{H} and a thermodynamic contribution N^{T} to the normal stress differences N^{part}.

The simulation results for the first normal stress difference are shown in Fig. 2.37. The normal stress values are given in dimensionless units with respect to the shear stress of the solvent (η_s denotes the viscosity of the solvent alone). The relative thermodynamic contribution $N_1^{\mathrm{T}}/\eta_s\dot{\gamma}$ is positive and decreases with increasing shear rate, which means that the non-reduced values N_1^{T} grow only sublinearly, in agreement with the results in section 2.4. We conclude that this behavior is generally valid for the thermodynamic contribution, whether only single- or also many-body hydrodynamic interaction are considered in the particle dynamics. The relative hydrodynamic contribution $N_1^{\mathrm{H}}/\eta_s\dot{\gamma}$ is negative and becomes even more negative as the shear rate is raised. Due to this difference in shear rate dependence, the hydrodynamic term dominates over the thermodynamic term, resulting in an increasingly negative total first normal stress difference at higher shear rates. Theoretical considerations and computer simulations for lower shear rates have shown that the thermodynamic contribution may be larger than the hydrodynamic part, leading to a positive first normal stress difference at low shear rates [95Bra, 96Phu].

The second normal stress difference results are shown in Fig. 2.38. Firstly, the thermodynamic contribution is negative, which agrees with the simulation results in section 2.4 where many-body hydrodynamic interactions have been neglected. Secondly, the absolute value of $N_2^{\mathrm{T}}/\eta_s\dot{\gamma}$ decreases when going to higher shear rates, similar to our previous results in section 2.4. The hydrodynamic contribution $N_2^{\mathrm{H}}/\eta_s\dot{\gamma}$ is negative in the whole range of shear rates and decreases even further for higher shear rates. Similar to the first normal stress difference, the second normal stress difference is dominated by the hydrodynamic contribution when going to high shear rates.

The shear rate dependence for the hydrodynamic and the thermodynamic contributions of both the first and the second normal stress difference correspond to the simulation results of others [96Phu]. Finally, we emphasize that the relative errors are larger for the thermodynamic than for the hydrodynamic contribution. It is only due to the comparably small weight of the thermodynamic stress that the errors on the total stress are mainly dominated by the hydrodynamic contribution errors.

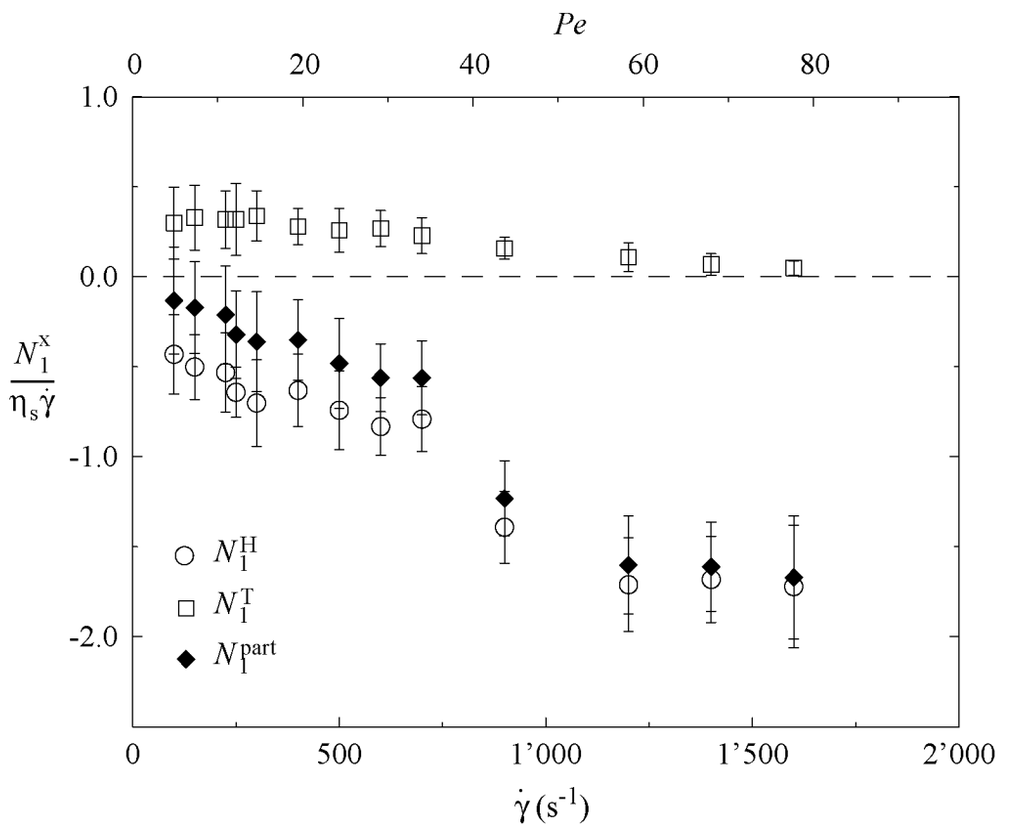

Fig. 2.37: Hydrodynamic N_1^H, thermodynamic N_1^T, and total first normal stress difference N_1^{part} for a shear thickening suspension for $\phi = 0.4$.

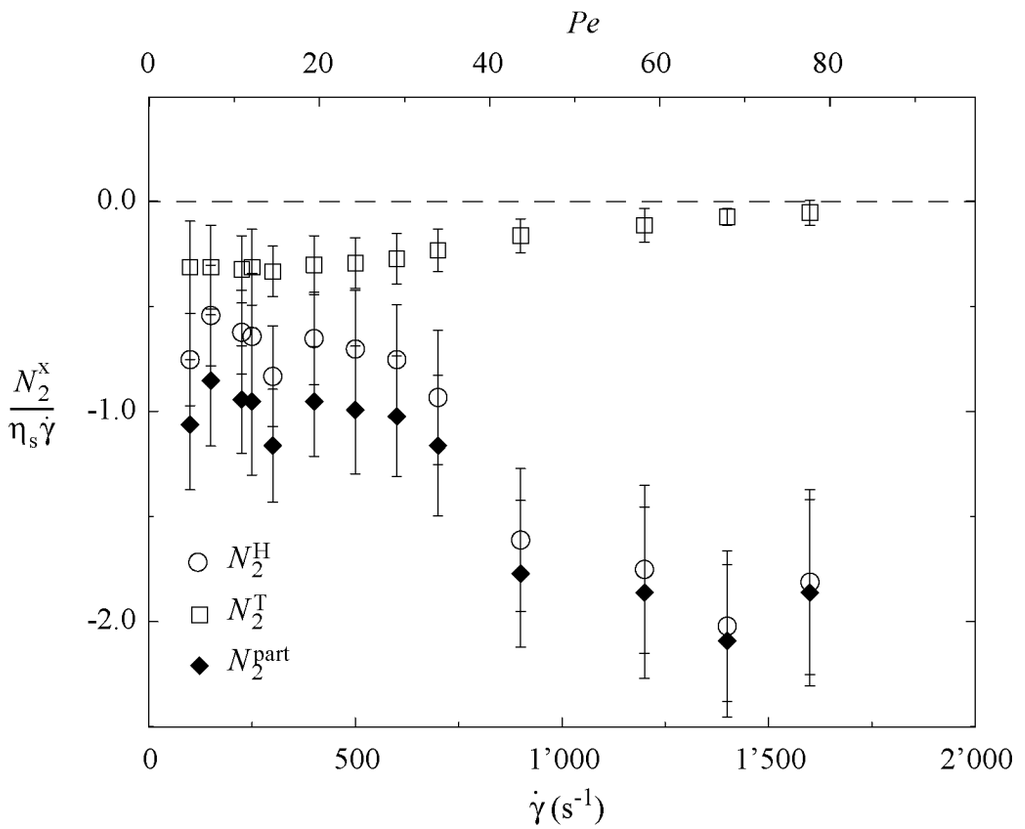

Fig. 2.38: Hydrodynamic N_2^H, thermodynamic N_2^T, and total second normal stress difference N_2^{part} for a shear thickening suspension for $\phi = 0.4$.

Summary

Both the first and the second normal stress difference are dominated by the hydrodynamic stress contributions when going to high shear rates. In contrast to the sublinear growth when neglecting many-body hydrodynamic lubrication, this interaction changes the behavior significantly to a stronger-than-linear shear rate dependence.

2.7.4 Performance

Since the aim of section 2.7 is to show the applicability of the simulation method proposed in sections 2.5 and 2.6, its performance is discussed in the following. It has been mentioned previously that the relation between the number N_{flop} of floating point operations and the number of particles N in the system is crucial for a possible up-scaling of the system to large particle numbers. It has been shown in section 2.5 that the only part with a nonlinear $N_{\text{flop}} \leftrightarrow N$-relation is the conjugate gradient technique to 'invert' the resistance matrix. To achieve a given accuracy of the solution, the iterative solver needs a certain number of iterations, N_{iter}. Because the resistance matrix depends on the particle configurations, this number of iterations is influenced by both the flow situation and the number of particles in the system. Since the number of flops associated with a single matrix multiplication is in our case $O(N)$ (see subsection 2.5.2), the total number of flops implied in one call of the conjugate gradient routine is

$$N_{\text{flop}} \sim N_{\text{iter}}(\dot{\gamma}, N)\, N \tag{2.83}$$

In the following, the dependence of the number of iterations N_{iter} on the shear rate $\dot{\gamma}$ and the number of particles N is discussed.

a) Shear Rate Dependence

The conjugate gradient technique is employed twice in every time step, once in the 'predictor' step (eqn. (2.60)) and once in the 'corrector' step (eqn. (2.61)). The number of iterations to reach a given accuracy of the solution strongly depends on the starting value. For the predictor step, no systematic procedure could be developed to find a reasonable starting value. In contrary, the number of iterations in the corrector step could be reduced substantially by using the solution from the predictor step as first estimate. The results for the simulations with $N = 125$ particles are shown in Fig. 2.39. The influence of a good choice of the starting value on the number of iterations is obvious: for all shear rates under consideration the number of iterations is almost cut in half. Furthermore, we note that more iterations are needed as the shear rate is raised, both in the predictor step as well as in the corrector step. The reason for this may be the following: the higher the shear rates, the closer the particles approach due to the high shear forces. As a consequence, the corresponding matrix elements are much larger than the others which results in a numerically badly conditioned resistance matrix.

We summarize that the numerical integration scheme proposed in sections 2.5 and 2.6 becomes less efficient as the shear rate is increased.

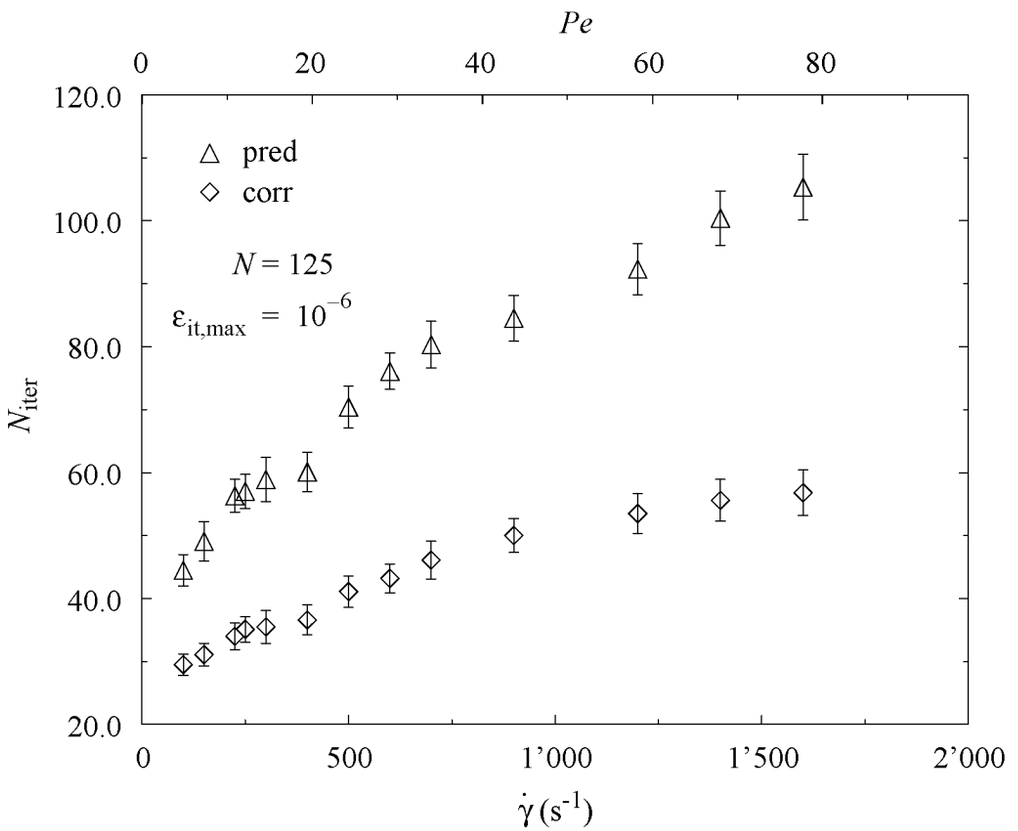

Fig. 2.39: Influence of the shear rate $\dot{\gamma}$ on the number of iterations N_{iter} in the predictor and the corrector step, respectively.

b) System Size Dependence

The simulation of colloidal suspensions at high shear rates with hydrodynamic lubrication has only been performed for $N = 125$ particles. This is because the simulations are still very time-consuming, although we managed to reduce the computational effort from $O(N^3)$ to far below $O(N^2)$. Nevertheless, we examined the possibility of up-scaling with the following preliminary procedure. The idea behind it is to perform the conjugate gradient step on a large set of particle configurations without explicitly performing an entire Brownian dynamics simulation. To achieve this, configurations of N particles in the range $125 \le N \le 32'768$ have been generated for different solid contents. Then, the configurations were shaken by applying only random displacements, which were sufficiently large to alter the particle configuration significantly, even allowing very close approach of particles. To make sure that a large amount of the particle configuration phase space is being probed by this procedure, we calculated the mean square displacement for all particles between their position in the first configuration and the last configuration. We terminate the phase space sampling if the particles have

moved on average more than the particle diameter. The number of iterations we have determined by this 'static' method correspond to the predictor step values in Fig. 2.39 since no starting value has been used. Fig. 2.40 shows the values for the performance for different solid contents. The number of iterations ranges from $N_{\text{iter}} \approx 50$ (for $N = 125$) up to $N_{\text{iter}} \geq 750$ (for $N = 32'768$ and $\phi = 0.5$).

In order to see whether the influence of the solid content is only in a prefactor or really in the functional dependence on N, a double-logarithmic plot is shown in Fig. 2.41. Because the slope increases when raising the solid content, one concludes that it is indeed the functional dependence of N_{iter} on N which is changing. The exponent in the power law $N_{\text{iter}} \propto N^{\alpha}$ raises from $\alpha = 0.24$ for $\phi = 0.3$ to $\alpha = 0.49$ for $\phi = 0.5$. The fact that the number of iterations N_{iter} does not only depend on (i) the number of particles N but also on (ii) the solid content ϕ, and on (iii) the required accuracy ε_{it} is reflected by the different α-values reported by others. In particular, Ball and Melrose [97Bal], who use almost the same technique as in our study, find for $\phi = 0.52$ and for $\varepsilon_{\text{it}} = 10^{-8}$ the value $\alpha \approx 0.75$.

It is not clear in as far this method leads to the same dependence of N_{iter} on N and on ϕ as one would obtain from full Brownian dynamics simulation runs. Nevertheless, we expect the two main characteristics to be the same. First, the

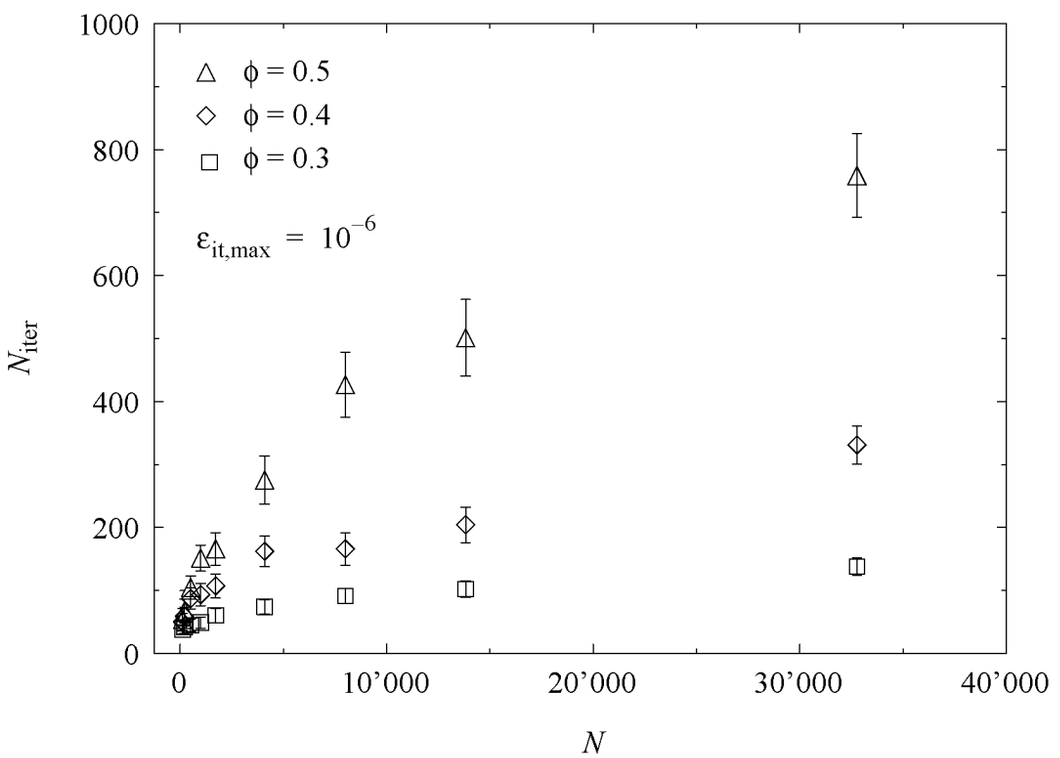

Fig. 2.40: Influence of the number of particles N on the number of iterations N_{iter} in the predictor step.

number of iterations increases when up-scaling the system, i.e. when adding more particles. Second, the performance of the iteration scheme drops for larger solid contents. The reason for the latter is twofold. On the one hand, the average particle separation is smaller for the higher solid contents and, hence, more pairs of very close particles occur, leading to a badly conditioned resistance matrix. On the other hand, the number of particles which are within the hydrodynamic interaction range $r_{\text{cutoff}}^{\text{lubr}}$ becomes larger (until a saturation point for solid contents close to random loose packing).

We showed that the performance of the conjugate gradient technique drops if the system is up-scaled to larger numbers of particles. Furthermore, raising the solid content lowers the computational efficiency as well since the exponent in the powerlaw relation $N_{\text{iter}} \leftrightarrow N$ increases.

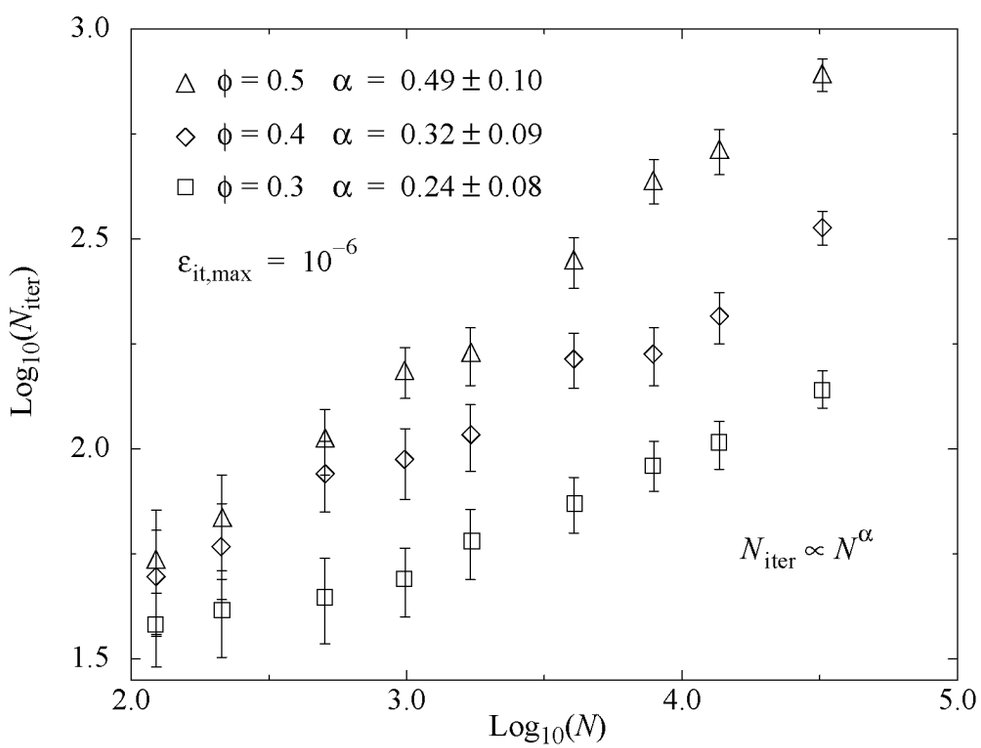

Fig. 2.41: Double-logarithmic plot of the influence of the number of particles N on the number of iterations N_{iter} in the predictor step.

2.7.5 Summary and Conclusions

The effect of short range hydrodynamic lubrication on the suspension rheology has been examined in section 2.7. When splitting the total particle stress into a hydrodynamic term and a thermodynamic term, the former is dominant at high shear rates. The thermodynamic viscosity exhibits shear thinning, which is overcompensated by the hydrodynamic term. Thus, the shear thickening in dense colloidal suspensions can be attributed to many-body hydrodynamic interaction effects. The normal stress differences show a similar dominance of the hydrodynamic contribution over the thermodynamic contribution at high shear rates. However, in contrast to the simulations which did not account for many-body hydrodynamic interaction, the total first and second normal stress difference are not of opposite sign here. Whereas only the corresponding thermodynamic contributions behave as the normal stresses in the non-hydrodynamic study in section 2.4, the dominant hydrodynamic contribution is negative for both normal stresses. As a consequence of these results for the viscosity and for the normal stress differences, high-shear rate rheology primarily probes hydrodynamic interaction effects rather than potential interaction mechanisms.

The performance of the simulation method has been tested by measuring the influence of the shear rate and of the system size on the limiting step in the scheme, the only which is not $O(N)$: the conjugate gradient routine. The performance drops when raising the shear rate over the shear thickening regime. This may be attributed to the close approach of particles leading to a badly conditioned matrix. Preliminary studies have shown that raising the system size lowers the performance as well. The number of iterations depends on the particles number through a power law, where the corresponding exponent depends on the solid content. The more dense the system, the higher is the exponent and, hence, the more iterations are needed.

The benefit of being able to model the shear thickening by including hydrodynamic lubrication is at a high cost. First, the conjugate gradient technique prevents an $O(N)$-scaling scheme which is highly desirable when studying large system sizes. Since the system includes only nearest neighbor interactions and is therefore ***physically*** $O(N)$, the current scheme is still not completely satisfactory. The second problem in this technique is that much smaller integration time steps are needed than if hydrodynamic interaction were absent. Therefore, much more integration steps need to be performed in order to cover a given physical time span. Because of these two reasons, the simulations of hydrodynamically interacting particles is still very time-consuming.

In this study, hydrodynamic interaction is only accounted for in terms of the short range lubrication contribution. The reason has been that this mode is supposed to dominate over lower order terms in dense suspensions. However, it is not clear whether long-range interactions would give raise to an additional shear thickening.

2.8 Summary and Conclusions

The behavior of stable colloidal suspensions in equilibrium and under shear flow have been studied in Chapter 2. Special attention has been paid to the relation between the microstructure and the particle dynamics on the one hand and the material properties on the other hand.

a) Equilibrium and Linear Viscoelasticity

The stress autocorrelation function and the mean square displacement have been measured for the suspension in equilibrium. Nevertheless, both quantities provide us also with information about the low-shear rate behavior of the suspension.

As a result of the linear response theory, the relaxation function of the off-diagonal stress components is related, first, to the linear viscoelastic memory function and, second, to the zero-shear rate viscosity. It is by these two relations that a thorough study of the stress relaxation function at equilibrium is of special interest. Our simulation results show that the decay in the stress relaxation, and hence in the linear viscoelastic memory, is well described by a stretched exponential function. Furthermore, the suspension exhibits increasingly solid-like behavior in terms of a finite long-time memory when raising the solid content. By using the Green-Kubo relation one thus finds that the suspension has an infinite zero-shear rate viscosity at the higher solid contents. This can be attributed to the increasing degree of hindrance of free particle motion, which finally leads to caging and solid-like behavior at the highest solid content.

The decreasing particle mobility upon raising the solid content has been quantified by measuring the mean square displacement, including the short- and the long-time diffusion regime. For the interaction potential under consideration, we observe that the particle motion is not only hindered at longer times but already the short-time diffusion is lowered. This is due to significant particle interaction already at the lowest solid content in this study. Beyond the short-time regime, the mean square displacement bends off into a long-time diffusive behavior with a lower diffusion coefficient. This transition is well described by a stretched exponential function. The characteristic time scales both for the stress relaxation function and for the transition in the mean square displacement decreases towards higher solid contents.

The experimental techniques to access the linear viscoelastic properties of colloidal suspensions are usually mechanical ones, such as stress-jump or stress-relaxation measurements, as well as frequency-sweep experiments. In order to allow an alternative method, an extended Stokes-Einstein relation between the stress relaxation function and the mean square displacement has been tested. It would allow to reconstruct the linear viscoelastic properties from the self-diffusion of the particles in the suspension. However, for none of the solid contents under consideration this relation is respected. We emphasize that the relation has

been applied experimentally by comparing rheological with diffusing-wave spectroscopy data. Satisfactory agreement has been found as mentioned previously. It is hence not clear whether the failure of the relation with our simulation data is due to the used fit-functions for the corresponding data sets or whether the reason is more fundamental. It may well be that the hydrodynamic interactions, which have been neglected at this stage of the simulation, play a crucial role also for the low-shear rate properties.

b) Shear Flow Rheology

The shear flow rheology of stable suspensions has been examined. The increase in the shear stress and in the normal stresses due to raising the solid content is quantified. Furthermore, it is found that the external force does not only drive the system into a non-Newtonian flow regime but also induces structural transitions. At low shear rates, a finite stress is needed to restructure the equilibrium configuration for the higher solid contents. This results in a non-zero yield stress at zero shear rate which agrees with the infinite Green-Kubo viscosity obtained from the equilibrium simulations.

At higher shear rates, the results for the shear stress show a pronounced shear thinning which is enhanced when raising the solid content. However, the flow curves do not reveal any other characteristic differences between the various solid contents. Only the mean square displacement indicates that for high solid content a disorder-order transition takes place upon raising the shear rate. Whereas the diffusion along the flow direction shows a significant drop as the structure orders under shear, the diffusion for motion in the other directions is completely suppressed. Snapshots of the particle configuration show that the particle arrange in a hexagonally ordered array of strings which move along the stream lines. In this shear ordered state, the particles which are grouped to bigger units can only exert collective motions. It is observed in the mean square displacement data that these strings move over each other in a zigzag-motion restricted to the shear plane. Since the self-diffusion of particles is more sensitive to changes in the microstructure than the viscosity, the further improvement and the use of scattering techniques to probe the particle dynamics is highly desirable. Although the material properties such as viscosity and normal stress differences are often of primary interest, a thorough examination of the self diffusion may help to tailor the desired material behavior.

The simulation results show that the shear thickening, which is typical for dense suspensions, cannot be reproduced with our model as long as hydrodynamic interactions are neglected. An integration scheme has been developed which accounts for short range hydrodynamic lubrication. The simulation results prove, in agreement with experimental results, that the shear stress at high shear rate is dominated by the hydrodynamic contribution and that shear thickening can hence be attributed to hydrodynamic interactions. Furthermore, both normal

stress differences are negative, in contrast to simulations without hydrodynamic interactions.

Although the reason for accounting for hydrodynamic interactions was the failure of the previous model to show shear thickening, it has not been studied here in as far also the low-shear rate rheology and the equilibrium properties are affected by this change. It may well be that the failure of the generalized Stokes-Einstein relation at equilibrium is due to neglecting hydrodynamic interactions. This would also explain why this relation has been tested successfully in experiments.

It has been discussed in detail that the inclusion of hydrodynamic interaction goes at the cost of handling a large, configuration-dependent resistance matrix which makes the simulation of large systems very time-consuming. Therefore, a substantial part of this thesis is devoted to reduce the computational needs, in particular the scaling of the number of floating point operations versus the system size. We emphasize that the only limiting part, which does not scale linearly in the number of particles, in the whole scheme is the conjugate gradient technique, or more generally speaking the 'inversion' of the resistance matrix. It is not clear whether this undesirable behavior is inherent to the model only or also to the real system itself. We have attempted several methods to transfer the $O(N)$-scaling from the physical system to the simulation algorithm. The most promising among them was to handle the pair-resistance matrices rather than their sum and account for the errors in a subsequent step. However, we did not succeed in deriving a systematic method. None of the physical implications behind the many-body resistance matrix could be exploited to deduce a more efficient algorithm than the one presented here. We conclude that the solution to this problem can most probably only be found in developing and applying other numerical techniques.

2.9 References

[06Ein] A. Einstein, "Eine neue Bestimmung der Moleküldimension", *Ann. Physik*, *19*, 289–306 (1906)

[11Ein] A. Einstein, "Berichtigung zu meiner Arbeit: Eine neue Bestimmung der Moleküldimension", *Ann. Physik*, *34*, 591–592 (1911)

[36Boe] J. H. de Boer, "The influence of van der Waals forces and primary bonds on binding energy, strength and orientation, with special reference to some artificial resins", *Trans. Farad. Soc.*, *32*, 10–38 (1936).

[37Ham] H. C. Hamaker, "The London-van der Waals attraction between spherical particles", *Physica*, *4*, 1058–1072 (1937).

[48Ver] E. J. W. Vervey and J. Overbeek, *Theory of the stability of lyophobic colloids*, Elsevier, Amsterdam (1948).

[66Kub] R. Kubo, "The fluctuation-dissipation theorem", *Rep. Prog. Phys.*, *29*(I), 255–284 (1966).

[72Hof] R. L. Hoffman, "Discontinuous and dilatant viscosity behaviour in concentrated suspensions", *Trans. Soc. Rheol.*, *16*, 155–173 (1972).

[72Lee] A. W. Lees and S. F. Edwards, "The computer study of transport processes under extreme conditions", *J. Phys. C: Solid State Phys.*, *5*(15), 1921 (1972).

[75Goo] J. W. Goodwin, *Colloid Science*, Vol. 2, Chemical Society, London, chapter: The rheology of dispersions (1975).

[75Mew] J. Mewis and R. de Bleyser, "Concentration effects in viscoelastic dispersions", *Rheol. Acta*, *14*(8), 721–728 (1975).

[78Fix] M. Fixman, "Simulation of polymer dynamics. I. General theory", *J. Chem. Phys.*, *69*, 1527–1537 (1978).

[78Sch] G. Schoukens and J. Mewis, "Nonlinear rheological behaviour and shear-dependent structure in colloidal dispersions", *J. Rheol.*, *22*(4), 381–394 (1978).

[78Wil] S. J. Willey and C. W. Macosko, "Steady shear rheological behavior of PVC plastisols", *J. Rheol.*, *22*(5) (1978).

[83Nap] D. H. Napper, *Polymeric stabilization of colloidal dispersions*, Academic Press, London (1983).

[84Bos] G. Bossis and J. F. Brady, "Dynamic simulation of sheared suspensions. I. General method", *J. Chem. Phys.*, *80*(10), 5141–5154 (1984).

[84Eu] B. C. Eu and Y. G. Ohr, "Theory of non-Newtonian viscosity and normal stress coefficients of fluids", *J. Chem. Phys.*, *81*(6), 2756–2770 (1984).

[84Jef] D. J. Jeffrey and Y. Onishi, "Calculation of the resistance and mobility functions for two unequal rigid spheres in low-Reynolds-number flow", *J. Fluid Mech.*, *139*, 261–290 (1984).

[85Bra] J. F. Brady and G. Bossis, "The rheology of concentrated suspensions of spheres in simple shear flow by numerical simulation", *J. Fluid Mech.*, *155*, 105–129 (1985).

[85Gar] C. W. Gardiner, *Handbook of stochastic methods of physics, chemistry and the natural sciences*, Springer, Berlin, 2nd ed. (1985).

[85Kam] M. R. Kamal and A. Mutel, "Rheological properties of suspensions in Newtonian and non-Newtonian fluids", *J. Polym. Eng.*, *5*(1), 293–382 (1985).

[85Pus] P. N. Pusey and R. J. A. Tough, *Dynamic light scattering: applications of photon correlation spectroscopy*, Plenum Press, New York, chapter: Particle interactions (1985).

[87All] M. P. Allen and D. J. Tildesley, *Computer simulation of liquids*, Clarendon Press, Oxford (1987).

[87Bir] R. B. Bird, R. C. Armstrong, and O. Hassager, *Dynamics of polymeric liquids*, Wiley-Interscience Pub., New York (1987).

[88Ack] B. J. Ackerson and P. N. Pusey, "Shear-induced order in suspensions of hard spheres", *Phys. Rev. Lett.*, *61*(8), 1033–1036 (1988).

[88Bra] J. F. Brady and G. Bossis, "Stokesian dynamics", *Ann. Rev. Fluid Mech.*, *20*, 111–157 (1988).

[88Pin] D. J. Pine, D. Weitz, P. M. Chaikin, and E. Herbolzheimer, "Diffusing-wave spectroscopy", *Phys. Rev. Lett.*, *60*(12), 1134–1137 (1988).

[88Wag] N. J. Wagner and G. G. Fuller, "The dichroism and birefringence of a hard-sphere suspension under shear", *J. Chem. Phys.*, *89*(3), 1580–1587 (1988).

[89Bar1] H. A. Barnes, J. F. Hutton, and K. Walters, *An introduction to rheology*, No. 3 in Rheology, Elsevier, Amsterdam, Netherlands (1989).

[89Bar2] H. A. Barnes, "Shear-thickening (dilatancy) in suspensions of nonaggregating solid particles dispersed in Newtonian liquids", *J. Rheol.*, *33*(2), 329–366 (1989).

[89Hun] R. J. Hunter, ***Foundations of colloid science***, Clarendon Press, Oxford (1989).

[89Rus] W. B. Russel, D. A. Saville, and W. R. Schowalter, ***Colloidal dispersions***, Cambridge Univ. Press (1989).

[89Wer] J. C. V. der Werff and C. G. de Kruif, "Hard-sphere colloidal dispersions: the scaling of rheological properties with particle size, volume fraction, and shear rate", ***J. Rheol.***, ***33***(3), 421–454 (1989).

[90Bha] D. Bhattacharia and E. Clementi, "Brownian dynamics simulations of a complex fluid system", MOTECC (1990).

[90Kli] Y. Klimontovich, "Itô, Stratonovich and kinetic forms of stochastic equations", ***Physica A***, ***163***(2), 515–532 (1990).

[90Wag] N. J. Wagner and W. B. Russel, "Light scattering of a hard-sphere suspension under shear", ***Phys. Fluids A***, ***2***(4), 491–502 (1990).

[90Wer] J. C. V. der Werff and C. G. de Kruif, "The rheology of hard-sphere dispersions: the micro-structure as a function of shear rate", ***Progr. Coll. Polym. Sci.***, ***81***, 113–119 (1990).

[91Isr] J. Israelachvili, ***Intermolecular and surface forces***, Academic Press, London, 2nd ed. (1991).

[91Kim] S. Kim and S. J. Karrila, ***Microhydrodynamics: principles and selected applications***, Butterworth-Heinemann series in Chemical Engineering, Stoneham MA (1991).

[91Kub] R. Kubo, M. Toda, and N. Hashitsume, ***Statistical physics II: nonequilibrium mechanics***, No. 31 in 'Solid-State Sciences', Springer, 2 ed. (1991).

[91Wag] N. J. Wagner, R. Krause, A. R. Rennie, B. D'Aguanno, and J. Goodwin, "The microstructure of polydisperse, charged colloidal suspensions by light and neutron scattering", ***J. Chem. Phys.***, ***95***(1), 494–508 (1991).

[92Boe] W. H. Boersma, J. Laven, and H. N. Stein, "Viscoelastic properties of concentrated shear thickening dispersions", ***J. Coll. Interf. Sci.***, ***149***(1), 10–22 (1992).

[92DHa] P. D'Haene, G. G. Fuller, and J. Mewis, ***Theoretical and applied rheology***, Elsevier, Amsterdam, Netherlands, chapter: Shear thickening effect in concentrated dispersions, pp. 595–597 (1992).

[92Jef] D. J. Jeffrey, "The calculation of the low Reynolds number resistance functions for two unequal spheres", ***Phys. Fluids A***, ***4***(1), 16–29 (1992).

[92Kli] Y. Klimontovich, "Alternative description of stochastic processes in nonlinear systems. 'Kinetic form' of master and Fokker-Planck equations", *Physica A*, *182*(1-2), 121–132 (1992).

[92Klo] P. E. Kloeden and E. Platen, ***Numerical solution of stochastic differential equations***, Springer, Berlin (1992).

[92Lau] M. H. Laun, R. Bung, S. Hess, W. Loose, O. Hess, K. Hahn, E. Hädicke, R. Hingmann, F. Schmidt, and P. Lindner, "Rheological and small angle neutron scattering investigation of shear-induced particle structures of concentrated polymer dispersions submitted to plane Poiseuille and Couette flow", *J. Rheol.*, *36*(4), 743–787 (1992).

[92Ngu] Q. D. Nguyen and D. V. Boger, "Measuring the flow properties of yield stress fluids", *Annu. Rev. Fluid Mech.*, *24*, 47–88 (1992).

[92Pre] W. H. Press, S. A. Teukolsky, W. T. Vetterling, and B. P. Flannery, ***Numerical recipes in fortran: the art of scientific computing***, Cambridge Univ. Press, 2nd ed. (1992).

[92Sch] J. D. Schieber, "Do internal viscosity models satisfy the fluctuation-dissipation theorem?", *J. Non-Newt. Fluid Mech.*, *45*, 47–61 (1992).

[92Bla] A. van Blaaderen, J. Peetermans, G. Maret, and J. K. G. Dhont, "Long-time self-diffusion of spherical colloidal particles measured with fluorescence recovery after photobleaching", *J. Chem. Phys.*, *96*(6), 4591–4603 (1992).

[93Hey] D. M. Heyes and J. R. Melrose, "Brownian dynamics simulations of model hard-sphere suspensions", *J. Non-Newt. Fluid*, *46*(1), 1–28 (1993).

[93Koe] J. M. V. A. Koeman and P. J. Hoogerbrugge, "Dynamic simulations of hard-sphere suspensions under steady shear", *Europhys. Lett.*, *21*(3), 363–368 (1993).

[93Mel] J. R. Melrose and D. M. Heyes, "Simulations of electrorheological and particle mixture suspensions - agglomerate and layer structures", *J. Chem. Phys.*, *98*(7), 5873–5886 (1993).

[93Wei] D. A. Weitz and D. J. Pine, ***Dynamic light scattering: the method and some applications***, Clarendon Press, Oxford, chapter: Diffusing-wave spectroscopy (1993).

[94Che] L. B. Chen, B. J. Ackerson, and C. F. Zukoski, "Rheological consequences of microstructural transitions in colloidal crystals", *J. Rheol.*, *38*(2), 193–216 (1994).

[94Hey1] M. D. Heyes and P. J. Mitchell, "Linear viscoelasticity of concentrated hard-sphere dispersions", *J. Phys.: Condens. Matter*, *6*(32), 6423–6436 (1994).

[94Hey2] M. D. Heyes and P. J. Mitchell, "Self-diffusion and viscoelasticity of dense hard-sphere colloids", *J. Chem. Soc. Farad. Trans.*, *90*(13), 1931–1940 (1994).

[95Bal] R. C. Ball and J. R. Melrose, "Lubrication breakdown in hydrodynamic simulations of concentrated colloids", *Adv. Coll. Interf.Sci.*, *59*, 19–30 (1995).

[95Ben] J. W. Bender and N. J. Wagner, "Optical measurement of the contributions of colloidal forces to the rheology of concentrated suspensions", *J. Coll. Interf. Sci.*, *172*(1), 171–184 (1995).

[95Bra] J. F. Brady and M. Vivic, "Normal stresses in colloidal dispersions", *J. Rheol.*, *39*(3), 545–566 (1995).

[95Cho] M. K. Chow and C. F. Zukoski, "Nonequilibrium behaviour of dense suspensions of uniform particles: volume fraction and size dependence of rheology and microstructure", *J. Rheol.*, *39*(1), 33–60 (1995).

[95Hey] D. M. Heyes and P. J. Mitchell, "Nonequilibrium molecular and Brownian dynamics simulations of shear thinning of inverse power fluids", *Mol. Phys.*, *84*(2), 261–280 (1995).

[95Mac] M. E. Mackay and B. Kaffashi, "Stress jumps of charged colloidal suspensions, measurement of th elastic-like and viscous-like stress components", *J. Coll. Interf. Sci.*, *174*, 117–123 (1995).

[95Mas] T. G. Mason and D. A. Weitz, "Optical measurements of frequency-dependent linear viscoelastic moduli of complex fluids", *Phys. Rev. Lett.*, *74*(7), 1250–1253 (1995).

[96Ben] J. W. Bender and N. J. Wagner, "Reversible shear thickening in monodisperse and bidisperse colloidal dispersions", *J. Rheol.*, *40*(5), 899–916 (1996).

[96But] S. Butler and P. Harrowell, "Shear induced ordering in simulations of colloidal suspensions: oscillatory shear and computational artefacts", *J. Chem. Phys.*, *105*(2), 605 (1996).

[96Cla] S. M. Clarke and A. R. Rennie, "Ordering and structure at interfaces of colloidal dispersions under flow", *Farad. Discuss.*, *104*, 49–63 (1996).

[96Dho] J. K. G. Dhont, *An introduction to dynamics of colloids*, Vol. 2 of *Studies in interface science*, Elsevier (1996).

[96Mel] J. R. Melrose, J. H. van Vliet and R. C. Ball, "Continuous shear thickening and colloid surfaces", *Phys. Rev. Lett.*, *77*(22), 4660–4663 (1996).

[96Ött] H. C. Öttinger, ***Stochastic processes in polymeric fluids***, Springer, Berlin (1996).

[96Phu] T. N. Phung, J. F. Brady, and G. Bossis, "Stokesian dynamics simulation of Brownian suspensions", *J. Fluid Mech.*, *313*, 181–207 (1996).

[96Ras] S. R. Rastogi, N. J. Wagner, and S. R. Lustig, "Rheology, self-diffusion and microstructure of charged colloids under simple shear by massively-parallel nonequilibrium Brownian dynamics", *J. Chem. Phys.*, *104*(22), 9234–9248 (1996).

[97Bal] R. C. Ball and J. R. Melrose, "A simulation technique for many spheres in quasi-static motion under frame-invariant pair drag and Brownian forces", *Physica A*, *247*, 444–472 (1997).

[97Boe] E. S. Boek, P. V. Coveney, H. N. W. Lekkerkerker, and P. van der Schoot, "Simulating the rheology of dense colloidal suspensions using dissipative particle dynamics", *Phys. Rev. E*, *55*(3), 3124–3133 (1997).

[97Dux] C. Dux and H. Versmold, "Light diffraction from shear-ordered colloidal dispersions", *Phys. Rev. Lett.*, *78*(9), 1811–1814 (1997).

[97Git] F. Gittes, B. Schnurr, P. D. Olmstedt, F. C. MacKintosh, and C. F. Schmidt, "Microscopic viscoelasticity: shear moduli of soft materials determined from thermal fluctuations", *Phys. Rev. Lett.*, *79*(17), 3286–3289 (1997).

[97Mas1] T. G. Mason, H. Gang, and D. A. Weitz, "Diffusing-wave-spectroscopy measurements of viscoelasticity of complex fluids", *J. Opt. Soc. Am.*, *14*(1), 139–149 (1997).

[97Mas2] T. G. Mason, K. Ganesan, J. H. van Zanten, D. Wirtz, and S. C. Kuo, "Particle tracking microrheology of complex fluids", *Phys. Rev. Lett.*, *79*(17), 3282–3285 (1997).

[97Rag] S. R. Raghavan and S. A. Khan, "Shear-thickening response of fumed silica suspensions under steady oscillatory shear", *J. Coll. Interf. Sci.*, *185*, 57–67 (1997).

[97Ras] S. R. Rastogi and N. J. Wagner, "Quantitative predictions of suspension rheology by nonequilibrium Brownian dynamics and hydrodynamic preaveraging", *J. Rheol.*, *41*(4), 893–899 (1997).

[97Tse] R. Tsekov, "Stochastic equations for thermodynamics", *Farad. Trans.*, *93*(9), 1751–1753 (1997).

[97Wat] H. Watanabe, M. Yao, K. Osaki, T. Shikata, H. Niwa, and Y. Morishima, "Nonlinear rheology of a concentrated spherical silica suspension", *Rheol. Acta*, *36*(5), 524–533 (1997).

[98Dux] C. Dux, S. Musa, V. Reus, H. Versmold, D. Schwahn, and P. Lindner, "Small angle neutron scattering experiments from colloidal dispersions at rest and under shear conditions", *J. Chem. Phys.*, *109*(6), 2556–2561 (1998).

[98Hof] R. L. Hoffman, "Explanations for the cause of shear thickening in concentrated colloidal suspensions", *J. Rheol.*, *42*(1), 111–123 (1998).

[98Kal] J. Kaldasch, J. Laven, and H. N. Stein, "Shear thickening as a consequence of an acoustic resonance in sheared colloidal crystals", *J. Rheol.*, *42*(6), 1285–1301 (1998).

[98Kas] A. Kasper, E. Bartsch, and S. H., "Self-diffusion in concentrated colloid suspensions studied by digital video microscopy of core-shell tracer particles", *Langmuir*, *14*, 5004–5010 (1998).

[98Wag] N. J. Wagner, "Rheo-optics", *Curr. Opinion in Coll. & Interf. Sci.*, *3*(4), 391–400 (1998).

[98Wat] H. Watanabe, M. Yao, K. Osaki, T. Shikata, H. Niwa, Y. Morishima, N. P. Balsara, and H. Wang, "Nonlinear rheology and flow-induced structure in a concentrated spherical silica suspension", *Rheol. Acta*, *37*(1), 1–6 (1998).

[98Wil] A. W. Willemse, H. G. Merkus, and B. Scarlett, "Development of a heterodyne photon correlation spectroscopy measuring probe for highly concentrated dispersions", *J. Coll. Interf. Sci.*, *204*(2), 247–255 (1998).

[98Xu] R. Xu, "Shear plane and hydrodynamic diameter of microspheres in suspension", *Langmuir*, *14*, 2593–2597 (1998).

Chapter 3

Coagulation

Abstract

The focus of Chapter 3 is on the destabilization of colloidal suspensions. After a brief introduction into the field of unstable suspensions (section 3.1), we motivate and discuss the necessary modifications (e.g. the handling of bonds) to the simulation algorithm from Chapter 2. In the following, the influence of solid content and surface potential is studied. The simulation results are presented with special emphasis on characteristic coagulation times and reaction rates on one hand (section 3.3) and on the development of the network structure on the other hand (section 3.4).

3.1 Introduction

The connection between the particle interaction potential and the colloidal stability will be illustrated at the beginning of this introduction (subsection 3.1.1). The coagulation of the suspension, which can be provoked by an appropriate change in the interaction potential, is then discussed in subsection 3.1.2. It includes a description of experiments, models, and simulations which try to establish a link between the change in the interparticle potential and the coagulation kinetics of the suspension. The characterization of the particle network structure in subsection 3.1.3 concludes this introduction. The reader is referred to "Introduction to Modern Colloid Science" [93Hun] or to "Particle Deposition and Aggregation" [95Eli] for more information.

3.1.1 Colloidal Stability

The liquid-solid transition in colloidal suspensions is induced by changing the interaction potential between the particles. This is in contrast to atomic systems, where the phase transition is usually caused by a change in pressure or in temperature for fixed interaction potential between the single atoms. Since the interaction between colloidal particles depends on parameters such as pH, ionic strength, and characteristics of the surfactant, the criterion for the stability of the suspension is to be given in terms of these quantities. In this introduction we will concentrate on electrostatically stabilized suspensions because no sterically stabilized suspensions are examined in this study.

For electrostatically stabilized suspensions, the total interaction potential is given (according to the DLVO-theory) by the sum of the van der Waals attraction V^{vdW} and the double layer repulsion V^{el} :

$$V^{\mathrm{DLVO}} = V^{\mathrm{vdW}} + V^{\mathrm{el}} \tag{3.1}$$

It can be seen from the corresponding expressions (2.4-5) that the van der Waals attraction increases dramatically for close particles whereas the double layer repulsion remains finite. This illustrates that the total interaction potential V^{DLVO} is always attractive at short particle separations. But how can a system be stable if the interaction potential has its absolute minimum for touching particles? The answer is that stable suspensions coagulate at such a low rate that they can practically be considered as being stable for the following reason: from equilibrium statistical mechanics it is known that in a system at a temperature T, the characteristic energy scale is set by the thermal energy $k_{\mathrm{B}}T$. Particles can only surmount energy barriers with a reasonable probability if the thermal energy fluctuations are of the same order of magnitude. If the energy barrier is much larger, as for a stable suspension, the rate of particles to surmount the energy barrier is very low, not to say practically zero. The stability of dilute colloidal suspensions has been found to be adequately described by the stability ratio W [95Eli]. This is the ratio between the number of collisions between particles and the number of collisions which result in an overcoming of the energy barrier. One can show that

$$W = d\int_{d}^{\infty} \exp\left[\frac{V^{\mathrm{DLVO}}(r)}{k_{\mathrm{B}}T}\right] h(r)\ \frac{dr}{r^2} \qquad (3.2)$$

The particle radius is denoted by d, r is the center-to-center separation between two particles. Hydrodynamic interactions are accounted for in the function $h(r)$ where $h = 1$ if hydrodynamic interaction is neglected [71Hon]. The stability ratio is normalized to $W = 1$ for non-interacting colloidal particles. One finds $W \gg 1$ for strongly repelling particles with a high energy barrier. Although stable and unstable suspensions can be distinguished only relatively by their rate of coagulation as mentioned above, $W \approx 10$ is a good estimate of the separation between them [89Rus].

Eqn. (3.2) accounts for the full interaction potential. For strongly repelling particles, a reduced version can be obtained when noting that the integral is dominated by the energy barrier $\Delta_{\mathrm{t}}E$ in the interaction potential (Fig. 3.1(a-b)). This leads to stability ratios that depend only on the height of the energy barrier in units of the thermal energy [54Ree, 83Ben, 84Dic].

An alternative method to characterize the stability of colloidal suspensions is to reduce the full interaction potential to two parameters, not only for strongly repelling particles but for particles interacting arbitrarily: the energy barriers $\Delta_{\mathrm{t}}E$ and $\Delta_{\mathrm{r}}E$. Fig. 3.1. shows different pair interaction potentials and their corresponding energy barriers $\Delta_{\mathrm{t}}E$ and $\Delta_{\mathrm{r}}E$. The ***total*** energy barrier $\Delta_{\mathrm{t}}E$ is equal to the local maximum. It indicates whether thermal excitation is necessary that particles which approach from infinity (① in (a-d)) can reach the primary minimum (③ in (a-d)). The ***relative*** energy barrier $\Delta_{\mathrm{r}}E$ measures the energy difference between the secondary minimum (② in (b-c)) and the local maximum. If the relative energy

barrier $\Delta_r E$ is larger than zero, particles which are captured in the secondary minimum can reach the primary minimum only by thermal excitation. The criterion for stability of the suspension in terms of the reduced energy barrier formulation is that (i) there is no secondary energy minimum and that (ii) the total energy barrier is much larger than the thermal energy $\Delta_t E \gg k_B T$.

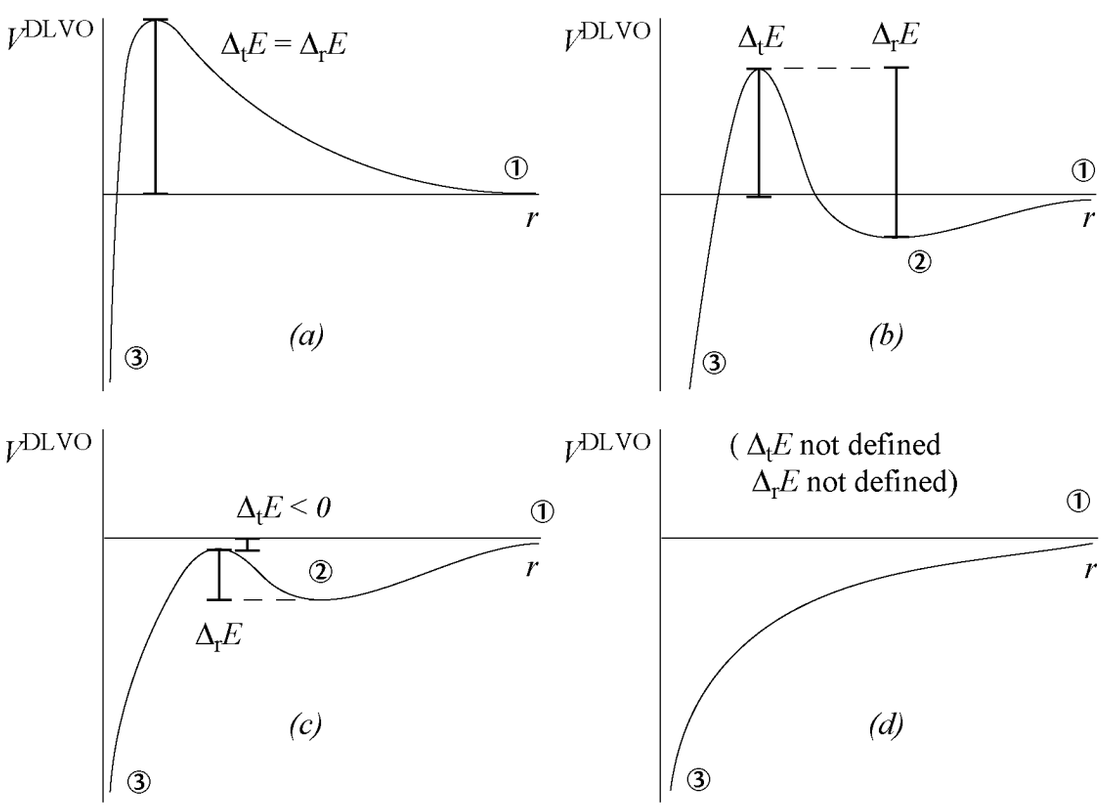

Fig. 3.1: Typical DLVO-interaction potentials and the corresponding energy barriers. Particle positions of special interest: ① far separation, ② secondary minimum, ③ primary minimum. The potentials correspond to the following situations: (a) stable suspension (if $\Delta_t E \gg k_B T$), (b) weak bonds in secondary minimum, (c) weak bonds in secondary minimum and strong bonds in primary minimum, (d) only strong bonds in primary minimum.

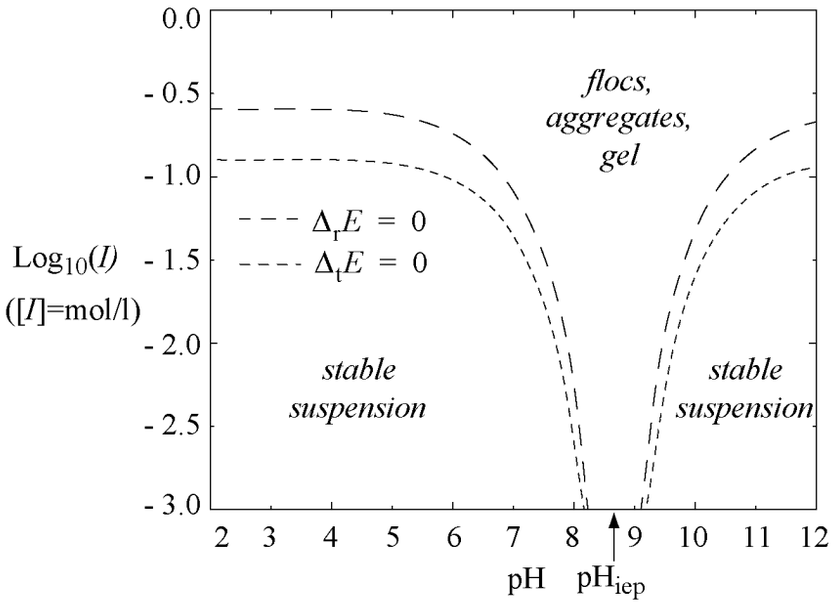

Fig. 3.2: Stability regions for an Al_2O_3-suspension for which the isoelectric point is $pH_{iep} = 8.7$. The particle diameter is $d = 0.5$ μm. The ionic strength is denoted by I.

The stability ratio defined in eqn. (3.2) or the corresponding criteria on the energy barriers $\Delta_t E$ and $\Delta_r E$ can be used to determine the stability of the suspension depending on the pH and on the ionic strength I. Fig. 3.2 shows the stability regions for an Al_2O_3 suspension, which has the isoelectric point, i.e. the pH of no electric double layer repulsion, at $pH_{iep} = 8.7$. The surface potential is assumed to obey the Nernst equation of the form $\psi_0 = 2.303\,(k_B T/e)\,(pH_{iep} - pH)$ [93Hun].

Even though the DLVO-potential and the stability criteria (ratio W and energy barriers $\Delta_t E$ and $\Delta_r E$) may not agree exactly with the real system due to the high solid contents under consideration, the following characteristics can be read from Fig 3.2. Around the isoelectric point, where the total surface charge is zero, the surface potential is low and the double layer repulsion is weak, which leads to coagulation. Further away from the isoelectric point, the surface potential increases. If the ionic strength is high, the double layer is compressed so that electrostatic repulsion is too weak to oppose the van der Waals attraction sufficiently which leads to coagulation. The suspension is only stable at lower ionic strengths where the double layer is thick enough. Therefore it is the combination of relatively high surface potential and low ionic strength which results in a stable suspension.

One concludes from Fig. 3.2 that there are two ways to destabilize a colloidal suspension: either through increase in ionic strength or through a shift of the pH towards the isoelectric point. Both are used nowadays in ceramic processing techniques [94Gra, 99Bal].

3.1.2 Coagulation Kinetics

Besides the interaction potential, also the solid content has a profound influence on the resulting structure of the particle network. A critical value is the percolation threshold ϕ_{perc} which is the limit below which no space-filling network can be built. Below the threshold, the destabilized suspension forms loose flocs whereas above the threshold at a percolating network is built. For a detailed discussion the reader is referred to the book "Fractal Growth" by Viscek [92Vis] and to Chapter 8 therein in particular.

In dilute suspensions, the formation of particle clusters is well described by the Smoluchowski approach. It formulates rate equations for the formation of clusters with given size. If n_k denotes the number of clusters consisting of k primary colloidal particles, the Smoluchowski equation reads [87Son, 95Eli]

$$\frac{dn_k}{dt} = \left(\frac{1}{2} \sum_{\substack{i=1 \\ i+j=k}}^{k-1} K_{ij} n_i n_j \right) - n_k \left(\sum_{i=1}^{\infty} K_{ik} n_i \right) \qquad (3.3)$$

The second order rate constants K_{ij} may depend on a number of factors, such as on the sizes of particles and on the transport mechanisms. The first term on the right hand side of eqn. (3.3) represents the formation of k-fold clusters by the collision of two smaller clusters, such that $i + j = k$. The second term stands for the recombination of k-fold clusters with any other clusters which leads to a decrease in the population n_k. The solution of eqn. (3.3) crucially depends on the choice for the reaction constants as analytical studies [86Ern] and computer simulations have shown [88Mea1, 88Mea2].

The cluster size distribution measured in scattering experiments showed that the Smoluchowski approach is a fair representation of the real system in the dilute regime, i.e. at solid contents $\phi < 1$ vol % [86Wei, 87Cam, 96Bar].

The situation in non-dilute suspensions is more complicated. The applicability of the Smoluchowski equation is in principle limited by the following restrictions. First, it seems to hold only for the early stages of the coagulation process: The mobility of the small clusters is only weakly influenced by the presence of the other clusters. The effect of interpenetrating clusters after longer times can only be included in the rate constants K_{ij} which is a difficult problem. A further difficulty is the occurrence of triple and even higher order collision events which are not considered in eqn. (3.3) as well. Despite these restrictions, the Smoluchowski equation has been applied for systems with $\phi \leq \phi_{perc}$ and even $\phi > \phi_{perc}$ [83Hen, 87Mar]. For example, it was possible to determine critical exponents for the diverging cluster mass and cluster radius near the gelation time. Although the

Smoluchowski equation (3.3) can also be applied to non-dilute systems, such models still fail to establish a link between their predictions and the equations of motions for the particles (2.12) on the microscopic level.

A good selection of the characteristics monitored during coagulation is essential. It is questionable whether the populations n_k of k-fold particles are the only useful parameters to study the coagulation process in non-dilute systems. One would also need quantities which characterize the development of the network on a finer level, e.g. coordination number and bond angle distribution. The identification of the relevant quantities will be discussed in more detail in the subsections 3.3 and 3.4, where the simulation results are presented.

Generally, one can say that the results from modeling and from experiments are further apart for dense suspensions than for dilute suspensions. This was one of the reasons for using the Brownian dynamics simulation technique in this study. It allows us to study the coagulation behavior on the basis of the particle dynamics. Thereby, a direct link between the destabilizing interaction potential and the resulting network structure can be established.

3.1.3 Structure of the Particle Network

The destabilization of a colloidal suspension leads to the formation of bigger units, which range from loose flocs at low solid contents to percolating particle networks at high solid contents.

At low solid contents, the flocs (Fig. 3.3(a)) are fractal objects, where the fractal dimension depends on the interaction potential, i.e. on the sticking probability between particles. In so-called 'fast' aggregation, where any two approaching particles are bonded, the structure is open and has a low fractal dimension ($d_f \approx 1.8$). In contrast, 'slow' aggregating systems with sticking probability less than 1 allow the particles to penetrate deeper into the already existing structure leading to denser systems with relatively high fractal dimension ($d_f \approx 2.1$). The fractal dimensions calculated from lattice models and from computer simulations [88Mea1, 88Mea2, 95Mea] are in good agreement with the values determined in scattering experiments [84Wei, 85Wei, 86Wei, 87Cam, 97Bur]. Thus, the floc structure in dilute coagulating systems can be considered as being well known.

For solid contents in the range of the percolation threshold ϕ_{perc} or above, the structure of the particle configuration changes drastically. Fractal scaling on all length scales of the particle configuration must break down for really dense systems because there is simply not enough room for stringy open structures to grow. The particles form a space-filling network (Fig. 3.3(b)). This structure can be examined with three different spacial resolutions [87Dic]. First, on the scale of a few particle diameters the particle configuration is very heterogeneous due to only short range order and due to the excluded volume effects (small circle in Fig. 3.3(b)). Second, in an intermediate regime the network shows fractal properties. This has been observed both in experiments [86Sch, 87Hor, 92Bre] and in simulations [95Bij, 97Whi]. However, in highly dense systems the fractal regime may be missing at all as simulations have shown [96Bos]. And third, when resolving only very long length scales the network looks uniform and homogenous and no structure can be detected. This is because the average pore size is at most a few particle diameters and therefore too small to be resolved.

In order to determine the structures of the clusters and of the final percolating network in dense suspensions, we use the Brownian dynamics simulation technique. In contrast to current experimental techniques, it allows to 'construct' the structure from fundamental equations of motion, rather that vice versa.

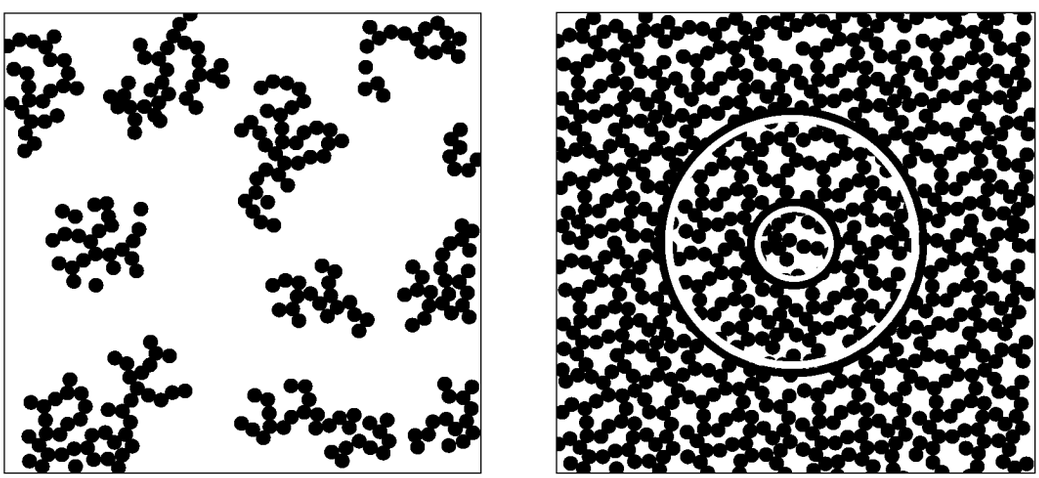

(a) Flocs ($\phi < \phi_{perc}$)

(b) Network, Gel ($\phi \geq \phi_{perc}$)

Fig. 3.3: Schematic two-dimensional representation of the particle configurations in a destabilized suspension far below and above the percolation threshold ϕ_{perc}: (a) flocs for $\phi < \phi_{perc}$, (b) space-filling network for $\phi \geq \phi_{perc}$. The circles in (b) indicate the different length scales in the percolated network.

3.2 Simulation Details

The simulation algorithm which has been used to study the coagulation in dense colloidal suspensions is based on the predictor-corrector scheme explained in section 2.2 for stable suspensions. This section presents the necessary modifications and details of the simulation algorithm used to study the destabilization process. It begins with a description of the routine to handle touching particles. In the following the reason for neglecting many-body hydrodynamics is given. Since the choice of thermodynamic variables is crucial when studying phase transitions, it is explained why constant-volume simulations are appropriate for studying the liquid-solid transition in colloidal suspensions. The subsection concludes with a list of the simulation input, in particular interaction potential and starting configuration.

3.2.1 Rigid versus Stiff Bonds

It has been mentioned in the previous subsection that the absolute minimum in the van der Waals interaction is at the separation $r = d$, i.e. for touching particles. Therefore, the destabilization of the suspension leads to a very close approach of particles. However, a regulative mechanism which would account for the rigidity of the particles (i.e. for the excluded volume) is not included in the DLVO-interaction. Therefore, once the particles are in the range of the dominant attractive force at small separations, the enormous force leads to overlapping particles. One can formally account for the excluded volume of particles by setting the potential for overlap to infinity

$$V(r) \equiv \infty \qquad (r < d) \tag{3.4}$$

This definition cannot be used in computer simulations and other ways must be found to handle the problem of touching, but non-overlapping particles. In the following, several methods are illustrated, some of which introduce ***rigid*** bonds, whereas others use only very ***stiff*** bonds.

a) Rigid Constraints

The diverging van der Waals attraction and the non-overlap condition for the particles suggest the particle separation for bonded particles is ***exactly*** equal to the particle diameter $r = d$. Imagine two particles that come into contact. By the constraint $r = d$, the number of degrees of freedom is reduced: both of the single particles have three translational degrees of freedom each, but the particle doublet has only three translational (x, y, z) plus two rotational (θ, φ) degrees of freedom (Fig. 3.4(a)). This means that the equations of motion have to be adjusted by either introducing constraint forces or generalized coordinates (for a detailed dis-

cussion see [95Gra, 96Ött]). As the coagulation of the whole suspension proceeds, more and more constraints have to be introduced into the equations of motion. When studying samples which contain several thousands of particles, this method is clearly unfeasible due to the enormous computational effort. An approximate version of these rigid constraints is realized in the SHAKE-algorithm [77Ryc, 84All, 92Pre] which is an iterative procedure to account for the constraints within a certain small tolerance. Nevertheless, it is computationally very time-consuming as well.

b) Separate Displacement

Another possibility to account for bonded particles is shown in Fig. 3.4(b). Once two particles are in the primary minimum, i.e. are very close, a separate displacement is introduced into the equations of motion. It moves both particles symmetrically such that the actual surface-to-surface separation is reduced by a factor 2. In the ideal situation of particles in contact, the surface-to-surface separation should be reduced to zero. However, this would be a very crude correction on the configuration because it may lead to complications with other neighbors which are attached to one of the two particles under consideration.

This algorithm has the advantage of being very efficient and has therefore been chosen in our simulations. The main drawback is that in late stages of the coagulation process the high number of neighbors to each particle leads to a strong coupling of different constraints. In particular for loops of particles, this occasionally leads to an increased number of correction steps needed. In our simulations the tolerance for applying the above algorithm was

$$\varepsilon_{\mathrm{tol}} \equiv \frac{|r-d|}{d} = 0.01 \qquad (3.5)$$

If the relation $|r-d|/d < \varepsilon_{\mathrm{tol}}$ was not respected for any two bonded particles, the particle configuration was subjected to the above procedure without propagating the system. In other words, in this 'relaxation' step only the bond-displacements and no displacements due to Brownian motion or interaction forces are acting. The performance of this algorithm in our simulations is discussed in subsection 3.2.5.

c) Constraining Force

The 'rigid constraints' algorithm leads to correct equations of motion because it does not depend on the integration step size. The method just described above clearly fails to have this property as the size of the corrector displacements does not depend on the time step of integration but only on the current geometrical situation. It can therefore not be reinterpreted as an additional force contribution to the equations of motion. Such a force would be a spring force around $r = d$ (Fig. 3.4(c)). The choice of the spring constant f is then regulating the efficiency of

this regulator force. We note that in the above 'separate displacement' method which we use in our simulations, we would have $f \sim \Delta t^{-1}$ what obviously does not correspond to a physical force.

d) 'No-sliding' Constraint

All three procedures discussed above in principle consider the bonds only on the two-particle level. If a particle is attached to more than two neighbors, questions about the variability of the bond angles arise in addition to the excluded volume restriction. Fig 3.4(d) shows three particles where the sites of initial bond formation are denoted by small dots. If high friction prevents the particles from sliding on each other, the bond angle θ between the bond sites would remain constant. An algorithm has been proposed which holds the bond angles approximately constant and only allows small deviations, i.e. the separation distance between two initial bond sites δ is limited [94Dic, 97Whi] (Fig. 3.4(d)).

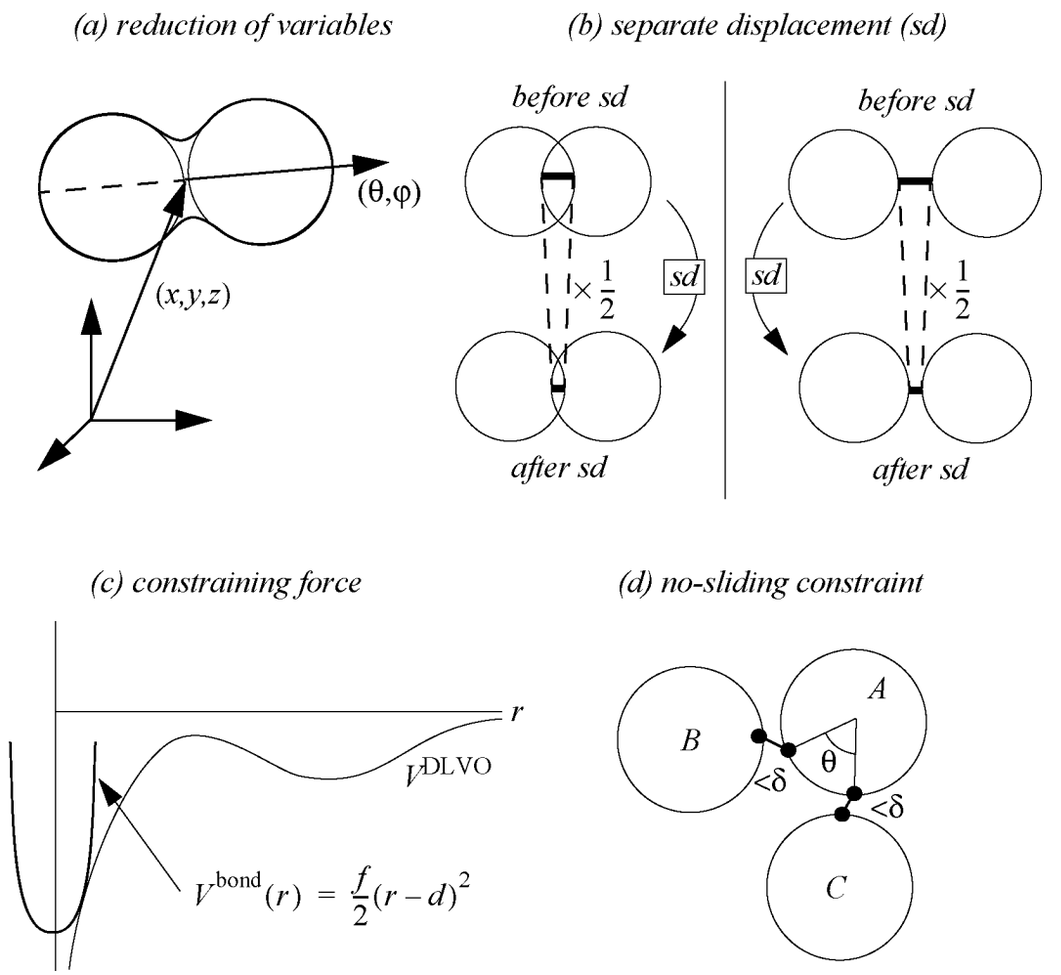

Fig. 3.4: Illustration of different mechanisms to handle touching particles: (a) exact and (b, c) approximate methods for treating particle separation as constant; (d) method to keep the bond angles fixed.

In our simulation, no constraints have been imposed on the bond angles because we expect essential contributions in gel-aging from changes in bond angles. Nevertheless, the real colloidal system exhibits friction which prevents the particles from freely sliding over each other. Therefore, a proper treatment should be intermediate between fixing the bond angles and the freely sliding particles.

3.2.2 Neglecting Hydrodynamic Interaction

The substantial part of Chapter 2 was devoted to include the many-body hydrodynamic lubrication forces which are responsible for shear thickening at high shear rates. It is clear that they are also present under equilibrium conditions and should in principle be accounted for in the destabilization process [90Dic].

Simulations have shown that long-range hydrodynamic interactions have a substantial effect on the sedimentation of aggregates but are much less important for processes where Brownian forces dominate [87Ans1]. Studies on the rheology of aggregated systems have shown that including the short-range lubrication forces is difficult [97Sil].

In this study on the coagulation of dense colloidal suspensions, many-body hydrodynamic interactions have not been included for the following two reasons.

Firstly, it is not completely clear in which way one should account for hydrodynamic interaction between touching particles. Apart from the lubrication approximation, two particles which roll over each other should experience some hindrance due to the viscous and incompressible solvent.

The second reason why hydrodynamic interactions are not considered here is that results on large systems cannot be obtained within reasonable time on the hardware at our disposal. In contrast to the simulations of stable suspensions, the configuration of particles changes while the simulation proceeds: the system is not in a steady state but undergoes a phase transition. Structural information such as correlation functions can therefore only be obtained from a simple snapshot of the process and not by averaging over different times. In order to get statistically relevant results, one can either do several simulations under exactly the same conditions or one can do just one simulation but with a very large number of particles. The latter possibility has been chosen in this study. Nevertheless, both methodologies require a lot of computation time, whether hydrodynamic interactions are included or not.

3.2.3 Liquid-Solid Transition at Constant Volume

Special care must be taken to the choice of thermodynamic variables when studying phase transitions. In particular, we here discuss the choice between the sample volume V and the pressure p. Usually, either of the two is held constant during the transition where the change in the other is adjusted by the system itself.

In computer simulations it is much simpler to fix the sample volume, i.e. the volume of the simulation box, than the external pressure. It is shown in the following that constant volume simulations are appropriate for studying the liquid-solid transition in colloidal suspensions, even if the experiment in the laboratory are carried out at constant (air) pressure.

Fig. 3.5 gives a schematic representation of the destabilization process. The total volume of particles plus solvent is constant over the transition. There is no change even if the ***particle network*** shrinks (b) or fills the whole simulation cell (c), i.e. percolates. Assuming constant volume does therefore ***not*** impose a restriction on the possibility of shrinkage, usually referred to as syneresis, of the particle network. The occurrence or absence of network syneresis will rather be a result of our simulations.

There are only two reasons for a change in the total volume in the real system: chemical processes and drying. For example, the Direct Coagulation Casting process [94Gra] uses the decomposition of urea to destabilize the suspension. This

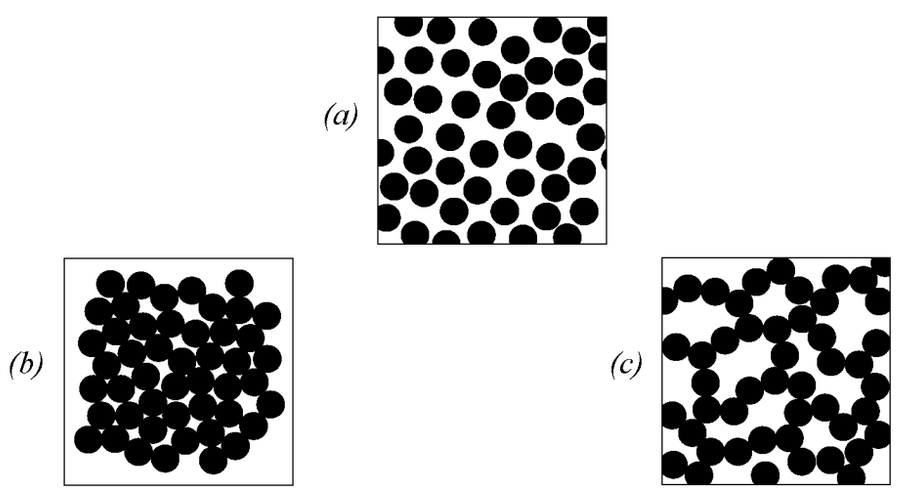

Fig. 3.5: Possible pathways of coagulation in a dense suspension (a): shrinking (b) and non-shrinking (c) network. Both conserve the total volume.

chemical reaction is associated with a change in volume which has also been observed in experiments [99Hel]. Solvent evaporation is also a common origin for the loss in sample volume and shall not be considered in this study.

3.2.4 Simulation Input

The input parameters for the simulation can be divided into physical parameters and in parameters which originate from the numerical implementation on a computer. On the one hand, the physical parameters describe the particles, their interaction, and the suspending solvent. On the other hand, the numerical input deals with the integration steps, the linked-cell list algorithm and the starting configuration. Although most of the parameters are the same as in the previous chapter, they are all listed here for completeness.

a) Interaction Potential

The parameters for the interaction potential given by eqn. (2.4-5) are listed in Table 3.1. The readers attention shall be drawn to the values for the surface potential ψ_0 and the inverse Debye screening length κ. The range of the surface potential and the value for the screening length are chosen so that some of the corresponding interaction potentials include a secondary minimum (Fig. 3.6).

Parameter	Symbol	Value	Units (SI)
Hamaker Constant of Al_2O_3 in Water	A_H	$4.76\ 10^{-20}$	J
Particle Diameter	d	$5\ 10^{-7}$	m
Relative Dielectric Constant of Water	ε_r	81	-
Absolute Temperature	T	293	K
Valency of Ions	z	1	-
Surface Potential	ψ_0	0.0 to 0.015	V
Inverse Debye Screening Length	κ	10^{+8}	m^{-1}

Table 3.1: Potential parameters for the coagulating suspension.

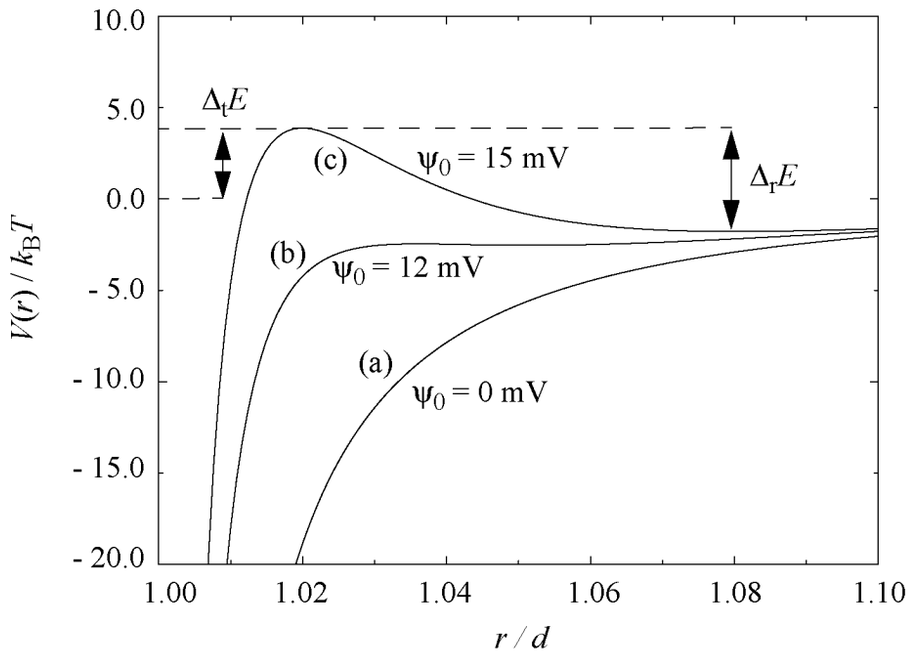

Fig. 3.6: DLVO-interaction for different surface potentials: (a) pure van der Waals attraction, (b) lowest surface potential at which an energy barrier occurs, (c) highest energy barrier.

With the corresponding parameters from Table 3.1, the surface potential $\psi_0 = 12$ mV is the lowest at which an energy barrier occurs. Table 3.2. lists the relation between the energy barriers $\Delta_r E$ and $\Delta_t E$ and the surface potential ψ_0.

ψ_0 (mV)	0 - 11.0	12.0	12.5	13.0	13.5	14.0	14.5	15.0
$\Delta_r E$ ($k_B T$)	0	0.076	0.522	1.20	2.07	3.01	4.31	5.65
$\Delta_t E$ ($k_B T$)	0	-2.46	- 1.81	-0.977	0.015	1.15	2.45	3.87

Table 3.2: Energy barriers $\Delta_r E$ and $\Delta_t E$ as a function of surface potential ψ_0.

As for the stable suspensions in Chapter 2, we introduce a cut-off in the potential at $r_{cutoff} = 1.8\,d$. The interaction potential for larger separation is set to zero. We note that for all surface potentials under consideration the descent towards the primary minimum is already present at separations of $r/d \approx 1.01$. Therefore, the value $\varepsilon_{tol} = 0.01$ (see eqn. (3.5)) for the bond length variability is suitable for

the simulations in this study. Throughout this study it is assumed that particles in the primary minimum cannot be separated, i.e. that a "primary bond" is unbreakable and holds for ever.

b) Solvent

The viscosity value used in all simulations is $\eta_s = 10^{-3}$ Pa s , which corresponds to the viscosity of water at room temperature. No flow field was imposed on the system which reads in the equations of motion as $\boldsymbol{v}^{\infty} \equiv 0$.

c) System Size and Linked-Cell List Algorithm

All simulations in this section were performed with $N = 8'000$ particles. The cubic simulation box was subdivided into cubic cells for the linked-cell list algorithm. The number of cells in each of the x-, y- and z-direction was chosen to be `Ncell` = 12. In total, the simulation box consisted of `Ncell`^{3}=1728 small cells, leading to approximately 4.63 particles per cell on average.

For a fixed number of particles N and particle diameter d, the solid content ϕ of the suspension is tuned by varying the size of the cubic simulation box. The box length `Lbox` is then given by equating the given solid content to the ratio of particle volume and suspension volume

$$\phi = \frac{N d^3 \pi / 6}{\texttt{Lbox}^3} \tag{3.6}$$

The simulations in this study have been performed at nine different solid contents in the range $0.2 \le \phi \le 0.4$ with steps of $\Delta\phi = 0.025$. For all solid contents, the length `Lcell` of the linked-cells

$$\texttt{Lcell} = \frac{\texttt{Lbox}}{\texttt{Ncell}} \tag{3.7}$$

was smaller than the interaction range r_{cutoff} of the potential, which is a necessary condition as mentioned in subsection 2.2.3.

d) Integration Steps

The time step used for all coagulation runs was smaller than that for the stable suspension. The 'separate displacement'-algorithm which accounts for the touching particles becomes inefficient if the particle displacements ($\Delta \boldsymbol{r}_t$ in eqn. (2.14)) are getting too large. The following value for the integration step has been used

$$\Delta t = 10^{-6} \text{ s} \approx 2 \cdot 10^{-5} \, \tau_{\text{Br}} \tag{2.8}$$

τ_{Br} denotes the characteristic Brownian time scale according to subsection 2.3.1. The number of integration steps was not limited in advance. The system could evolve until all particles were part of the same cluster. This was the criterion for stopping the simulation.

e) Starting Configurations

The previous chapter has shown that the stable suspensions show a tendency to order due to strong electrostatic repulsion of the DLVO-potential. All starting configurations used in this chapter for the destabilization study were well equilibrated and non-crystalline. They were generated by an equilibrium simulation with a short range but strongly repulsive Yukawa-potential $V(r) \sim (1/r)\ \exp(r/r_0)$. The latter has been preferred over the DLVO-potential, because it is difficult to tune the DLVO-parameters in such a way that the suspension does not crystallize at a solid content as high as $\phi = 0.4$. The primary interest was to start with non-crystalline configurations for all solid contents in order to achieve a better comparison among the different simulations.

The starting configurations were then subjected to the equations of motion for the particles with the corresponding destabilizing interaction potential defined in Table 3.1.

3.2.5 Performance of the Stiff-Bond Algorithm

It has been mentioned in subsection 3.2.1 that the bonds between particles are not rigid but rather very stiff, which has been implemented in terms of the 'separate displacement' algorithm. Because this procedure does respect the geometric constraints only in an approximate manner, it may happen that the surfaces of certain particles separate more than the tolerance value ε_{tol} which has been defined in eqn. (3.5). In that case, the positions of the corresponding particles need to be corrected appropriately by additional artificial particle displacements (see subsection 3.2.1).

Since the separate displacement scheme is independent of the integration step size and can hence not be translated into a systematic force contribution, a careful study about the performance of this scheme with respect to the specific input parameters is necessary. The efficiency of the scheme is shown for three different simulations in Fig. 3.7. There, the numbers of bonds which needed to be corrected in each time step, N_{crct}, is shown as a function of the total number of bonds in the system, N_{bonds}. It betrays that the solid content has a much stronger influence on the performance than a change in the interaction potential, even for large variations in the potential including an energy barrier. The samples at a solid content $\phi = 0.4$ show an almost linear increase in N_{crct} for large values of N_{bonds}. On the contrary, the performance drops significantly if the solid content is lowered to $\phi = 0.2$: the number of 'incorrect' bonds, which need a correction, shows a strong increase as the coagulation proceeds, i.e. at higher values of N_{bonds}.

The performance of the stiff-bond scheme relative to the total number of bonds is shown in Fig. 3.8. One can see that at a solid content $\phi = 0.4$ less than 3 ‰ of all bonds need to be corrected in each time step as the number of bonds increases. However, at the lower solid content $\phi = 0.2$ the efficiency drops significantly as the relative performance N_{crct} / N_{bonds} shows a strong increase for high numbers of bonds.

Irrespective of the solid content and of the surface potential, the effort to respect all constraints, i.e. bonds, within a given tolerance grows with increasing number of bonds. This makes clear that the simulations become increasingly difficult as the coagulation proceeds: before a time step can be completed, an increasing number of bond-correction steps needs to be performed. Therefore, the above scheme to treat the constraints of fixed bond length is better suited for simulating the early and intermediate stages of the coagulation process rather than for studying gel aging or properties of the final network.

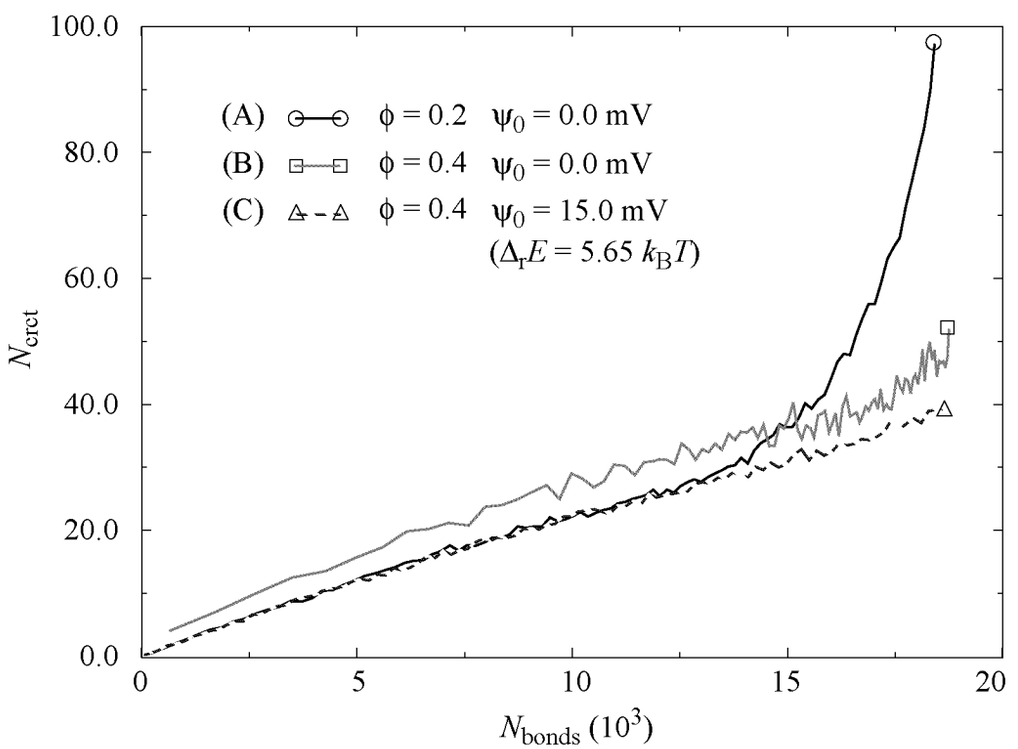

Fig. 3.7: Performance of the stiff-bond scheme: number of necessary bond corrections N_{crct} per integration step vs. total number of bonds N_{bonds}.

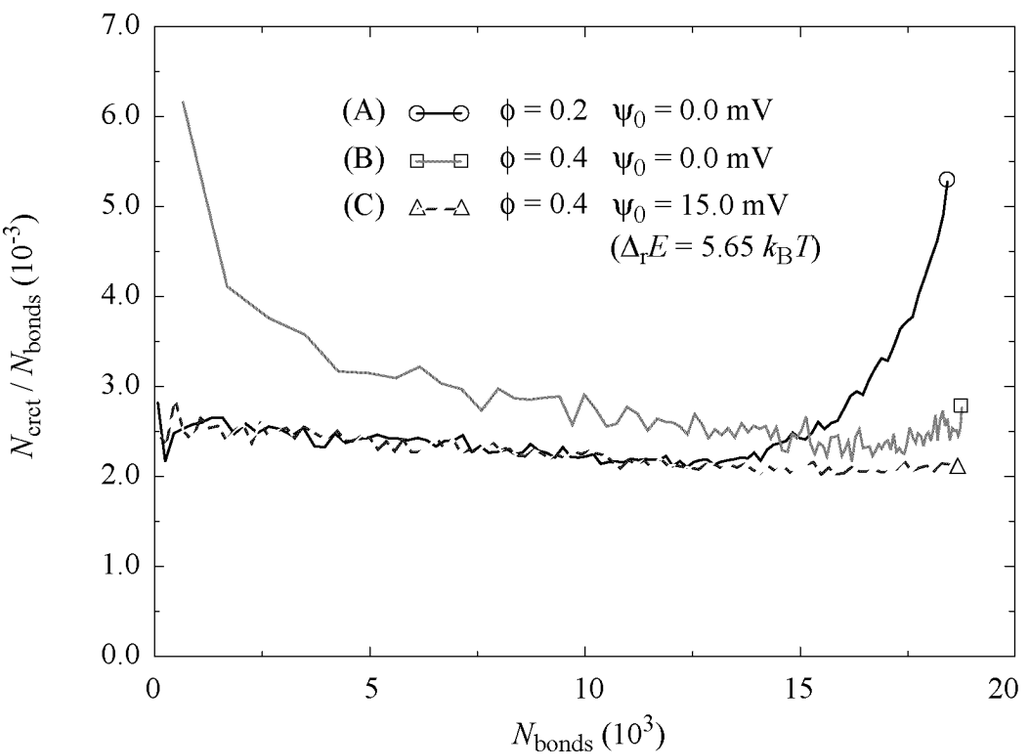

Fig. 3.8: Performance of the stiff-bond scheme: relative number of necessary bond corrections N_{crct} / N_{bonds} per integration step vs. total number of bonds N_{bonds}.

3.3 Reaction Rates

The process of coagulation in dense suspensions is studied under various conditions. A selection of the parameters which are monitored during the destabilization is made in subsection 3.3.1. The dependence of the coagulation time on the solid content and the surface potential is discussed in 3.3.2.

3.3.1 Monitoring the Coagulation

There are several experimental techniques to observe the coagulation of colloidal suspensions in the laboratory [95Eli]. The simplest way is the optical examination where the opaqueness or the appearance of visible flocs give a measure for the coagulation. Scattering experiments reveal more of the particle configuration in terms of size and fractal dimensions of the aggregates. In highly dense systems, where optical or scattering methods are not feasible, the liquid-solid transition can be measured by mechanical impedance spectroscopy [93In, 98Yan]. All of these experimental techniques finally aim at linking the observed material characteristics to the fundamental particle dynamics. With the computer simulations in this study we try to do the reverse: we start from the equations of motion for the particles, destabilize the suspension by directly altering the interaction potential and observe the dynamics of the particles and hence the coagulation process.

In the following, we propose a set of variables which will be used to monitor the coagulation process. The selection of these quantities is with the intention to provide an alternative understanding than what can be derived from experiments. Whether both concepts can be related or not will be discussed later.

a) Number of Free Particles

When the colloidal suspension is destabilized, more and more particles touch each other and form bonds. The number of not bonded, free particles N_f decreases from the total number of primary particles N to finally zero, because each particle is either captured by one of the clusters or by the particle network.

Fig. 3.9 shows the number of free particles N_f relative to N for solid content $\phi = 0.3$ and surface potential $\psi_0 = 0.0$ mV. The simulation was stopped at $\tau_{gel} = 12.7 \cdot 10^{-3}$ s when all particles were part of a single cell-filling network, i.e. a gel. One can see that the number of free particles is decreasing dramatically at the beginning: after carrying out 5 % of the simulation already 50 % of all particles had at least one neighbor (see inset in Fig 3.9). Already after less than 15 % of the time only 10% of all free particles are left. Beyond, the coagulation behavior is better derived from monitoring parameters which describe the clusters rather than the free particles as shown in the following.

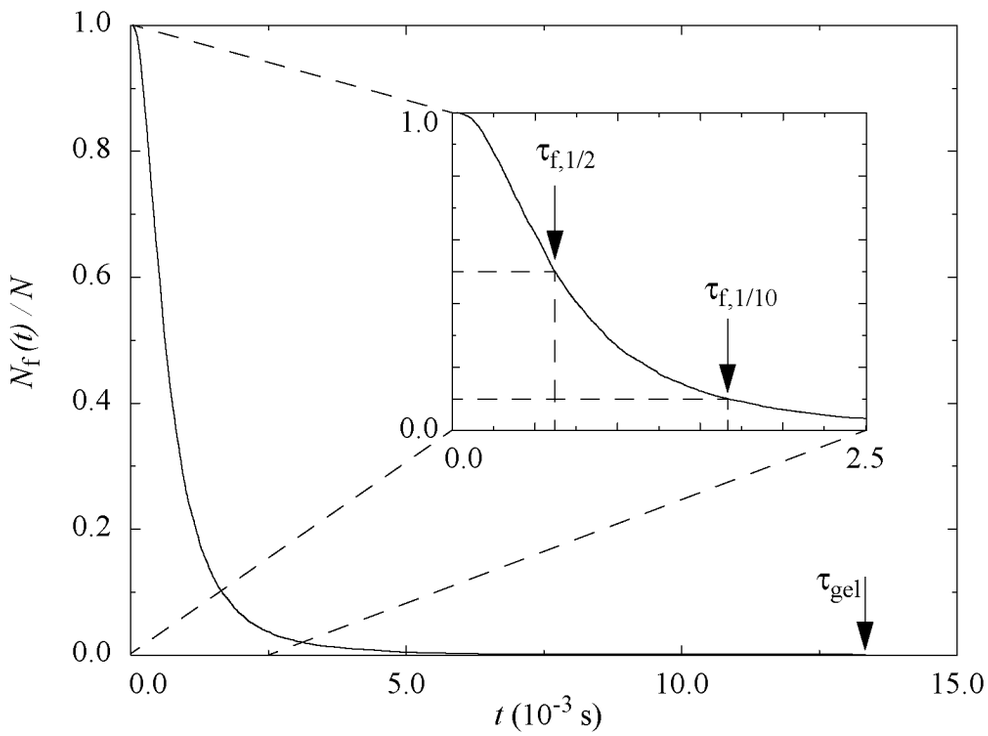

Fig. 3.9: Destabilization of a suspension at $\phi = 0.3$ and $\psi_0 = 0.0$ mV: number of free particles N_f. The inset shows the short-time behavior. $\tau_{f,1/2}$ and $\tau_{f,1/10}$ denote the time when the number of free particles decayed to 1/2 or 1/10 respectively.

b) Number of Clusters

The number of particle agglomerates or clusters N_c is a crude measure for the effectiveness of the destabilization process.

Fig. 3.10 shows the simulation result for the same sample as in Fig. 3.9, i.e. solid content $\phi = 0.3$ and surface potential $\psi_0 = 0.0$ mV. The strong initial decrease in free particles N_f described above is obviously accompanied by an equivalent growth of the number of clusters N_c. At its maximum, we find $N_c \approx 0.2\,N$ which means that the clusters consist of less than five particles on average. We also note that N_c is decaying rapidly again as the clusters coalesce. For most of the time the number of clusters is very small and does not reveal interesting information about the coagulation behavior. The motion of the particles merely leads to the formation of new intra-cluster bonds, which cannot be determined, neither from the number of clusters N_c nor from the number of free particles N_f.

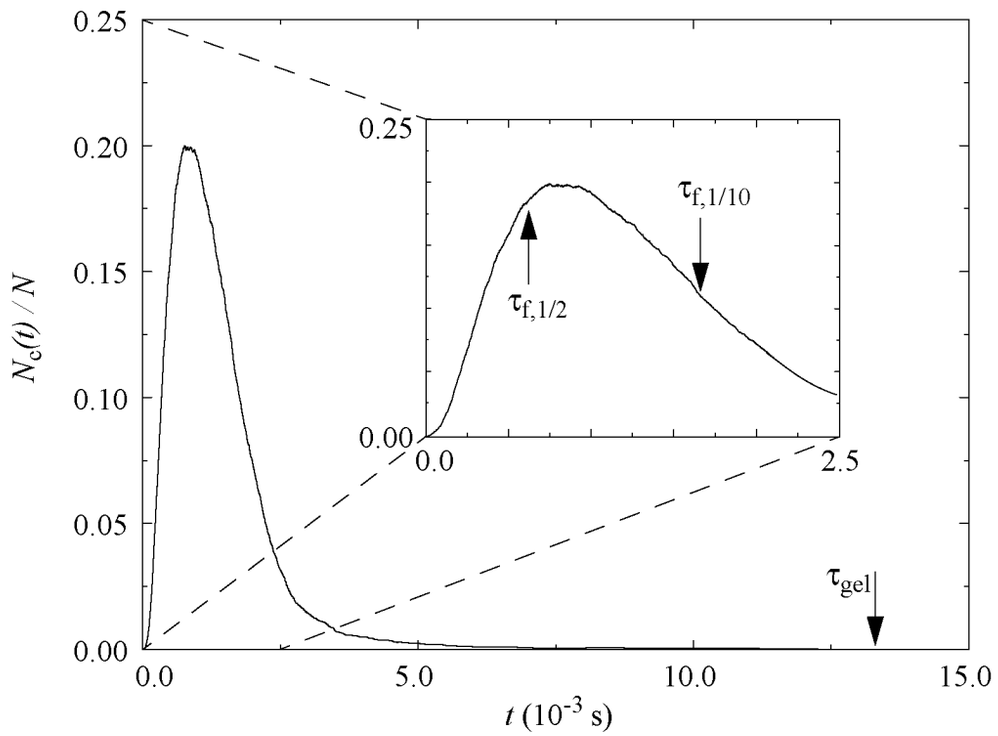

Fig. 3.10: Destabilization of a suspension at $\phi = 0.3$ and $\psi_0 = 0.0$ mV: number of clusters N_c. The inset shows the short-time behavior. $\tau_{f,1/2}$ and $\tau_{f,1/10}$ denote the time when the number of free particles decayed to $1/2$ or $1/10$ respectively.

c) Average Coordination Number

In order to get a better understanding of the linking in the structure we now consider the average number of bonds per particle Π_b, i.e. the coordination number. If $N^{(k)}$ denotes the number of particles with k attached neighbors (in primary minimum), Π_b is given by

$$\Pi_b = \frac{1}{12N} \sum_{k=1}^{12} k\, N^{(k)} \tag{3.9}$$

The average coordination number is normalized such that we would have $\Pi_b = 1$ for the face centered cubic- (fcc) or hexagonal close packed- (hcp) structure at $\phi = 0.74$, where each particle has the geometric maximum of twelve attached neighbors. In general, the upper limit on Π_b depends on the structure and the solid content and is smaller than 1 for any other structure than fcc or hcp, $\Pi_{b,max}(\phi) < 1$. The coordination is a steadily growing number irrespective of the stage of coagulation since primary bonds cannot be resolved: in the early stages it increases due to the formation and coalescence of small clusters, in the later stages due to bonds formed within the clusters and within the network.

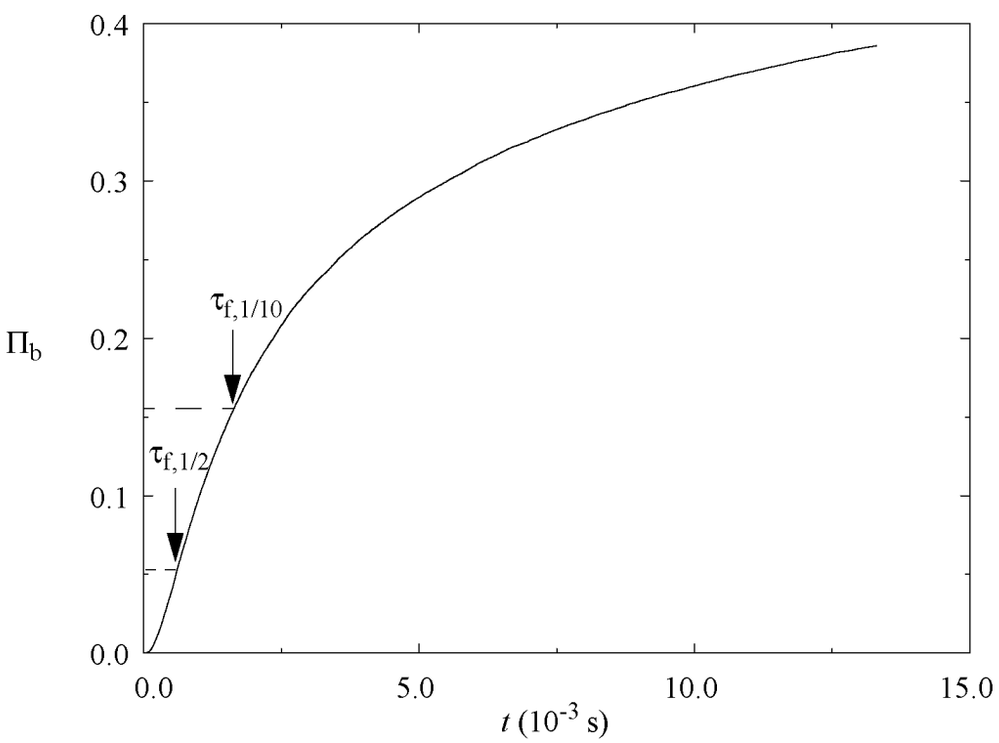

Fig. 3.11: Destabilization of a suspension at $\phi = 0.3$ and $\psi_0 = 0.0$ mV: average coordination number Π_b. $\tau_{f,1/2}$ and $\tau_{f,1/10}$ denote the time when the number of free particles decayed to 1/2 or 1/10 respectively.

Fig. 3.11 shows a typical example for the time behavior of the coordination in a destabilized suspension. We observe that the rate of bond formation is higher for small times than for long times. This can be explained by the reduced particle mobility in the later stages of coagulation due to the bonds between the particles. At the time $\tau_{f,1/10}$ (where only a tenth of all free particles are left) not even half of the bonds of the final structure have formed. A comparison with Fig. 3.10 shows that the further increase in the coordination number can not only be attributed to the coalescence of clusters, since the cluster number is already very small. The reason therefore must be the formation of intra- rather than inter-cluster bonds.

The average coordination number Π_b is not only a further parameter among others (N_f and N_c) for studying the destabilization process. One should notice that $6\,N\,\Pi_b$ corresponds to the total number of bonds in the system and therefore Π_b is a direct measure for the activity of bond formation. In the following, we will explain why it is more appropriate to monitor the coagulation as a function of Π_b rather than as a function of time t.

It is obvious that the coagulation time strongly depends on the solid content and on the interaction potential: the lower the solid content and the stronger the double layer repulsion, the longer is the coagulation time. Therefore the question arises of how the destabilization ***processes*** under such different conditions can be compared. It is likely that the coagulation for different solid contents and surface potentials cannot be related by a simple rescaling of the coagulation time. The large discrepancy in time obscures further more subtle differences. In this study we argue that it is sensible to monitor the coagulation process versus the coordination number Π_b rather than versus the time t. This is a well defined procedure because the coordination number is a monotonically increasing function of time, i.e. the mapping $t \leftrightarrow \Pi_b$ is one-to-one. The main advantage in the process parameter Π_b over t is that it measures in units of bonding activity: Π_b resolves sequences of high activity much better than t (large slope in Fig. 3.11), whereas windows of low activity are compressed (small slope in Fig. 3.11). Fig. 3.12 illustrates the procedure for the number of clusters N_c. The plot on the upper left is the same $t \leftrightarrow N_c$-representation as in Fig. 3.10 with poor resolution at short times and redundant resolution at long times. The $t \leftrightarrow \Pi_b$-plot (same as Fig. 3.11) on the lower right shows how the poor resolution at low times is blown up: the cluster number as a function of the coordination number, $\Pi_b \leftrightarrow N_c$ (upper right), has a resolution which agrees to the activity of bond formation.

One could imagine that the coordination number distribution behind the value Π_b depends on the solid content and on the surface potential under consideration. Fig. 3.13 shows that this dependence is only very weak, at least for the values probed by the simulations in this study. At three different stages of the coagulation process ($\Pi_b = 0.1, 0.2, 0.3$), the three systems exhibit almost the same coordination number distribution.

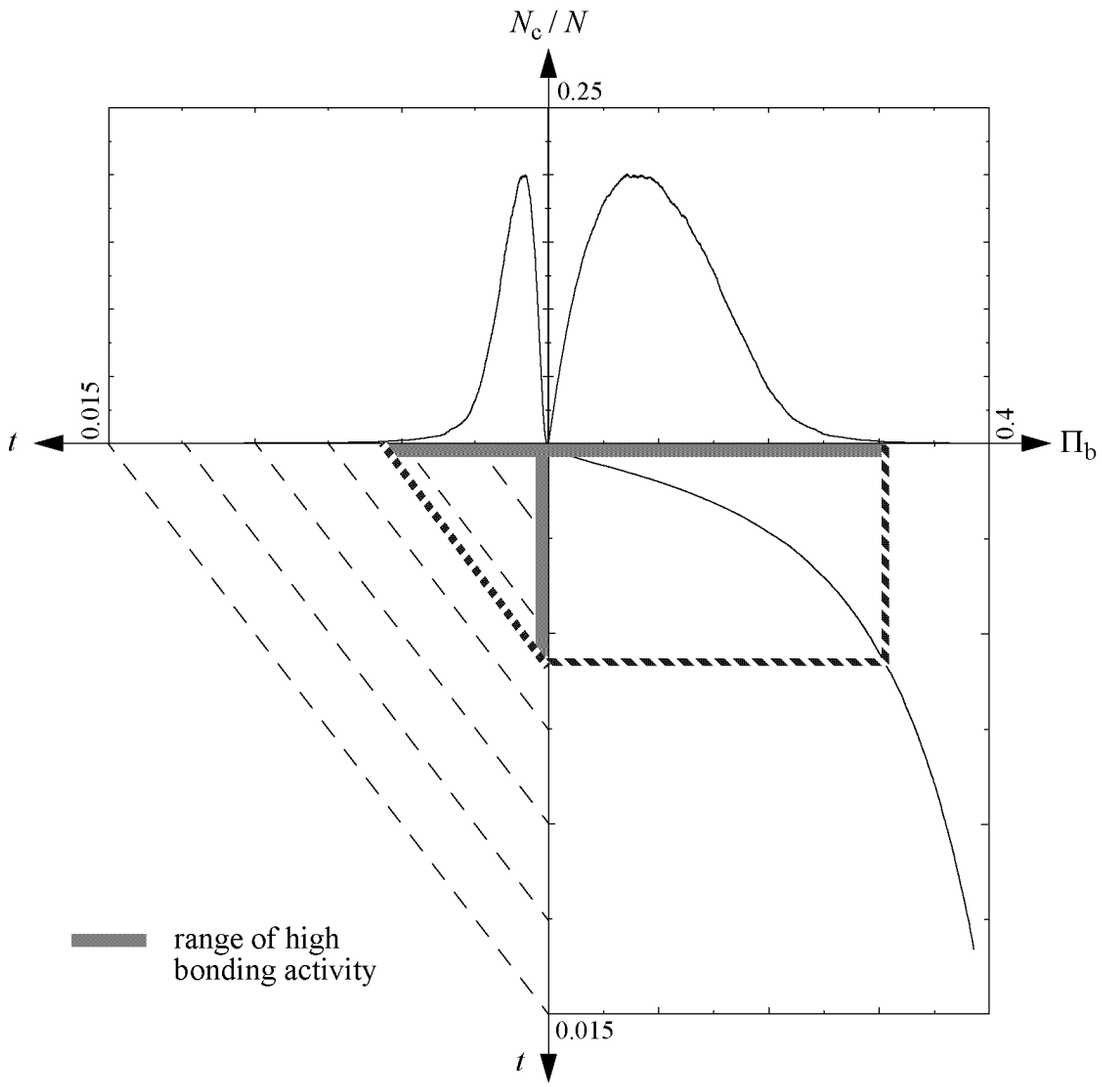

Fig. 3.12: Number of clusters N_c / N as a function of physical time t (upper left) and as a function of bonding activity Π_b (upper right). The latter has enhanced resolution in the high bonding activity stages, whereas resolution is low if the bonding activity is low.

We note that the distribution function for $\phi = 0.4$ and $\psi_0 = 0.0$ mV (□) has a slightly larger maximum and lower adjacent sides leading to a somewhat narrower distribution. Nevertheless, the distribution functions converge if plotted versus the average coordination number Π_b. The sequence of snapshots in Fig. 3.13 from top to bottom illustrates how the distribution around the mean value Π_b is moving to higher values as the coagulation proceeds. A comparison of the situations at $\Pi_b = 0.2$ and $\Pi_b = 0.3$ suggests that the distribution does not experience a broadening. Furthermore, we notice that the distribution at $\Pi_b = 0.3$ is approximately symmetric.

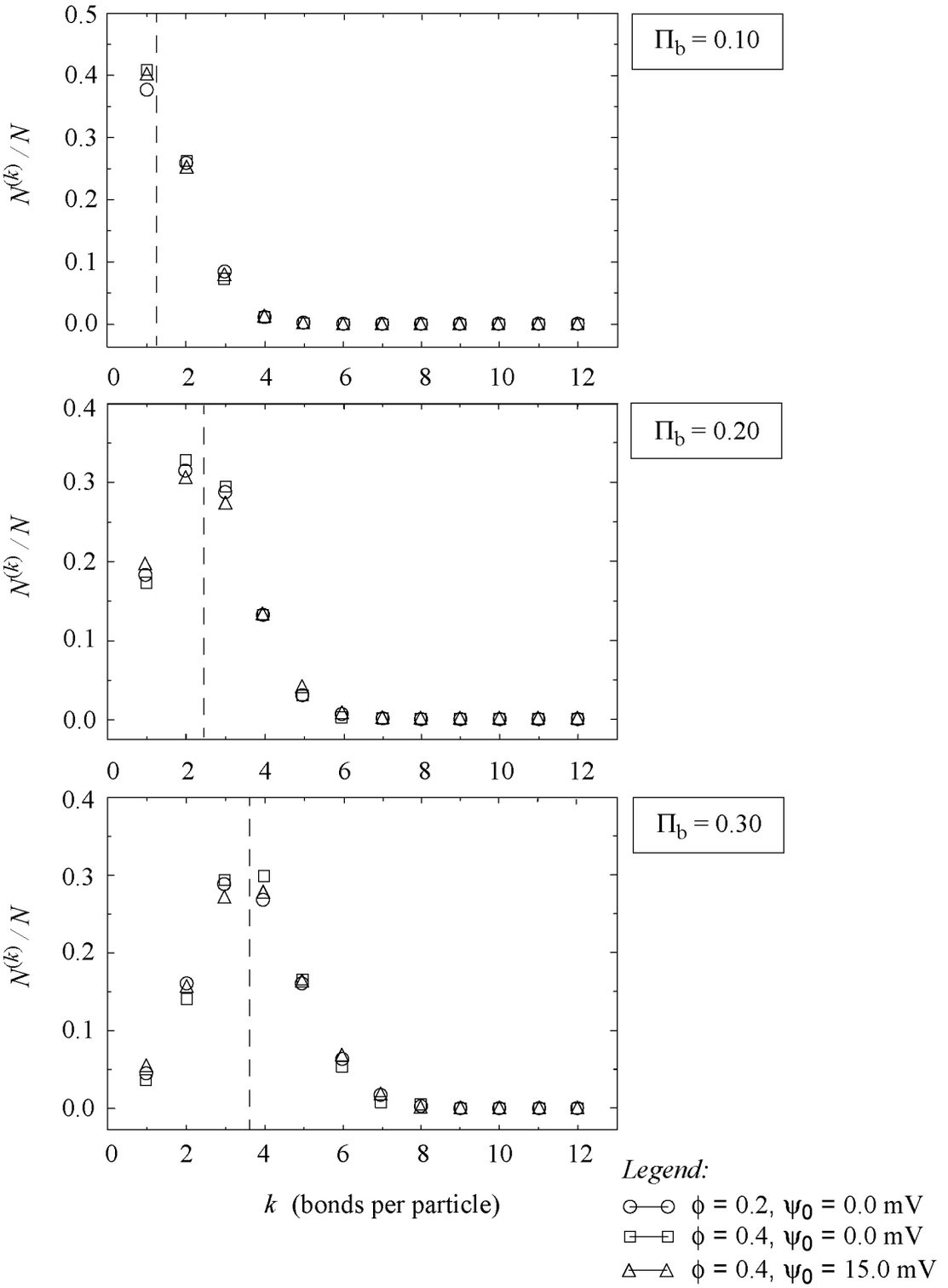

Fig. 3.13: Comparison of the coordination number distribution for different solid contents and surface potentials (excl. free particles). The dashed vertical lines represent the average (corresponding to the Π_b-value).

3.3.2 Characteristic Time Scales

It has been stated above that the coagulation may well be monitored as a function of the average coordination number rather than as a function of time if one is interested in the finer details of the process. However, the dependence of the overall coagulation *time* is also of interest because it is more related to the experimental setup than the average coordination number. To study the influence of the solid content ϕ and of the surface potential ψ_0 on the rate of destabilization we considered the following three characteristic time scales.

(1) *Number of free particles*
The time $\tau_{f,1/2}$, after which the number of free particles has dropped to half of its initial value N is directly read from the simulation data. It has fair statistics as it does not depend on a single particle event (the formation of the final cluster by coalescence of two clusters or by capture of the last free particle would have very poor statistics because it depends on a single event).

(2) *Number of clusters*
We have found that the time behavior of the number of clusters N_c (see for example Fig. 3.10) is well described by the function

$$\frac{N_c}{N} = \alpha_1 \, t \, \exp\left(-\left[\frac{t}{\tau_c}\right]^{\alpha_2}\right) \tag{3.10}$$

In all simulations in this study, the error integral for this fit-function was less than 2 %. In the following, we only use the fitted time scales τ_c.

(3) *Average coordination number*
As shown in Fig. 3.11, the average coordination number Π_b does not level off to a constant value during the simulation, i.e. before the formation of the final cluster. Because the end of the simulation strongly depends on single particle events as mentioned previously, the final value of Π_b does not have any physical meaning. A procedure for determining a characteristic time scale as for the number of free particles is therefore not appropriate. A solution was found in fitting the time dependence of the coordination number by [97Whi]

$$\Pi_b = \alpha_1 \frac{(t/\tau_b)^{\alpha_2}}{1 + (t/\tau_b)^{\alpha_2}} \tag{3.11}$$

This function mimics the smooth transition from zero to the stationary value α_1 within a characteristic time τ_b. We should mention that

the function (3.11) lead to slightly better results with respect to the error integral criterion than the following two:

$$\Pi_b = \alpha_1 \left[\frac{(t/\tau_b)}{1 + (t/\tau_b)} \right]^{\alpha_2} \tag{3.12}$$

$$\Pi_b = \frac{\alpha_1 t + \alpha_2 t^2}{\alpha_3 + \alpha_4 t + \alpha_5 t^2} \tag{3.13}$$

The expression (3.12) has also been studied by others and found to be inferior to (3.11) [97Whi]. The quality of the fitting results of the two functions (3.12-13) are comparable. Both tend to underestimate the slope at the long time end of the $t \leftrightarrow \Pi_b$-function. This was the major reason to favor (3.11) over (3.12-13). In the following we only use the fitted time scales τ_b from eqn. (3.11).

We would like to emphasize that the above selection of characteristic time scales is not completely arbitrary but follows certain criteria. Firstly, we only considered parameters which are statistically relevant, i.e. which do not crucially depend on a single particle event. Secondly, time scales from both the raw simulation data and from the fitted parameters are used. And thirdly, the time scales describe fundamentally different quantities: the number of free particles and of clusters consider the system basically in the early stages (see Fig. 3.9-10), whereas the average coordination number merely probes the whole process of coagulation (see Fig. 3.11).

a) Solid Content Dependence

The effect of the solid content on the characteristic coagulation time becomes clear if one thinks in terms of the particle dynamics. At lower solid contents the particles have to move further before they come in the strongly attractive interaction range of another particle and can form a bond. Also in the later stages the coagulation is slow at low solid contents because the long fingers (particle strings) of the clusters have to wander about long distances before they meet the fingers of another cluster.

Simulations have been performed at surface potential $\psi_0 = 0.0$ mV, i.e. for pure van der Waals attraction (see Fig. 3.6), and solid contents in the range $0.2 \leq \phi \leq 0.4$ in steps of $\Delta\phi = 0.025$. The three characteristic time scales $\tau_{f,1/2}$, τ_c and τ_b described at the beginning of this subsection are shown in Fig. 3.14. They are all normalized with respect to the lowest value, i.e. the value at the highest solid content, in order to make the comparison easier. We note that all three time

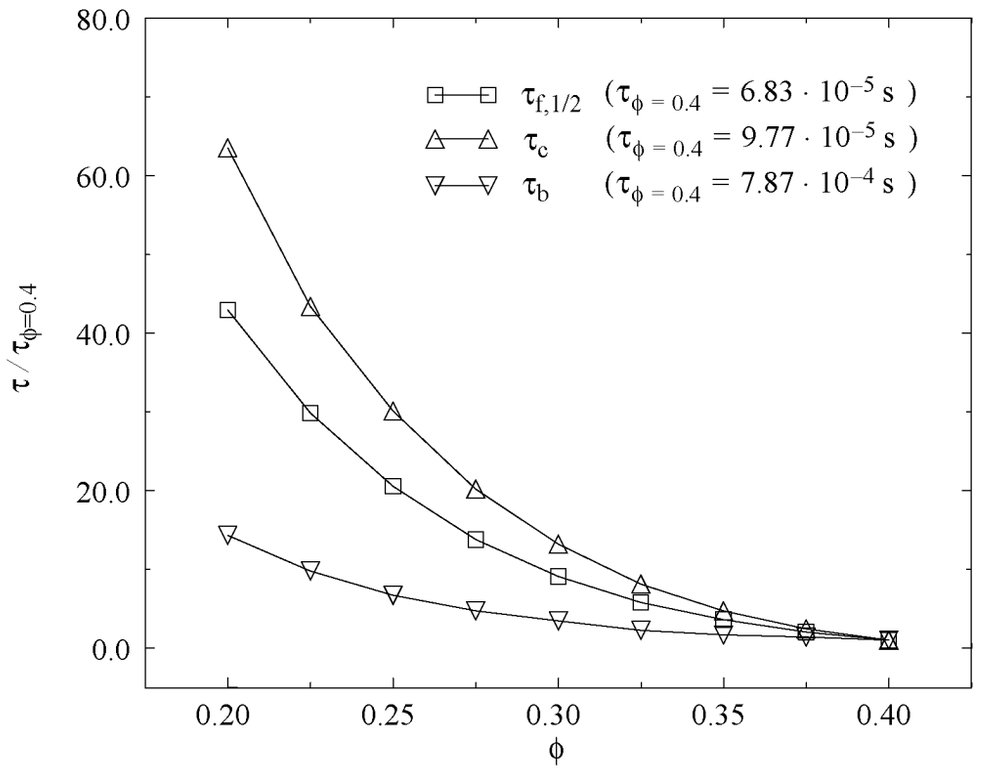

Fig. 3.14: Dependence of the characteristic coagulation times on the solid content. All curves are normalized with respect to the value at $\phi = 0.4$. The surface potential is $\psi_0 = 0.0$ mV. The lines are drawn as visual guide.

scales exhibit an increase as the solid content is lowered. In the range probed by our simulations, τ_b varies by a factor of approximately 14, $\tau_{f,1/2}$ by 43, and the increase in τ_c is more than 63 times. Because $\tau_{f,1/2}$ and τ_c describe only early processes in comparison to τ_b which is a measure for the overall coagulation time, one concludes from Fig. 3.14 that the early stages of the destabilization are more sensitive to the solid content than the later stages.

In the following, we test whether the longer coagulation times for lower solid contents can solely be attributed to the larger distances between the particles. In other words: does the coagulation time relate to the traveling time from one particle to its nearest neighbor? Since $\tau_{f,1/2}$ is the most associated with the freely mobile particles (in comparison to τ_b and τ_c), the following argumentation should hold best for the scaling in $\tau_{f,1/2}$.

For a certain particle configuration with a maximum solid content ϕ_m (e.g. $\phi_m = 0.74$ for face centered cubic), the surface to surface separation s_{nn} between two nearest neighbors is given by

$$s_{nn} = d\left(\sqrt[3]{\frac{\phi_m}{\phi}} - 1\right) \tag{3.14}$$

where d denotes the particle diameter. One can see that the surface to surface separation s_{nn} tends to zero as ϕ reaches the maximum solid content. If the solid content dependence of the coagulation time is only due to the different approaching times of the particles, we propose the relation

$$\tau = \alpha_1'(s_{nn})^{\alpha_2} = \alpha_1\left(\sqrt[3]{\frac{\phi_m}{\phi}} - 1\right)^{\alpha_2} \tag{3.15}$$

The exponent α_2 distinguishes between deterministic and diffusive (i.e. random) particle trajectories. If the particles approach by deterministic motion, the relation between distance and time is linear which leads to $\alpha_2 = 1$. In the case of diffusive motion, the characteristic linear growth of the mean square displacement $\langle \Delta r^2(t) \rangle \sim t$ reads in terms of eqn. (3.15) $\alpha_2 = 2$.

Fig. 3.15 shows the fit of the coagulation time $\tau_{f,1/2}$-data and the corresponding fit-function. The excellent agreement of the fit proposed in eqn. 3.15 (solid line) is obvious. We mention that the error bars on all $\tau_{f,1/2}$-data points are smaller than 1% of the corresponding values (and hence smaller than the symbol size), $\Delta\tau_{f,1/2} \leq 0.01\ \tau_{f,1/2}$. This upper limit has been estimated from the roughness of the $\tau_{f,1/2} \leftrightarrow t$-curve from which the plotted values are determined. Under the assumption that $\Delta\tau_{f,1/2} = 0.01\tau_{f,1/2}$, these errors on the data points then result in errors in the fitted parameters as described in subsection 2.3.2. We note that this estimate on the error bars is valid for all $\tau_{f,1/2}$-data presented in this subsection. Therefore, the error bars on all fitted parameters throughout this subsection are based on this estimated upper limit.

Firstly, we will discuss the fitted values for the maximum solid content ϕ_m and the exponent α_2 of the fit represented by the solid line in Fig. 3.15. This is followed by a discussion of the dashed line fit.

One could imagine that the coagulation time tends to zero if the solid content is so high that the particles already touch each other right from the beginning. However, the maximum solid content of $\phi_m = 0.479$ is significantly different from the expected value for random close packing $\phi_{rcp} = 0.637$ [89Ger]. A possible interpretation can be given by considering the interaction potential for $\psi_0 = 0.0$ mV shown in Fig. 3.6. The separation at which the particles are strongly attracted is slightly away from the particle surface. Therefore, the particles do not have to travel the whole distance between their surfaces but only a fraction of it until they reach their interaction range. Having this idea in mind, one can attribute an effective diameter d_{eff} to the particles which is larger than the real diameter d. If the

expected maximum solid content ϕ_{rcp} is to hold with respect to this effective particle diameter we find

$$\frac{d_{eff}}{d} = \sqrt[3]{\frac{\phi_{rcp}}{\phi_m}} \tag{3.16}$$

Inserting the value for ϕ_m, the effective particle diameter becomes $d_{eff}/d \approx 1.10$. A comparison with the potential curve in Fig. 3.6 shows that the potential energy is approximately twice the thermal energy $k_B T$ at $r/d \approx 1.10$. The comparison of the maximum solid content ϕ_m with the random ***close*** packing fraction is somewhat arbitrary. We could also use the value for random ***loose*** packing $\phi_{rlp} = 0.601$ [89Ger] which would lead to $d_{eff}/d \approx 1.08$.

The exponent α_2 is the second point of interest in the fit-function of Fig. 3.15. Since the equations of motion include Brownian forces, one would have expected the value $\alpha_2 = 2$. It is not completely clear if the value $\alpha_2 = 2.23$, which has been determined in the fitting procedure (see Fig. 3.15), really indicates sub-diffusive behavior of the particles. It may also well be that the approximations involved in eqn. (3.15) are too crude, i.e. that the physics behind the function (3.15) includes more than just simple diffusion of coagulating particles. Nevertheless, we would like to emphasize that this fit-function is able to give a good representation of the data in a rather wide range of solid contents $0.2 \le \phi \le 0.4$. Further studies will be needed to possibly extend this range, both above and below.

In order to quantify the effect of $\alpha_2 \neq 2$, the simulation data have also been fit with forcing the exponent $\alpha_2 \equiv 2$ in eqn. (2.15) which is the ideal diffusive case. The result is represented by the dashed line in Fig. 3.15. Due to the lower value of the exponent α_2, the curvature of the fitted function is slightly lower. This results in overestimating the simulation data at intermediate solid contents and in underestimating the data at the sides of the solid content range. A further consequence is that the maximum solid content ϕ_m is lowered by approximately 6 % of the previous value $\phi_m = 0.479$ to $\phi_m = 0.449$. The effective particle diameter d_{eff} determined above is thereby increased by approximately 2 %. One concludes that setting the exponent $\alpha_2 \equiv 2$ leads to a noticeable, although only weak, loss in the accuracy of the fitted function and hence of the fitted parameters.

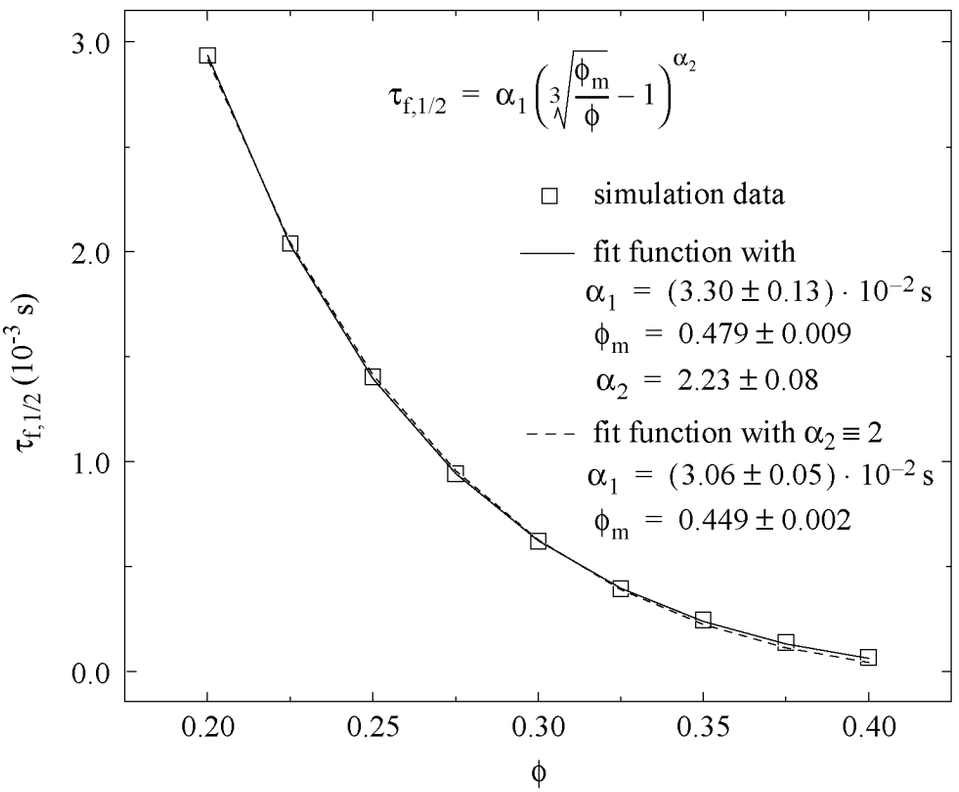

Fig. 3.15: Fit for the dependence of the time scale $\tau_{f,1/2}$ on the solid content ϕ. The surface potential is $\psi_0 = 0.0$ mV.

b) Surface Potential Dependence Without Energy Barrier

It has been illustrated above that the solid content has a substantial influence on the characteristic coagulation time. Also the surface potential ψ_0 alters the time scales. We now demonstrate that not only energy barriers delay the coagulation. Already small surface potentials which do not lead to an energy barrier (Fig. 3.6) result in an increase in the characteristic time.

The suspension with a solid content $\phi = 0.4$ was studied for surface potentials in the range $0 \text{ mV} \le \psi_0 \le 11 \text{ mV}$ for which the interaction potential does not have an energy barrier (see Fig. 3.6). Fig. 3.16 shows the characteristic time scales $\tau_{f,1/2}$, τ_c and τ_b. They are again normalized with respect to the lowest value, i.e. the value at the lowest surface potential, in order to simplify the comparison. Since the increase in the surface potential stands for growing double layer repulsion, it be-

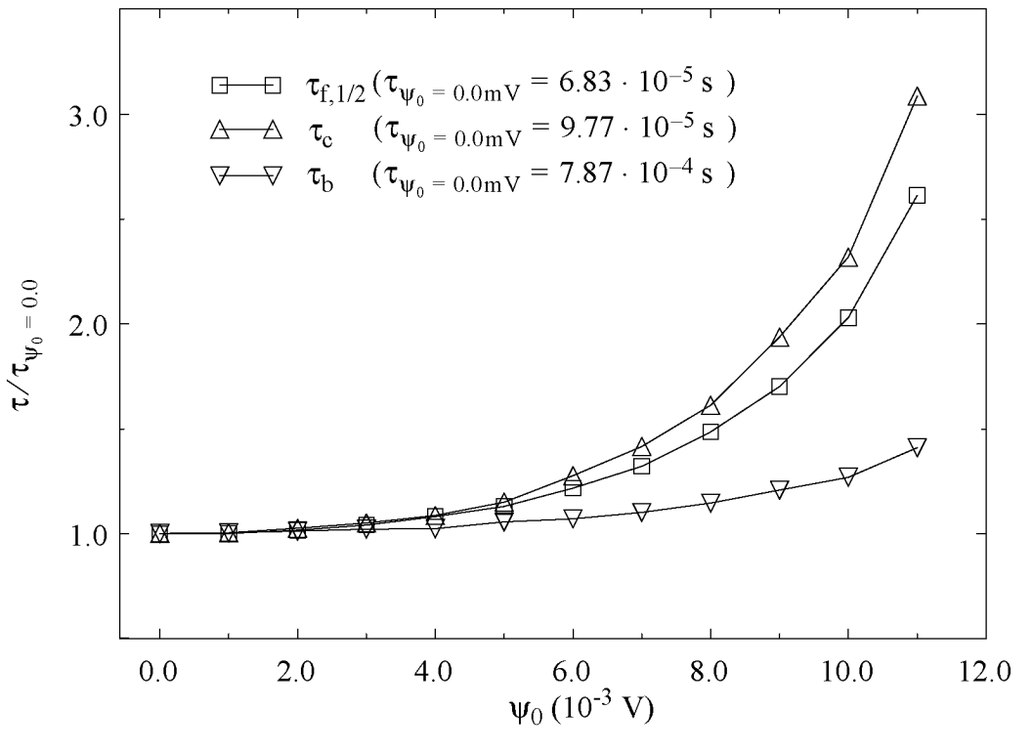

Fig. 3.16: Dependence of the characteristic coagulation times on low values of the surface potential at solid content $\phi = 0.4$. All curves are normalized with respect to the value at $\psi_0 = 0.0$ mV. The lines are drawn as visual guide.

comes clear that all times rise accordingly. Although the range of surface potentials probed by our simulations ranges right up to the appearance of an energy barrier (at $\psi_0 = 12$ mV), the change in the time scales is moderate. τ_b varies by less than a factor of 1.5, the increase in τ_c is around 3 times. As for the scaling with respect to the solid content ϕ, the variation is smallest for τ_b, larger for $\tau_{f,1/2}$, and strongest for τ_c. Therefore, the overall rate constant of the process is less sensitive than the reactions in the early stages of coagulation.

Calculations of the stability ratio given by eqn. (3.2) have shown that the latter underestimates the increase in the coagulation rates in this range of surface potentials by far. This may be attributed to the fact that the derivation of eqn. (3.2) assumes high dilution in the suspension which is incompatible with our solid contents. Therefore, we propose an alternative explanation for the delay in coagulation caused by moderate double layer repulsion. The effect of the surface potential can be reduced to the corresponding change in the interaction range between the particles: the potential curve in Fig. 3.6 indicates that the interaction range is decreased for increasing surface potential which leads to a decrease in the effective, i.e. 'capture', particle diameter

$$d < d_{\mathrm{eff}}(\psi_0 > 0) < d_{\mathrm{eff}}(\psi_0 = 0) \tag{3.17}$$

This decrease in the interaction range d_{eff} is equivalent through eqn. (3.16) to an increase in the maximum solid content ϕ_m

$$\phi_m(\psi_0 = 0) < \phi_m(\psi_0 > 0) < \phi_{rcp} \tag{3.18}$$

In this study, we concentrated on the surface potential (ψ_0) dependence of the maximum solid content ϕ_m rather than of the effective particle diameter d_{eff} because it is more directly related to experimentally measurable quantities. The moderate surface potentials under consideration justify the following first order approximation for the change in the effective maximum solid content ϕ_m

$$\phi_m(\psi_0) = \phi_m(\psi_0 = 0)\left(1 + \left[\frac{\psi_0}{\tilde{\psi}}\right]^{\alpha_3}\right) \tag{3.19}$$

Here $\tilde{\psi}$ and α_3 are two fit-parameters. One may now extend the solid content dependence of the coagulation time in eqn. (3.15) by the replacement $\phi_m \rightarrow \phi_m(\psi_0)$, and one then finds for the surface potential dependence

$$\tau = \alpha_1\left(\sqrt[3]{\frac{\phi_m}{\phi}\left(1 + \left[\frac{\psi_0}{\tilde{\psi}}\right]^{\alpha_3}\right)} - 1\right)^{\alpha_2} \tag{3.20}$$

Fig. 3.17 shows the fitting result for the time scale $\tau_{f,1/2}$. The parameters α_1, ϕ_m and α_2 are adopted from the solid content fit in Fig. 3.15, where only α_1 has been slightly changed in order to match the value at $\psi_0 = 0.0$ mV exactly (which was not the case in the previous fit).

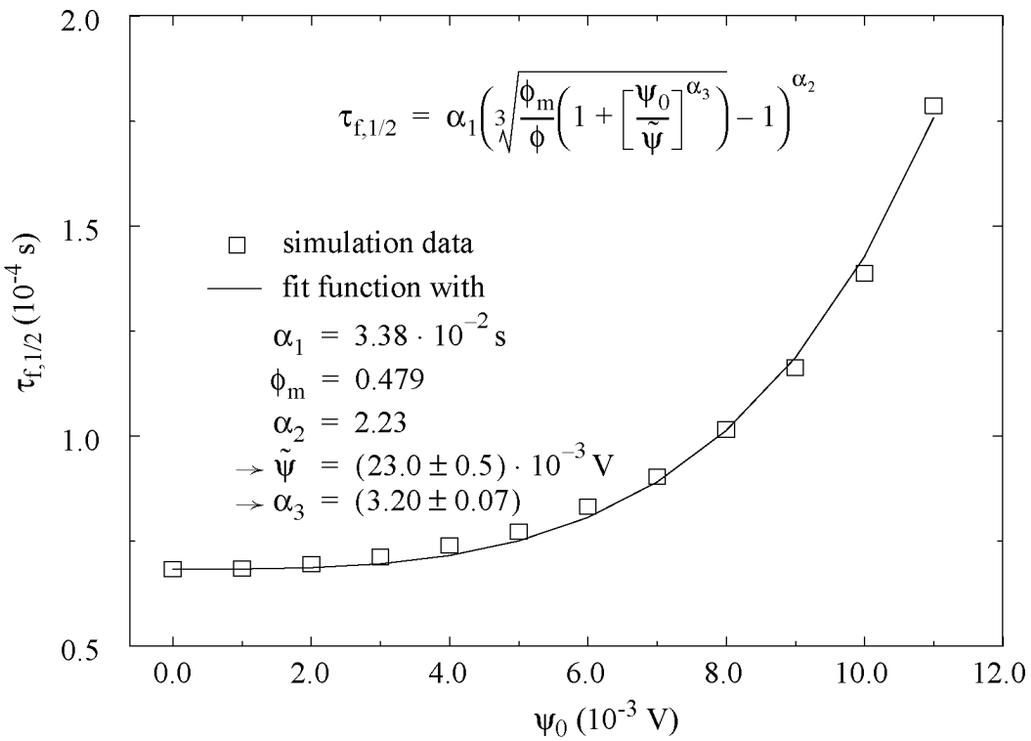

Fig. 3.17: Fit for the dependence of the time scale $\tau_{f,1/2}$ on the surface potential ψ_0 at solid content $\phi = 0.4$. Only the parameters α_3 and $\tilde{\psi}$ are fitted here, whereas α_1, ϕ_m and α_2 are adopted from Fig. 3.15.

The fact that the value for the parameter $\tilde{\psi}$ is twice as large as the largest value for ψ_0 in our simulations does not mean that the relation (3.20) holds for $\psi_0 > 11$ mV. It only illustrates that the effect of the surface potential on the maximum solid content by eqn. (3.19) is small since the $\psi_0/\tilde{\psi} < 1/2$ and therefore $(\psi_0/\tilde{\psi})^{3.22} < 1/8$. Fig. 3.17 shows that the fit-function is too low for surface potentials $\psi_0 < 8$ mV and overestimates the real data above. Nevertheless, the main influence of the moderate surface potentials can be absorbed in a variable maximum solid content $\phi_m(\psi_0)$ given in eqn. (3.19).

c) Surface Potential Dependence With Energy Barrier

The effect of different interaction potentials without an energy barrier could be reduced to an appropriate rescaling of the interaction range. We now consider values for the surface potential $\psi_0 \geq 12$ mV which lead to an energy barrier in the interaction potential (Fig. 3.6). The corresponding energy barrier values are listed in Table 3.2.

The primary effect of an energy barrier is that it hinders the particles from reaching the primary minimum and hence from forming strong bonds. Particles which reach the shallow secondary minimum need thermal activation to surmount the repulsive barrier. We therefore reduce the whole interaction potential to the relative energy barrier $\Delta_r E / k_B T$. It still needs to be shown whether this crude approximation is capable of capturing the main effect of the higher surface potentials. For example, the curvature at the secondary energy minimum, which is equivalent to the strength of a spring force, is not included in our considerations.

Fig. 3.18 shows the characteristic time scales $\tau_{f,1/2}$, τ_c and τ_b. All three parameters are again normalized with respect to the lowest value, i.e. the value at the lowest surface potential. We notice that the coagulation process is delayed for increasing double layer repulsion. An energy barrier of $\Delta_r E/k_B T = 5.65$ for $\psi_0 = 15$ mV increases the coagulation times by more than a factor 20. In contrast to the dependence on the solid content and on low surface potentials, here the variation is ***strongest*** for τ_b, less for $\tau_{f,1/2}$, and ***smallest*** for τ_c. In other words, the early stages of the destabilization are less sensitive to the energy barrier than the overall rate of coagulation.

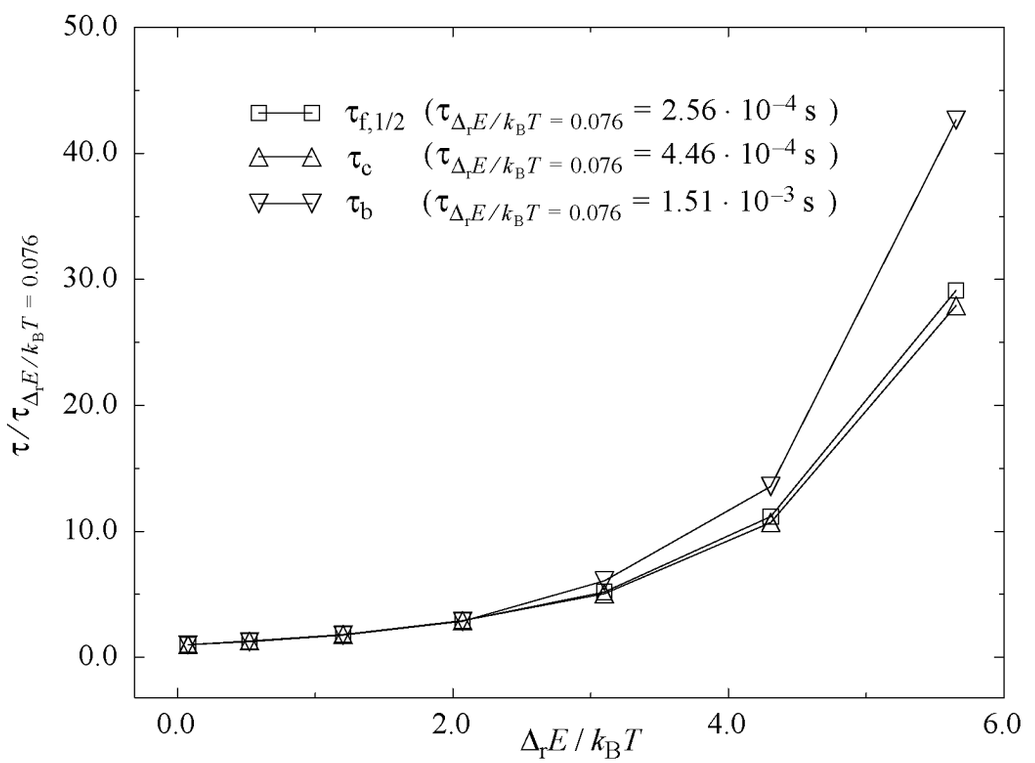

Fig. 3.18: Dependence of the characteristic coagulation times on high values of the surface potential which lead to an energy barrier at solid content $\phi = 0.4$. All curves are normalized with respect to the value at $\Delta_r E/k_B T = 0.076$. The lines are drawn as visual guide.

The slowing down of any process which is hindered by an energy barrier is usually described by an exponential dependence of the corresponding rate constants and reaction constants, respectively, which is derived from the stability ratio (3.2). We notice right away from Fig. 3.18 that this is not the case here: the time scales should then increase as much as $\exp(5.65) \approx 285$ times. Recently, an alternative form of the energy barrier dependence of rate constants and time scales has been proposed [91Wan] which explicitly accounts for the Brownian motion of the particles:

$$\tau = \alpha \frac{\exp(\Delta_r E / k_B T)}{1 + \Delta_r E / k_B T} \tag{3.21}$$

This function contains only a single parameter that allows to adjust the overall time scale, the functional dependence on the energy barrier, however, is fixed. The expression (3.21) has been fitted to the data for the time scale $\tau_{f,1/2}$ as shown in Fig. 3.19.

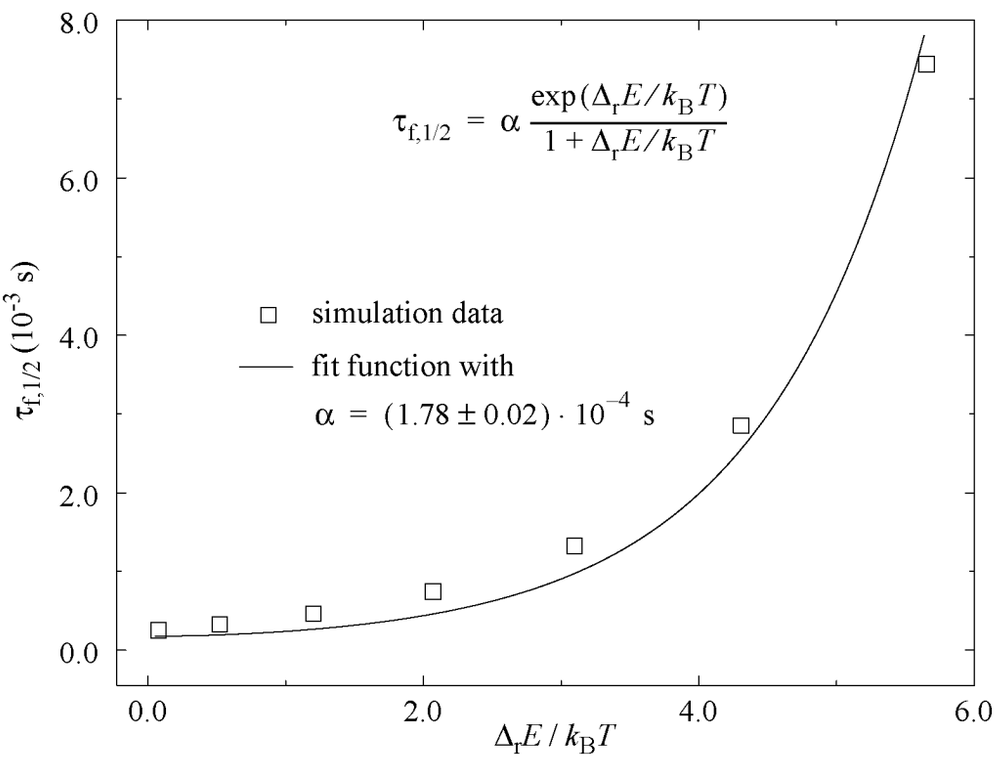

Fig. 3.19: 1-parameter fit for the dependence of the time scale $\tau_{f,1/2}$ on the energy barrier $\Delta_r E$ at solid content $\phi = 0.4$.

First, we notice by the use of eqn. (3.21) that the fit-function with $\alpha = 1.78 \cdot 10^{-4}$ s strongly underestimates the time $\tau_{\Delta_r E/k_B T = 0.076} = 2.56 \cdot 10^{-4}$ s (see Fig. 3.18) at the lower end of the energy barrier range. Furthermore, the dependence of the time scale on the energy barrier is still too strong and not well represented by the above expression (3.21), although it reduces the exponential growth by a linear function. It is not clear whether this discrepancy can be attributed to the circumstance that eqn. (3.21) has been derived on the basis of a two-particle system and is now applied to a dense many-particle system. In order to get a better representation of the simulation data we have expanded expression (3.21) to

$$\tau = \alpha_1 \frac{\exp(\Delta_r E/k_B T)}{(1 + \alpha_2 \Delta_r E/k_B T)^{\alpha_3}} \tag{3.22}$$

which reduces to eqn. (3.21) with $\alpha_2 = 1$ and $\alpha_3 = 1$. The result of this extended version can be seen in Fig. 3.20.

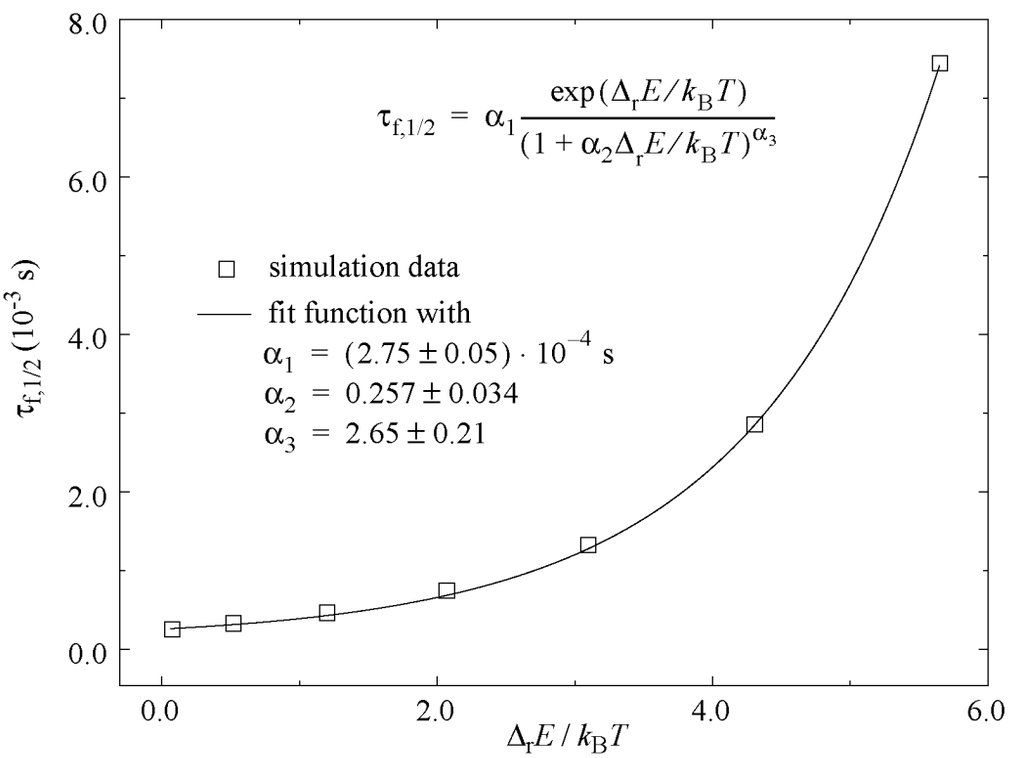

Fig. 3.20: 3-parameter fit for the dependence of the time scale $\tau_{f,1/2}$ on the energy barrier $\Delta_r E$ at solid content $\phi = 0.4$.

This fit-function (3.22) with $\alpha_1 = 2.74 \cdot 10^{-4}$ s shows much better agreement with the value $\tau_{\Delta_r E/k_B T = 0.076} = 2.56 \cdot 10^{-4}$ s (see Fig. 3.18) for the lowest energy barrier. The fact that even this smallest value is represented with high relative accuracy is in favor of eqn. (3.22). Furthermore, the dependence of the time scale on the energy barrier is well reproduced. Nevertheless, we cannot offer an interpretation for the values α_2 and α_3. It may well be that both parameters tend towards 1 as the suspension is diluted and the two-body approximation implied in eqn. (3.21) becomes applicable. This would then mean that the difference between a dilute and a dense suspension could be absorbed in these parameters, i.e. $\alpha_i = \alpha_i(\phi)$ with $\alpha_i(\phi \to 0) \to 1$ for $i = 2,3$.

3.3.3 Summary and Conclusions

In this section, the increase of the characteristic coagulation times due to lower solid content and due to higher surface potential has been quantified. Appropriate functions could be found which reproduced the simulation data of the time scale $\tau_{f,1/2}$ in a satisfactory manner. In particular, it has been noticed that the influence of low surface potentials, which do not lead to an energy barrier in the interaction potential, could be reinterpreted in terms of an effective 'capture' diameter of the particles and an effective solid content respectively.

The different behavior of the short and long time scales has not been discussed so far. Whereas the short time scales $\tau_{f,1/2}$ and τ_c have shown a stronger dependence on solid content and on low surface potentials than the long time scale τ_b, the reverse was the case for the energy barrier dependence. This means that a change in solid content or a low surface potential have a greater effect on the earlier than on the later stages of the coagulation process. This is in contrast to a change in the energy barrier which primarily influences the long time behavior. These circumstances shall be elucidated in the following. Since the case of low surface potential has been found to essentially reduce to a solid content interpretation, we now concentrate on two situations: solid content dependence and energy barrier dependence.

In the absence of an energy barrier, each pair of closely approaching particles forms a primary bond. We therefore say that the reaction efficiency is equal to one. In the early stages of the coagulation, single particles have to scan a three-dimensional space before they find another partner to make a bond. This is not the case for the later stages. There, due to the constrained dynamics, the fingers of clusters or of the network sweep only over a lower dimensional space to search another finger in order to make a bond. Therefore, the efficiency for finding a bonding partner decreases more for the single particles than for entire particle strings (fingers) as the solid content decreases. An equivalent statement is the following: in three dimensions cross-linking two beams (particle strings) is easier than bringing two spheres (single particles) into contact.

Because the particle interactions are short range and attractive on all scales, it is concluded that the short time mobility of a single particle or a particle string does in first approximation not depend on the solid content (in the range probed in our simulations). Therefore, the above geometrical argument about scanning volumes translates into the following conclusion: the early stages of the coagulation process are more sensitive to the solid content than the overall coagulation time, as noticed in Fig. (3.14) and (3.16).

In the presence of an energy barrier, the above geometrical argument does not directly translate into a statement on the characteristic time scales. The single particle bonding efficiency is not 100% because not every particle approach leads to a primary bond. Nevertheless, in the early stages of coagulation every single par-

ticle is free to make as many attempts as possible. Sooner or later it will succeed and reach the primary minimum. The situation changes drastically for strings of particles in the later stages of the coagulation. The two particles which try to cross-link two strings are subjected to strong constraints by the presence of their neighbors. Therefore, two particles of different strings can only surmount the energy barrier if in one of the two strings a whole segment is moved. In other words, a 'collective' attempt must be made before a bond can be realized. This becomes even more difficult if the other particles of the corresponding segments may also lie within a secondary minimum with third particles (this was not possible in the above argumentation for the solid content dependence). The existence of weak bonds in the secondary minimum is an additional constraint which substantially reduces the mobility of each particle in this structure. We argue that these additional constraints are the reason for the stronger dependence of the long time scales on the energy barrier rather than that of the short time scales.

An experimental method, which is close to our model, is the Direct Coagulation Casting (DCC) since the interaction potential between the particles is altered by internal reactions and not by any external influence [94Gra, 95Baa, 99Gau]. Our simulation results for the characteristic coagulation times are compared to the results reported in the experimental studies.

Firstly, the coagulation processes in our study occurs on a sub-second time scale, whereas the real system coagulates only after minutes or even several hours. This large discrepancy can be attributed to the different ways of destabilization. In the simulations reported here, the interaction potential is switched from repulsive to attractive in a single instant. In contrast, the experimental change in the interaction occurs on the scale of minutes and hours. In the DCC method, the rate limiting step is the decomposition of urea to change the pH and hence to alter the surface potential [99Bal]. Therefore, a comparison with the much smaller simulated time scales suggests that the particle configuration in the system is in 'equilibrium' with the corresponding interaction potential at every stage of the coagulation. The limiting factor for achieving fast solidification of the suspension is thus not the particle dynamics but rather the method to reduce repulsive forces. In the case of DCC, shorter coagulation times could be achieved by increasing the urease and/or urea concentration.

Secondly, the simulations predict a decrease in the coagulation time when raising the solid content. Although the reason for this is evident, significant experimental results in the DCC method are difficult to obtain. This is due to the strong influence of the urease concentration on the coagulation time and due to the temperature dependence of the urease activity, which both make accurate measurements of the coagulation time difficult. Therefore, the more subtle influence of the solid content on the dynamics of the particles and on the characteristic coagulation time for a given interaction potential is obscured.

3.4 Structural Development

This section deals with the development of the particle configuration from small aggregates to the final percolating network. The nucleation process will be studied by the size and the number of growth sites (3.4.1). The structure of the latter is characterized by their fractal dimension which allows to distinguish loose from dense aggregates. The progressing cross-linking of the network, which is related to the mechanical stability, is monitored over the destabilization process (3.4.2). A detailed discussion of the evolving particle structure (3.4.3) in terms of particle density correlation and bond angle distribution will conclude the section.

3.4.1 Nucleation

It is known from the study of crystallization and glass transitions that the solidification of a liquid does not occur homogeneously over the whole sample but is rather a kinetic process starting at specific sites. Therefore the nucleation and the growth of small nuclei is a key issue. The liquid-solid transition in colloidal suspensions can be examined under the same aspects as will be shown in the following.

The evolution of the number of clusters N_c is shown in Fig. 3.21 for different solid contents and surface potentials. The reader should notice that the curves are all plotted with respect to the average coordination number (which is proportional to the relative number of bonds in the system) and not with respect to the physical time. This allows to compare equivalent stages of different destabilization processes as mentioned previously. One can see that the three samples approximately agree in the early stages of coagulation ($\Pi_b < 0.05$) whereas they differ significantly in the intermediate stages ($0.05 < \Pi_b < 0.3$). In the following we concentrate on comparing the different samples in the intermediate regime.

A comparison of samples (A) and (B) in Fig. 3.21 indicates that more clusters are present at lower than at higher solid contents which can be explained as follows. The bonding mechanism in both (A) and (B) is diffusion limited because only the diffusion of particles and small aggregates limits the formation of new bonds and no energy barrier delays the reaction. The influence of the solid content becomes apparent when one compares the possibilities of particle-particle-, particle-cluster-, and cluster-cluster-bond formation. At lower solid contents, the formation of a small cluster leads to an increase of void space around it, which makes it difficult for other particles and clusters to approach this cluster. The probability that any approaching object is attached somewhere else before reaching this cluster is high which results in many small and evenly distributed clusters throughout the sample volume. At higher solid contents this effect is reduced by the much shorter distances between the small clusters which leads to more cluster-cluster-bonds than at lower solid contents.

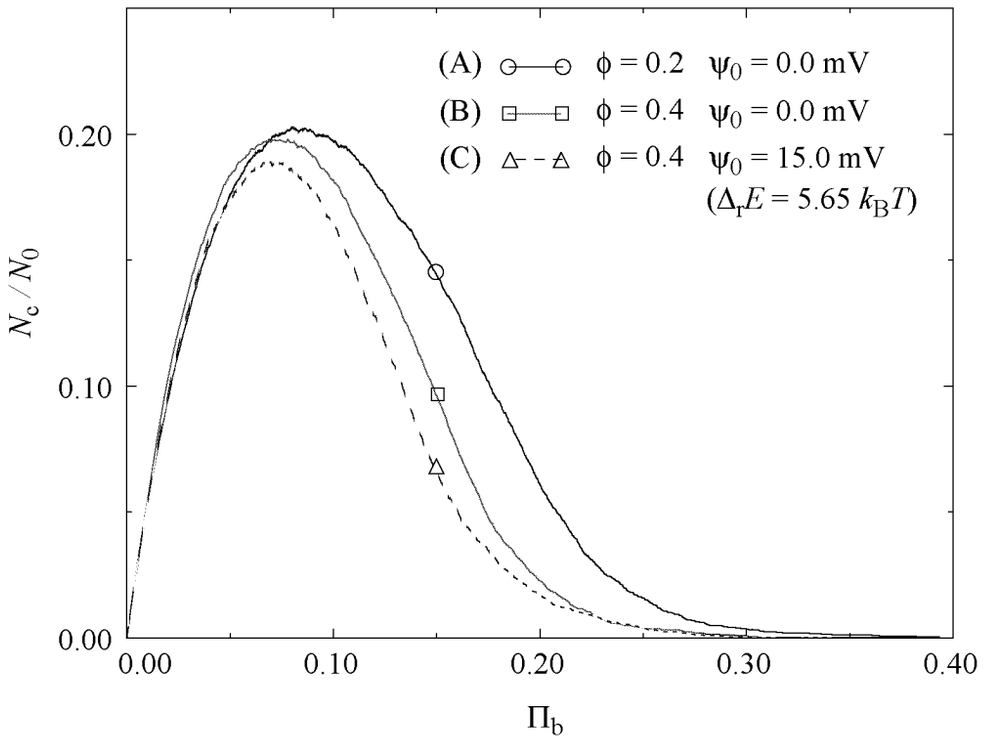

Fig. 3.21: Evolution of the number of clusters N_c vs. the average coordination number Π_b.

The effect of an energy barrier in the interaction potential can be observed when comparing samples (B) and (C) in Fig. 3.21: the higher the barrier, the lower is the number of clusters (nevertheless, we notice that the difference is not as large as for the variation in the solid content discussed above). It is difficult to give an explanation for the energy barrier dependence on the number of clusters and the following is only a suggestion that needs further testing. The presence of an energy barrier implies the existence of a secondary minimum. This means that any two particles first remain in this secondary minimum before the primary bond is established. There is also a small chance that two particles in a secondary minimum separate again rather than that they form a bond. However, if a particle approaches a neck between *two* already bonded particles, it is within the secondary minimum of *two* particles and an escape is less probable. This could be the reason for the slight tendency towards fewer clusters if the energy barrier is increased.

The development of nucleation sites can not only be observed by the number but also by the mass of the clusters. Fig. 3.22 shows the solid content and surface potential dependence of the average cluster mass. The appearance of steps in the later stages of the coagulation process ($\Pi_b > 0.3$) originates from the coalescence of already large clusters by a single bonding event. One can see that the data in Fig. 3.22 correspond to Fig. 3.21 in the following manner. The highest number of

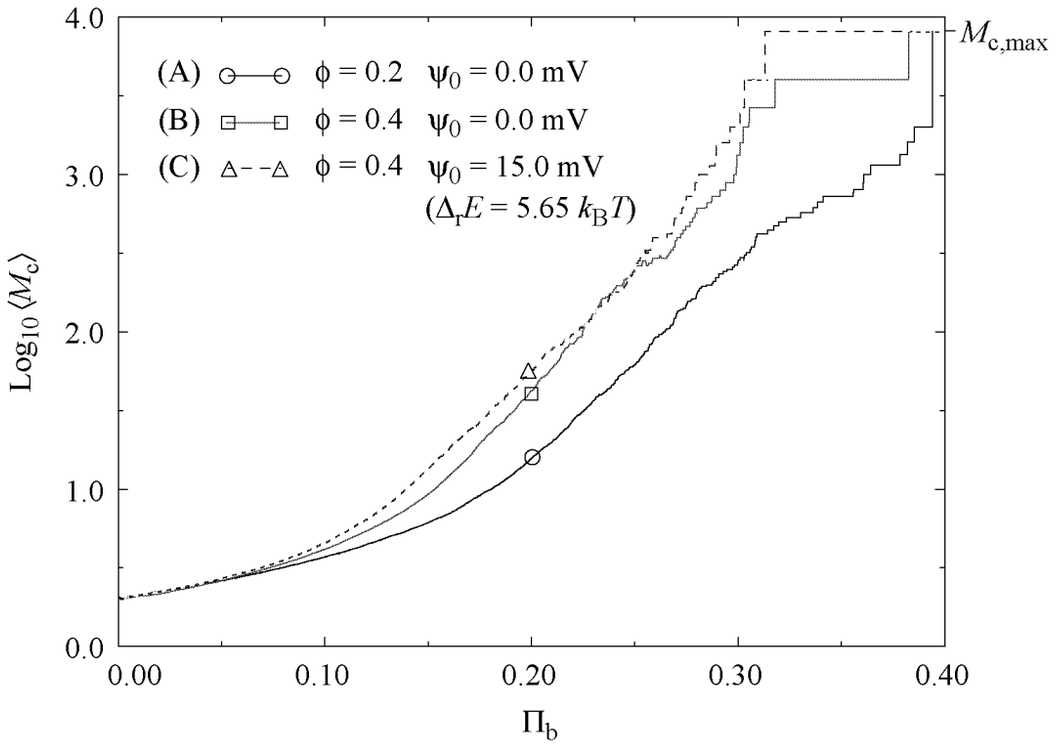

Fig. 3.22: Evolution in the number of clusters $\langle M_c\rangle$ vs. the average coordination number Π_b. The mass of the final percolating cluster is denoted by $M_{c,max}$.

clusters for sample (A) goes along with the lowest average cluster mass. Likewise, the lowest number of clusters for sample (C) corresponds to the highest average cluster mass.

From the above observations on the number and average mass of the intermediate clusters, we conclude that lower solid contents favor the formation of more and smaller clusters. On the other hand, an energy barrier leads to fewer and heavier clusters than in the absence of an energy barrier.

The structure of the final gel is supposed to depend not primarily on the number (and hence the mass) of the intermediate clusters but much more on their internal structure. Since the strength of the solidified suspension is intimately related to the network structure, we will discuss in the following the structure of the intermediate clusters which are the building blocks for the final percolating network.

The structure of the intermediate clusters has been characterized by their fractal dimension according to the following procedure. For each cluster of mass M_c, the radius of gyration which measures the average extension of a cluster has been determined

$$R_g = \sqrt{\frac{1}{M_c}\sum_{i=1}^{M_c} \langle (\boldsymbol{r}_i - \boldsymbol{r}_{cm})^2 \rangle} \tag{3.23}$$

Here, the summation goes over all particles contained in this specific cluster and $\boldsymbol{r}_{cm}$ denotes the center-of-mass position. Thereafter, all values for each M_c are averaged. The set of all M_c-values lead to a distribution function $R_g = R_g(\langle M_c \rangle)$. We determined the fractal dimension d_f in two ways: by fitting a power law

$$R_g = q \langle M_c \rangle^{1/d_f} \tag{3.24}$$

or by reading the slope from the corresponding logarithmic data

$$\log(R_g) = \log(q) + \frac{1}{d_f} \log \langle M_c \rangle \tag{3.25}$$

Here q is an arbitrary constant. It can be seen from eqn. (3.24) that low values for d_f mean stringy structures whereas high values (with a maximum $d_f = 3$) stand for dense structures. The average of the fractal dimensions determined from eqn. (3.24) and (3.25) is shown in Fig. 3.23, where the evolution for different solid contents and surface potentials is given. Fig. 3.24 shows the determination of the fractal dimension for one particular data point in Fig. 3.23 in order to give an idea on the errors implied by the fitting procedure.

The calculation of the fractal dimensions through eqns. (3.24) and (3.25) has only been performed if the distribution function $R_g = R_g(\langle M_c \rangle)$ contained a reasonable number of points. This criterion was not respected in the later stages of coagulation where only very few and large clusters existed. There, the structure is examined by the pair distribution function as described in subsection 3.4.3, which is equivalent to studying the mass distribution within these large clusters.

We notice that the fractal dimension of all three samples increases as the coagulation proceeds. This is equivalent to a densification of the existing clusters. In the case of no energy barrier for (A) and (B), where the coagulation is purely diffusion limited, the observed clusters develop to significantly denser objects, i.e. have higher fractal dimension, contrary to the predictions for dilute suspensions. This is due to the absence of void space necessary for the development of open structures. The same tendency is also found for the reaction-limited case (C): our simulation results overshoot the dilute suspension prediction, which is again due to the absence of void space. Nevertheless, the qualitative difference (denoted by the thick dashed line in Fig. 3.23) between denser structures for reaction limited aggregation (C) on one hand and looser structures for diffusion limited aggregation (A and B) on the other hand agrees with the difference for dilute suspensions. These observations for the intermediate structures in non-dilute suspensions cor-

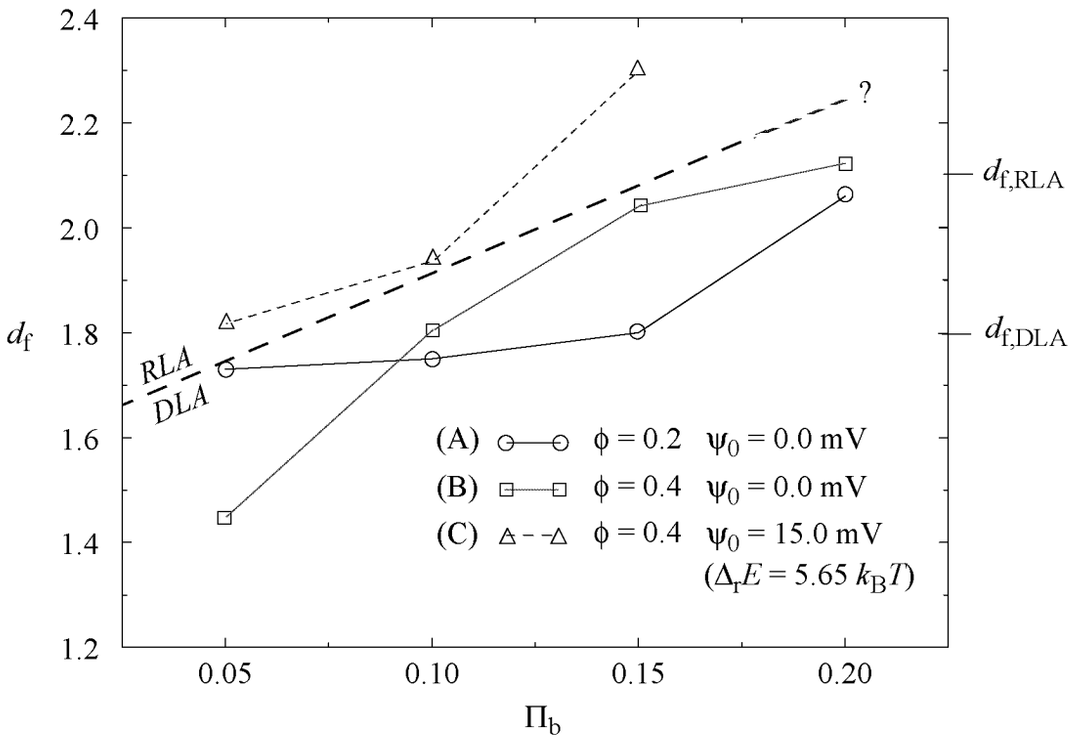

Fig. 3.23: Evolution in the fractal dimension d_f vs. the average coordination number Π_b. The predicted fractal dimensions in dilute suspensions ($\phi \rightarrow 0$) for diffusion-limited aggregation (DLA) and reaction-limited aggregation (RLA) are denoted by $d_{f,DLA}$ and $d_{f,RLA}$, respectively. The lines are drawn as visual guide.

respond to other simulation results about final structures at comparable solid contents and interaction potentials [87Ans1, 87Ans2].

The high discrepancy in d_f for the different solid contents in the earliest stages ($\Pi_b = 0.05$) is not clear. We can not exclude the possibility of an artifact due to the selection of the initial configuration which may influence the coagulation kinetics in the early stages.

Summary

Decreasing solid content has shown to have little effect on the density of the clusters, i.e. fractal dimension, and only leads to more and smaller clusters.The existence of a weak energy barrier leads to fewer, heavier and relatively dense intermediate clusters whereas in the absence of an energy barrier there are more, smaller and less dense objects.

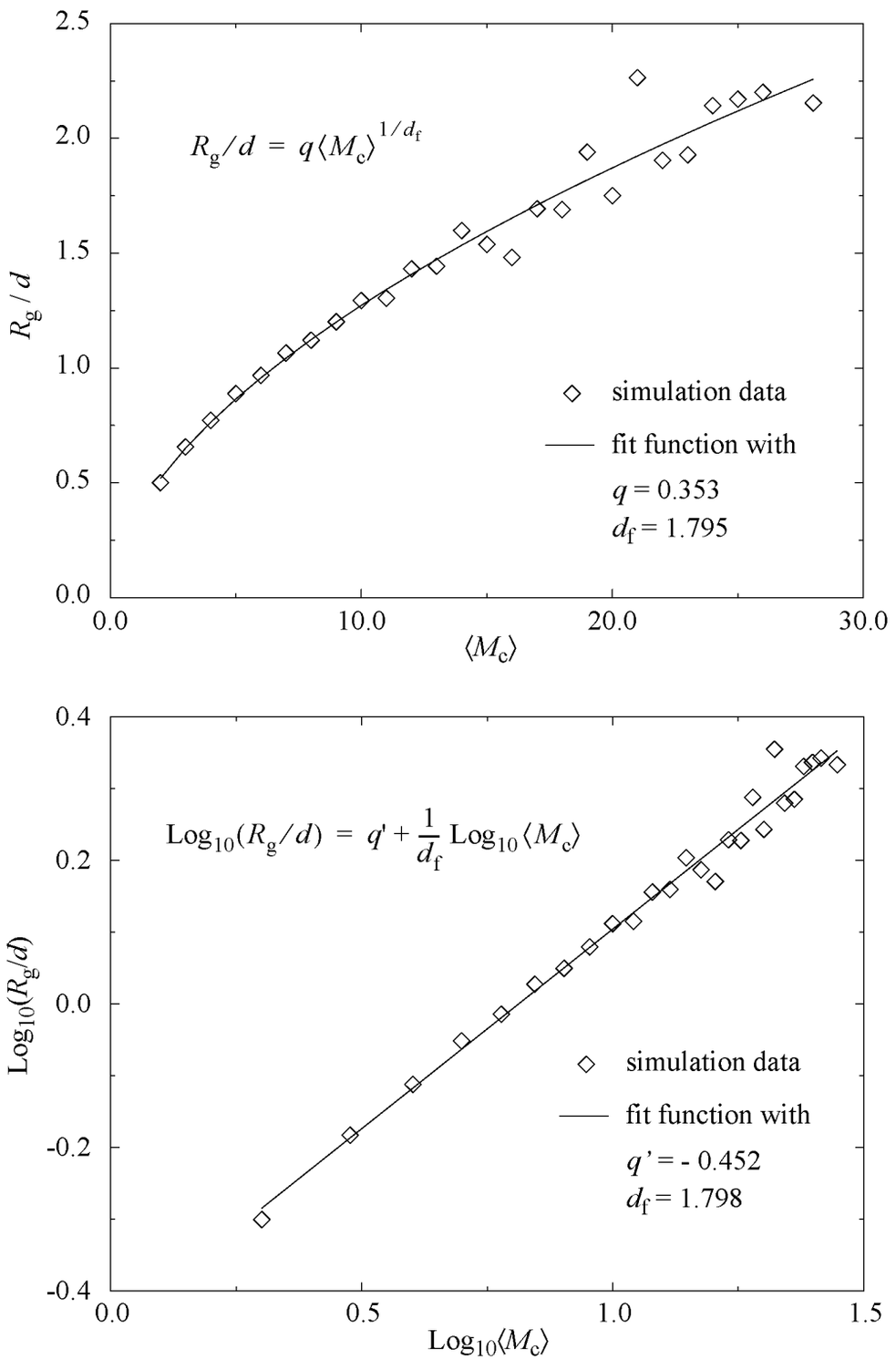

Fig. 3.24: Determination of the fractal dimension d_f according to eqn. (3.24) and eqn. (3.25), respectively, for $\phi = 0.4$ and $\psi_0 = 0.0\,mV$ at $\Pi_b = 0.1$.

3.4.2 *Cross-Linking*

All of the above results were concerned with the size and structure of intermediate clusters. We now proceed to the another aspect of the destabilization process which is the increasing degree of cross-linking. It is a criterion for distinguishing a loose connection of clusters from a mechanically stable network.

It has been mentioned previously that the clusters assemble to bigger and bigger units as the coagulation proceeds. But what about syneresis? Does the particle network shrink? Is the volume occupied by the particle network smaller than the overall sample volume? In our simulations, syneresis should be observable by relatively large void regions within the particle network. However, no shrinkage has been observed for any of the solid contents in this study, $0.2 \leq \phi \leq 0.4$. In all samples, the final structure was a percolating network which filled the whole simulation box and no large heterogeneities could be detected. Although the samples are percolating, the question about the stiffness of this network still remains. The average coordination number studied above is only a measure for the average number of bonds. A better criterion for the stiffness of a network is in our view what we call the ***cross-linking parameter*** Π_c for which we propose the following definition:

$$\Pi_c = \frac{1}{N} \sum_{k=3}^{12} N^{(k)} \tag{3.26}$$

where $N^{(k)}$ denotes the number of particles with k attached neighbors (in primary minimum). Since the sum runs only over particles with three or more attached neighbors, this parameter is a direct measure of the cross-linking in the network: particles which are at the end or in the middle of a linear string are not counted, only particles which are at a crossing of particle string enter into Π_c. The normalization in eqn (3.26) is such that the cross-linking parameter, which is zero for stable suspensions, has a maximum of 1 if all particles have three or more neighbors. Fig. 3.25 shows an example for the increasing cross-linking during coagulation. In the beginning of coagulation small and stringy flocs develop with low cross-linking (a). They connect to form loose and stringy objects (b) which will mainly afterwards increase their stiffness and the stiffness of the network (c).

The evolution of the cross-linking for different solid contents and surface potentials is shown in Fig. 3.26. If Π_b is only considered as the parameter describing the course of destabilization, this figure is primarily a kinetic representation. If the parameter Π_b is read in its original meaning as a measure of the number of bonds in the system, Fig. 3.26 gives an idea about which average coordination number relates to what degree of cross-linking, in the sense of a static interpretation.

We notice that all three curves merge nicely apart from the slightly higher values for sample (B) in the late stages of the process. At least for the solid contents and surface potential range probed in our simulations, one can say that the $\Pi_b \leftrightarrow \Pi_c$-relation in Fig. 3.26 is universal and merge to a master curve.

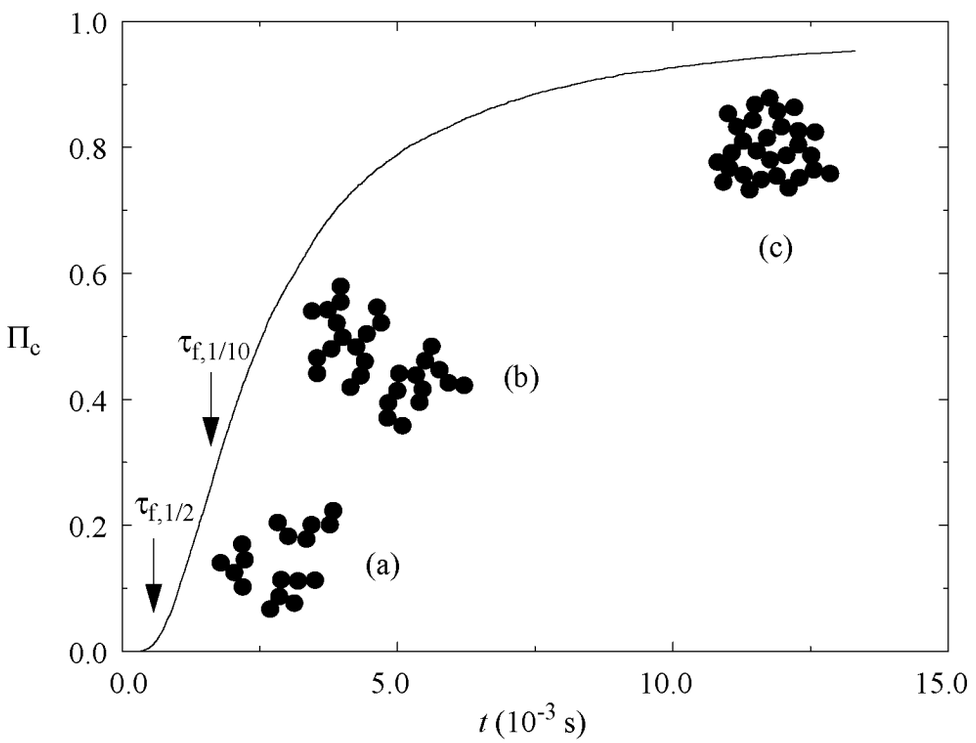

Fig. 3.25: Destabilization of a suspension at $\phi = 0.3$ and $\psi_0 = 0.0$ V: cross-linking parameter Π_c. $\tau_{f,1/2}$ and $\tau_{f,1/10}$ denote the time when the number of free particles decayed to 1/2 or 1/10 respectively. Particle configurations with increasing cross-linking: (a), (b), and (c).

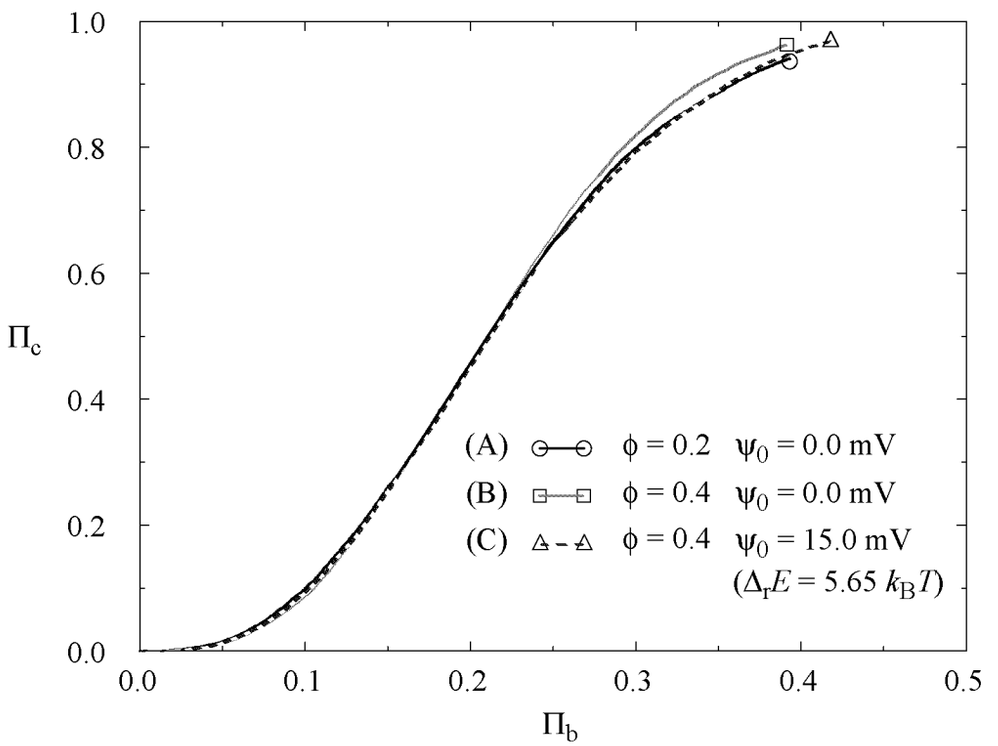

Fig. 3.26: Evolution in the cross-linking parameter Π_c vs. the average coordination number Π_b.

As described in subsection 3.2, the simulations were stopped when all particles were part of the same cluster. It should go without saying that this instant is physically not well defined in the sense that it depends on a single particle event. The structure at the end of the simulations is therefore not the stationary equilibrium configuration but rather a preliminary network that may still undergo further changes. In order to find the proper stationary solution, the simulations would have to be carried on by a multiple of our simulation times because the rearrangements are significantly delayed as the cross-linking in the network proceeds. Nevertheless, it is still possible to predict some characteristics of the final structure without ever calculating it.

In the following, we extrapolate the average coordination number Π_b and the cross-linking parameter Π_c to their stationary value, which shall help to characterize the stable, equilibrated structure. Both quantities were fitted in the simulated time span with suitable fit-functions from which the stationary value was then determined. We have already found in subsection 3.3 that the following fit-function gives a good representation of the simulated data for the average coordination number Π_b:

$$\Pi_b = \Pi_b^{(\infty)} \frac{(t/\tau_b)^\alpha}{1 + (t/\tau_b)^\alpha} \tag{3.27}$$

As $t \to \infty$, we notice that the prefactor $\Pi_b^{(\infty)}$ is the stationary value for the network. As far as the cross-linking parameter is concerned, the similarity of Fig. 3.11 and Fig. 3.25 suggests that one may use one of the three fit-functions (3.11-13). We have found that eqn. (3.13), which is used in the following to fit the Π_c-data, gives the best results

$$\Pi_c = \frac{\alpha_1 t + \alpha_2 t^2}{\alpha_3 + \alpha_4 t + \alpha_5 t^2} \tag{3.28}$$

Here the stationary value ($t \to \infty$) is found to be $\Pi_c^{(\infty)} = \alpha_2/\alpha_5$. In the fitting procedure the error integral criterion was used for optimization. Although the time behavior could be well represented, it has been found to be difficult to determine the stationary value with high accuracy. The fit-function often had a slightly steeper slope than the simulation data in the latest stages of coagulation and in the absence of an energy barrier. We hence expect somewhat too high values for $\Pi_c^{(\infty)}$. In the presence of an energy barrier, the shape of the $t \leftrightarrow \Pi_c$-relation changed in such a way that the fit function (3.28) even reproduced the slope in the late stages of the coagulation with high accuracy.

a) Solid Content Dependence

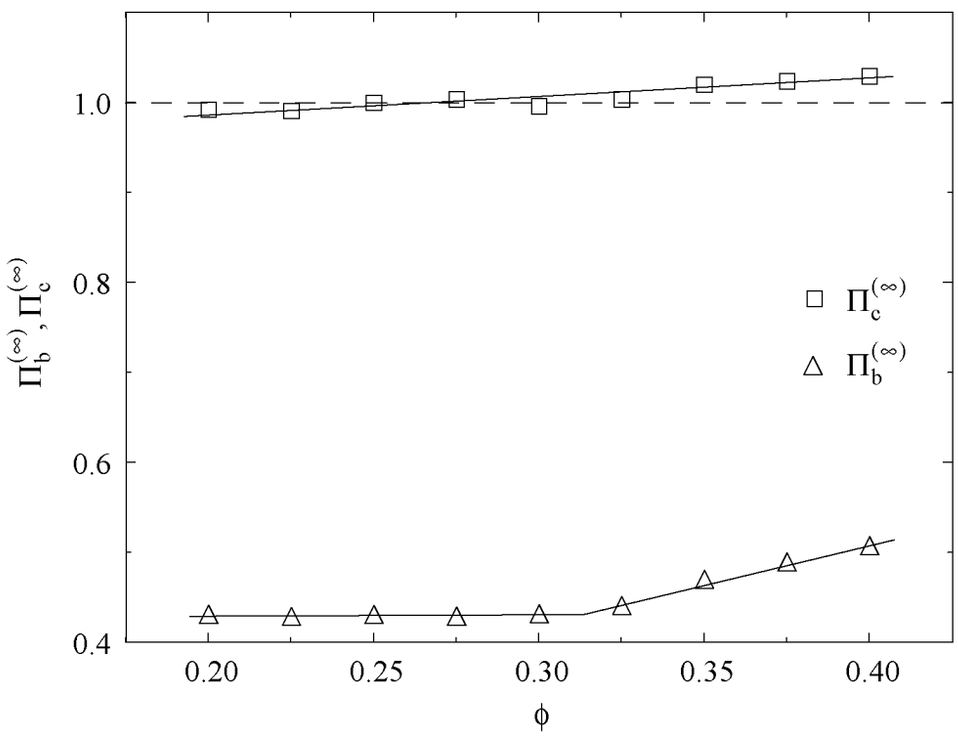

Fig. 3.27: Stationary values for the average coordination number $\Pi_b^{(\infty)}$ and the cross-linking parameter $\Pi_c^{(\infty)}$: dependence on solid content for surface potential ψ_0 = 0.0 mV.

Fig. 3.27 shows the dependence of the stationary values both for the average coordination number and for the cross-linking parameter on the solid content. The lines are drawn as visual guide. We notice that the average coordination number is constant $\Pi_b^{(\infty)} \approx 0.43$ in the range $0.2 \le \phi \le 0.3$ and rises thereafter continuously to $\Pi_b^{(\infty)} \approx 0.51$ at $\phi = 0.4$. This does not quite meet the expectation of an increasing $\Pi_b^{(\infty)}$ over the whole range of solid contents. It seems to be beyond questions that raising the solid content, which leads to less void space, should increase the number of possible bonds in the system. It is not understood why the computer simulations differ from this model. The cross-linking parameter $\Pi_c^{(\infty)}$ shows the expected increase with rising solid content. It has been observed in the fitting procedure that the stationary values are systematically overestimated. Therefore the fact that the curve in Fig. 3.27 raises above the maximal '1' is not surprising. The tendency of the solid content dependence is still evident.

We conclude that increasing solid content leads to a higher average coordination number and a higher degree of cross-linking as expected, apart from the anomalous behavior in $\Pi_b^{(\infty)}$ at lower solid contents.

b) Surface Potential Dependence Without Energy Barrier

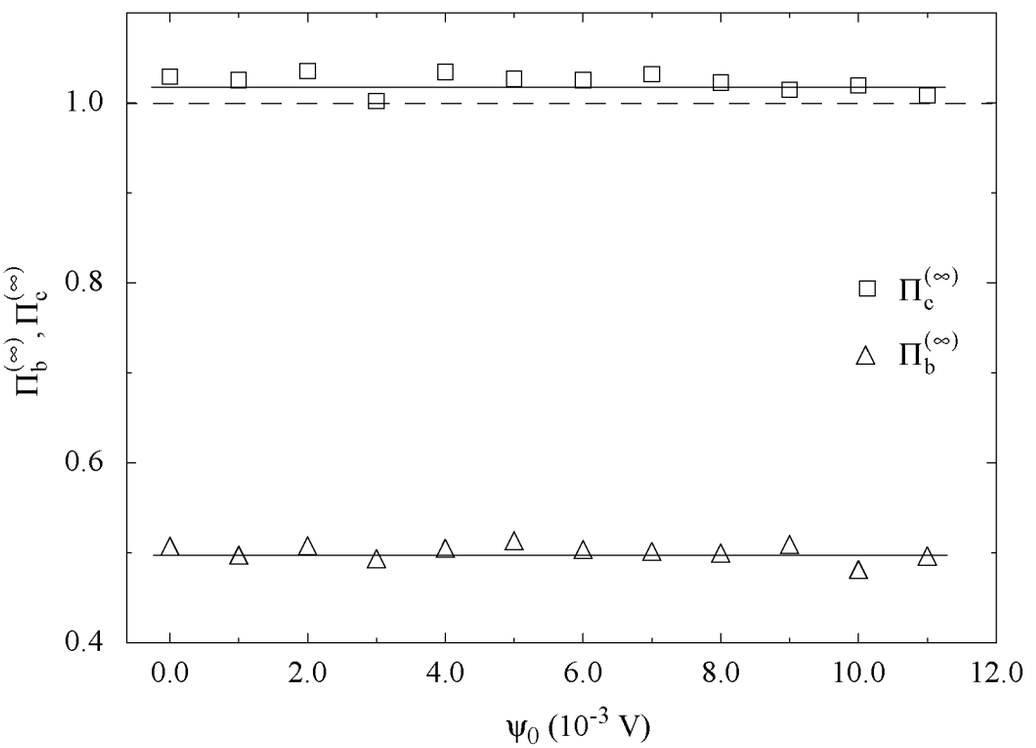

Fig. 3.28: Stationary values for the average coordination number $\Pi_b^{(\infty)}$ and the cross-linking parameter $\Pi_c^{(\infty)}$: dependence on surface potential without energy barrier for solid content $\phi = 0.4$.

It has been argued in subsection 3.3.3 that the effect of low surface potentials, which do not result in an energy barrier in the interaction potential, can be reduced to a change in the effective solid content (see eqn. (3.19)). There, the surface potentials under consideration, $\psi_0 \leq 11$ mV translated into a change of the solid content of only a few percent. It is therefore not surprising that the values for $\Pi_b^{(\infty)}$ and $\Pi_c^{(\infty)}$ in Fig. 3.28 agree almost over the whole surface potential range with the values for $\phi = 0.4$ and $\psi_0 = 0.0$ mV (upper end in Fig. 3.27 and lower end in Fig. 3.28), within the uncertainty in the fitting procedure. It is also evident that without any change in the solid content and in the absence of an energy barrier, nothing hinders the system from forming any bond and attaining a certain degree of cross-linking because no geometric or energetic restrictions are imposed. Only the rate at which the final state is achieved alters with changing surface potential.

We conclude that surface potentials, which do not result in an energy barrier, have negligible effect on the final coordination number and cross-linking; they rather only delay the rate of bond formation.

c) Surface Potential Dependence With Energy Barrier

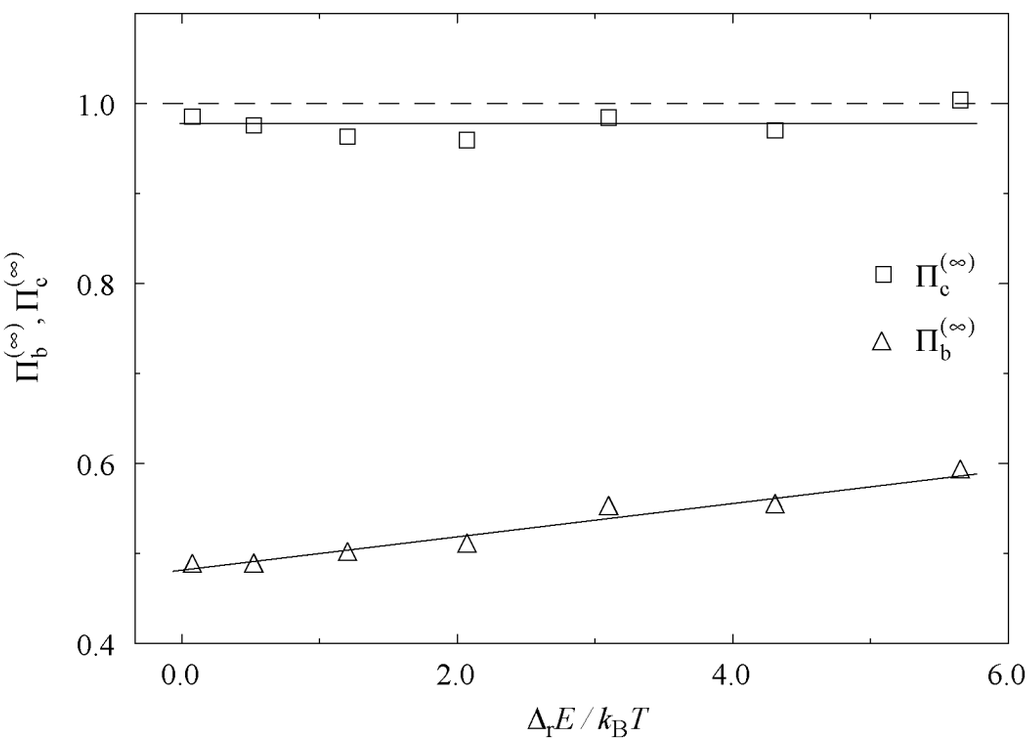

Fig. 3.29: Stationary values for the average coordination number $\Pi_b^{(\infty)}$ and the cross-linking parameter $\Pi_c^{(\infty)}$: dependence on energy barrier for solid content $\phi = 0.4$.

Fig. 3.29 shows the dependence of the final degree of bonding and cross-linking on the energy barrier in the interaction potential. The average coordination number shows a clear increase from $\Pi_b^{(\infty)} \approx 0.5$ to $\Pi_b^{(\infty)} \approx 0.6$ as the energy barrier rises. This may be attributed to the secondary minimum: before making a stable bond in the primary minimum, two particles in the shallow secondary minimum can separate again; if, however, a particle approaches the neck of two bonded particles and is in the secondary minimum of both of these particles, an escape is less probable. This explains the tendency of an increasing number of primary bonds as the energy barrier is raised. As far as the cross-linking parameter $\Pi_c^{(\infty)}$ is concerned, we do not notice a significant influence of the variable energy barrier. In comparison to the $t \leftrightarrow \Pi_c$-curves for low surface potentials, $\psi_0 \leq 11$ mV, the fit-function (3.28) showed no systematic overestimating of the final cross-linking value. The data points for $\Pi_c^{(\infty)}$ indicate that more than 95 % of all particles have at least three attached neighbors, which should finally result in a mechanically rather stable network.

We conclude that a moderate energy barrier in the interaction potential substantially increases the average coordination number of the final network, but has no significant influence on the (high) degree of cross-linking.

Summary

It has been shown above that rising the solid content results in an increased number of bonds, i.e. average coordination number, and in a higher degree of cross-linking in the final structure. The influence of the surface potential can be divided into two regimes. For increasing low surface potentials in the absence of an energy barrier, both the final number of bonds and the final degree of cross-linking are unaltered. At higher surface potentials, which lead to moderate energy barriers, the final network attains a higher number of bonds, the cross-linking being unchanged at a high level.

3.4.3 Network Structure

In this subsection, the network structure will be characterized by the pair distribution function and the bond angle distribution. The former is used to scan the structure in a range of a few particle diameters, whereas the bond angle distribution gives a closer view on the local structure and particle arrangement.

a) Pair Distribution Function

In dilute systems, where only single particle scattering occurs, a good description of the particle configuration is obtained by measuring the static structure factor [89Rus]. In contrast, it is difficult to determine the structure of non-dilute systems. One way to overcome this problem in non-dilute suspensions is to make the sample very thin in the direction of the scattering beam in order to reduce multiple scattering. Another method is to use the novel cross-correlation technique. It allows to separate the multiple scattered signal from the single scattered signal from which the structure can be determined [97Ove, 98Abe, 98Urb]. However, the experimental determination of particle arrangements at solid contents in the range of $0.2 \leq \phi \leq 0.4$ is still not feasible. Nevertheless, we will present pair distribution data on the network structures obtained in our computer simulations for the following two reasons. Firstly, experimental techniques are developing fast and might soon be able to examine suspensions at solid contents comparable to ours which would allow a direct comparison of simulation and experiment. And secondly, one can read certain information on the stability from the pair distribution function as shown in the following.

The pair distribution function $g(\boldsymbol{r})$ gives the probability that any two particles in the system are separated by the given vector $\boldsymbol{r}$, where the normalization is done with respect to a completely homogeneous sample ($g(\boldsymbol{r}) \equiv 1$). Since the starting configurations of the coagulation simulations were well equilibrated and because the system with $N = 8'000$ particles is reasonably large, we assume that the particle structure of the network is isotropic. We hence use only the radial dependent version of the pair distribution function, $g(r)$, which gives the probability that any two particles in the systems are separated by the distance $r = |\boldsymbol{r}|$. It is defined by

$$g(r + \delta r/2) = \frac{\delta N_r(r, r + \delta r)}{\frac{4\pi}{3}\rho[(r + \delta r)^3 - r^3]} \tag{3.29}$$

where $\delta N_r(r, r + \delta r)$ is the number of particle centers within a spherical shell between r and $r + \delta r$ from the center of a reference particle and ρ is the number density of particles per volume.

The excluded volume effect due to the impenetrable spheres leads to $g(r) = 0$ for $r < d$. For separations $r \gg d$, we get $g(r) = 1$ because the chance of finding a

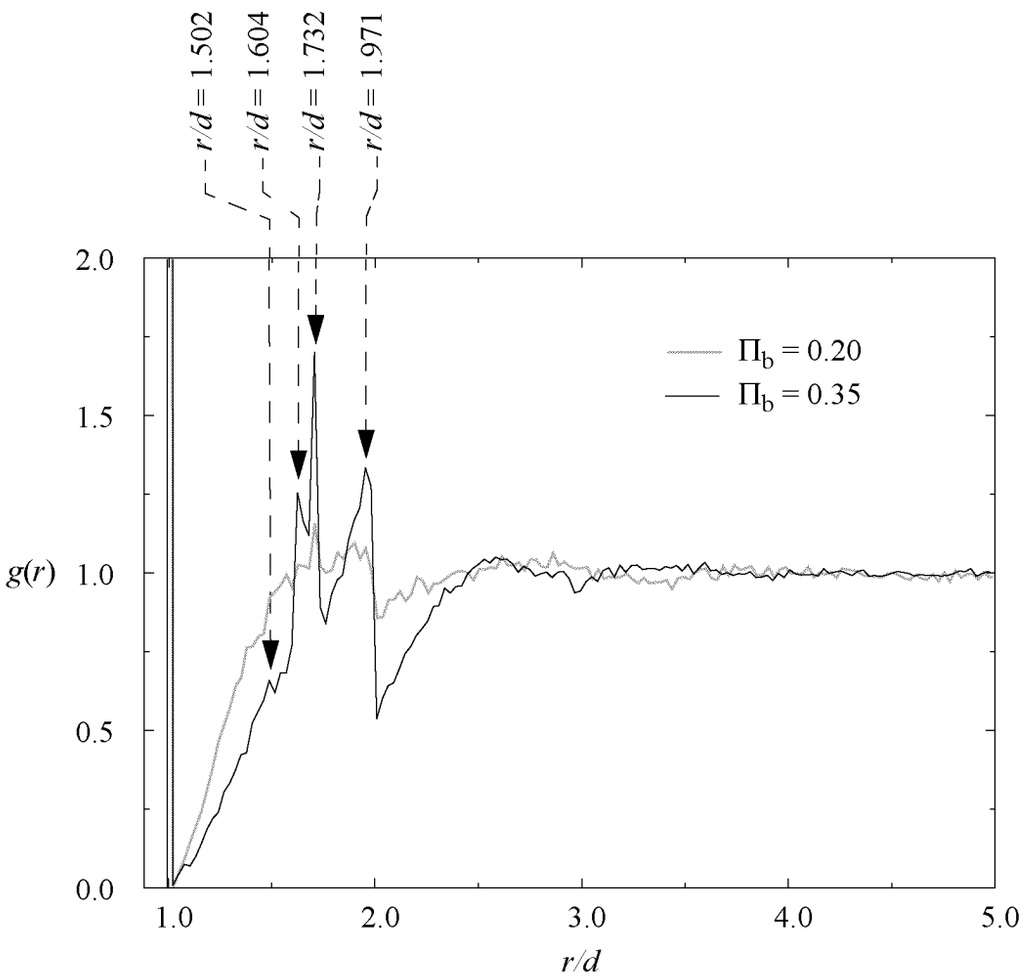

Fig. 3.30: Pair distribution function for $\phi = 0.2$ and $\psi_0 = 0.0$ mV at two stages of the coagulation process, $\Pi_b = 0.20$ and $\Pi_b = 0.35$.

number of particles close to the homogeneous average approaches unity. The interesting region is therefore given by $r \gtrsim d$ as shown in Fig. 3.30-3.32.

Fig. 3.30 shows the pair distribution function for purely attractive van der Waals interaction at two different stages of the coagulation process. Three particular features of the $g(r)$ plot are worthy a note. (i) There is a sharp peak at $r = d$ corresponding to particles in contact, followed by a dramatic drop above. This is attributable to the strong attraction for close particles: if two particles are very close they are necessarily bonded in the next instant, leading to a depletion zone above $r = d$. (ii) The function shows a steady linear increase in the range $d < r \leq 2d$ apart from the peaks at $r \approx 1.7d$. The sudden drop above $r = 2d$ is due to the strong attraction at close surface-to-surface separations, similar to the drop above $r = d$. There is a high probability of finding almost linear three-

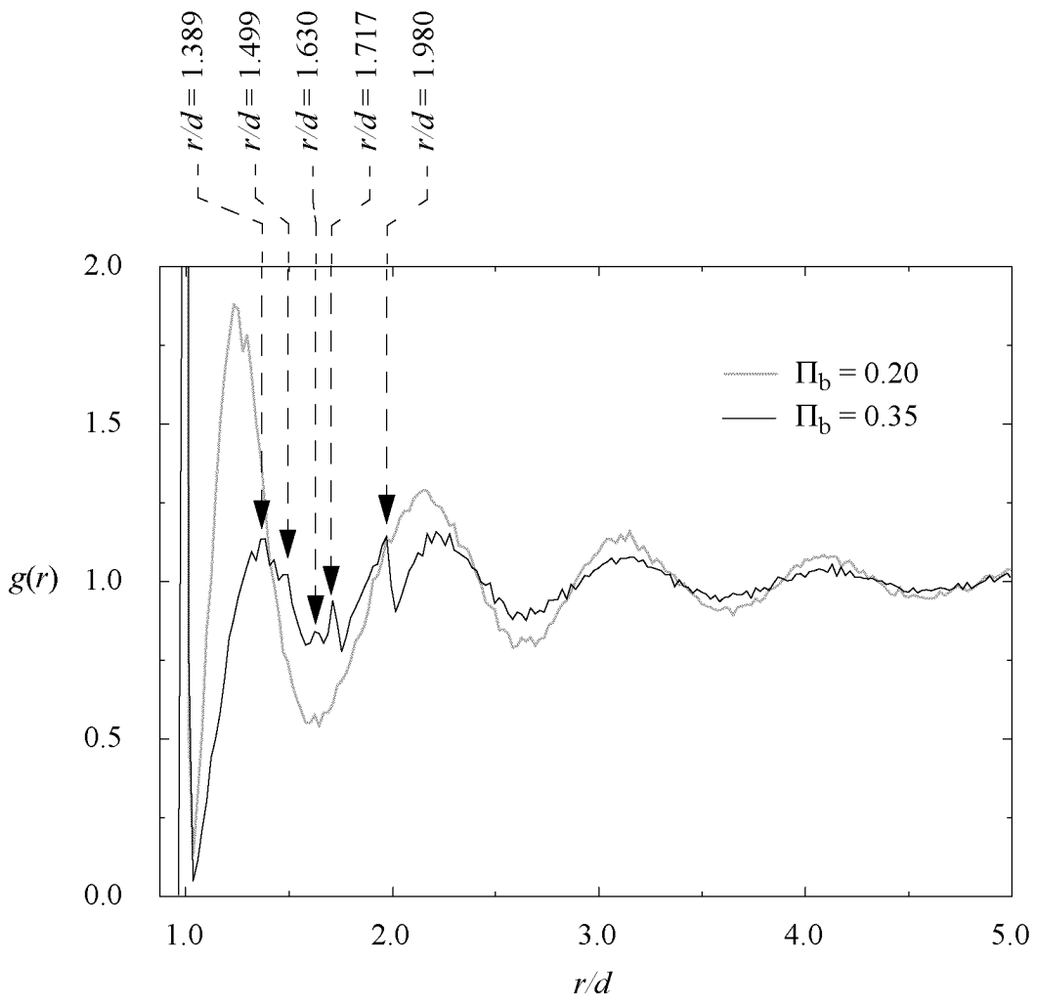

Fig. 3.31: Pair distribution function for $\phi = 0.4$ and $\psi_0 = 0.0$ mV at two stages of the coagulation process, $\Pi_b = 0.20$ and $\Pi_b = 0.35$.

particle configurations ($r \leq 2d$), whereas configurations with $r > 2d$ are less probable. (iii) The pair correlation function is already constant for $r > 4d$ in contrast to the oscillations typically observed in liquids.

The influence of the solid content on the network structure can be seen when comparing Fig. 3.30 and 3.31. Whereas a low solid content of $\phi = 0.2$ allows real particle diffusion before coagulation, the pair distribution function displayed in Fig. 3.31 shows that this is not the case at $\phi = 0.4$. We notice that not only in the intermediate state ($\Pi_b = 0.2$) but also afterwards ($\Pi_b = 0.35$) the coagulation preserves the short and long range oscillations typical for liquids. We therefore conclude that the starting configuration is actually frozen, i.e. quenched, when the interaction potential is switched from repulsive to purely attractive. The depletion zone $r \geq 2d$, which was very pronounced at $\phi = 0.2$, is less strong in the

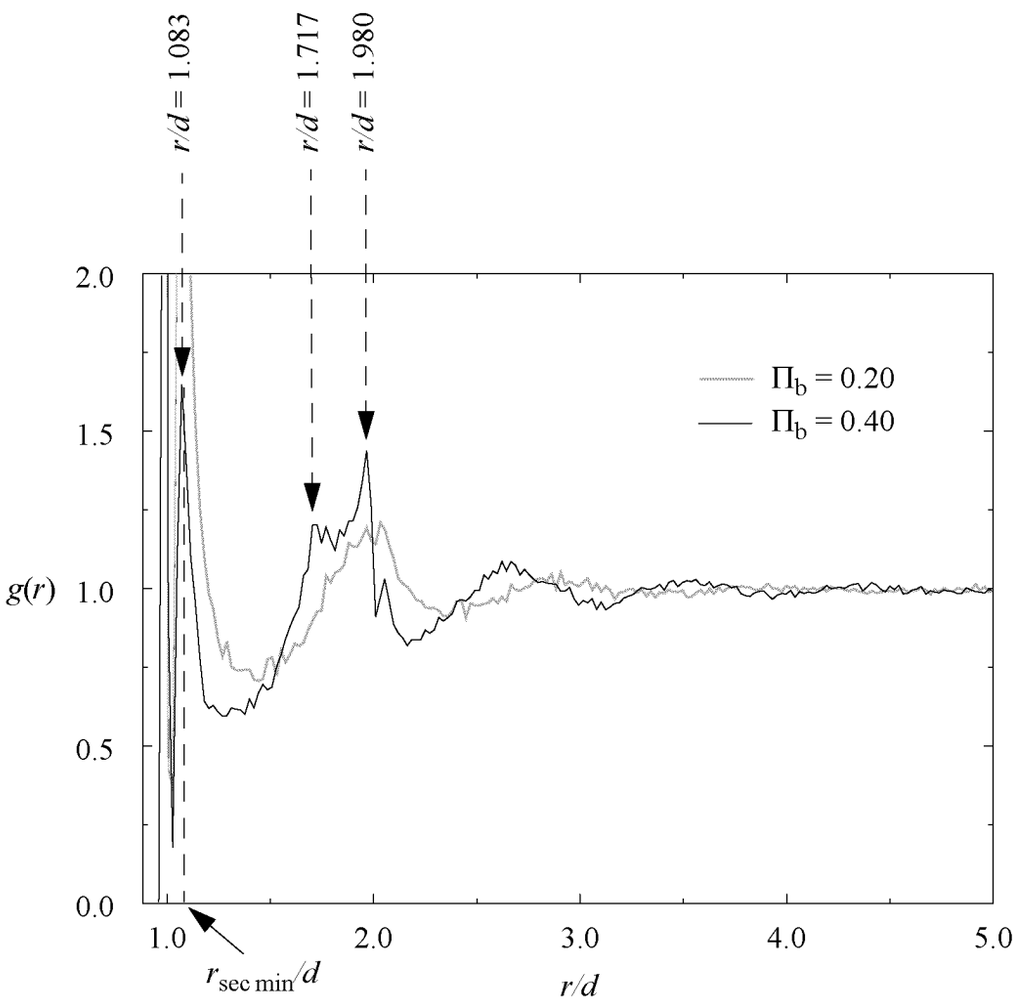

Fig. 3.32: Pair distribution function for $\phi = 0.4$ and $\psi_0 = 15\ mV$ ($\Delta_r E = 5.65\ k_B T$) at two stages of the coagulation process, $\Pi_b = 0.20$ and $\Pi_b = 0.40$.

quenched state for $\phi = 0.4$ as shown above. Furthermore, the long range oscillations do not decay after a few particle diameters as for the lower solid content but remain up to $r \approx 5d$ and even beyond.

Fig. 3.32 shows the pair distribution function for a delayed reaction mechanism due to the presence of an energy barrier in the interaction potential. The structure differs significantly from what has been observed for the purely attractive network (Fig 3.31). The following two points shall be highlighted in particular. (i) The sharp peak at $r = 1.083\ d$ is the twin of the peak at $r = d$. Whereas the latter describes particles in contact, the former originates from particles in secondary minimum: the potential curve in Fig. 3.6 shows that the secondary minimum is at $r_{sec\ min} \approx 1.08\ d$. The height of this peak decreases as the coagulation

proceeds. Although there might be an equilibrium between particles which escape from secondary minimum and such that are captured by it from farther away, surmounting the energy barrier and making a (primary) bond is an irreversible process. This leads to a decreasing population of secondary minimum pairs. (ii) The long range oscillations in the pair distribution functions are lost in the course of coagulation (black curve for $\Pi_b = 0.40$ in Fig. 3.32) in contrast to the situation without an energy barrier (black curve $\Pi_b = 0.35$ in Fig. 3.31). The energy barrier seems to prevent the system from being frozen and allows for more rearrangement before particles come into contact.

It has been mentioned in the introduction (subsection 3.1.3) that a thorough analysis of the pair correlation function indicates whether the network has fractal scaling on an intermediate length scale. Our simulation results do not show any such scaling for all solid contents under consideration. This is in agreement with the results of other groups which report that in highly dense systems the fractal regime may be missing at all [96Bos].

b) Bond Angle Distribution

The pair distribution function defined in eqn. (3.29) allows us to study the order over distances of many particle diameters. However, it fails to give detailed information about the arrangement of nearest neighbors since all this information is concentrated in the interval $d \le r \le 2d$. Rather than a ***radial*** distribution function, we need the distribution of bond ***angles*** between particles, which is defined in Fig. 3.33. Particularly in dense suspensions, such short range structural information helps to identify the building blocks which amount to the mechanical properties of the network. We find the following relation between the separation r of the two outer particles and the bond angle θ $(\pi/3 \le \theta \le \pi)$:

$$\theta = 2 \arcsin\left(\frac{1}{2}\frac{r}{d}\right) \tag{3.30}$$

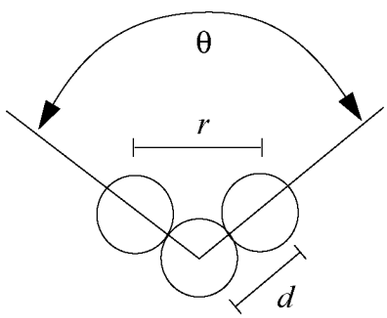

Fig. 3.33: Definition of the bond angle θ.

The bond angle distribution which shall be used to characterize the particle network is given by

$$p(\theta + \delta\theta/2) = \frac{\delta N_\theta(\theta, \theta + \delta\theta)}{\left(\frac{3}{2\pi}\right)\delta\theta\, N_\theta^t} \tag{3.31}$$

Here $\delta N_\theta(\theta, \theta + \delta\theta)$ is the number of particle triplets with a bond angle between θ and $\theta + \delta\theta$, and N_θ^t is the total number of particle triplets. The normalization for $p(\theta)$ is with respect to $p(\theta) \equiv 1$ $(\pi/3 \le \theta \le \pi)$ for a uniform distribution of bond angles.

Studies on bond angle distributions in particulate systems are much less common than studies on the pair distribution function. They are usually not applied to analyze the arrangement of touching particles but to characterize the order over various shells of particles [62Ber, 90McG, 92Bal, 92Can]. It has been noted that two different structures with similar pair distribution functions may still ex-

hibit a significantly different bond angle distribution [92Can]. This underlines the necessity to study both quantities rather than just one. In this study, we will use the bond angle analysis only for touching particles.

The bond angle distribution functions for the various conditions, which were previously considered in terms of pair distribution function (Fig. 3.30-3.32), are given in Fig. 3.34-3.36.

The situation for the destabilization with pure van der Waals attraction ($\psi_0 = 0.0$ mV) at a solid content $\phi = 0.2$ is presented in Fig. 3.34. A schematic representation of the particle configuration for some characteristic bond angles is shown above the plot (a-g). The stars denote bond angles for which no such representation could be found. The following four points in Fig. 3.34 are worth to comment on. (i) The strong peak at $\theta = \pi/3$ originates from the equilateral triangle of particles (a). Because each of the three particles has two neighbors in contact this configuration is very stable and no rearrangements within this block are possible. (ii) The relative amount of bond angles in the interval $\pi/3 < \theta < 0.6\pi$ is lowered as the coagulation proceeds. This is due to the stable configuration (a) at the lower end and the configurations (d-f) at the upper end of this interval respectively. (iii) The three intermediate bond angles (d-f) become more important in the course of the process, which supports the reasoning in (ii). Whereas the peak of the tetrahedral angle (d) is quite narrow, this is not the case for the in-plane configuration (f). There, the distribution is rather wide below the peak value and shows a sharp decrease above. It can be attributed to the fact that this configuration is a three-dimensional array of particles stretched to its limits ($\rightarrow$ sharp decrease above). Less stretched configurations can be obtained by rolling the particle on the left in (f) on the two middle particles. (iv) The relative occurrence of configurations in the interval $2\pi/3 < \theta < \pi$ is not significantly altered with progressing coagulation, apart from the small peak at $\theta = 0.937\pi$.

The maximum value of a peak is not the only measure for the importance of the corresponding bond angle. In order to account also for the width of the peak we have calculated the integral of $p(\theta)$ over the peak-interval (denoted by $\llcorner\!\lrcorner$ in Fig. 3.34-3.36) and normalized this number with respect to the integral over all possible bond angles. The resulting value, which we will denote by $\Re_\theta$, is a measure for the relative occurrence of bond angles in the vicinity of the angle θ. For the most significant angles, the $\Re_\theta$-values are given in Fig. 3.34-3.36.

The bond angle distribution for the same, purely attractive, potential but at a solid content $\phi = 0.4$ is given in Fig. 3.35. The considerations of the pair distribution function have shown that the coagulating system is quenched at this high solid content and only marginal restructuring occurs. As far as the bond angle distribution is concerned, the readers attention shall be drawn to the three main differences in comparison to Fig. 3.34. ($\phi = 0.2$). (i) The bond angle distribution shows a rather broad local maximum in the interval $\pi/3 < \theta < 0.6\pi$ which de-

creases and shifts as the coagulation proceeds. It is not clear in as far this is a general feature of frozen, or quenched, configurations similar to the one studied here. Nevertheless, the data suggest that if the coagulation were followed up to the stable configuration ($t \to \infty$) this peak would be leveled out in favor of the more stable configurations (a) and (c, d). (ii) The peak for the in-plane bond angle (d) and in particular for the tetrahedral bond angle (c) are less pronounced than at lower solid content. (iii) The bond angle distribution drops almost linearly in the interval $2\pi/3 < \theta < \pi$.

It has already been noticed in the pair distribution functions (Fig. 3.30-32) that the existence of an energy barrier strongly affects the structure of the particle network. A comparison of Fig. 3.35 and 3.36 reveals the influence of the energy barrier. Two main differences are discussed in the following. (i) In the intermediate range $\pi/3 < \theta < 0.6\pi$, the broad peak in Fig. 3.35 is replaced by a relatively narrow peak around $\theta = 0.365\pi$. This corresponds to a particle configuration in which the two adjacent particles are not within a primary minimum ((a1) in Fig. 3.36) but only within a secondary minimum ((a2) in Fig. 3.36). The finite separation between particles due to the secondary minimum is indicated by the grey bar in the schematic drawing. We notice that the peak (a2) decreases with increasing process time, similar to the broad peak in Fig. 3.35. Bond angles in this intermediate range are therefore either transformed to primary bonds (a1) or shifted to stable configurations with larger bond angles (b-d2). In principle, every peak that corresponds to an arrangement with only primary bonds should have a twin (e.g. (a1,a2)) where one of the bonds between adjacent particles is replaced by a secondary bond. However, the amplitude of the second twin is much smaller than the amplitude of the first one, which suggests that the occurrence of twins can only be observed for very pronounced peaks. (ii) Fig. 3.36 shows the twin-phenomenon also for the in-plane configuration (d1), where the corresponding twin is shown in (d2).

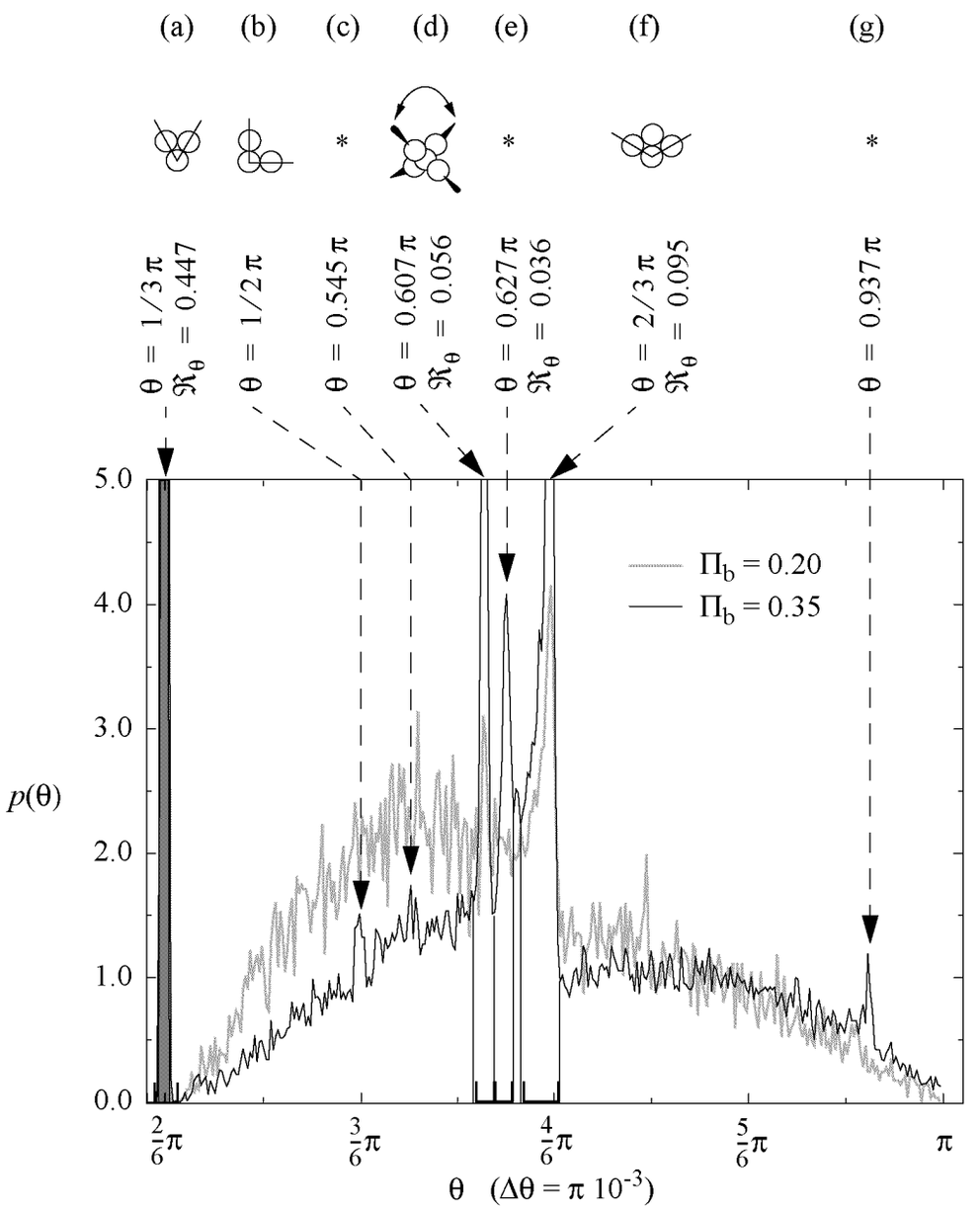

Fig. 3.34: Bond-angle distribution for $\phi = 0.2$ and $\psi_0 = 0.0$ mV at two stages of the coagulation process, $\Pi_b = 0.20$ and $\Pi_b = 0.35$.

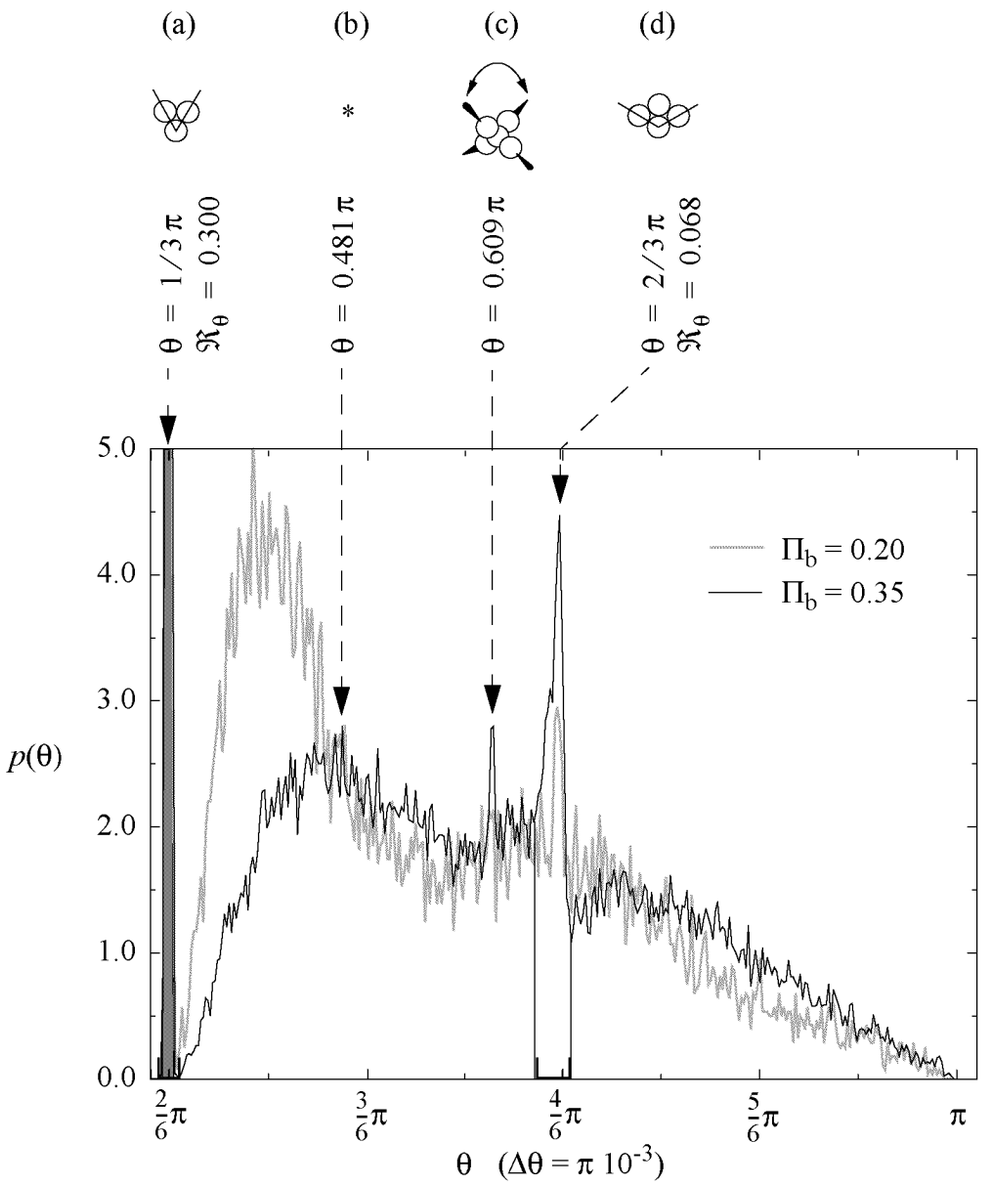

Fig. 3.35: Bond-angle distribution for $\phi = 0.4$ and $\psi_0 = 0.0$ mV at two stages of the coagulation process, $\Pi_b = 0.20$ and $\Pi_b = 0.35$.

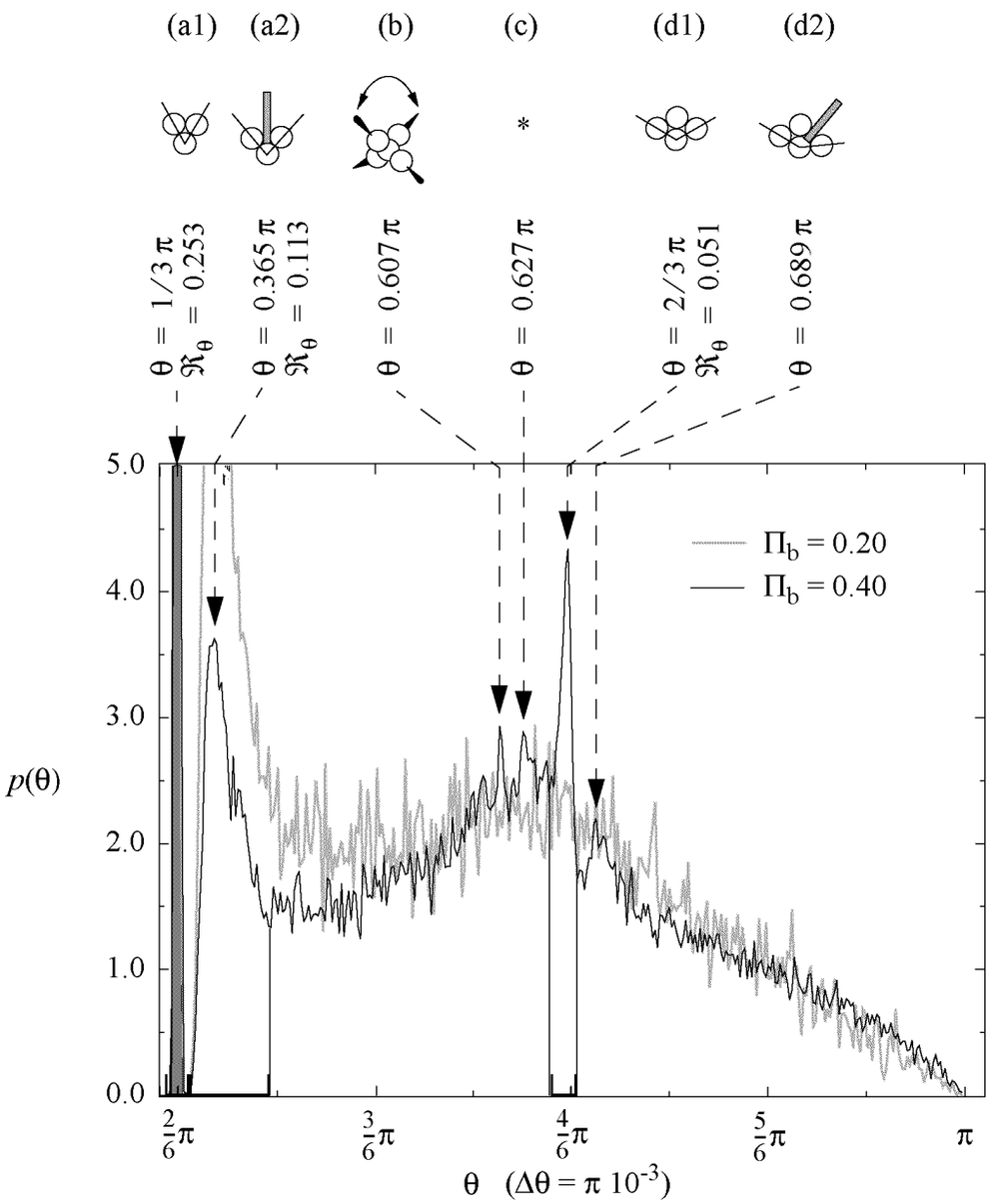

Fig. 3.36: Bond-angle distribution for $\phi = 0.4$ and $\psi_0 = 15\ mV$ ($\Delta_r E = 5.65\ k_B T$) at two stages of the coagulation process, $\Pi_b = 0.20$ and $\Pi_b = 0.40$.

c) Comparing Particle Separations and Bond Angles

The information contained in the interval $1 \leq r/d \leq 2$ of the pair distribution function $g(r)$ and in the interval $\pi/3 \leq \theta \leq \pi$ of the bond angle distribution $p(\theta)$ do not necessarily have the same origin. Not every peak in $g(r)$ corresponds to a bond angle through eqn. (3.30) because also other characteristic particle separations may exist within the network.

Table 3.3 gives a comparison of all characteristic separations r and bond angles θ found in Fig. 3.30-32 and Fig. 3.34-36 respectively. The characteristics are numbered by No. 1 to No. 10c. Different peaks, which have probably the same origin but differ slightly in their values, are indexed by a, b, and c. For several separations read from the pair distribution function, the corresponding angle has not been observed in the bond angle distribution. In this case the angle is listed in brackets (see e.g. No. 3b). The same is also valid for angles where the corresponding separation was not found which is hence listed in brackets (see e.g. No. 4). The three columns at the left of the table show in which system (i.e. for which solid content and for which surface potential) the corresponding peak has been observed. If the characteristic was read from the $g(r)$-data, the entry is 'r' for moderate peaks and 'rr' for strong peaks. Likewise, the observation of favored bond angles is listed by 'a' and 'aa' depending on the sharpness and height of the peak.

On one hand, the bond angle distribution is able to reveal structures which are not captured by the pair distribution function. The single strong peak at $r = d$ stands for any pair of touching particles. Only the bond angle distribution proves the existence of equilateral triangles of particles. Furthermore, particle configurations like No. 4, No. 7, and No. 9 can only be identified by the bond angle distribution and are not detectable in the pair correlation function. On the other hand, No. 10a to No.10c indicate that not all particle separations necessarily correspond to a bond angle: although the peaks in the pair distribution function are well defined and sharp they do not appear in the bond angle distribution.

No.	$r\,(d)$	$\theta\ (\cdot\,\pi)$	$\phi = 0.2$, $\psi_0 = 0$ mV	$\phi = 0.4$, $\psi_0 = 0$ mV	$\phi = 0.4$, $\psi_0 = 15$ mV
1	1.000	0.333	rr/aa	rr/aa	rr/aa
2	1.083	$0.364 \approx 0.365$	-	-	rr/aa
3a	(1.371)	0.481	-	(a)	-
3b	1.389	(0.489)	-	rr	-
4	(1.414)	0.500	a	-	-
5a	1.499 / 1.502	(0.539/0.541)	r	r	-
5b	(1.511)	0.545	a	-	-
6a	1.604	(0.592)	r	-	-
6b	1.630	$0.607 \approx 0.609$	aa	r/aa	a
7	(1.666)	0.627	aa	-	a
8a	1.717	(0.657)	-	r	r
8b	1.732	0.667	rr/aa	aa	aa
9	(1.766)	0.689	-	-	a
10a	1.971	(0.891)	rr	-	-
10b	1.980	(0.910)	-	rr	rr
10c	(1.990)	0.937	a	-	-

Table 3.3: Comparison of characteristic particle separations r and characteristic bond angles θ for different particle networks. Features showing a moderate or a strong peak, respectively, in the pair distribution function are denoted by 'r' and 'rr'; characteristics observed in the bond angle distribution are correspondingly denoted by 'a' and 'aa'.

Summary

The influence of the solid content and of the surface potential on the structure of the particle network has been quantified. Our results correspond to other simulations where the fractal dimension of the final structure and the pair distribution function have been examined [87Ans1, 87Ans2, 87Dic]. In our study, we have combined these informations with the data on the average coordination number, the cross-linking parameter, and the bond angle distribution function to give a better interpretation of the coagulation process.

At low solid content, the particles have enough time for rearrangement, whereas at higher solid content the purely attractive interaction tends to quench the system and preserve the long range oscillations in the pair distribution function which are typical for liquids. Quenching has been found to disappear by the introduction of an energy barrier in the interaction potential. It delays the coagulation in such a way that the system has enough time for particle rearrangement. The bond angle distribution is particularly sensitive in the range $\pi/3 < \theta < 0.6\,\pi$. Since the systems were percolating and showed no shrinkage for all solid contents $0.2 \leq \phi \leq 0.4$, it becomes clear that small bond angles are less probable at low solid content than at higher solid content. For $\phi = 0.4$, the energy barrier narrows the angle distribution within the range of intermediate angles $\pi/3 < \theta < 0.6\,\pi$. Nevertheless, the relative amount of these intermediate bond angles decreases with increasing coagulation because they migrate to more stable configurations.

3.4.4 Summary and Conclusions

The focus of section 3.4 was on the structure of the particle network in percolating systems. The effect of solid content and of surface potential has been studied in detail. With emphasis on the design of good mechanical properties of the resulting gel, we summarize the main results again.

Increasing the solid content has shown to lead to fewer and heavier nucleation sites. However, no significant difference in the compactness of these clusters in terms of the fractal dimension could be detected. In accordance with the expectations, the average coordination number as well as the cross-linking of the stable configuration raised with the solid content. Nevertheless, the pair distribution function and the bond angle distribution function have revealed that the higher the solid content the more does the network correspond to a quenched liquid structure. We therefore conclude that the positive effect of the higher solid content due to an increase in the number of bonds is diminished by the unrelaxed, frozen structure.

The presence of an energy barrier was found to decrease the number of nucleation sites which become heavier and more compact for increasing energy barrier. However, this does not necessarily mean that the final network of samples with higher energy barrier is more heterogeneous and is therefore mechanically less stable. The considerations on the average coordination number and the cross-linking parameter have shown the positive influence of the energy barrier. The network structure has been examined with the pair distribution function: in the absence of an energy barrier the particle structure is quenched whereas its presence allows rearrangements which probably lead to a more stable network. The bond angle distribution function was employed to characterize the local structure and to identify the building blocks. Which of these have what effect on the mechanical stability of the network needs to be shown in additional work. We consider however a low probability for bond angles in the intermediate range $\pi/3 < \theta < 0.6\,\pi$ to be a good criterion for a stable and not-quenched sample. This should influence the mechanical stability of the network in a positive manner.

In order to achieve a particle network with high mechanical stability we would make the following suggestions. It is favorable to work at the highest possible solid content which still allows a reasonable handling of the liquid state. The upper limit on the solid content depends on the preparation of a well dispersed suspension and on the highly viscous and shear thickening behavior. Once the solid content is fixed, the surface potential and hence the shape of the interaction potential has to be tuned. Our simulation results suggest that the presence of an energy barrier by-passes the problem of quenching as it allows rearrangements and a better scanning of the phase space. Although not tested in our simulations, we assume that these un-quenched structures attain higher mechanical stability in their final state. However, we would like to mention that these advantages go along with a delayed reaction mechanism as shown in section 3.3. Another diffi-

culty is the experimental realization of such an interaction potential. Only a subtle combination of all parameters in the interaction potential leads to a shallow secondary energy minimum as used in our simulations.

3.5 Summary and Conclusions

The destabilization of colloidal suspensions was the topic of Chapter 3. In this summary, special attention is drawn to the relation of our computer simulation results to the real system behavior. In particular, it will be shown in as far our simulations narrow the gap between the idealized model system and the complex material properties observed in the laboratory.

In laboratory experiments, the destabilization of a colloidal suspension is monitored and quantified by the change in the mechanical properties and in the particle configuration. Whereas the mechanical criterion can in principle by used for arbitrary solid contents, scattering experiments to determine the arrangement of particles are not feasible in dense suspensions. A link between structural information and mechanical properties can therefore not be achieved on an experimental level for dense suspensions. The computer simulations in this study have proposed a first step away from the fundamental equations of motion of the particles towards a better understanding of the material properties. An algorithm has been presented (section 3.2) which allows us to study the transition from the stable suspension to a percolating network as summarized in the following.

a) Characteristic Time Scales

Several characteristic time scales have been identified. Their dependence on the solid content and on the surface potential, including energy barriers, has been examined (subsection 3.3.2). Each of these dependencies could be captured by simple formulas. Although not all of the values for the fitted parameters meet the expectations, a better understanding of the coagulation mechanism was gained. Generally speaking, the higher the solid content and the less the double layer repulsion, the faster is the coagulation process. In addition, short and long time scales do not depend to the same degree on the variation of the solid content and of the surface potential. From this, we have deduced the different cluster-cluster bonding mechanisms between the presence of an energy barrier and its absence (subsection 3.3.3). We would like to emphasize that such a result is rather difficult to obtain directly in large systems as they are studied here. The analysis of the characteristic time scales, however, was the direct way to this phenomenon.

The coagulation time scales reported here for given attractive interaction potential are much shorter than the characteristic coagulation times observed in experiments. This suggests that the time limiting factor in the solidification of the real system is not the particle dynamics but rather the slow change in the interaction potential itself.

b) Labelling the Stage of Coagulation

Due to the large differences in time scales with respect to the solid content and to the surface potential, we have introduced the average coordination number as parameter to label the different stages of coagulation (subsection 3.3.1). It allows

to compare equivalent stages (equivalent with respect to the number of bonds) of systems which coagulate at very different rates. This has been used to elucidate the different structural developments in the network. It is evident that this procedure is not applicable in experiments, since the measurement of such a parameter is not feasible with current techniques. However, we propose that an equivalent procedure should be followed also in experiments, e.g. to label the stages with respect to the relative amount of turbidity in the suspension.

c) Development of the Network Structure

Structural information has been obtained from the characterization of the intermediate nucleation sites, i.e. of the clusters, (subsection 3.4.1) and of the final percolating network (subsection 3.4.3). The whole coagulation process has also been followed with respect to the average coordination number and the degree of cross-linking (subsection 3.4.2). The analysis of the structure is divided into two regimes. In the early stages of coagulation, the nucleation sites have been characterized by their number, mass, and fractal dimension. In the later stages, the development of the structure has been followed by the pair distribution function and the bond angle distribution. Finally, the stiffness of the stationary network has been measured by the steady state value of the average coordination number and of the cross-linking parameter.

Raising the solid content has the following effects on the developing structure. (i) It leads to fewer and heavier nucleation sites, but has only little effect on their compactness. (ii) The pair distribution function and the bond angle distribution have shown that the degree of quenching is increased, which most probably leads to worse mechanical properties. (iii) Both the average coordination number as well as the cross-linking reach higher values. From these three points, we conclude that increasing the solid content has not only advantages as soon as also mechanical aspects are of interest (see point (ii)). However, it will be shown in the following that the occurrence of the disadvantageous quenching can be reduced by changing the interaction potential appropriately.

Switching on the double layer repulsion to an extent which results in a secondary minimum affects the coagulation in the following manner. (i) There are only slightly fewer and heavier nucleations sites with significantly increased internal density. (ii) Both the pair distribution function as well as the bond angle distribution indicate that quenching is substantially reduced. (iii) The average coordination number and the cross-linking of the final network reach higher values.

The above summary of the structural information gained from the computer simulations leads us to the following conclusion. A high solid content is not the only criterion for obtaining a network with high mechanical stability. The presence of a shallow secondary energy minimum and of an energy barrier are desirable since they allow for the necessary relaxation of the structure. These rearrangements are crucial in order to avoid a rapid quenching. The ideal experimental process would therefore be the following. First, the stable suspension

should be driven to a state in which the interaction potential has a shallow secondary minimum and a large enough energy barrier which prevents coagulation in the primary minimum. Thereby, the system can do a better scanning of the phase space to find the most stable and stress-free configuration. Due to the large energy barrier, primary bonds do not occur whereas secondary bonds can be made and resolved whenever the system wants to switch to a 'better' configuration. Only after these rearrangements, the double layer repulsion shall be reduced further until the energy barrier disappears and all secondary bonds change to primary bonds. We expect that this procedure results in a particle network with a good structure and a high degree of cross-linking.

d) Applicability and Limitations of the Current Technique

Finally, we would like to add the following general comments on the methodology by which the evolution of a particle arrangement is examined.

First, it has been shown (subsection 3.2.5) that the simulations become increasingly time-consuming as the solid content is lowered which renders the study of dilute systems more difficult. This is in contrast to scattering experiments. As the solid content is raised, multiple scattering becomes important and reduces the relative amount of single scattering significantly. Therefore, it is extremely difficult to get structural information on coagulating systems for solid contents as high as the ones considered in this study. We conclude that the use of computer simulations becomes more important and more useful the higher the solid content gets.

Second, the simulation technique used in this study does not allow to probe the mechanical response of the network to an applied strain or stress. This limitation occurs because the bonds between particles have been considered as geometrical constraints on the mobility of the particles rather than as dynamical quantities. For a detailed study of the linear and/or nonlinear viscoelastic properties of the network, contact forces as well as the finite elasticity of the particles should be accounted for.

3.6 References

[54Ree] H. Reerink and J. T. G. Overbeek, "The rate of coagulation as a measure of the stability of silver iodide sols", *Disc. Farad. Soc*, *18*, 74–84 (1954).

[62Ber] J. D. Bernal, "The Bakerian lecture, 1962: The structure of liquids", *Proc. Roy. Soc. London A*, *280*, 299–322 (1962).

[71Hon] E. P. Honig, G. J. Roebersen, and P. Wiersema, "Effect of hydrodynamic interaction on the coagulation rate of hydrophobic colloid", *J. Coll. Interf. Sci.*, *36*, 97–109 (1971).

[77Ryc] J.-P. Ryckaert, G. Ciccotti, and H. J. C. Berendsen, "Numerical integration of the cartesian equations of motion of a system with constraints: molecular dynamics of n-alkenes", *J. Comput. Phys.*, *23*, 327–341 (1977).

[83Ben] C. N. Bensley and R. J. Hunter, "The coagulation of concentrated colloidal dispersions at low electrolyte concentrations", *J. Coll. Interf. Sci.*, *92*(2), 436–447 (1983).

[83Hen] E. M. Hendriks, M. H. Ernst, and R. M. Ziff, "Coagulation equations with gelation", *J. Stat. Phys.*, *31*(3), 519–563 (1983).

[84All] S. A. Allison and J. A. McCammon, "Transport properties of macromolecules", *Biopolymers*, *23*, 167–186 (1984).

[84Dic] E. Dickinson, "Kinetic theory of coagulation for a concentrated dispersion", *J. Coll. Interf. Sci.*, *98*, 587–589 (1984).

[84Wei] D. A. Weitz and M. Oliveria, "Fractal structures formed by kinetic aggregation of aqueous gold colloids", *Phys. Rev. Lett.*, *52*(16), 1433–1436 (1984).

[85Wei] D. A. Weitz, J. S. Huang, M. Y. Lin, and J. Sung, "Limits of the fractal dimension for irreversible kinetic aggregation of gold colloids", *Phys. Rev. Lett.*, *54*(13), 1416–1419 (1985).

[86Ern] M. H. Ernst, "Kinetics of clustering in irreversible aggregation", in *Fractals in physics*, L. Pietronero and E. Tosatti, Eds., Fractals in physics, Trieste, Italy, ICTP, North-Holland, Elsevier, pp. 289–302 (July 9–12, 1985 1986).

[86Sch] D. W. Schaefer and K. D. Keefer, "Structure of random silicates: polymers, colloids, and porous solids", in *Fractals in physics*, L. Pietronero and E. Tosatti, Eds., Fractals in physics, Trieste, Italy, ICTP, North-Holland, Elsevier, pp. 39–45 (July 9–12, 1985 1986).

[86Wei] D. A. Weitz and Y. Lin, "Dynamic scaling of cluster-mass distributions in kinetic colloid aggregation", *Phys. Rev. Lett.*, *57*(16), 2037–2040 (1986).

[87Ans1] G. C. Ansell and E. Dickinson, "Brownian-dynamics simulation of the formation of colloidal aggregate and sediment structure", *Farad. Disc. Chem. Soc.*, *83*, 167–177 (1987).

[87Ans2] G. C. Ansell and E. Dickinson, "Short-range structure of simulated colloidal aggregates", *Phys. Rev. A*, *35*(5), 2349–2352 (1987).

[87Cam] C. Cametti, P. Codastefano, and P. Tartaglia, "Light-scattering measurements of slow coagulation in colloids: deviations from assymptotic time scaling", *Phys. Rev. A*, *36*(10), 4916–4921 (1987).

[87Dic] E. Dickinson, "Short-range structure in aggregates, gels and sediments", *J. Coll. Interf. Sci.*, *118*(1), 286–289 (1987).

[87Hor] D. S. Horne, "Determination of the fractal dimension", *Faraday Discuss. Chem. Soc.*, *83*, 259–270 (1987).

[87Mar] J. E. Martin, *Time-dependent effects in disordered materials*, Vol. 167 of *NATO ASI, Series B: Physics*, Plenum Press, N.Y., chapter: Polymer dynamics and gelation, pp. 425–449 (1987).

[87Son] H. Sonntag and H. Strenge, *Coagulation kinetics and structure formation*, Plenum Press, New York (1987).

[88Mea1] P. Meakin, "Fractal aggregates", *Adv. Coll. Interf. Sci.*, *28*, 249–331 (1988).

[88Mea2] P. Meakin, "Models for colloidal aggregation", *Ann. Rev. Phys. Chem.*, *39*, 237–267 (1988).

[89Ger] R. M. German, *Particle packing characteristics*, Metal Powder Industries Federation (1989).

[89Rus] W. B. Russel, D. A. Saville, and W. R. Schowalter, *Colloidal dispersions*, Cambridge Univ. Press (1989).

[90Dic] E. Dickinson, *The structure, dynamics and equilibrium properties of colloidal systems*, Vol. 324 of *ATO ASI Series; Series C: Mathematical and Physical sciences*, Kluwer Academic, Dordrecht, chapter: Computer simulation of the coagulation and flocculation of colloidal particles, pp. 707–727 (1990).

[90McG] R. L. McGreevy and L. Pusztai, "The structure of molten salts", *Proc. Roy. Soc. London A*, *430*, 241–261 (1990).

[91Wan] Q. Wang, "On colloidal suspension Brownian stability ratios: theoretical approaches", *J. Coll. Interf. Sci.*, *145*(1), 99–107 (1991).

[92Bal] U. Balucani and R. Vallauri, "Evolution of bond-angle distribution from liquid to glassy states", *Chem. Phys. Lett.*, *166*(1), 77–81 (1992).

[92Bre] L. G. B. Bremer, *Fractal aggregation in relation to formation and properties of particle gels*, PhD thesis, Wageningen Agricultural University, Netherlands (1992).

[92Can] M. Canales and J. A. Padró, "On the bond-angle distribution in liquids and liquid solutions", *Mol. Sim.*, *8*, 335–344 (1992).

[92Pre] W. H. Press, S. A. Teukolsky, W. T. Vetterling, and B. P. Flannery, *Numerical recipes in fortran: the art of scientific computing*, Cambridge Univ. Press, 2nd ed. (1992).

[92Vis] T. Viscek, *Fractal growth phenomena*, World Scientific, Singapore, 2nd ed. (1992).

[93Hun] R. J. Hunter, *Introduction to modern colloid science*, Oxford Science Publications, Oxford, chapter: Particle interaction and coagulation, pp. 262–298. (1993).

[93In] M. In and R. K. Prud'homme, "Fourier transform mechanical spectroscopy of the sol-gel transition in zirconium alkoxide ceramic gels", *Rheol. Acta*, *32*, 556–565 (1993).

[94Dic] E. Dickinson, "Computer simulation of particle gel formation", *J. Chem. Soc. Farad. Trans.*, *90*(1), 173–180 (1994).

[94Gra] T. J. Graule, F. H. Baader, and L. J. Gauckler, "Enzyme catalysis of ceramic forming", *J. Mat. Edu.*, *16*, 243–267 (1994).

[95Baa] F. H. Baader, "Enzymkatalisiertes Formgebungsverfahren für Aluminium-Keramiken", PhD thesis, Diss ETH No. 11208, ETH Zürich, Switzerland (1995).

[95Bij] B. H. Bijsterbosch, M. T. A. Bos, E. Dickinson, J. H. J. van Opheusden and P. Walstra, "Brownian dynamics simulation of particle gel formation: from Argon to yoghurt", *Farad. Discuss.* 101, 51–64 (1995)

[95Eli] M. Elimelech, J. Gregory, X. Jia, and R. Williams, *Particle deposition and aggregation*, Colloid and surface engineering, Butterworth-Heinemann (1995).

[95Gra] P. S. Grassia, E. J. Hinch, and L. C. Nitsche, "Computer simulations of Brownian motion of complex systems", *J. Fluid Mech.*, *282*, 373–403 (1995).

[95Mea] P. Meakin, "Progress in DLA research", *Physica D*, *86*, 104–112 (1995).

[96Bar] S. Barany, M. A. C. Stuart, and G. J. Fleer, "Coagulation rate of silica dispersions investigated by single-particle optical sizing", *Coll. Surf. A*, *106*(2-3), 213–221 (1996).

[96Bos] M. T. A. Bos and J. H. J. van Opheusden, "Brownian dynamics simulation of gelation and aging in interacting colloidal systems", *Phys. Rev. E*, *53*(5), 5044–5050 (1996).

[96Ött] H. C. Öttinger, *Stochastic processes in polymeric fluids*, Springer, Berlin (1996).

[97Bur] J. L. Burns, Y. Yan, G. J. Jameson and S. Biggs, " A light scattering study of the fractal aggregation behaviour of a model colloidal system", *Langmuir*, *13*(24), 6413–6420 (1997).

[97Ove] E. Overbeck, C. Sinn, T. Palberg, K. Schatzel, "Probing dynamics of dense suspensions: three-dimensional cross-correlation technique", *Coll. Surf. A*, *122*(1-3), 83–87 (1997).

[97Sil] L. E. Silbert, J. R. Melrose, and R. C. Ball, "Colloidal microdynamics: Pair-drag simulations of model-concentrated aggregated systems", *Phys. Rev. E*, *56*(6), 7067–7077 (1997).

[97Whi] M. Whittle and E. Dickinson, "Brownian dynamics simulation of gelation in soft sphere systems with irreversible bond formation", *Mol. Phys.*, *90*(5), 739–757 (1997).

[98Abe] L. B. Aberle, P. Hulstede, S. Wiegand, W. Schroer, W. Staude, "Effective superposition of multiply scattered light and dynamic light scattering", *Appl. Optics*, *37*(27), 6511–6524 (1998).

[98Urb] C. Urban, P. Schurtenberger, "Characterization of turbid colloidal suspensions using light scattering techniques combined with cross-correlation methods", *J. Coll. Interf. Sci. 207*(1), 150–158 (1998).

[98Yan] J. A. Yanez, E. Laarz, and L. Bergström, "Viscoelastic properties of particle gels", (submitted to *J. Coll. Interf. Sci.*on 3/1998).

[99Bal] B. Balzer and M. K. M. Hruschka and L. J. Gauckler, "Coagulation kinetics and mechanical behavior of wet alumina green bodies produced via DCC", (submitted to *J. Coll. Interf. Sci.* on 1/1999).

[99Gau] L. J. Gauckler, T. J. Graule, F. H. Baader, J. Will, "Enzyme Catalysis of Alumina Forming", *Key Eng. Mat. 159–160*, 135–150 (1999).

[99Hel] J. Helbig, M. Hütter, and U. Schönholzer, "Lack of syneresis during gelation of dense colloidal suspensions", submitted to *J. Coll. Interf. Sci.* march 1999.

Chapter 4

Outlook

Outlook

The aim of this thesis was to relate the macroscopically observed material properties of colloidal systems to the underlying microstructure which, in turn, is determined by the interaction potential and the solid content. To achieve this, assumptions have been made throughout this work which need to be discussed in more detail. Furthermore, the simulations (and thus also the results) are limited in their applicability to the real system. The goal of this section is to collect the main points which need to be addressed in future work.

4.1 Stable Suspension

4.1.1 General

The following three points are of general interest, irrespective of whether hydrodynamic interactions are included or not. They are related to the equilibrium properties of the suspension and to the extended Stokes-Einstein relations discussed previously in this study.

- *Mean square displacement*

  In order to get a better understanding of the particle dynamics in a suspension at equilibrium, the mean square displacement has been measured (subsection 2.3.2). For all solid contents under consideration, the system has high diffusivity for short times. Beyond, there is a continuous transition to a regime where the diffusion is hindered by the presence of other particles. In order to quantitatively compare the mean square displacement for different solid contents, fit-functions have been used to characterize the transition regime. Although the stretched exponential function is a good representation of the simulation data for intermediate and long times, the implication of an infinitely large short-time diffusion is unsatisfactory. This has two consequences. Firstly, it is not possible to quantify the short-time diffusion coefficient. Secondly, the frequency-dependent Stokes-Einstein relation cannot be fulfilled. It is therefore necessary to find a description of the mean square displacement data (and the corresponding parameters β_1, β_2,...) of the form

  $$\langle \Delta \boldsymbol{r}^2(t) \rangle = g(t;\beta_1, \beta_2, \ldots)$$

  which (i) allows to fit the finite short- and long-time diffusion coefficients independently and (ii) gives a good representation of the transition range.

- *Stress autocorrelation function*

  The stress autocorrelation function at equilibrium is a decreasing function of time. However, the determination of the long-time tail is a difficult task due to the large relative errors (subsection 2.3.3). In order to improve the statistics of the long-time values, one needs to examine larger systems over a longer time span. Only then, one can judge whether the decay is a stretched exponential function or follows another law. Once the appropriate fit-function of the form

$$C_s(t) = f(t;\alpha_1, \alpha_2, \ldots)$$

  and the corresponding parameters (α_1, α_2,...) are known, the linear viscoelastic behavior can be derived and discussed.

- *Extended Stokes-Einstein relation*

  The extended frequency dependent (subsection 2.3.4) Stokes-Einstein relation, which has been tested in this study, is of big interest. It provides an alternative route to determine the linear viscoelastic behavior from the self-diffusion data of the particles, or vice versa. The simulation results have shown that this relation is not valid for any of the solid contents under consideration and, surprisingly enough, that best agreement is found not for the lowest but rather for one of the higher solid contents. The potential use of this extended relation justifies that the reason for this failure is clarified.

4.1.2 Hydrodynamic Interaction

The simulation results have shown that the short range hydrodynamic lubrication has a significant influence on the high shear rate rheology of the suspension. In particular, it leads to shear thickening which has been of primary interest in the second part of Chapter 2. Nevertheless, some points need additional detailed analysis:

- *Extended Stokes-Einstein relation*

  The effect of the hydrodynamic interaction on the stress autocorrelation function and on the self-diffusion of the particles has to be examined since it may improve the validity of the frequency dependent Stokes-Einstein relation at equilibrium. It probably clarifies why the relation has been successfully applied in experiments but fails in our simulations (subsection 2.3.4).

- *Determination of nearest neighbors, cut-off, and regularization*

  The hydrodynamic interaction has been accounted for in terms of the short range lubrication mode (subsection 2.5.1). Since this limit of interaction is valid for close particles only, special care must be taken in how to determine nearest neighbors and in where to cut the interaction range off. In this study, the form of the close-approach limit of the interaction has been used up to a certain cut-off separation (subsection 2.5.2). In future work, one should consider to regularize, i.e. to smooth, the interaction below the cut-off. A first improvement is to account for the higher order terms in the lubrication limit, which can be found in the corresponding literature [84Jef, 91Kim, 92Jef].

- *Inversion of resistance matrix*

  Although the inclusion of hydrodynamic interaction is physically reasonable, its applicability is limited to small systems. The manipulations with second- and higher-rank tensors make an up-scaling difficult. Nevertheless, this study has shown that the only remaining problem is the inversion of the resistance matrix. Here, the pre-conditioned conjugate gradient technique has been employed (subsection 2.5.2). However, the results indicate that the relative performance drops when raising the shear rate and, in particular, when increasing the number of particles (subsection 2.7.4). Since hydrodynamic interactions are important in dense colloidal suspensions, investigations of other solutions which render large-scale simulations feasible are necessary.

4.2 Coagulation and Particle Gel

The simulation results have shown that the Brownian dynamics technique is useful for studying the coagulation in dense colloidal systems. Both characteristic time scales as well as structural information is obtained, which is a first step away from the fundamental equations of motion for the colloidal particles towards the macroscopically observed material properties. Nevertheless, the technique needs to be refined and improved in order to allow a better comparison with the experimental results.

4.2.1 Way of Destabilization

- *Continuous variation of interaction*

  The characteristic coagulation times in our simulations are valid for an instantaneous destabilization, i.e. for a discrete switch from a repulsive to an attractive interaction potential (subsection 3.2.4). However, the experimental results show that the coagulation in the real system occurs on a much larger time scale which is given by the limited rate of change in the interaction potential [99Bal]. A comparison of the simulation results and the experimental results suggest that the particle configuration in the real system is in (or close to) equilibrium with the corresponding potential at every instant of the coagulation process. Further simulation studies on the destabilization of colloidal system should therefore account for a continuously progressing destabilization. It is crucial that the rate of interaction potential change is much slower than the coagulation times calculated from the switch-potential technique.

- *Spatial inhomogeneities in the interaction*

  In a model system, the interaction potential can be changed simultaneously between any pair of particles throughout the whole sample volume. However, this is often not the case in experimental systems. Even in the Direct Coagulation Casting [95Baa, 99Gau], where the interaction potential is changed intrinsically by an enzyme reaction, the potential change starts from discrete points given by the location of the enzymes. It is therefore desirable to examine in future studies the influence of the spatial inhomogeneities in the interaction potential on the structure of the percolating network.

4.2.2 Bonds and Their Effects

- *Rigid versus stiff bonds, constraints*

  The destabilization of a colloidal suspension invokes a transition from an assembly of freely moving particles to clusters and, finally, to a network of linked particles. It has been mentioned in the corresponding subsections 3.2.1 and 3.2.5, that the increasing number of constraints on the particle dynamics during coagulation is a substantial problem. The following points should be investigated in more detail. Firstly, there are several possible algorithms to keep touching particles at fixed separation. One should thus examine and quantify in as far the choice of the algorithm influences the coagulation kinetics and the structure of the final network. This may be relevant particularly in the later stages of coagulation where a lot of bonds are already formed and where rearrangements take place. Secondly, the bond angles in our simulation are allowed to change without any hindrance due to surface friction. Nevertheless, the possibility of a finite or even an infinite surface friction needs to be considered since it may well alter the process of rearrangement in the network. We emphasize that this implies to include rotational degrees of freedom. Such simulations have been performed at solid contents $\phi \leq 0.15$ [95Bij, 97Whi], however, it is desirable to study also systems with solid contents as high as $\phi = 0.5$ commonly used in colloidal processing.

- *Gel aging*

  The results of this study are concerned with the coagulation, i.e. with the solidification of a stable suspension. The simulations stop when all particles are part of one single network (subsection 3.3.1). No simulations have been performed beyond this point since we expect that the choice of the bond-handling algorithm has a stronger influence on the particle dynamics the more the gelation proceeds (see above). Nevertheless, it is evident that the real system can still perform rearrangements in the network, which is known as gel aging [90Bri]. In order to quantify in as far gel aging alters the structure and the stability of the network, the Brownian dynamics technique provides a useful tool.

- *Mechanical properties*

  Apart from the intriguing coagulation kinetics and structure formation in dense colloidal suspensions, the major interest in material science is in the properties of the final material. In this study, we have provided detailed information on the preferably formed structure and on the building blocks therein (section 3.4). However, this is only a first step towards a better understanding of the material properties of

the final coagulated wet body. In order to give a better interpretation of the experimental results on the mechanical behavior, it is necessary to perform simulations which probe the following characteristics: (i) the linear and (ii) the nonlinear viscoelastic behavior, particularly (iii) the yield stress.

The linear viscoelastic properties have been studied by computer simulation for Lennard-Jones gels [96Lod] and for colloidal gels for low solid content ($\phi = 0.05$) [97Whi]. Recently, simulations are reported which examine strain hardening, yield stress characteristics, and stress recovery, although for low solid contents only ($\phi = 0.05$) [98Whi]. It is necessary to extent such simulations to higher solid contents which are common to colloidal processing techniques of dense suspensions.

The response of a dry particle system to an external force has been studied in detail. One of the most important results is the existence of so-called load-bearing strings, also called 'force chains', which contribute the major part to the mechanical stability of the system whereas other regions in the network are comparably free of stress [86Tho, 95Liu, 98Rad]. It may be fruitful to do a thorough analysis of the relation between wet and dry particle systems.

4.3 References

[84Jef] D. J. Jeffrey and Y. Onishi, "Calculation of the resistance and mobility functions for two unequal rigid spheres in low-Reynolds-number flow", *J. Fluid Mech.*, *139*, 261–290 (1984).

[86Tho] C. Thornton and D. J. Barnes, "Computer simulated deformation of compact granular assemblies", *Acta Mechanica*, *64*, 45–61 (1986).

[90Bri] C. J. Brinker and G. W. Scherrer, *Sol-gel science*, Academic Press, London (1990).

[91Kim] S. Kim and S. J. Karrila, *Microhydrodynamics: principles and selected applications*, Butterworth-Heinemann series in Chemical Engineering, Stoneham MA (1991).

[92Jef] D. J. Jeffrey, "The calculation of the low Reynolds number resistance functions for two unequal spheres", *Phys. Fluids A*, *4*(1), 16–29 (1992).

[95Baa] F. H. Baader, "Enzymkatalisiertes Formgebungsverfahren für Aluminiumoxid-Keramiken", PhD thesis, Diss. ETH No. 11208, ETH Zürich, Switzerland (1995).

[95Bij] B. H. Bijsterbosch, M. T. A. Bos, E. Dickinson, J. H. J. van Opheusden, and P. Walstra, "Brownian dynamics simulation of particle gel formation: from argon to yoghurt", *Farad. Discuss.*, *101*, 51–64 (1995).

[95Liu] C. h. Liu, S. R. Nagel, D. A. Schecter, S. N. Coppersmith, S. Majumdar, O. Narayan, and T. A. Witten, "Force fluctuations in bead packs", *Science*, *269*, 513–515 (1995).

[96Lod] J. F. M. Lodge and D. M. Heyes, "Brownian dynamics simulations of aggregation and gel-formation in Lennard-Jones fluids", *Phys. Chem. Liquids*, *31*, 209–230 (1996).

[97Whi] M. Whittle and E. Dickinson, "Brownian dynamics simulation of gelation in soft sphere systems with irreversible bond formation", *Mol. Phys.*, *90*(5), 739–757 (1997).

[98Rad] F. Radjai, D. E. Wolf, M. Jean, and J.-J. Moreau, "Bimodal character of stress transmission in granular packings", *Phys. Rev. Lett.*, *80*(1), 61–64 (1998).

[98Whi] M. Whittle and E. Dickinson, "Large deformation rheological behaviour of a model particle gel", *J. Chem. Soc. Farad. Trans.*, *94*(16), 2453–2462 (1998).

[99Bal] B. Balzer and M. K. M. Hruschka and L. J. Gauckler, "Coagulation kinetics and mechanical behavior of wet alumina green bodies produced via DCC", (submitted to *J. Coll. Interf. Sci.* on 1/1999).

[99Gau] L. J. Gauckler, T. J. Graule, F. H. Baader, and J. Will, "Enzyme catalysis of alumina forming", *Key Eng. Mat., 159–160*, 135–150 (1999).

Appendix

Calculation of the Resistance Tensors

This appendix contains the explicit expressions for the tensors $\boldsymbol{R}_{FV}$, $\boldsymbol{R}_{FE}$, $\boldsymbol{R}_{SV}$, and $\boldsymbol{R}_{SE}$ from section 2.5 in the lubrication approximation. Due to the pairwise additivity of hydrodynamics which has been assumed in this study, the expressions are only given for two interacting particles. For a comprehensive overview of the hydrodynamic interaction tensors, the reader is referred to the Book "Microhydrodynamics" by Kim and Karrila [91Kim] and to the publications by Jeffrey and Onishi [84Jef, 92Jef].

The tensors under consideration give a linear relationship between the particle velocities $\boldsymbol{w}_i$ (relative to the background flow) and the rate of strain tensor $\boldsymbol{E}^{\infty}$ on one hand and the hydrodynamic forces $\boldsymbol{F}_i^{\mathrm{H}}$ and particle stresslets $\boldsymbol{S}_i$ (stress $\sigma = (1/V)\sum_i \langle \boldsymbol{S}_i \rangle$) on the other hand

$$\begin{pmatrix} \boldsymbol{F}_1^{\mathrm{H}} \\ \boldsymbol{F}_2^{\mathrm{H}} \\ \boldsymbol{S}_1 \\ \boldsymbol{S}_2 \end{pmatrix} = \eta_s \begin{pmatrix} -\boldsymbol{A}_{11} & -\boldsymbol{A}_{12} & \tilde{\boldsymbol{G}}_{11} & \tilde{\boldsymbol{G}}_{12} \\ -\boldsymbol{A}_{21} & -\boldsymbol{A}_{22} & \tilde{\boldsymbol{G}}_{21} & \tilde{\boldsymbol{G}}_{22} \\ -\boldsymbol{G}_{11} & -\boldsymbol{G}_{12} & \boldsymbol{M}_{11} & \boldsymbol{M}_{12} \\ -\boldsymbol{G}_{21} & -\boldsymbol{G}_{22} & \boldsymbol{M}_{21} & \boldsymbol{M}_{22} \end{pmatrix} \cdot \begin{pmatrix} \boldsymbol{w}_1 \\ \boldsymbol{w}_2 \\ \boldsymbol{E}^{\infty} \\ \boldsymbol{E}^{\infty} \end{pmatrix} \tag{A1}$$

The viscosity of the suspending liquid is denoted by η_s. The following relations between eqn. (A1) and the tensors $\boldsymbol{R}_{FV}$, $\boldsymbol{R}_{FE}$, $\boldsymbol{R}_{SV}$, and $\boldsymbol{R}_{SE}$ from section 2.5 hold:

$$\boldsymbol{R}_{FV} = \begin{pmatrix} \boldsymbol{A}_{11} & \boldsymbol{A}_{12} \\ \boldsymbol{A}_{21} & \boldsymbol{A}_{22} \end{pmatrix} \tag{A2}$$

$$\boldsymbol{R}_{FE} = \begin{pmatrix} \tilde{\boldsymbol{G}}_{11} & \tilde{\boldsymbol{G}}_{12} \\ \tilde{\boldsymbol{G}}_{21} & \tilde{\boldsymbol{G}}_{22} \end{pmatrix} \tag{A3}$$

$$\boldsymbol{R}_{SV} = \begin{pmatrix} \boldsymbol{G}_{11} & \boldsymbol{G}_{12} \\ \boldsymbol{G}_{21} & \boldsymbol{G}_{22} \end{pmatrix} \tag{A4}$$

$$\boldsymbol{R}_{SE} = \begin{pmatrix} \boldsymbol{M}_{11} & \boldsymbol{M}_{12} \\ \boldsymbol{M}_{21} & \boldsymbol{M}_{22} \end{pmatrix} \tag{A5}$$

Let us denote the separation vector between two particles by $\boldsymbol{r} = \boldsymbol{x}_2 - \boldsymbol{x}_1$ and the unit vector along the line of center by $\boldsymbol{n} = \boldsymbol{r}/|\boldsymbol{r}|$. Cartesian components are represented with latin letters *i, j, k, l*. The submatrices $\boldsymbol{A}_{\alpha\beta}$, $\boldsymbol{G}_{\alpha\beta}$, $\tilde{\boldsymbol{G}}_{\alpha\beta}$, and $\boldsymbol{M}_{\alpha\beta}$ are then in the lubrication limit given as:

$$\boldsymbol{A}_{11,\,ij} = \boldsymbol{A}_{22,\,ij} = -\boldsymbol{A}_{12,\,ij} = -\boldsymbol{A}_{21,\,ij} = \left\{\frac{3}{8}\pi\frac{d}{\xi}\right\} n_i n_j \tag{A6}$$

$$\boldsymbol{G}_{11,\,ijk} = -\boldsymbol{G}_{22,\,ijk} = -\boldsymbol{G}_{12,\,ijk} = \boldsymbol{G}_{21,\,ijk} = \left\{\frac{3}{16}\pi\frac{d^2}{\xi}\right\}\left(n_i n_j - \frac{1}{3}\delta_{ij}\right)n_k \tag{A7}$$

$$\tilde{\boldsymbol{G}}_{11,\,ijk} = -\tilde{\boldsymbol{G}}_{22,\,ijk} = \tilde{\boldsymbol{G}}_{12,\,ijk} = -\tilde{\boldsymbol{G}}_{21,\,ijk} = \left\{\frac{3}{16}\pi\frac{d^2}{\xi}\right\} n_i\left(n_j n_k - \frac{1}{3}\delta_{jk}\right) \tag{A8}$$

$$\boldsymbol{M}_{11,\,ijkl} = \boldsymbol{M}_{22,\,ijkl} = \boldsymbol{M}_{12,\,ijkl} = \boldsymbol{M}_{21,\,ijkl} = \left\{\frac{3}{32}\pi\frac{d^3}{\xi}\right\}\left(n_i n_j - \frac{1}{3}\delta_{ij}\right)\left(n_k n_l - \frac{1}{3}\delta_{kl}\right) \tag{A9}$$

Here d stands for the particle diameter and ξ is the reduced surface-surface separation between interacting particles $\xi = (r-d)/d$.

The above expressions include only the highest order contributions of the lubrication approximation. All less divergent terms are not considered here. It should go without saying that this form (A6-A9) holds only for hydrodynamic interaction between nearest neighbors.

References

[84Jef] D. J. Jeffrey and Y. Onishi, "Calculation of the resistance and mobility functions for two unequal rigid spheres in low-Reynolds-number flow", ***J. Fluid Mech.***, ***139***, 261–290 (1984).

[91Kim] S. Kim and S. J. Karrila, ***Microhydrodynamics: Principles and selected applications***, Butterworth-Heinemann series in Chemical Engineering, Stoneham MA (1991).

[92Jef] D. J. Jeffrey, "The calculation of the low Reynolds number resistance functions for two unequal spheres", ***Phys. Fluids A***, *4*(1), 16–29 (1992).

Curriculum Vitae

Personal data

Date and place of birth:	April 10, 1969, Zürich, Switzerland
National origin:	Switzerland

Education

4/1976 to 3/1982	Primary School, Gockhausen near Zürich, Switzerland
4/1982 to 9/1988	Gymnasium / Grammar School Rämibühl, Zürich, Switzerland (Maturität Typus B)
11/1990 to 3/1995	Physics studies, Swiss Federal Institute of Technology, ETHZ, Zürich, Switzerland
4/1995 to 8/1995	Diploma work "Gaussian Approximation of Stochastic Differential Equations in Connection with Linear Response Theory" Polymer Physics Group, Prof. Dr. H. C. Öttinger, Swiss Federal Institute of Technology, ETHZ, Zürich, Switzerland
1/1996 to 3/1999	Ph.D. study "Brownian Dynamics Simulation of Stable and of Coagulating Colloids in Aqueous Suspension", Polymer Physics Group, Prof. Dr. H. C. Öttinger, and Institute for Nonmetallic Inorganic Materials, Prof. Dr. L. J. Gauckler, Swiss Federal Institute of Technology, ETHZ, Zürich, Switzerland

Professional experience

10/1988 to 12/1988	Practical work at Enso-Gutzeit Oy, Research Laboratory, Dipl. Ing. T. Linnahalme, Imatra, Finland

List of Symbols

Latin Symbols

A_H	(J)	Hamaker constant
$\boldsymbol{B}$	$(\mathrm{m}/\sqrt{\mathrm{s}})$	Choleski-decomposition of diffusion matrix
$\tilde{\boldsymbol{B}}$	$(\mathrm{N}\sqrt{\mathrm{s}})$	Choleski-decomposition of resistance matrix
$C_\mathrm{s}(t)$	(Pa^2)	Stress autocorrelation function at equilibrium
d	(m)	Particle diameter
d_eff	(m)	Effective 'capture' particle diameter
d_f	(-)	Fractal dimension of aggregates
D_0	(m^2/s)	Single particle diffusion coefficient
D_{ik}	(m^2/s)	Components of the diffusion tensor
D^L	(m^2/s)	Long-time diffusion coefficient
D^S	(m^2/s)	Short-time diffusion coefficient
e	(C)	Elementary charge
$\boldsymbol{E}^\infty$	(s^{-1})	Strain rate tensor
$\Delta_\mathrm{r}E$	(J)	Relative energy barrier (local maximum-secondary minimum)
$\Delta_\mathrm{t}E$	(J)	Total energy barrier (local maximum)
$\boldsymbol{F}^\mathrm{B}$	(N)	Brownian force
$\boldsymbol{F}^E$	(N)	Strain rate force
$\boldsymbol{F}^\mathrm{H}$	(N)	Hydrodynamic force
$\boldsymbol{F}^\mathrm{pot}$	(N)	Potential interaction force
$g(r)$	(-)	Pair distribution function
I	(mol/l)	Ionic strength
k_B	(J/K)	Boltzmann constant
K_{ij}	(m^3/s)	Rate constants of Smoluchowski equation
L, `Lbox`	(m)	Box length
`Lcell`	(m)	Length of the cells for the linked-cell list algorithm
m	(kg)	Particle mass
M_c	(-)	Cluster mass (in units of particle mass)

n_k	(m^{-3})	Volume density of clusters consisting of k primary particles
N	(-)	Number of particles in simulation box
N_{bonds}	(-)	Number of bonds
N_c	(-)	Number of clusters
N_{crct}	(-)	Number corrected bonds per integration step
N_f	(-)	Number of free (unbonded) particles
N_{flop}	(-)	Number of floating point operations
N_{iter}	(-)	Number iterations in the conjugate gradient routine
$N^{(k)}$	(-)	Number particles with k attached neighbors
$N_{1,2}$	(Pa)	First and second normal stress differences
`Nbin`	(-)	Number of potential and force values stored in the corresponding lists
`Ncell`	(-)	Number of small cells for the linked-cell list algorithm in each direction
`Ncell`^{3}	(-)	Total number of small cells for the linked-cell list algorithm
`Nstep`	(-)	Number of integration time steps
$p(\theta)$	(-)	Bond angle distribution
pH_{iep}	(-)	pH at the isoelectric point
$\boldsymbol{P}_{12}$	(-)	Projection operator on connector vector
r	(m)	Particle separation (center-center)
$\boldsymbol{r}$	(m)	Particle separation vector (center-center)
r_{cutoff}	(m)	Cut-off separation in the interaction potential
$r_{\text{cutoff}}^{\text{lubr}}$	(m)	Cut-off separation in the lubrication interaction
$r_{\text{sec min}}$	(m)	Separation of secondary minimum in the interaction potential
r_{st}	(m)	Particle separation within a string (center-center)
$\Delta\boldsymbol{r}(t)$	(m)	Particle displacement
$\boldsymbol{R}_{FV}$	(N s/m)	Hydrodynamic resistance matrix (second rank)

$\boldsymbol{R}_{FE}$	(N s)	Force-strain rate relating tensor (third rank)
$\boldsymbol{R}_{SV}$	(J s/m)	Stress-particle velocity relating tensor (third rank)
$\boldsymbol{R}_{SE}$	(J s)	Stress-strain rate relating tensor (forth rank)
$\Re_\theta$	(-)	Probability of bond angles in the vicinity of θ
s	(s^{-1})	Laplace variable, Laplace frequency
s_{nn}	(m)	Surface to surface separation between nearest neighbors
$t,t',\ldots$	(s)	Time
Δt	(s)	Time step in the integration scheme
T	(K)	Absolute temperature
$\boldsymbol{v}$	(m/s)	Velocity
$\boldsymbol{v}^\infty$	(m/s)	Imposed flow field for infinite dilution
V	(m^3)	Volume of simulation box
$V(r)$	(J)	Interaction potential between colloidal particles
V_0	(J)	Strength of the Yukawa potential
$\boldsymbol{w}$	(m/s)	Particle velocity relative to background flow
$\boldsymbol{W}$	($\sqrt{s}$)	Wiener process (stochastic calculus)
w	(-)	Order of weak convergence of a numerical integration scheme
$\Delta\boldsymbol{x}$	(m)	Particle displacement relative to background flow field
z	(-)	Valency of ions

Greek Symbols

$\alpha, \alpha_i,\ldots$	(-)	Fitting parameters
$\beta, \beta_i,\ldots$	(-)	Fitting parameters
$\dot{\gamma}$	(s^{-1})	Shear rate
$\dot{\gamma}_{order}$	(s^{-1})	Shear rate for the disorder-order transition
Γ	(s^{-1})	Velocity gradient tensor of fluid flow field
$\delta(t)$	(s^{-1})	Dirac delta function
ε_0	(C/Vm)	Dielectric constant

ε_r	(-)	Relative dielectric constant
$\varepsilon_{it,max}$	(-)	Accuracy criterion for the conjugate gradient technique
ε_{tol}	(-)	Maximal tolerance on bond length fluctuations
ζ	(kg/s)	Single particle friction coefficient
η	(Pa s)	Viscosity
η^{part}	(Pa s)	Particle contribution to the suspension viscosity
η_s	(Pa s)	Viscosity of the suspending liquid
θ	(-)	Bond angle
κ	(m^{-1})	Inverse of the Debye screening length
κ_0	(-)	Inverse of the Yukawa screening length (in units of d^{-1})
ξ	(-)	Rescaled surface-surface separation between particles
ξ_{cutoff}^{lubr}	(-)	Rescaled surface-surface cut-off separation in the lubrication interaction
Π_b	(-)	Reduced average coordination number
$\Pi_b^{(\infty)}$	(-)	Reduced average coordination number of the stationary network
Π_c	(-)	Reduced connectivity/cross-linking parameter
$\Pi_c^{(\infty)}$	(-)	Reduced connectivity/cross-linking parameter of the stationary network
σ_{ik}	(Pa)	Components of stress tensor
σ^B	(Pa)	Brownian stress contribution
σ^H	(Pa)	Hydrodynamic stress contribution
σ^{part}	(Pa)	Particle contribution to the total stress
σ^P	(Pa)	Potential interaction stress contribution
σ^{total}	(Pa)	Total stress of the suspension
σ^T	(Pa)	Thermodynamic stress contribution
τ	(s)	Characteristic time scale
τ_{Br}	(s)	Brownian time scale
τ_b	(s)	Characteristic time scale associated with the time evolution of the reduced average coordination number

τ_c	(s)	Characteristic time scale associated with the time evolution of number of clusters
τ_d	(s)	Transition time for short- to long-time diffusion
τ_{Eu}	(s)	Eu-Ohr time scale
$\tau_{f,1/2}$	(s)	Time after which the number of free particles has reduced by a factor 1/2
$\tau_{f,1/10}$	(s)	Time after which the number of free particles has reduced by a factor 1/10
τ_{gel}	(s)	Endpoint of all coagulation runs: time when all particles become part of the same cluster
τ_{jump}	(s)	Characterstic jumping time for the sliding strings
τ_p	(s)	Time scale of momentum relaxation
τ_{res}	(s)	Time scale of highest resolution in the mean square displacement data
τ_s	(s)	Characteristic decay time of the stress autocorrelation function
τ_{span}	(s)	Physical time span covered by the simulation
ϕ	(-)	Solid content of the suspension
ϕ_m	(-)	Maximum solid content of the suspension
ϕ_{perc}	(-)	Percolation threshold
ϕ_{rcp}	(-)	Maximum solid content for random close packing
ϕ_{rlp}	(-)	Maximum solid content for random loose packing
$\Phi(t)$	(Pa)	Stress relaxation function
ψ_0	(V)	Surface potential
$\tilde{\psi}$	(V)	Rescaling parameter for surface potential